WARSAW UNIVERSITY OF TECHNOLOGY

Institute of Electrical Machines

Ph.D. THESIS

Torsten Wichert, M.Sc.

Design and Construction Modifications of Switched Reluctance Machines

Supervisor
Pawel Staszewski, Ph.D., D.Sc.
Hans Kuß, Prof. Dr.-Ing. habil.

Warsaw, 2008

DESIGN AND CONSTRUCTION MODIFICATIONS OF SWITCHED RELUCTANCE MACHINES

(Abstract)

Information on the structure of considered drive system with reluctance motor, principle of operation and mathematical model of the motor, principle of the energy conversion in analysed system and elementary types of supply devices have been presented in initial part of the thesis in context of the large world wide bibliography. The principal design procedures of Switch Reluctance Motor (SRM) as: main dimensions calculation, number of poles and air-gap determination, correlation of dimensions in pole zone and principles of winding design have been discussed in this part as well.

Proposed by author algorithms of calculation of parameters and operation SRM characteristics have been described in main part of this thesis. The method of winding inductance and static torque characteristic calculation are presented. The analysis and the methods of determination of motor and converter losses are the very important parts of the research. The new calculation method of SRM's iron losses on the basis of a modified STEINMETZ-equation is developed. The influence of magnetic circuit saturation on motor operation characteristics is discussed and the model of motor dynamic behaviour is presented. Based on presented calculation algorithms the hybrid 3-parts effective design program for SRM's has been finally proposed. The first part of this program "Design SRM" enables the realization of numerous effective design calculations using analytical quick methods. The second part of the program performs the field analysis of chosen construction version of the machine by numerical calculation of electromagnetic circuit using finite element method. This part is the complimentary tool for evaluation of machine construction during design procedure and can be used in case when the construction modifications are considered for improvement of machine parameters and characteristics. The third part of hybrid design program refers to the simulation of the drive dynamics. These problems are useful for evaluation of the properties of whole drive system. Model of motor dynamics is elaborated using Simplorer 4.2 software. The motor parameters calculated in earlier design procedures are used in this model. The modelling of dynamics takes into account the different methods of motor control.

The exemplary design calculations have been made for three SRM's destined to the different industrial drives. Three motor prototypes made by factories were tested in laboratories. The calculation and measurement results have been compared. The correctness and effectiveness of proposed design procedures was finally confirmed. The structural analysis of calculation and measurement errors was made in the thesis as well.

The principal personal records of the author as well as future research areas have been presented in final part of the thesis.

PROJEKTOWANIE I MODYFIKACJE KONSTRUKCJI MASZYN RELUKTANCYJNYCH PRZEŁĄCZALNYCH

(Streszczenie)

W początkowej części pracy przedstawiono w oparciu o bogatą literaturę podstawowe informacje o strukturze rozpatrywanego układu napędowego z silnikiem reluktancyjnym, zasadę działania silnika i jego model matematyczny, zasadę przemiany energii w analizowanym układzie, podstawowe typy zasilaczy oraz sposoby sterowania. W syntetyczny sposób przedstawiono zasadnicze elementy projektowania maszyn reluktancyjnych przełączalnych: obliczanie głównych wymiarów, dobór liczby biegunów, określenie szczeliny powietrznej i proporcji wymiarowych w strefie biegunowej oraz zasady projektowania uzwojenia.

W głównej części pracy opisano stosowane przez autora algorytmy obliczeń parametrów i charakterystyk silnika. Przedstawiono metodę obliczeń indukcyjności uzwojenia i wyznaczenia charakterystyk momentu statycznego. Duży nacisk położono na analizę i metody wyznaczania strat silnika i przekształtnika. Zaproponowano nową metodę obliczania strat w żelazie na podstawie zmodyfikowanego równania STEINMETZ'A. Przedstawiono model obliczeń dynamicznych silnika i przeanalizowano wpływ nasycenia obwodu magnetycznego na jego charakterystyki. W oparciu o przedstawione algorytmy obliczeń zaproponowano w rezultacie hybrydowy 3-częściowy program efektywnych obliczeń projektowych silnika. Pierwsza część tego programu „Design SRM" umożliwia wykonanie sprawnych, wielokrotnych obliczeń projektowych w oparciu o szybkie metody analityczne. Druga część realizuje polową analizę wybranej wersji konstrukcyjnej maszyny w oparciu o numeryczne obliczenia obwodu elektromagnetycznego metodą elementów skończonych. Część ta ma charakter komplementarnego narzędzia analizy projektu silnika oraz może służyć celom modyfikacji konstrukcji silnika pod kątem poprawy jego parametrów i charakterystyk. Trzecia część hybrydowego programu projektowania dotyczy symulacji dynamiki napędu, co jest przydatne dla oceny całego układu napędowego. Model dynamiczny opracowano w oparciu o oprogramowanie Simplorer 4.2. W modelu wykorzystano obliczone we wcześniejszych etapach parametry silnika. Modelowanie uwzględnia różne metody sterowania silnika.

Przykładowe obliczenia projektowe wykonano dla trzech silników reluktancyjnych przeznaczonych do różnych napędów przemysłowych. Fabrycznie wykonane trzy prototypy silników zostały przetestowane w warunkach laboratoryjnych. Porównano wyniki obliczeń i pomiarów potwierdzając w rezultacie poprawność i efektywność zaproponowanych procedur projektowania. Dokonano strukturalnej analizy błędów obliczeniowych i pomiarowych.

W końcowej części pracy przedstawiono elementy oryginalne autora i wskazano dalsze kierunki badań.

DESIGN AND CONSTRUCTION MODIFICATIONS OF
SWITCHED RELUCTANCE MACHINES

Preface

Switched Reluctance Machines (SRMs) applied in adjustable speed drives are receiving during the last two decades considerable attention from industry since they are characterised by rigid construction, high operation reliability, high efficiency, high torque to inertia ratio and finally low manufacturing costs. The successful realization of a SRM drive demands inter alia of the determination of the best motor construction from the point of view of the requirements of considered drive. Each motor construction is described by a set of static and dynamic parameters and operation characteristics. The application of the effective calculation and design algorithms of considered motors enables the quick receiving of these data.

Although the design principles of the SRMs are available in different fragments in numerous bibliography positions, there no exists, according to knowledge of author, the complex design procedure of whole drive system taking into account the SRM, control system and supply device as well.

The hybrid design method for SRM drives with application of new analytical calculation methods, finite element method and simulation models is proposed in this thesis. The calculation/design system is characterised by important effectivity and reliability. The new possibilities in analytical determination of saturation effects and core losses under the different modes of control, including sensorless method, are also taken into account. The correctness of the proposed design algorithms was verified by laboratory tests made on three motor prototypes manufactured in industry.

This dissertation provides the elements indispensable for more accurate and complex analysis and design of drives with switch reluctance motors. The elements of electrical motor and control system design as well as the considerations on the choice of supply device and controller subsystems are jointed in the thesis for final receiving of the design tool for considered industrial drive system.

The dissertation was made during my work as scientific assistant at the 'Centre of Applied Researches and Technology Dresden e.V.' (ZAFT e.V) from June 2004 to December 2007. It is a cooperative PhD procedure between the University of Applied Science (HTW) Dresden (FH) and the Electrical Engineering Faculty of Warsaw University of Technology.

PROJEKTOWANIE I MODYFIKACJE KONSTRUKCJI MASZYN RELUKTANCYJNYCH PRZEŁĄCZALNYCH

Przedmowa

Przełączane silniki reluktancyjne stosowane w napędach o regulowanej prędkości obrotowej przyciągają w ostatnich dwóch dekadach coraz większą uwagę przemysłu ze względu na prostotę budowy, niezawodność działania, wysoki stosunek wytwarzanego momentu do momentu bezwładności oraz niskie koszty produkcji. Wykonanie dobrego projektu napędu elektrycznego z przełączalnym silnikiem reluktancyjnym związane jest między innymi z opracowaniem możliwie najlepszej z punktu widzenia rozważanego napędu wersji konstrukcyjnej tego silnika opisanej zbiorem jego statycznych i dynamicznych parametrów i charakterystyk. W celu uzyskania tych danych niezbędna jest znajomość efektywnych metod obliczeń i projektowania tego typu maszyny.

Pomimo iż metody projektowania przełączanych silników reluktancyjnych są w różnych aspektach szeroko opisywane w literaturze, brak jest w rozeznaniu autora kompleksowej procedury projektowania całego układu napędowego z uwzględnieniem sposobu sterowania i zasilania.

W pracy zaproponowano hybrydową metodę projektowania omawianych napędów z wykorzystaniem nowych analitycznych metod obliczeniowych, metody elementów skończonych i modeli symulacyjnych. Zastosowany aparat obliczeniowo-projektowy charakteryzuje się dużą efektywnością, niezawodnością oraz dostarcza nowych możliwości w badaniu efektów nasycenia i strat w żelazie podczas sterowania przełączanego silnika reluktancyjnego za pomocą różnych metod (w tym bezczujnikowych). Poprawność zastosowanych metod obliczeniowo-projektowych zweryfikowana została poprzez badania laboratoryjne trzech prototypów silników wykonanych w warunkach przemysłowych.

Niniejsza rozprawa dostarcza wiedzy niezbędnej do dokładniejszej i bardziej kompleksowej analizy i projektowania napędów z przełączanymi silnikami reluktancyjnymi łącząc zagadnienia projektowania maszyny elektrycznej, układu sterowania oraz doboru zasilacza energoelektronicznego.

Prezentowana rozprawa doktorska została wykonana podczas mojej pracy na stanowisku asystenta naukowego w Zentrum fur Angewandte Forschung und Technologie w okresie od czerwca 2004 do kwietnia 2007. Pracę doktorską wykonano w oparciu o porozumienie pomiędzy Hochschule fur Technik und Wirtschaft w Dreznie a Wydziałem Elektrycznym Politechniki Warszawskiej.

Table of contents

List of symbols and abbreviations

FEM	Finite Elements Method	
HIC	Hard Initial Charge	
SIC	Soft Initial Charge	
SRG	Switched Reluctance Generator	
SRM	Switched Reluctance Machine	
SRM I	Manufactured prototype I with modified rotor geometry for vacuum cleaner	
SRM II	Manufactured prototype II for high speed textile spindle drive	
SRM III	Manufactured prototype III for use in an automatic truck gear	
SR drive	Switched Reluctance drive	
TSF	Torque Sharing Function	
TUW	University of Technology Warsaw	

α	STEINMETZ coefficient	[-]
α_{Cu}	Temperature coefficient of copper	[K]
β	STEINMETZ coefficient	[-]
β_r, β_s	Rotor- and stator pole angle	[deg]
χ_{Cu}	Electrical conductivity of copper	[S/mm]
γ_r, γ_s	Angle of the rotor and stator pole edges in case of trapezoidal (tapered) form	[deg]
Δi	Hysteresis band width	[A]
η	Efficiency	[%]
Φ	Magnetic flux	[Vs]
φ_{slot}, φ_{Fe}	Slot fill factor; iron fill factor	[-]
λ_u	Unsaturated inductance ratio	[-]
μ	Magnetic permeability	[Vs/Am]
Θ	Rotor position angle	[deg]
Θ_{el}, Θ_{mech}	Rotor position angle in electrical and in mechanical degree	[deg]
Θ_{end}	End angle when commutated phase current is reduced to zero again	[deg]
Θ_{est}	Estimated rotor position angle	[deg]
Θ_d	'dwell' angle	[deg]
Θ_{on}, Θ_{off}	Turn-on and turn-off angle of the phase current	[deg]
Θ_s	Phase shift angle between adjacent motor phases	[deg]
Θ_{sk}	Stroke angle	[deg]
σ	CARTER's coefficient	[-]
σ_a	Aligned saturation factor	[-]
τ_r, τ_r	Rotor- and stator pole pitch	[mm]

ω	Angular frequency	[1/s]
ψ	Magnetic flux-linkage	[Vs]
A	Cross section area	[mm^2]
A_s	Specific electric loading	[A/mm]
A_{wc}	Winding cross section area	[mm^2]
$A_{w, slot}$	Slot area	[mm^2]
a	Gravity	[m/s^2]
B	Flux density	[T]
$\hat{B}$	Maximum value of flux density	[T]
B_r, B_t	Radial and tangential flux density component	[T]
b_c	Width of rectangular stator coil	[mm]
C_m	STEINMETZ coefficient	[-]
D	Bore diameter respectively inner stator diameter	[mm]
D_{sh}	Shaft diameter	[mm]
D_r, D_s	Rotor and stator outer diameter	[mm]
D_w	Wire diameter	[mm]
EC	Energy ratio	[-]
e	Back-emf (electromotive force)	[V]
F	Sum of mmf drops	[A]
F_r, F_t	Radial and tangential force	[N]
f, f_s	Frequency, switching frequency	[Hz]
f_{eq}	Equivalent frequency	[Hz]
g, g_f	Air gap length; fictitious uniform air gap	[mm]
H	Magnetic field strength	[A/m]
h_c	Height of rectangular stator coil	[mm]
h_r, h_s	Height of the rotor and stator poles	[mm]
I, I_{ref}, I_{rms}	Constant current; reference current; r.m.s. current	[A]
I_p, I_{max}	Peak current, maximum current value	[A]
i	Instantaneous current	[A]
J	Current density	[A/mm^2]
J_i	Moment of inertia	[kgm^2]
k_{fr}	Friction coefficient	[Ws^2/m^4]
L	Inductance	[H]
L_a, L_u	Aligned (maximum) and unaligned (minimum) phase inductance	[H]
l	Rotor length	[mm]
l_{eff}	Effective core length	[mm]

l_{Fe}, l_{stk}	Iron length; stack length	[mm]
l_{oh}	Winding overhang length	[mm]
m	Number of simultaneously conducting phases	[-]
mmf	Magnetomotive force	[A]
n	Rotor speed	[rpm]
N_p, N_{ph}	Number of turns per pole; Number of turns per phase	[-]
N_s, N_r	Number of stator- and rotor poles	[-]
P_{Conv}	Converter losses	[W]
P_{Cu}, P_{Fe}	Copper losses; Core losses	[W]
P_{Fa}, P_s	Average conducting losses; Switching losses	[W]
P_{fr}	Friction losses	[W]
P_n	Rated output power	[W]
P_{mech}, P_{el}	Mechanical power; electrical power	[W]
p	Number of pole pairs	[-]
p_{Fe}	Specific core losses	[W/kg]
q	Number of phases	[-]
R, R_{ph}	Resistance; phase resistance	[Ω]
$\mathfrak{R}$	Reluctance	[A/Vs]
V	mmf drop	[A]
V_s, V_{dc}	Supply voltage (dc); dc link voltage	[V]
v_r	Rotor circumferential speed	[m/s]
T, T_n, T_e	Torque; rated torque value; electromagnetic torque	[Nm]
T_{av}, T_{max}	Average torque; maximum torque value	[Nm]
T_{mech}	Mechanical time period for one rotor revolution	[s]
T_{fr}, T_l	Friction torque; load torque	[Nm]
T_{ref}	Reference torque	[Nm]
t	Time	[s]
t_r, t_s	Width of the stator and rotor poles	[mm]
t_{ry}, t_{sy}	Width of the rotor and stator poles at the pole base	[mm]
t_{rpl}	Torque ripple coefficient	[-]
W_c, W_F	Magnetic coenergy; magnetic field energy	[Ws]
W_m	Mechanical work	[Ws]
y_r, y_s	Rotor and stator yoke thickness	[mm]

Introduction and motivations for research

The functionality of Switched Reluctance Machines (SRM) is already known for more than 150 years, but only the enormous improvements of the power electronics and their integration in drive technologies have made the great progress of adjustable speed drives with SRMs possible. Today the designing engineer can select from a number of different converter configurations adapted to the specific application. For current and torque control high efficient micro-controllers and digital signal processors (DSP) are available.

A SRM has salient poles on both stator and rotor. Each stator pole has a simple concentrated winding and there are no conductors of any kind on the rotor. Diametrically opposite windings are connected together either as a pair or in groups to form motor phases. For each phase a circuit with a single controlled switch is sufficient to supply an unidirectional current during appropriate intervals of rotor rotation. For forward motoring, the appropriate stator phase winding must remain excited only during the period when rate of change of phase inductance is positive. Else, the motor would develop braking torque or no torque at all.

Due to its simple and rugged construction, low manufacturing cost, fault tolerance capability and high efficiency the Switched Reluctance Motor is gaining more and more recognition in the electric drive market. Despite these advantages, the SRM has some drawbacks: it requires an electronic control and shaft position sensor, a huge capacitor is needed in the DC link and the double salient structure causes noise and torque ripple. Further, SRMs are typically designed to operate in magnetic saturation region to achieve a good utilization in terms of converter rating [1], [3], [8]. But the operation with magnetic saturation results in a strongly nonlinear relationship of output torque and input parameters, i.e. current and rotor position. That complicates the analytically calculation and control of this machine type considerably.

The SRM is pushed in many publications in the literature. Nevertheless, with these general publications the usage of that machine type for adjustable speed drives in industrial applications can not be assumed to be scientifically and technically solved since the prevailing papers just dealing with specific parts of SRMs problems [20, 37, 40-42, 44, 54-57, 64, 66, 78, 80, 86, 97, 100, 133, 139, 170, 178, 181]. The investigation and optimization of the whole drive system, consisting of motor, electronics and control occurs only in a very small scale. Therefore, the presented thesis has the intention to make a contribution to the hybrid design of complete SRM drive systems.

In recent times, approaches using machine design to influence the machine performance becoming more and more equivalently to efforts at current and hence torque control. The design of SRMs by numeric methods with FEM-programs (Finite Element Method) provides the most precise and proof results. However, calculations by FEM are time consuming and require special, relatively complicated and expensive software. For a complete design of new type series of machines with different dimension's variants the way of using only the FEM is

at present not practicable. Therefore software is necessary that can abbreviate considerably the preparation time for the following FEM-calculation. Also the dynamic operational behaviour and the combination of the electric machine with other components like energy storage, converter or mechanical elements must be considered. In that case parameters calculated during the design stage have to be involved in a simulation model.

To meet these requirements for an effective and reliable machine design, this thesis is aimed to find solutions to the above mentioned problems in terms of a new hybrid time-economic design-, calculation- and simulation procedure.

In context of the questions discussed above the **OBJECTIVE** of the thesis is:

1. **Elaboration of effective hybrid design program for SRM's taking into account all losses in drive system, field verification and modeling of dynamic operation as well.**

2. **Application of this program to the design calculation of three different SRM's destined to concrete industrial drives.**

3. **Demonstration of the correctness of proposed program by comparison of the calculation and measurement results made for three prototypes of SRM's manufactured in industry.**

Results of the research evaluated from the point of view of the presented above objective enable the formulation of the **THESIS TO BE PROVED** related to the PhD thesis:

The proposed in the thesis hybrid design program for SRM's enables the effective and more complex motor design from the point of view of considered drive requirements, in comparison with proposals published up to now and known by author from the bibliography.

In the proposed hybrid design program at first analytical and then field calculation methods and finally dynamic simulations have been developed. This program can perform:

1. Machine and winding design.

2. Steady-state calculations like torque-, flux- and inductance characteristics, copper and core losses of the motor, converter losses and finally system efficiency.

3. Verification of the projects by application of numerical field method (FEM).

4. Dynamic calculations like current waveform in dependence of speed and mode of control.

FEM models have been developed as the complimentary tool in respect to the analytical models. By means of a simulation model in SIMPLORER$^{®}$ the operational behaviour of the whole drive system can be investigated during various control modes. Also sensorless control can be researched.

The structure of this thesis presents the typical complete scheme of scientific technical research. After presentation in introduction some motivations for research the general description of Switch Reluctance Machines is given in Chapter 1. Next, the synthetic

informations on conventional design procedures for these machines are presented in Chapter 2. The most important Chapter 3 demonstrates the main calculation models, design algorithms and programs applied by author for solution of the complex technical problems as: calculation of machine parameters, operation characteristics, machine and drive losses etc… The dynamic calculations and influence of saturation are also presented. Finally the Hybrid Design Program is proposed by author and discussed. Simulation model of the SRM with application of SIMPLORER® software is presented in Chapter 4. After presentation the calculation models and design programs/tools the design examples of three industrial prototypes of SRM are shown in Chapter 5. The prototypes of 6/4-SRM for vacuum cleaner (conventional and modified versions), 6/4-SRM for an electric textile spindle drive and 8/6-SRM for an automatic truck gear are presented. When calculation models and design procedures give in final solution the concrete machine constructions described by calculation parameters and operation characteristics then usually the experimental verification and error's analysis is needed. These questions are the subject of Chapter 6. Laboratory tests are made for all SRM's constructions. The comparison of both calculation and experimental results was made. Personal contributions of the author in presented elaboration together with indication for future investigations and large summary of this work are the subject of the Chapters 7 and 8. Important bibliography (182 positions) is presented at the end of the thesis.

1   Fundamentals of Switched Reluctance Machines

1.1   General structure of SRM Drives

A SRM has salient poles on both stator and rotor. Its magnetic core consists of laminated steel. Each stator pole has a simple concentrated winding and there are no conductors of any kind on the rotor. Diametrically opposite windings are connected together either as a pair or in groups to form motor phases. For each phase a circuit with a single controlled switch (e.g. power transistor or IGBT) is necessary and sufficient to supply an unidirectional current during appropriate intervals of rotor rotation. Fig. 1.1 shows the typical cross sectional arrangement for a 4-phase SRM having N_s=8 stator and N_r=6 rotor poles ('8/6-SRM').
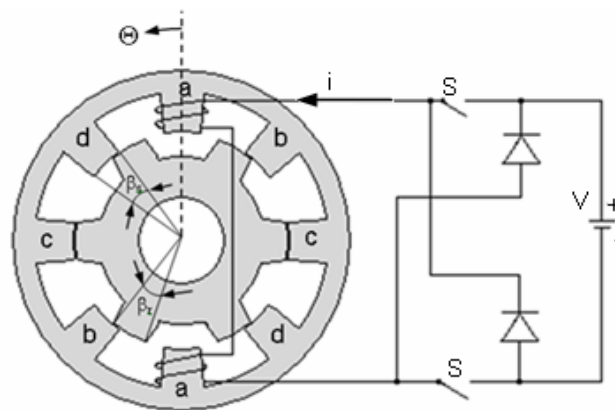

Fig. 1.1   Arrangement of a 4-phase 8/6-SRM with switching circuit for one phase

The main dimensions are the bore diameter D, the rotor length l, the stator outer diameter D_s and the stator- and rotor pole arc β_s and β_r, respectively. The angle Θ describes the rotor position. The starting point Θ=0 corresponds to the *unaligned position*, where the midpoint of the interpolar rotor gap faces the stator pole, as shown in Fig. 1.1 in the case of phase a. When current i is flowing in phase a, there is no torque in this position. If the rotor is displaced to either side of the unaligned position, there appears a torque that tends to displace the rotor still further and attract it towards the next *aligned position* where the centre of the stator and rotor poles are coinciding. The unaligned position is one of unstable equilibrium. When current is flowing in aligned position (phase c in Fig. 1.1), there is also no torque because the rotor is in a position of maximum inductance. If the rotor is displaced to either side of the aligned position, there is a restoring torque that tends to return the rotor towards the aligned position. The aligned position is one of stable equilibrium for a q-phase machine. The number of phases q is calculated with the number of stator poles N_s and rotor poles N_r:

$$q = \frac{N_s}{|N_s - N_r|} \tag{1.1}$$

Each phase produces a strong chorded magnetic field with 2p poles. Generally, the number of pole pairs of a SRM is

$$p = \frac{1}{2} \cdot \frac{N_s}{q} \tag{1.2}$$

The rotor- and stator pole pitch τ_r and τ_s pitch are defined as

$$\tau_r = \frac{2\pi}{N_r} \tag{1.3}$$

$$\tau_s = \frac{2\pi}{N_s} \tag{1.4}$$

The phase shift between successive stator phase inductances or flux linkages is given as:

$$\Theta_s = \left(\frac{2\pi}{N_r}\right) \cdot \frac{1}{q} = \frac{\tau_r}{q} \tag{1.5}$$

With the number of stator and rotor poles and the pole pitches the stroke-angle Θ_{sk} is:

$$\Theta_{sk} = \tau_s - \tau_r \tag{1.6}$$

For the example of the 8/6-SRM in Fig. 1.1 the stroke angle is $\Theta_{sk}= -15°$. The negative sign indicates an opposite rotating direction of the magnetic field in the stator and the mechanical rotor rotation. If $N_r>N_s$ the rotating direction of the rotor and the magnetic stator field are identically. In order to produce a continuous torque the stator angle β_r and rotor angle β_s must be greater than Θ_{sk} ensuring that there is at each time an overlapping of at least 2 stator and rotor pole pairs. To avoid an unsymmetrical radial loading, that condition leads to an even but unequal number of N_r and N_s. The number of strokes per revolution results from the product of the number of rotor poles and the phase number. The switching frequency f_s of one phase is

$$f_s = n \cdot N_r \tag{1.7}$$

with the rotor speed n in 1/s. For a 4-quadrant operation at least 3 phases are necessary. 4-quadrant means operation with positive and negative torque, and with positive or negative speed; that is motoring or generating in either the forward or reverse direction. Motoring operation with negative speed is realised by reversing the energizing sequence of the phases so that the magnetic field in the stator turns the rotation direction. Whereas generating operation is induced by a delay of phase energizing with the angle $\tau_r/2$. Then the phase current is flowing during negative slope of inductance- characteristic and produces a breaking torque.

1.2 Operating principle

Due to the salient stator and rotor poles the resistance of the magnetic circuit, the reluctance $\Re$, is a function of the rotor position. In the unaligned position, the air gap and therefore the reluctance are maximal. Since no saturation occurs, the flux linkage is a linear function of current. If the rotor moves toward the aligned position, the air gap decreases. On

the one hand this eases the flux built-up; on the other hand it saturates the magnetic circuit. Saturation of a typical magnetization curve occurs in two stages. When the overlap between the rotor and stator pole corners is quiet small, the concentration of flux saturates the pole corners, even at low current, so these parts of the magnetic circuit saturate first and cause an enlargement of the effective air gap. Thus, linear relationship is lost between current and flux-linkage. When the overlapping poles are closer to the aligned position, the yokes saturate at high current, tending to limit the maximum flux-linkage. These interactions are represented by the relationships between the flux-linkages ψ vs. machine phase currents i as a function of the rotor position angle Θ as shown in Fig. 1.2a. The self-inductance of the stator poles is inverse proportional to the reluctance. The inductance of a stator phase is maximal in the aligned position (aligned inductance L_a) and minimal in the unaligned position (unaligned inductance L_u). The torque producing capability of a SRM mainly depends on the rate of change of the inductance vs. rotor position characteristic $dL/d\Theta$. An indicator for that is the inductance ratio L_a/L_u [8], [9], [133]. The inductance characteristics repeat periodically with the rotor pole pitch. Due to saturation of the magnetic material it is also a function of the current as it can be seen in Fig. 1.2b.
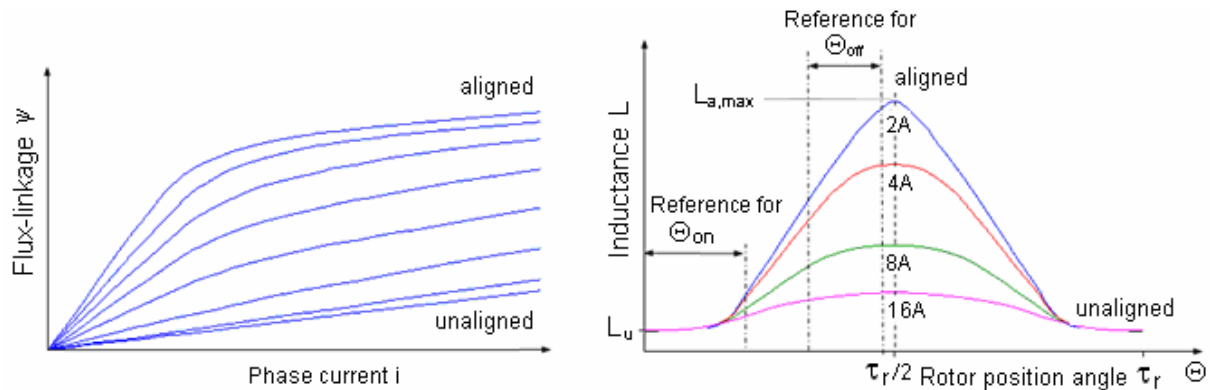

Fig. 1.2   a) Flux-linkage vs. phase current as a function of rotor position angle;
b) inductance vs. rotor position angle characteristic as a function of phase current

For motoring operation the stator phase must be excited when its inductance starts rising and must be de-excited when the phase inductance ceases to increase. Else, the motor would develop braking torque or no torque at all. The switching function thus must ensure that current in phase winding reaches its reference value at the desired instant of inductance rise and is again brought to zero when inductance reaches its maximum and does not increase further. Due to delay in current rise and fall on account of winding inductance, the switch must be closed at a turn-on angle Θ_{on} and must similarly be opened at a turn-off angle Θ_{off}. Fig. 1.2b presents the concept of turn-on and turn-off angles for any phase winding of SR motor. The practical range of turn-on angle and turn-off angle depends on the inductance profile and therefore on the configuration and pole geometry of the particular SRM.

Production of continuous torque

Basically, torque is developed by the tendency for the magnetic circuit to adopt a configuration of minimum reluctance, i.e. for the rotor to move into line with the stator poles and to maximise the inductance of the excited coils. Provided that there is no residual magnetization in steel the torque is independent of the direction of current flow, as it will be shown below. Hence, unidirectional currents can be used, permitting a simplification of the electronics. In contrast to the induction machine the SRM can not run directly connected with a three-phase supply system. The particular phases must be particularly energized in dependence of the rotor position. Therefore a converter and the corresponding electronic control unit are necessary. Moreover, the control unit has to posses the rotor position signal. It may be realised by a rotor position sensor or a sensorless control procedure, e.g. from analysing induced voltages in the phase windings [9]. Fig. 1.3 shows the basic components of a SRM drive for the example of a 3-phase 6/4 machine.
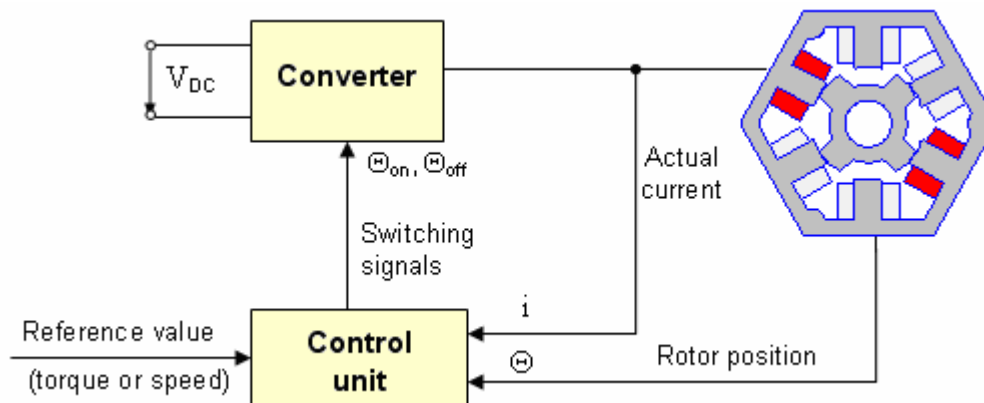

Fig. 1.3   Switched Reluctance Machine drive

Derived from the actual current value, rotor position angle and the reference value of torque or speed, the control unit determines the switching signals for the active switches (e.g. power transistors, IGBTs etc.) in the converter. The electromagnetic torque is independent from the current direction, thus an unipolar converter is sufficient. It is usually supplied by a constant dc-voltage V_{dc}. The optimum performance of an SRM depends on the appropriate positioning of the currents relative to the rotor angular position. The motor controller selects the turn-off angles Θ_{off} in such a way that the residual magnetic flux in the commutating phase decays to zero before the negative $dL/d\Theta$ region is reached in the motoring mode of operation. There exist in general two modes of control the phase current which will be discussed in point 3.7. In the low speed operation mode, torque is maintained constant by keeping the phase current constant. The independent stator phases contribute, in succession, to maintain continuous torque production in the direction of rotation. During commutation each of the two adjacent conducting phases produce torques which are additive. Torque ripple is inversely related to

the smoothness of current transfer between phases, and it is possible to minimize the ripple during transition by controlling currents in the overlapping phases.

If the current is controlled only in the incoming but not outgoing phase, the sum of the air gap torques contributed by the outgoing and incoming phases during this interval is usually not constant. The resulting torque has a trough during this commutation interval that increases the torque ripple. A measure for the torque ripple can be the following torque ripple coefficient, defined among others in [37]:

$$t_{rpl} = \left| \frac{T_{max} - T_{min}}{T_{av}} \right|$$ (1.8)

where T_{max} is the maximum, T_{min} the minimum and T_{av} is the average value of the resulting torque. In order to reduce the torque ripple by control strategy, several approaches are known in the literature. The most important control strategies are:

- Torque Sharing Functions (TSF) and optimized current waveforms [18], [46], [59], [103]
- Direct Instantaneous Torque Control (DITC) [87], [89]
- Direct Average Torque Control (DATC) [58]
- Fuzzy Logic control methods [46], [158], 159]
- Adaptive torque control methods [56], [80]

1.3   Mathematical model

Voltage equation

Investigating the operational behaviour of the SRM requires a mathematical model. The SRM is a nonlinear control structure and therefore it is important to develop a relevant model representing the plant dynamics under various operating conditions. An elementary equivalent circuit for the SRM can be derived neglecting the mutual inductance between the phases as follows. Assuming that a particular phase of the machine consists of a series connection of the winding resistance R and the inductance L(i,Θ), the applied voltage v to a phase is equal to the sum of the resistive voltage drop and the rate of flux linkages ψ(i,Θ):

$$v = Ri + \frac{d\psi(i,\Theta)}{dt}$$ (1.9)

with $\psi(i,\Theta) = L(i,\Theta) \cdot i$ (L-dynamic inductance)   (1.10)

Beside the rotor position the flux linkage depends on the current. The current dependence results from the magnetization characteristic, as described in Chapter 1.2. If the total differential of ψ is split, the following relationship results from (1.8):

$$v = Ri + \frac{\partial\psi}{\partial i} \cdot \frac{di}{dt} + \frac{\partial\psi}{\partial\Theta} \cdot \frac{d\Theta}{dt}$$ (1.11)

Substituting from (1.10) in the expression (1.11) finally gives the complete voltage equation:

$$v = Ri + \left(L(i,\Theta) + i \cdot \frac{\partial L(i,\Theta)}{\partial i} \right) \cdot \frac{di}{dt} + i \cdot \frac{\partial L(i,\Theta)}{\partial \Theta} \cdot \frac{d\Theta}{dt} \qquad (1.12)$$

In this voltage equation for one phase, the three terms on the right hand side represent the resistive voltage drop, inductive voltage drop, and induced emf, respectively. Note, the result is similar to the series excited dc motor voltage equation. The induced back-emf, e, is obtained with the angular frequency of the rotor ω as:

$$e = \frac{dL(i,\Theta)}{d\Theta} \cdot \frac{d\Theta}{dt} i = \frac{dL(i,\Theta)}{d\Theta} \cdot \omega \cdot i \qquad (1.13)$$

Since unipolar currents are normally employed the sign of i is always positive. Therefore, the sign of e is determined by dL/dΘ. When dL/dΘ>0, the back-emf is positive and tends to force the current to decrease, being against the applied voltage and converting the electrical power supplied into mechanical output (motoring). When dL/dΘ<0, the back-emf is negative and tends to increase the current and convert the mechanical power into electrical power (generating). The amplitude of the back-emf varies with the rotor speed ω and the behaviour of the current is determined by the relationship between e and v.

Calculation of electromagnetic torque

Multiplying (1.11) with the current i results in instantaneous input power given by:

$$vi = Ri^2 + i\frac{\partial \psi}{\partial i} \cdot \frac{di}{dt} + i\frac{\partial \psi}{\partial \Theta} \cdot \frac{d\Theta}{dt} \qquad (1.14)$$

The electromagnetic torque can be determined from a power balance. It is

$$vi \cdot dt = Ri^2 \cdot dt + i \cdot \frac{\partial \psi}{\partial i} di + i\frac{\partial \psi}{\partial \Theta} d\Theta \qquad (1.15)$$

The term on the left-hand side represents the change of the entire energy; the three terms on the right-hand side represent the change of Joule heat energy, the change of magnetic field energy dW_F and mechanical work dW_m. The expression for the change of magnetic field energy and mechanical work can be written as:

$$dW_F + dW_m = i\frac{\partial \psi}{\partial i} di + i\frac{\partial \psi}{\partial \Theta} d\Theta \qquad (1.16)$$

The magnetic field energy depends on the current and rotor position angle. Thus the change of magnetic field energy is

$$dW_F = \frac{\partial W_F}{\partial i} di + \frac{\partial W_F}{\partial \Theta} d\Theta \qquad (1.17)$$

Substituting from (1.17) in (1.16) gives an expression for dW_m:

$$dW_m = \left(i\frac{\partial \psi}{\partial \Theta} - \frac{\partial W_F}{\partial \Theta} \right) d\Theta + \left(i \cdot \frac{\partial \psi}{\partial i} - \frac{\partial W_F}{\partial i} \right) di \qquad (1.18)$$
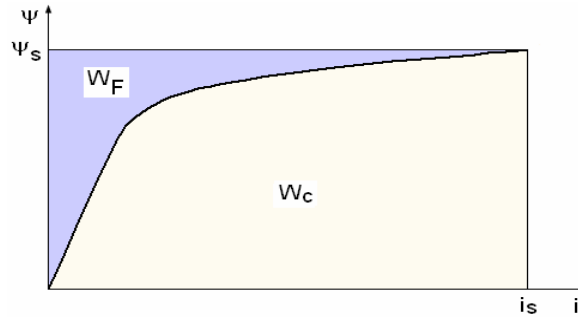
Fig. 1.4 Magnetisation curve at a specific rotor position; magnetic field energy W_F, coenergy W_c

By means of the magnetisation curve presented in Fig. 1.4, the magnetic field energy can be determined for a fixed rotor position angle as a function of flux-linkage and current [8]:

$$W_F = \int_0^{\psi_s} i \cdot d\psi \tag{1.19}$$

$$W_F = i\psi - \int_0^{i_s} \psi \cdot di \tag{1.20}$$

The partial derivation of the second expression gives [18]:

$$\frac{\partial W_F}{\partial i} = i \cdot \frac{\partial \psi}{\partial i} + \psi - \int_0^{i_s} \frac{\partial \psi}{\partial i} \cdot di = i \cdot \frac{\partial \psi}{\partial i} \tag{1.21}$$

By inserting (1.21) in (1.18), the second term on the right-hand side is eliminated:

$$dW_m = \left(i \cdot \frac{\partial \psi}{\partial \Theta} - \frac{\partial W_F}{\partial \Theta} \right) d\Theta \tag{1.22}$$

The change of mechanical work can be also expressed in terms of the produced electromagnetic torque T_s for one phase and the differentially change of rotor position angle:

$$dW_m = T_s \cdot d\Theta \tag{1.23}$$

$$T_s = \frac{dW_m}{d\Theta} = i \cdot \frac{\partial \psi}{\partial \Theta} - \frac{\partial W_F}{\partial \Theta} \tag{1.24}$$

That expression can be simplified by introducing the magnetic coenergy W_c:

$$W_c = \int_0^{i_s} \psi \cdot di \tag{1.25}$$

In the linear range of the magnetisation curve the magnetic field energy and coenergy are equal. However, in the non-linear range of middle and high saturation they can deviate considerable from each other. The entire input energy is:

$$W_F + W_c = i \cdot \psi \tag{1.26}$$

The partial derivation with respect to the rotor position angle Θ gives:

$$\frac{\partial W_c}{\partial \Theta} = i \cdot \frac{\partial \psi}{\partial \Theta} - \frac{\partial W_F}{\partial \Theta} \tag{1.27}$$

With expression (1.25) the instantaneous electromagnetic torque $T_s(i,\Theta)$, produced by each phase, is given from the partial derivative of the phase coenergy and is given by:

$$T_s(i,\Theta) = \left.\frac{\partial W_c(i,\Theta)}{\partial \Theta}\right|_{i=const} \qquad (1.28)$$

The total instantaneous electromagnetic torque T_e is the sum of the q individual phase torques

$$T_e = \sum_{s=1}^{q} T_s(i,\Theta) \qquad (1.29)$$

and the average torque T_{av} can be derived mathematically by integrating (1.29) as follows:

$$T_{av} = \frac{1}{\Theta_{sk}} \int_0^{\Theta_{sk}} T_e d\Theta \qquad (1.30)$$

(Θ_{sk}-stroke angle)

For a linear flux model it is $\psi(i,\Theta) = L(i,\Theta) \cdot i$. Thus, neglecting saturation gives

$$W_c = \int_0^{i_s} \psi \cdot di = \frac{1}{2} \cdot L(\Theta) \cdot i_s^{\,2}, \qquad (1.31)$$

hence $T_s = \frac{1}{2} \cdot i_s^{\,2} \cdot \frac{dL}{d\Theta}$ \qquad (1.32)

The above equation indicates that the SRM-torque is independent of the sign of the phase current, but it is determined by the sign of dL/dΘ. The absolute value of dL/dΘ contributes to the amount of mechanical torque. Therefore, SR Motors are designed to have a large L_{max}/L_{min} ratio, hence a large absolute value of dL/dΘ in order to obtain high torque. The quadratic dependence of the electromagnetic torque from the phase current practically occurs only for the case of very low currents. Usually, torque increases nearly linear with the current due to saturation of overlapping stator and rotor pole parts.

Mechanical equation

The in the drive engineering generally known equation of a fixed mechanically coupled chain completes the dynamic SRM model:

$$T_e - T_l - T_{fr} - \frac{J_i}{N_r}\frac{d\omega}{dt} = 0 \qquad (1.33)$$

where T_e is the electromagnetic torque, T_l is the load torque, T_{fr} is the friction torque, J_i is the moment of inertia, N_r is the number of rotor poles and ω represents the angular frequency. With the rotor speed n in 1/s it is defined as

$$\omega = 2\pi n = \frac{d\Theta}{dt} \qquad (1.34)$$

1.4 Electromechanical energy conversion

The dependence of the reluctance and inductance on the rotor position and phase current is essential for the description of the SRM. In a straight line it influences the magnetic characteristics of the machine as well as the energy conversion of the electrical energy input supplied by the converter into mechanical torque. The electromagnetic torque and the utilization factor of a SRM are commonly determined on the basis of energy relations. The coenergy, introduced in (1.24) that is available to be converted into mechanical work in each working stroke is equal to the area enclosed by the trajectory of the operating point in the ψ-i diagram. The magnetic field energy W_F physically corresponds to the stored field energy in the case of a specific rotor position and constant current in the machine. Fig. 1.5a shows the flux-linkage vs. current trajectories for an SR motor under chopping control. The current is established at a rotor position of minimum inductance Θ_{on} and is hold around a reference value by a hysteresis type current controller before the supply voltage is switched off and the phase is de-energized at the turn-off angle Θ_{off}. At this instant, the already in mechanical work converted energy corresponds to the area enclosed by the trajectory of the actual flux-linkage. The stored magnetic energy W_F is at its maximum. A major part of that stored energy is returned except hysteresis losses to the supply during commutation. However, the demagnetisation takes a certain time due to the larger inductance value near the aligned position. Hence, the rotor moves several degrees before the phase is de-energized and phase current is dropped off. Therefore a part of the magnetic energy is additionally converted into mechanical work during the commutation period, reducing W_F for the benefit of W_c. That is indicated in Fig. 1.5a by the crosshatched area. The energy conversion loop contains the energy available to convert into mechanical work W_m in each working stroke and, what is recognized rarer, the hysteresis losses W_{Fe}:

$$\Delta W_c = W_m + W_{Fe} \tag{1.35}$$

From the energy W_m the mechanical losses, e.g. friction losses, must be subtracted to obtain the available mechanical work provided on the shaft. If these loss energies and W_{Fe} are much smaller than the energy converted into mechanical work, ΔW_c can be used as scale for the appropriable energy [25], [26]. Accomplishments about the energy conversion in SRMs can be found in bibliography, e.g. in [31], [34], [121] and [170]. Neglecting resistive losses, the supplied energy from the converter for one stroke is equal to the sum of the conversion energy ΔWc and the energy ΔW_F returned to the supply. An energy ratio EC has been defined in [121] which tells how much energy conversion is obtained for a given input energy:

$$EC = \frac{\Delta W_c}{\Delta W_F + \Delta W_c} \tag{1.36}$$

That energy ratio is equivalent to the utilization of the SRM [33]. To achieve a good utilization, the proportion of the returned energy ΔW_F must be small compared to the conversion energy ΔW_c. Therefore, a large inductance ratio L_a/L_u is necessary, corresponding to a maximised cross section area of the magnetisation characteristics $\psi(i,\Theta)$. Due to wide teeth in stator and rotor and a small air gap the unsaturated aligned inductance is increased which decreases the area ΔW_F. Whereas the minimum inductance in the unaligned position can be reduced by narrower teeth, what increases the area ΔW_c. These contradictory requirements must be regarded in the machine design. Beside adapted machine geometry an iron with high permeability is favourable. Saturation of the iron plays a decisive role for SRMs. Without saturation, the magnetisation curves $\psi(i,\Theta)$ would be straight lines, as it is the case for very small currents. In spite of a high inductance ratio the energy ratio EC can not exceed more than 50%. In that case the field energy would be equal to the coenergy:

$$W_F = W_c = \frac{1}{2} L i^2 \qquad\qquad\qquad (1.37)$$

As it can be seen in Fig. 1.5a, the ratio of energy conversion ΔW_c increases compared to the returned field energy ΔW_F for the case of saturation. Hence the utilization, defined in (1.36), increases. For understanding the energy conversion see also Fig. 1.5b. Here the principle aligned and unaligned flux linkage curves as a function of current are shown for two different (theoretical) SRM designs. The first one experiences high magnetic saturation while the other one experiences no magnetic saturation. Both SRMs are designed for the same rotor speed, phase current and back emf. Furthermore the two machines are assumed to have the same dimensions except for the air gap length. The saturating machine has a much smaller air gap than the non-saturating one.
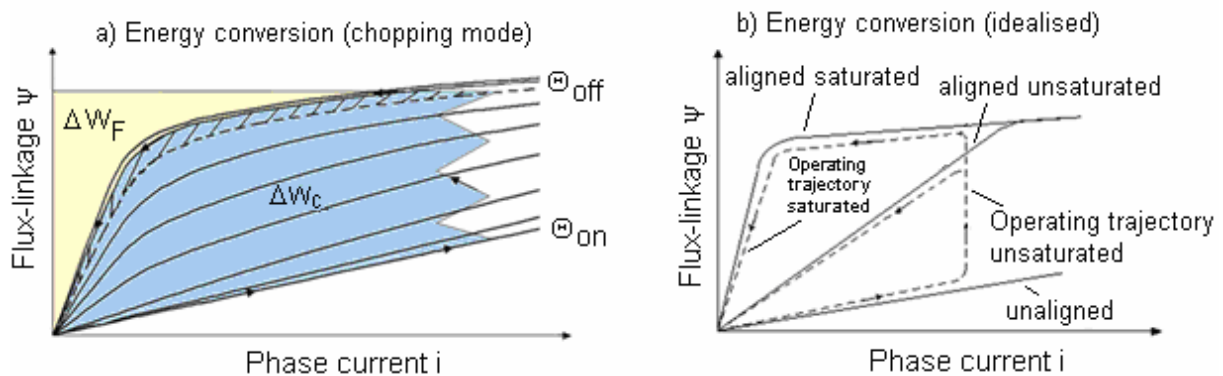

Fig. 1.5 ψ-i-characteristic a)chopping mode; b) idealised for saturating and non-saturating SRM

The potential that is available to be converted into mechanical work in each working stroke is proportional to the area enclosed by the trajectory of the operating point in the flux-linkage vs. current diagram. For the aligned curves the saturated machine has the potential to convert

approximately twice the energy of the unsaturated machine for the same peak current. This makes clear that the SRM requires a sufficiently small air gap to saturate the machine in the aligned position at a current value much less than its peak operating current. That maximizes the machines power density at a fixed inverter volt-ampere rating. In other words, a SRM with significant magnetic saturation has an effective power factor equal to about twice that of a non-saturated design.

In view of the fact that heavy saturation of the SRM improves its performance it cannot be ignored during the design and analysis of the machine. Saturation is desirable from this point of view, but must be localized on the tooth tips, since the electromagnetic energy conversion occurs in the air gap. Otherwise the iron losses would be too high and mutual couplings between phase bands would increase [18]. Consequently, the demand to operate the SRM partially in the range of saturation is not in the contradiction to the generally usual procedure to avoid the non-linear operation with electrical machines. A good utilization factor moreover reduces the volt-ampere requirement of the converter which influences the size of the power electronic devices as well as the iron and copper losses of the machine. Therefore, the drive efficiency is partially determined by the utilization [33]. Since the geometrical dimensioning of the machine mainly influences the shape of the $\psi(i,\Theta)$-characteristics and therefore the energy conversion, the basis for a SRM with a high utilization factor and efficiency is created already during the design stage. However, the design for itself is no guarantor for an optimized utilization and high efficiency. The control mode essentially influences the operational behaviour of the machine, which will be shown in Chapter 3.7.

1.5   Power electronic converters for SRM drives

An adjustable speed drive using a Switched Reluctance Motor, because of its ability to operate efficiently from unidirectional winding currents, enables the number of main switching devices in the inverter to be halved, thus only one switch per phase is sufficient, yielding a very economical brushless drive. This is contrary to the ac motor drives where at least two switches per phase are required for current control. Furthermore, the windings are not in series with switches in ac drives, leading to irreparable damage in shoot-through faults. SRM drives always have a phase winding in series with a switch. In the case of a shoot-through fault, the phase inductance limits the rate of rise in current and provides time to initiate protective relaying to isolate the faults. The SRM phases are independent and, in the case of one winding failure, uninterrupted operation of the motor drive operation is still possible, although with reduced power output.

The complete converter of a SRM drive normally consists, analogical to ac drives, of a rectifier, a dc link and the machine inverter. The rectifier and dc intermediate circuit are

identically designed as for ac drives, but the inverter differs due to the specific operational characteristics of the SRM. Generally, three important criteria must be considered for the choice of a suitable converter topology in order to fulfil the requirements of the application:

 (1) little complexity of power electronic devices,

 (2) high dynamics for current rising and falling and

 (3) high degree of freedom for influencing the current waveform.

It can be easily understand that the first point is contradictory to the point (2) and (3). A little complexity of power electronic devices leads to restrictions in the dynamic behaviour and the number of possible control parameters for current regulation. Various different topologies of converters have been described in the worldwide bibliography.
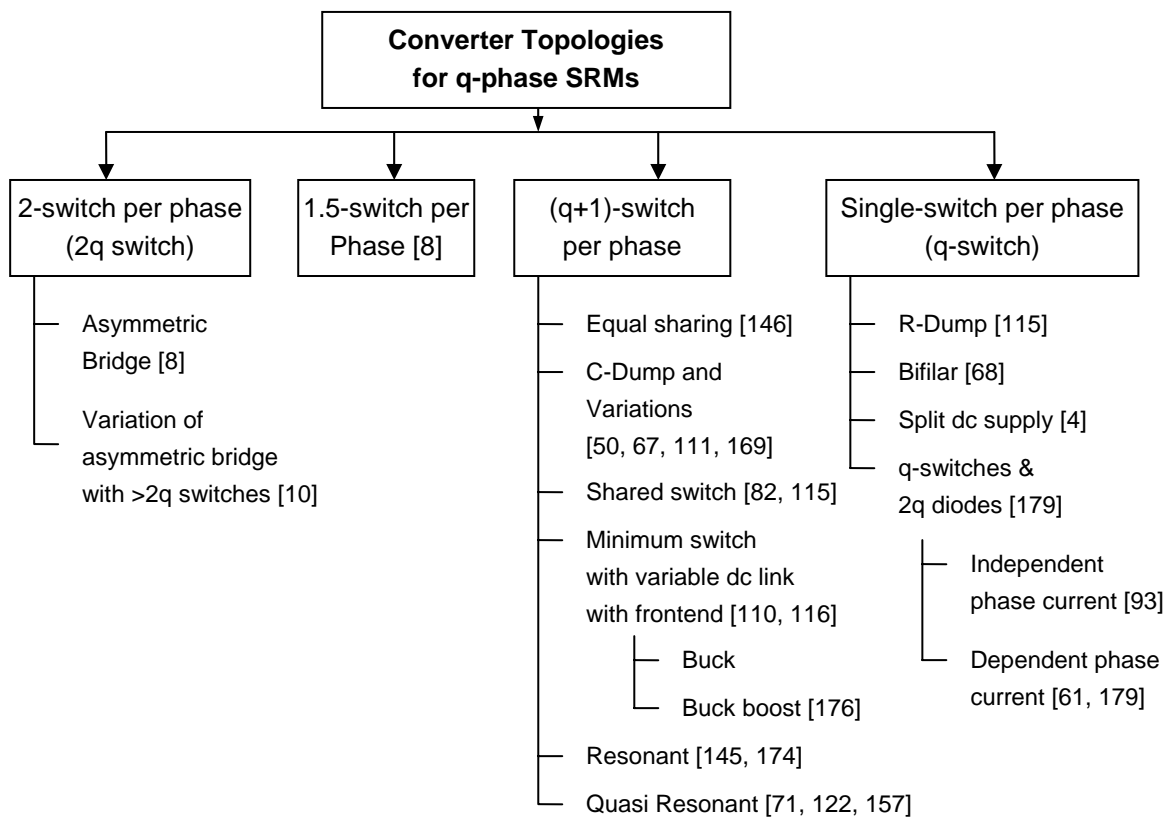
Converter Topologies for q-phase SRMs

- **2-switch per phase (2q switch)**
  - Asymmetric Bridge [8]
  - Variation of asymmetric bridge with >2q switches [10]
- **1.5-switch per Phase [8]**
- **(q+1)-switch per phase**
  - Equal sharing [146]
  - C-Dump and Variations [50, 67, 111, 169]
  - Shared switch [82, 115]
  - Minimum switch with variable dc link with frontend [110, 116]
    - Buck
    - Buck boost [176]
  - Resonant [145, 174]
  - Quasi Resonant [71, 122, 157]
- **Single-switch per phase (q-switch)**
  - R-Dump [115]
  - Bifilar [68]
  - Split dc supply [4]
  - q-switches & 2q diodes [179]
    - Independent phase current [93]
    - Dependent phase current [61, 179]

Fig. 1.6   Classification of power electronic converters for SRM drives

Fig. 1.6 gives an overview. In this sub-chapter a small selection of converter circuits frequently used for powering adjustable speed drives with SRM will be presented. One note that in the different converters analyzed below, the power switch is represented as a transistor. However, in industrial applications, there may be other types of power switches, mostly thyristors, power IGBTs or GTOs, or even MOSFETs. Furthermore, auxiliary circuitry such as snubbers, voltage spike suppressors, di/dt limiters, RC protective components, etc. are not represented. All converter topologies assume that a dc voltage source is available for their inputs. The dc source may be from batteries or mostly a rectified ac supply with a filter to provide a dc input source to the SRM converters. Beside a controlled rectifier also an

uncontrolled rectifier could be used to provide constant dc voltage at the bank capacitor terminals. However, adjustable voltage provides greater flexibility in variable speed reluctance drives. Detailed descriptions of such dc sources may be found in standard power electronics textbooks, e.g. [5] and [15].

Bridge converters

The most versatile SRM converter topology is the classic bridge converter topology shown in Fig. 1.7a, suitable for powering a 3-phase machine. Note that this asymmetric bridge converter requires 2q power switches and 2q diodes for a q-phase machine, resembling the conventional ac motor drives. The asymmetric bridge converter provides the maximum control flexibility, fault tolerance capability and efficiency, with a minimum of passive components and is therefore one of the most popular converter topology. Firstly, consider Phase *a*. The voltage applied to the phase winding is $+V_{DC}$ when the upper and lower transistors T1 and T2 are on. Phase current i_a then increases through both switches. If one transistor is off while the other is still on, the winding voltage will be zero. Phase current then slowly decreases by freewheeling through one transistor and one diode. When both transistors are off, the phase winding will experience $-V_{DC}$ voltage. Phase current then quickly decreases through both diodes. By appropriately coordinating the above three switching states, phase current of the SRM can be controlled. The main advantages of the asymmetric bridge converter are the independent control of each motor phase and the relatively low voltage rating of the inverter components. The major drawbacks are the total number of switches, the dc link filter and a relatively low demagnetizing voltage at high speeds [176].
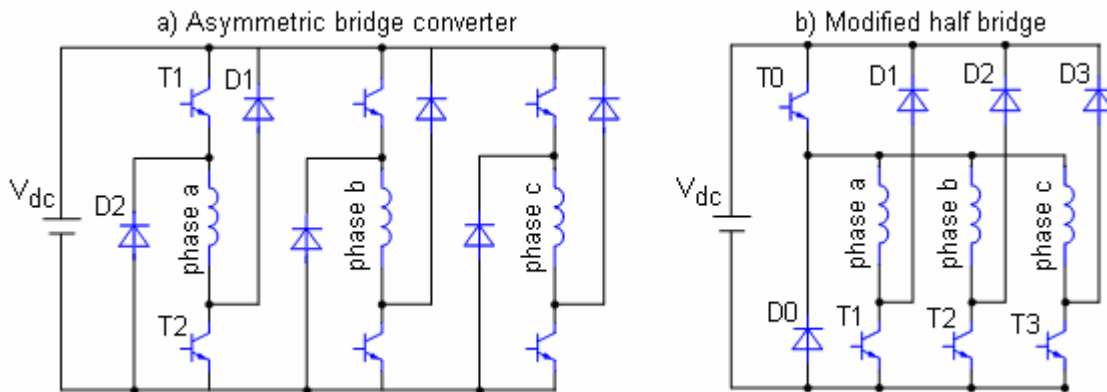

Fig. 1.7   Converter topologies of a 3-phase asymmetric half-bridge converter

In Fig. 1.7b the circuit has been modified [141]. The converter requires (q+1) switching devices for a q-phase machine. Firing a transistor T1…T4 selects which phase winding is excited. Transistor T0 is common switch to all the phases. This topology reduces the number of devices required per phase winding. However, three devices are always in series with the motor winding which increases conduction losses and decreases the voltage applied to the

winding. Current overlap in the conventional sense is not possible for phase windings within the same half bridge. Moreover, the reliability of the drive with such a converter topology is reduced. In [115] and [176] a shared switch asymmetric half bridge is proposed where the switches and diodes are shared between more than one phase winding. This is particularly advantageous for high numbers of phase windings, but even for two phase drives. It reduces the necessary number of power electronic components. The only limitation to operation is that for a pair of phase windings sharing a diode and a switch, one phase winding cannot have a positive voltage loop applied while the other has a negative voltage loop applied [49].

Converters with auxiliary voltage supply

The demagnetisation energy of a phase is feed in an auxiliary voltage supply with this converter type in order to restore the intermediate circuit or for directly energizing the succeeding phase. With the C-Dump-converter in Fig. 1.8a the phase current is controlled by only one switch per phase.
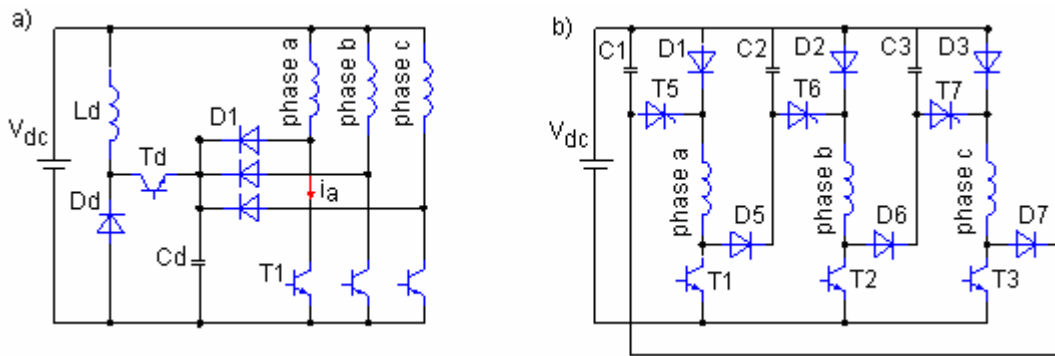

Fig. 1.8 Converters with auxiliary voltage supply (C-dump) a) Bass [50], b) Le-Huy [123]

Various forms of the C dump converter have been appeared in the literature, e.g. [50], [67], [111] and [169]. In all these topologies the energy from the off-going phase is dumped into a capacitor to achieve fast demagnetization. This energy is then returned to the source from the capacitor. The conduction of the phase is initiated by turning on the phase switch (T1 for L1) connected in series with the phase. The phases are demagnetized by turning off the phase switch. During the commutation period, diode Dd is forward-biased and the energy from the machine phase is transferred by a buck-chopper from this auxiliary voltage supply to the dump capacitor Cd. The voltage of the capacitor is maintained at twice the supply voltage to apply $-V_{dc}$ across the off-going phase for a faster demagnetization. The excess energy from the dump capacitor Cd is transferred into the source by turning on the switch Td. Dump switch Td is operated at a higher frequency than the phase switches. C-Dump converters offer many advantages:

- lower number of switching devices; only one-switch forward voltage drop
- full regenerative capability

- faster demagnetization of phases during commutation
- phase advancing is allowed

The major disadvantages of C-dump converter are the use of a capacitor and an inductor in the dump circuit. Also the voltage rating of the devices is twice the bus voltage. Dump capacitor voltage is maintained at $2V_{dc}$ to allow fast demagnetization. The monitoring of the dump capacitor voltage and control of the dump switch Qd makes the converter very complicated. Also, the converter does not allow freewheeling.

In the converter presented in Fig. 1.8b each phase has its own auxiliary voltage supply. The energy from the demagnetization is used to charge a capacitor which encourages the magnetization of the succeeding phase [123]. At the beginning of conduction period the auxiliary switch of the actual phase is turned on in addition to the main switch. Hence the voltage for magnetisation of the phase is the sum of the dc bus voltage and the capacitor voltage. The benefit of this converter topology is a very fast demagnetisation. Two switches and two diodes per phase are necessary. A restoring of energy to the supply is not possible. A further disadvantage is a high turn-on current due to the resonant circuit, which increases the torque ripple. Moreover, the switches and diodes must be dimensioned for these high current and voltage values.

Quasi-Resonant Converter

The selected power converter topologies hitherto discussed are known as hard-switched topologies because during turn-on and turn-off the power switch and diode voltages and/or currents are non-zero, thus causing significant power loss in these devices. During the switching instant, if the current or voltage is zero, then the device loss is zero. Topologies enabling such a condition are known as resonant circuits. In [4] and [8] 3-phase resonant converters were investigated in great detail. Quasi-resonant converters contain a resonating circuit which is not permanently active but initiated to oscillate by a switching signal. Target is to reduce the switching losses. Therefore a resonating circuit is dimensioned in that way that the power electronic devices can operate under zero-voltage or zero-current switching conditions. In the converter proposed by De Doncker [71] and Rim [157] the voltage over the controllable switching devices is removed in each switching instant and after the voltage-free turn on the voltage is increased on the dc bus voltage again. Therefore, an asymmetric bridge converter is extended by an additional quasi-resonant circuit.

2 Synthesis of design procedures for Switched Reluctance Machines

A specification of an electrical machine consists of requirements (e.g. torque, speed) and constraints (e.g. dimensions or supply voltage). Furthermore the design is based on the compliance of a number of prescriptions or agreements at the valid heating, mechanical stress, operational safety and the compliance of electrical limits. The designer's goal is the determination of the main dimensions and the electric and geometric data of all electromagnetic claimed parts from the required properties.

The design procedure for SRMs has been explored in detail in many publications. This dissertation attempts to modify the design procedure described in [117] fitting a manufacturer's requirements while helping a machine manufacturer with no background in SRM design to build and test prototypes. The actual machine design consists in the determination of main dimensions and the iterative modification of geometry, winding and material. There are embedded special demands like the optimal choice of the pole and phase number for the realization of optimal torque characteristics and minimization of iron losses due to high switching frequencies. Furthermore, a number of experience values can be effectively used in the design of these new machines, as they could use the commonality between these and the conventional machines to start with [4], [8], [9], [16]-[18], [43], [66], [69], [80], [117], [120], [150], [159] and [166]. Also R. Krishnan [4] developed an output equation similar to the output equation for induction and d.c. machines. However, this process requires extensive prior knowledge and experience in designing SRMs.

In fact, design by analysis and simulation of SRM drive systems and the development of new effective and reliable design software are one of the main subjects of the presented thesis.

2.1 Machine data

The design data for a SRM comprises of the required rated power output P_n, rated speed n_n, allowable peak phase current i_p and available dc bus voltage V_{dc} for the system. Knowing the speed and power output will automatically fix the rated torque T_n to be developed:

$$T_n = \frac{P_n}{2\pi \cdot n_n} \tag{2.1}$$

These parameters are often called as the principal designing specifications ([15], [16]) and correspond to the rated regime. However, by themselves, these specifications are not sufficient to determine unambiguously and quantitatively all the various motor parameters. Therefore, secondary specifications must be provided for this purpose like:

- maximum torque ripple $t_{rpl,max}$,
- the overall maximum machine axial length l_{max} and outer diameter D_{max} and
- the maximum working frequency of the converter power switches f_{smax}.

Improving material productivity of SRM manufacturing involves optimized utilization of machine and drives active materials, including iron and copper, drive electronics and control aspects for cost minimization. It is achievable through design optimization within manufacturing tolerance, where analytical and numerical analysis techniques combined with knowledge-based techniques are applied. Therefore, a design by analysis and calculation methods for SRMs is presented in the following chapters, leading to the development of special design software - the program 'DesignSRM', which is described in Chapter 3.8.

2.2   Sizing of main dimensions

The size of the active part of an electrical machine depends on two factors: the required torque and the effectiveness of the cooling system. For a given torque, the machine size may be reduced to some extend by improving the cooling effectiveness. But such improvement would increase the machine manufacturing cost. Once a means of cooling compatible with the fabrication cost has been chosen, the only parameter that determines the motor size is the magnitude of torque. In general, electrical machines are designed starting from the output equation, introduced in [8] and [16], which relates the bore diameter D (inner stator diameter), rotor length l, rated speed n, and magnetic and electric loadings to the rated output power P:

$$\frac{P}{n} = T = C \cdot D^2 \cdot l \tag{2.2}$$

C is the output coefficient and essentially depends on the machine dimensions and the cooling system. To determine the main dimensions, it is necessary to keep the rotor length l as a multiple or submultiples k of bore diameter.

$$l = k \cdot D \tag{2.3}$$

The substitution of l in the output power equation results in $P\sim D^3$. The ratio k is decided by the nature of application and space constrains. For non-servo applications, the range of k can be $0.25 < k < 0.7$ and for servo applications it is usually in the range of $1 < k < 3$ [4], [117]. However, no unique solution for the choice of these parameters exists. After several trials, convenient values of these parameters, compatible with the overall maximum motor axial length and diameter, as imposes in the machine specifications, may be found.

2.3   Pole selection

Usually, the designer determines a common number of stator and rotor poles N_s and N_r and deviates from this fixed value only for very special applications because then converter configurations and feedback devices can be standardized. There are many possible combinations for the number of poles resulting in different phase numbers. The choice of the

number of phases mainly depends on the desired application and their required properties how it has been explored in detail by Miller [8]. Generally, it is preferred to have the ratio between N_s and N_r is a noninteger. Even thought some at integer values have been attempted [117]. Based on this guideline, the stator and rotor pole combinations common in industrial designs are given below:

Table 2.1 Typical stator and rotor pole combinations

	Poles					
Stator N_s	4	6	12	8	12	10
Rotor N_r	2	4	8	6	10	8

This thesis primarily focuses on the popular combinations of two 3-phase prototypes with 6 stator and 4 rotor poles and one 4-phase motor with 8 stator and 6 rotor poles. The 8/6-machine has the advantage of smaller torque ripple than the 6/4 machine while having the disadvantage of using more switches in the converter, two extra terminals and higher core losses (assuming the same rotor speed) because of higher remagnetization frequency.

2.4   Air gap

To maintain balanced phase currents and minimize acoustic noise, the SRM needs a uniform air gap. The machine also requires a small air gap to maximize specific torque output and minimize the volt-ampere requirement in the converter. A small air gap decreases the minimum reluctance in the zone of stator-rotor-pole-overlapping and therefore increases the achievable torque, as described in Chapter 1.4. Nevertheless, the bending of the shaft and the expansion of the material with increasing temperature must be considered during design in addition to manufacturing tolerances. So the air gap should be chosen in such a way that the machine works reliable under common operating conditions in every operating point.

The air gap length *g* has strong influence on the maximum torque value as well as the flat torque range on the $T(i,\Theta)$-characteristics as it will be shown in Chapter 5 for industrial machine designs. As a conclusion, the machine with smaller air gap length, subjected to acceptable manufacturing tolerances, will produce higher average torque.

Miller [8] gives a rough guide to choose the air gap length about 0.5% of the rotor diameter if the ratio of stator stack length/rotor diameter l_{stk}/D_r is 1, increasing in proportion to l_{stk}/D_r. Chang [124] advises a ratio of rotor pole pitch to air gap length τ_r/g between 50 and 120. This agrees closely with the results in [80] and [84] that a maximum of torque is obtained with a high ratio of τ_r/g. In praxis, typical values of the air gap length are in the range of $0.2 \le g \le 0.6mm$, depending on the machine size and the properties of the application.

2.5 Stator and rotor pole angle selection

The pole arcs of stator and rotor β_s and β_r define the width of stator and rotor poles t_s and t_r:

$$t_s = D \cdot \sin \frac{\beta_s}{2} \tag{2.4}$$

$$t_r = (D - 2g) \cdot \sin \frac{\beta_r}{2} \tag{2.5}$$

The choice of the pole arcs basically depends on two criteria:

1. Self-starting requirement
2. Shaping of static torque vs. rotor position characteristics

These requirements can be included into the machine design by computing the minimum rotor and stator pole arcs β_r and β_s to achieve self starting [8]:

$$\min(\beta_s, \beta_r) \geq \frac{2\pi}{q \cdot N_r} \tag{2.6}$$

The minimum pole arcs are equal to the stroke angle Θ_{sk}, ensuring that in the ideal case with no fringing flux, torque can be produced at all rotor positions. An upper limit is placed on the overlap of stator and rotor teeth:

$$\beta_s < \frac{2\pi}{N_r} - \beta_r \tag{2.7}$$

That ensures that in the unaligned position there is a clearance between rotor and stator poles. In practice $\beta_r \geq \beta_s$ is preferred since it provides a slightly larger slot area without sacrificing aligned inductance [4], [8], [117]. It was shown in many publications ([18], [52], [53], [66], [80], [136], [139], [143], [166]) that increasing the rotor pole arc causes only changing of maximum torque with rotor position and influences the width of the torque impulse. The maximum value of torque is practically constant. There is an optimum value of rotor pole wide when the torque integral (area under characteristic) has its maximum [52], [53]. Investigations in Chapter 5 for practical industrial designs of SRM prototypes agree with theses statements. Increasing the stator pole arc leads to a smaller slot area and limits the maximum magneto motive force (mmf) and therefore the maximum torque. On the other hand it must be considered from the mechanical aspect that a narrower stator pole can be easier stimulated to oscillate, what influences acoustic noise negatively. The optimum stator and rotor pole arc is therefore a compromise between various conflicting requirements, and there is no single value that is appropriate for all applications. For very high efficiency designs the slot area needs to be maximized to minimize copper losses, leading to a narrow pole arc. But the starting capability may be compromised because of torque dips and extreme torque ripple. Wider pole arcs can avoid these problems, but the price paid is a smaller slot area and higher

copper losses. The choices depend on the entire torque/speed range and on the number of poles and phases. A good guide for the choice of suitable stator and rotor angle is LAWRENSON's feasible triangle [8], [121] which determines the possible β_r and β_s values.

Worth mentioning is the fact that making $\beta_r > \beta_s$ has many positive effects on operational behaviour considering the usual angle control strategy. With a wider rotor pole force production starts earlier but also ends earlier because of the wider overlapping zone of stator and rotor pole where $dL/d\Theta = 0$ close around the aligned position. That "dead zone" around the aligned position is given by ($\beta_r - \beta_s$) (see Fig. 2.1a). The flux linkage and therefore inductance remains constant for that moment with the consequence that force- and induction effect are breaking down. Thus no torque can be produced. It seems that variation of rotor pole width does not have a great influence on the average torque [53]. But if the operational behaviour with the common angle control strategy is considered, she shift of torque characteristics with increasing β_r characterized by higher torque towards the unaligned region and lower torque near the aligned position (Fig. 2.1b) is beneficial because is reduces generating of negative torque. Note, normally the commutated phase current continuous to flow for a short instant after the rotor passed the aligned position leading to negative and therefore breaking torque! Hence, many of practical SRMs have rotor pole arcs slightly greater or equal to stator pole.
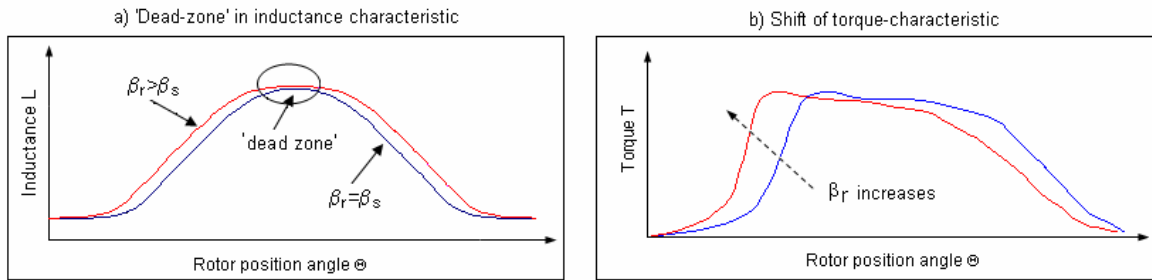

Fig. 2.1   Effect of making $\beta_r > \beta_s$ on a) inductance characteristic and b) torque characteristic

2.6   Ratio of pole width to pole pitch

Guidelines for the selection of stator and rotor pole arcs can be found e.g. in [80], [84], [124], [139] and [166]. In Krishnan ([4], [117]) both angles were varied for a given current and their effect on the average torque and aligned respectively unaligned inductance was studied to give a clearly identifiable range of practical pole arc values. A characteristic value for the pole geometry is the ratio of pole width to pole pitch t/τ. It can be written with the pole arcs for the stator and rotor and the air gap radius $r_g = D/2 - g$ as follows:

$$\frac{t_s}{\tau_s} = \frac{2 \cdot (r_g + g) \cdot \sin\left(\dfrac{\beta_s}{2}\right)}{\dfrac{2\pi}{N_s}} = \frac{N_s \cdot (r_g + g) \cdot \sin\left(\dfrac{\beta_s}{2}\right)}{\pi} \tag{2.8}$$

$$\frac{t_r}{\tau_r} = \frac{2 \cdot r_g \cdot \sin\left(\dfrac{\beta_r}{2}\right)}{\dfrac{2\pi}{N_r}} = \frac{N_r \cdot r_g \cdot \sin\left(\dfrac{\beta_r}{2}\right)}{\pi} \qquad (2.9)$$

Guidelines that follow from Krishnan's observations for practical t/τ ratios are in the range of

$$0.3 \le \frac{t_r}{\tau_r} \le 0.45 \quad \text{and} \quad 0.35 \le \frac{t_s}{\tau_s} \le 0.5 \qquad (2.10)$$

Those results agree well with the work of J. Faiz [80] where an optimal range for the t_r/τ_r-ratio between 0.33 and 0.4 has been found. Any further increase results in more iron volume and higher moment of inertia. A higher t_s/τ_s- ratio reduces the space for the stator windings and increases the stator weight, thus a poorer utilization of the material.

2.7   Determination of other internal dimensions

Once the main dimensions, pole numbers and preliminary pole arcs are fixed, the design of rotor and stator pole length, stator and rotor yoke thickness and shaft diameter finishes the first roughly design step. That parameter can be obtained as follows.

Rotor pole height h_r

Generally, a short rotor pole leads to a small inductance ratio L_a/L_u but allows a longer stator pole if the envelope dimensions of the magnetic core remain unchanged (e.g. diameter of stator and rotor yoke, shaft diameter and stator outer diameter). The bore diameter varies in this case. Hence more space for the stator windings is available. A larger rotor pole increases the air gap radius r_g, but at the same time the stator poles must be shorter. Therefore less space for the stator winding is available. On the other hand, for the same mmf the torque increases with h_r due to the larger bore diameter, referring to the output equation (2.2). The price paid are higher copper losses. Nevertheless, making the rotor poles to large has no benefit. In the unaligned position the stator pole flux tends to fringe into the sides of the rotor poles. If the angular clearance between the corners of the rotor and stator poles in the unaligned position is too small, the decrease in the unaligned inductance is marginal, and also the aligned inductance decreases. As a conclusion, there exists an optimum value for the rotor pole height in terms of induction ratio and torque production capability. Therefore, Chang [124] proposes a ratio of the rotor pole height to the rotor interpolar gap between 0.55 and 0.75. If the bore diameter D remains unchanged, the rotor pole height is constrained by the need to make the rotor yoke thick enough to carry the peak flux without saturating, and also by the requirement to make the shaft diameter as large as possible. In order to obtain a low unaligned inductance,

the rotor pole height should be at least 20-30 times the air gap length, as advised in [8]. K. Bienkowski [53] proposes a similar rotor pole height in the range of

$$h_r = k_{hr} g \quad \text{with} \quad 15 < k_{hr} < 35 \tag{2.11}$$

Rotor yoke thickness y_r

The rotor yoke thickness y_r is determined by the need of mechanical stiffness and the operating flux density. In a SRM with a two-pole flux pattern the main flux divides into two equal parts when it leaves the rotor pole and enters the rotor yoke. Therefore, y_r should be at least half of the stator pole width in order to carry the peak rotor flux without saturating. Regarding the fact that sections of the rotor yoke are shared between different phases which may overlap, it is submitted in [8] to choose the rotor yoke thickness about 20-40% more than $t_r/2$. Chang [124] gives a similar expression for the choice of y_r:

$$y_r = k_{yr} \cdot \frac{t_r}{2} \quad \text{with} \quad 1.1 < k_{yr} < 1.3 \tag{2.12}$$

The range of values to be chosen from has to account for the interpolar air gap to provide a sufficient high inductance ratio L_a/L_u, but also sufficient mechanical stiffness.

Shaft diameter D_s

In order to maximise the lateral stiffness a large shaft diameter D_{sh} is favourable. This also contributes to the minimization of acoustic noise and raises the first critical speed ([2], [8], [23]). If the height and width of the rotor poles and the rotor yoke thickness are fixed, then the shaft diameter can be obtained with the outer rotor diameter D_r as follows:

$$D_{sh} = D_r - 2(h_r + y_r) \tag{2.13}$$

Stator yoke thickness y_s

The stator yoke thickness y_s is determined on the basis of maximum flux density and by the addition factor of vibration minimization and reducing acoustic noise. These mechanical problems are caused mainly by the effect of *ovalisation*, which is explained in more detail in [33]. The stator yoke flux density is approximately half of that of the stator poles. Concerning that sections of the yoke are shared between different phases which may overlap, it is proposed to choose the stator yoke thickness about 20-40% greater than half of the stator pole width [8], similarly to the rotor yoke thickness. Due to considerations of mechanical robustness and minimization of vibrations, y_s could have in practice a value in the range of $0.5t_s < y_s < t_s$ [4]. It's recommended to choose a higher value for y_s than its minimum, regarding that stator yoke sections are longer than rotor yoke sections. In agreement with these statement, [124] proposes

$$y_s = k_{ys} \cdot \frac{t_s}{2} \quad \text{with} \quad 1.1 < k_{ys} < 1.3 \tag{2.14}$$

Stator pole height h_s

The stator pole height h_s should be as large as possible in order to maximise the winding area and to make it easy to insert enough copper for minimized copper losses. One note that the stator coil has to be held in place and therefore small space is required near the pole face. The coil seating at the pole root is not usually tight fitting, so some additional space is lost which must be accounted for the dimensioning of the stator pole height. If the outer diameter of stator lamination D_s is determined by choosing all the other electromagnetic dimensions of the stator, then h_s can be calculated as

$$h_s = \frac{1}{2}\left(D_s - D_r - 2(g + y_s)\right) \tag{2.15}$$

At this point of the design stage, a first preliminary machine design is achieved by determining all its electromagnetic parts, found by empirical formulas which are obtained from previous design experiences and extracted from the technical publications. Fig. 2.2 presents the determined geometric dimensions for the example of a four-phase 8/6-SRM.
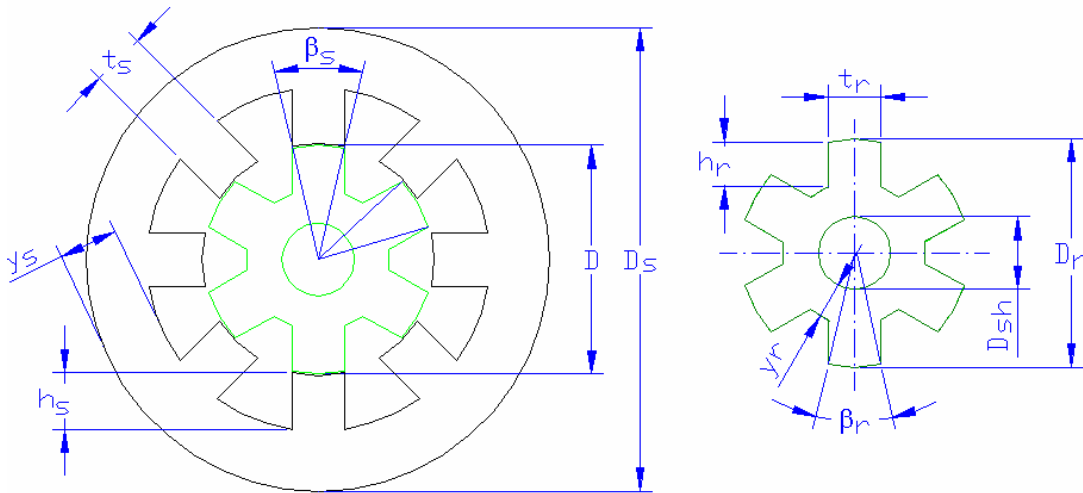
Fig. 2.2   Cross section of an 8/6-SRM showing stator and rotor dimensioning parameters

The presented design procedure involves the selection of various coefficients related to the motor geometry, magnetic and electric properties. The calculations are generally simple and can therefore be implemented in design software. The result is on the one hand a well working machine geometry to start with, but on the other hand the design is relatively inaccurate unless adequate design experience is accumulated. The final machine design is achieved through an iterative process of analytical steady-state and dynamic performance calculations, numerical FEM calculations and simulations as it will be pointed out in detail in the following chapters of this thesis.

2.8 Winding design

The slot area can be calculated by subdividing the stator slot into two geometric sections, as shown in Fig. 2.3a. Section (a) has a trapezoidal cross section; the cross section of section (b) is a segment of circle.
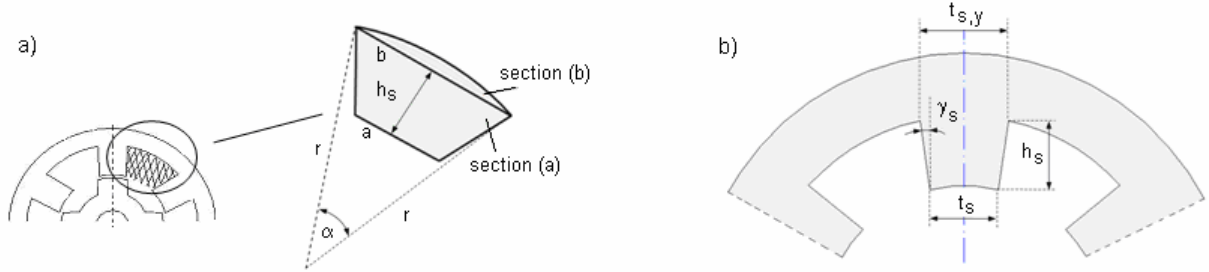

Fig. 2.3 Calculation of stator slot area

The cross section of the trapezoidal section $A_{(a)}$ can be calculated with:

$$A_{(a)} = \frac{1}{2} \cdot (a + b) \cdot h_s \tag{2.16}$$

with
$$a = \frac{D \cdot \pi}{N_s} - t_s \tag{2.17}$$

and
$$b = \frac{(D_s - 2 \cdot y_s) \cdot \pi}{N_s} - t_{s,y} \tag{2.18}$$

The parameter $t_{s,y}$ is the stator pole width at the pole base regarding tapered (trapezoidal) pole shapes. With respect to Fig. 2.3b it can be calculated with the tapering angle of the stator pole side γ_s as follows:

$$t_{s,y} = t_s + 2 \cdot h_s \cdot \tan(\gamma_s) \tag{2.19}$$

The cross section of the segment of circle $A_{(b)}$ in the stator slot is calculated with the angle α (in radian) which describes the free-space between two adjacent stator poles at the yoke, and the corresponding stator yoke radius r (see Fig. 2.3a for reference).

$$A_{(b)} = \frac{r^2}{2} (\alpha - \sin(\alpha)) \tag{2.20}$$

with
$$r = \frac{D}{2} + h_s \tag{2.21}$$

and
$$\alpha = \frac{2\pi}{N_s} - 2 \cdot \arcsin\left(\frac{t_{s,y}}{D + 2h_s}\right) \tag{2.22}$$

The total slot area A_{slot} is the sum of the pre-calculated sections:

$$A_{slot} = A(a) + A(b) = \frac{1}{2} \cdot (a + b) \cdot h_s + \frac{r^2}{2} (\alpha - \sin(\alpha)) \tag{2.23}$$
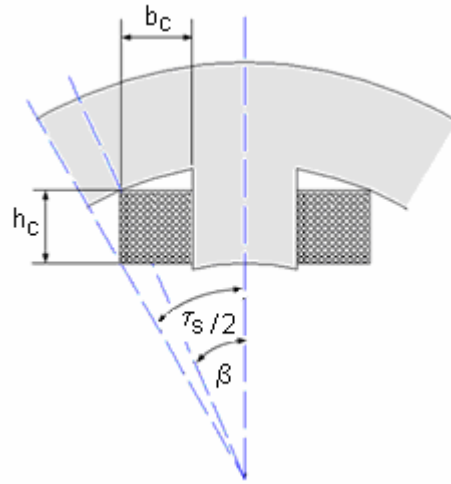
Fig. 2.4   Dimensions of rectangular stator coils

The *maximum stator coil dimensions* of a common rectangular cross section shown in Fig. 2.4 are given by their width b_c and height h_c, assuming a round outer stator core and straight stator poles:

$$b_c = \frac{D}{2}\tan\left(\frac{\pi}{N_s}\right) - \frac{t_s}{2} = \frac{D}{2}\tan\left(\frac{\tau_s}{2}\right) - \frac{t_s}{2} \tag{2.24}$$

$$h_c = \frac{b_c + \dfrac{t_s}{2}}{\tan\beta} - \frac{D}{2} \tag{2.25}$$

with $$\beta = \arcsin\left(\frac{b_c + \dfrac{t_s}{2}}{\dfrac{D}{2} + h_s}\right) \tag{2.26}$$

The *number of turns per phase* respectively the number of turns per pole can be roughly estimated with the assumption that the conduction ('dwell') angle Θ_d of the SRM at a particular speed has a certain value, maybe the stroke angle $\Theta_{sk} = (2\pi)/(q \cdot N_r)$. Under the condition of single pulse operation with no current chopping the maximum flux value is given by the law of induction (recessive voltage drops are neglected) with the dc supply voltage V_s:

$$\psi_{max} = \frac{V_s \cdot \Theta_d}{\omega} \tag{2.27}$$

Assuming that at the angular velocity ω the ampere-turns are sufficient to bring the stator pole to the flux density B_{sp} across the entire width at its base, the maximum flux-linkage is

$$\psi_{max} = 2p \cdot N_p \cdot \phi_{max} = 2p \cdot N_p \cdot B_{sp} \cdot l_{stk} \cdot t_s \tag{2.28}$$

N_p is the number of turns per pole and *2p* is pole-pair number, given by

$$2p = \frac{N_s}{q} \tag{2.29}$$

The maximum flux-linkage occurs typically when the overlap between the stator and rotor poles is about 2/3 of the stator pole arc β_s [8]. In this point B_s is usually between 1.35 and 1.8T. Combining the above equations gives an expression for the number of turns per pole and phase:

$$N_p = \frac{V_s \cdot \Theta_d}{\omega} \cdot \frac{1}{2p \cdot B_{sp} \cdot l_{stk} \cdot t_s} \qquad \text{(turns per pole)} \tag{2.30}$$

$$N_{ph} = 2p \cdot N_p = \frac{V_s \cdot \Theta_d}{\omega \cdot B_{sp} \cdot l_{stk} \cdot t_s} \qquad \text{(turns per phase)} \tag{2.31}$$

The decisive parameter which describes the electrical load of a conductor is the current density J. Its maximum allowable value determines the minimal conductor bare diameter D_w:

$$D_w = 2\sqrt{\frac{I_{rms}}{\pi \cdot J}} \tag{2.32}$$

where I_{rms} is the r.m.s phase current. Reference values of maximum current densities for electrical machines in dependence of the cooling system can be found among others in [8], [12], [13], [14], [17] and [18]. The winding cross sectional area of one coil A_{wc} is

$$A_{wc} = N_p \cdot \frac{\pi}{4}(1.08 D_w)^2 \tag{2.33}$$

The factor 1.08 accounts the wider wired diameter of an enamelled round wire [124]. With two coil sides per slot, the maximum available cross sectional area of one coil side (N_p turns) is half of that calculated with (2.33). Finally, with the fill factor of the stator slot φ_{slot} by the windings the total stator slot area is determined:

$$A_{w,slot} = \frac{A_{wc}}{\varphi_{slot}} \tag{2.34}$$

Usually, the slot fill factor φ_{slot} is in the range between 0.4 and 0.6 ([8], [16], [18], [33], [124]).

3 Calculation algorithms and programs

3.1 Generals

The AMPERE'S law forms the starting point for the computation of the magnetic circuit of electrical machines. It is given by

$$mmf = \oint H \cdot ds = \sum \int H \cdot ds = N_{ph} \cdot i \tag{3.1}$$

For the mmf calculation of an excitation winding it is favourable to choose the integration path in such a way that it totally encloses the winding and allows an easy determination of the mmf drop. The SRM is a doubly salient machine with concentrated coils around the stator poles. The magnetic circuit can be divided into five parts, as shown in Fig. 3.1a for the example of a simple '2-pole' pattern in the aligned position: (1) stator pole (index *sp*); (2) rotor pole (index *rp*); (3) stator yoke (index *sy*); (4) rotor yoke (index *ry*); (5) air gap (index *g*). Derived from (3.1) the mmf-equation for the main flux-path in Fig. 3.1a is

$$mmf = V_{sp} + V_g + V_{rp} + V_{ry} + V_{sy} \tag{3.2}$$

where V represents the mmf-drops in the various parts of the magnetic circuit.
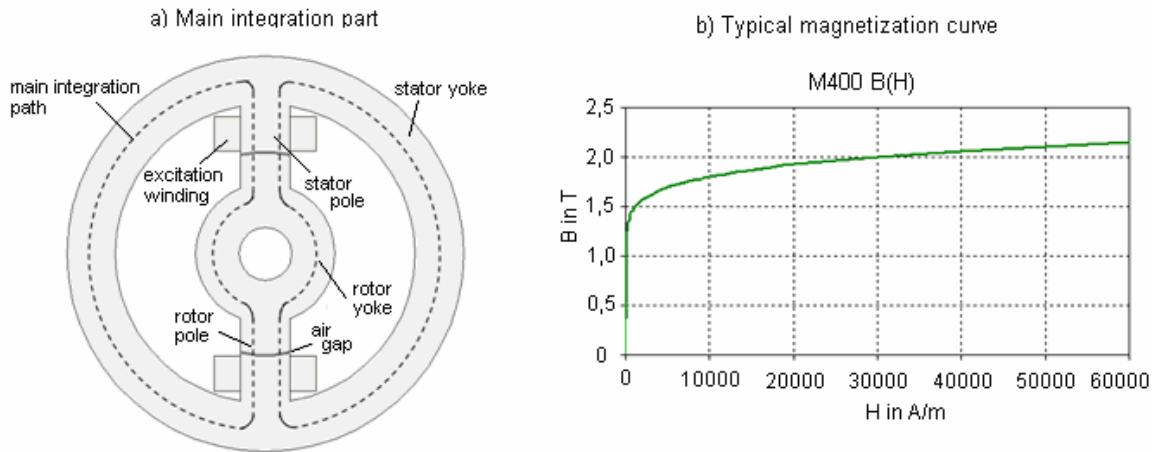
Fig. 3.1 a) Sections of the magnetic part for flux path (aligned position); b) typical B-H curve

The magnetic filed strength for calculation of V is obtained from the magnetic flux density:

$$B = \mu \cdot H \quad \text{with} \quad \mu = \mu_0 = 1.256 \cdot 10^{-6} Vs / Am \text{ (in vacuum)} \tag{3.3}$$

The relative permeability μ_r of ferromagnetic materials is significant greater than μ_0 and a function of the magnetic field strength. It is common to describe the relationship B(H) in form of the magnetization curve of the particular ferromagnetic material as shown in Fig. 3.1b.

The relationship between the magnetic flux Φ and magnetic flux density B is given by

$$\Phi = B \cdot A \tag{3.4}$$

assuming that the flux density is constantly distributed across the integration area A. The relationship B(H) cannot be written in an enclosed analytical form. Therefore (3.3) can not be

solved for each particular mmf-drop for a given mmf. Hence, the magnetization curve can only be determined by the iterative way

$$\Phi_g \rightarrow B \rightarrow H \rightarrow V \rightarrow mmf \quad \text{respectively} \quad B_{\max} \rightarrow \Phi_g \rightarrow B \rightarrow H \rightarrow V \rightarrow mmf$$

If the poles of the SRM are tapered, i.e. they have a trapezoidal profile, the cross section area changes with the pole high h_p. The entire mmf-drop V_p of such a pole can be calculated by using SIMPSON'S law which advises to consider the mmf drops at the pole base ($h_p=0$), at the middle of the pole ($h_p/2$) and at the pole tip (h_p) as follows:

$$V_p = \frac{1}{6} \cdot \left[H_p(0) + 4 \cdot H_p(h_p/2) + H_p(h_p) \right] \cdot h_p \qquad (3.5)$$

Magnetic disburdening of poles

In the case when the flux density in the stator or rotor poles exceeds 1.7T, the magnetic field in the adjacent slot (or other non-ferromagnetic parts), shown in Fig. 3.2, is considerable and cannot be neglected [16]. In this case, some pole flux lines also pass the slot area. Therefore partial magnetic fields or sections with different magnetization characteristics are situated side by side with respect to the field course. These sections are influencing each other. A relationship between the pole flux density $B_p(s)$ and the magnetic field strength $H_p(s)$ along the main integration path s shown in Fig. 3.2 is determined by [16]:

$$B_p(s) = \frac{\Phi_p(s)}{A_p(s)} = B_{ip}(s) - \mu_0 \cdot H_p(s) \cdot \frac{A_1(s)}{A_p(s)} \qquad (3.6)$$
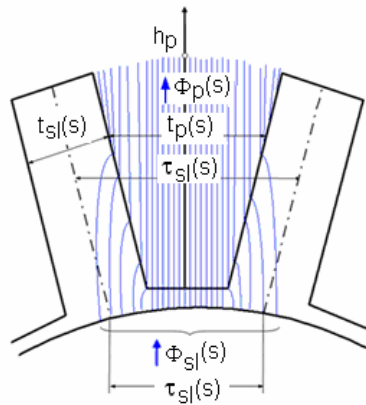

Fig. 3.2   Magnetic disburdening of the pole (here: stator pole) for B>1.7T

The difference between the slot pitch cross section $\tau_{sl}(s) \cdot l_{stk}$ and the pole cross section $A_p(s) = t_p(s) \cdot \varphi_{Fe} \cdot l_{stk}$ represents the cross section $A_1(s)$ of the parallel air paths. That area not only contains the slot cross section $t_{sl}(s) \cdot l_{stk}$ but also the cross section of the n_v ventilating channels (if existing) $t_p(s) \cdot n_v \cdot l_v$ with their length l_v and the cross section of the lamination insulation $t_p(s) \cdot (1 - \varphi_{Fe}) l_{stk}$. Hence,

$$A_1(s) = t_{sl}(s)l_{stk} + t_p(s)n_v l_v + t_p(s)(1-\varphi_{Fe})_{lstk} \tag{3.7}$$

with $\quad B_{pi} = \dfrac{\Phi_{sl}(s)}{A_p(s)}$ \hfill (3.8)

The 'imaginary' pole flux density B_{pi} would occur if the entire flux Φ_{sl} crosses the pole, which implies $\mu_{air}=0$. However, the flux part through the parallel air paths reduces the pole flux density compared to the ideal case for the factor $\mu_0 \cdot H_p(s) \cdot A_1(s)/A_p(s)$. That effect is often called 'magnetic disburdening' in bibliography [16].
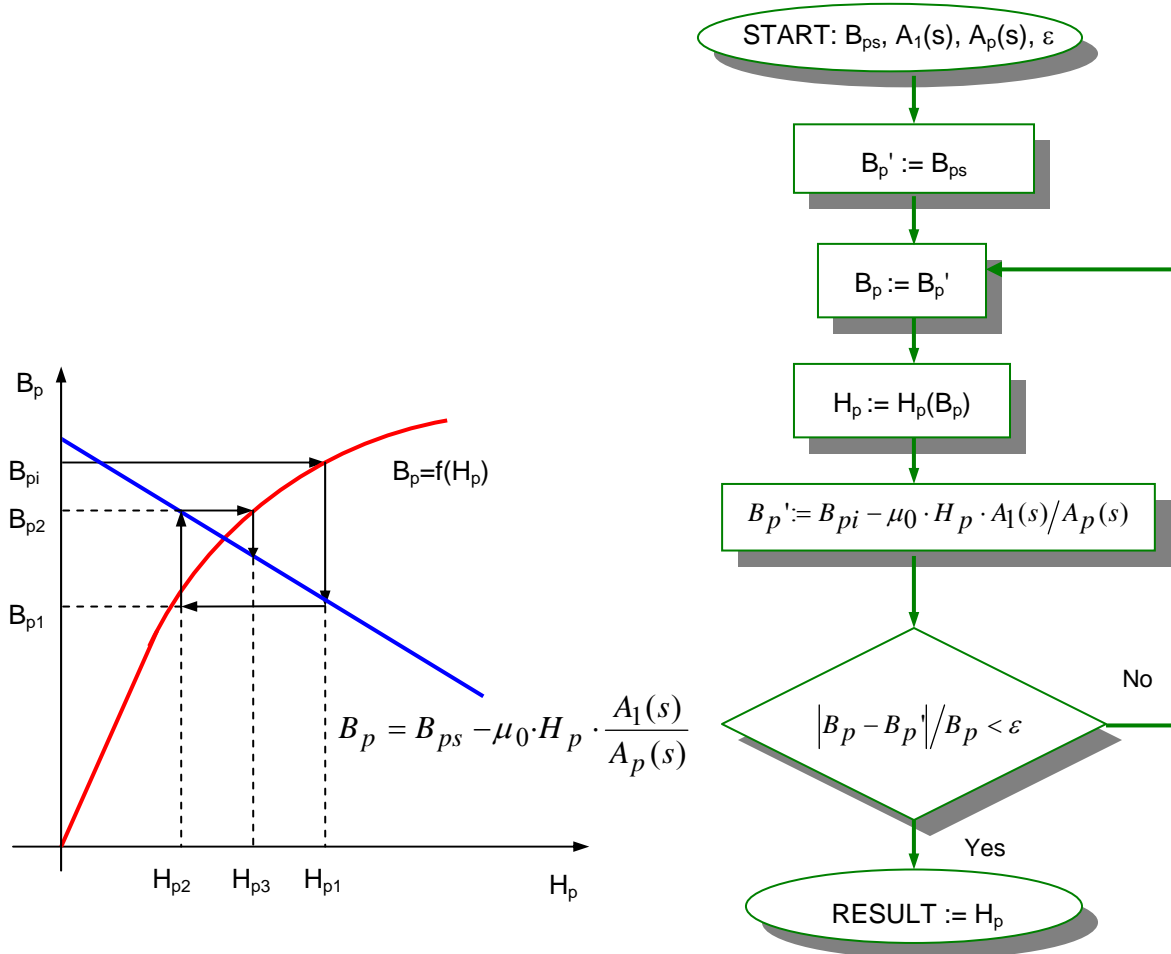
Fig. 3.3   Iterative calculation of the pole field strength H_p in the case of magnetic pole disburdening

In order to obtain a numerical solution for the effect of magnetic disburdening, [14] and [16] propose an iterative method. At first one chooses a certain value for B_p, e.g. the imaginary flux density B_{pi}, for which a first (too large) value for the corresponding field strength H_{p1} can be determined from the B(H)-characteristic. With H_{p1} a corrected (firstly too small) value B_{p1} can be obtained by means of (3.6). Now, with B_{p1} a new (now too small) H_{p2} and a corrected (too large) B_{p2} can be obtained by the same way. That iterative method is continued until the difference between the B_{pk}-value of the previous (k-1) and actual (k) iteration step is sufficient small. By studying the calculation algorithm in Fig. 3.3 it becomes clear that this algorithm does not converge for all cases. For example, if the absolute gradient of the straight

line in the point of intersection with the B(H)-curve is greater that the gradient of this magnetization curve, or if the first iteration step yields to a negative B_{p1}. Therefore, the field strength $H_{p(k)}$ is calculated for an intermediate value of B_p, for example the average value of $B_{p(k)}$ and $B_{p(k-1)}$ for further calculation.

3.2   Inductance calculation

The Finite Element Analysis offers a possibility for the performance computation of SRMs ([79], [112], [137], [144], [177] and [180]). Though FEM calculations are generally more accurate than analytical methods, they require much more set-up and execution time on a computer. Note that a change in one or many of the motor and control parameters requires an entire new FEM computation, either in two or three dimensions with a considerable amount of time. This is impractical in a typical industrial situation. It is advantageous for a machine designer to know of the quantitative relationships between parameters, however inaccurate they may be. Therefore, the need for an improved analytical calculation method, capable of predicting the machine inductance at every rotor position and excitation level exists. The procedure outlined in this thesis bases on a method firstly proposed in [4] and [38]. Additionally, an approximative procedure for estimating the inductance of intermediate rotor positions is presented, using a 'gage-curves' method proposed by [97] and [134]. The developed procedure includes:

- the prediction of inductance at any rotor position,
- investigation of straight and tapered stator and rotor pole profiles,
- magnetic disburdening of the stator and rotor poles for B>1.7T in aligned position,
- an allowance for fringe flux at the ends of core and
- the mmf-drop in the iron core and saturation effects in all rotor positions.

The following calculation approach uses analytical iterations to obtain inductance vs. current characteristics from the machine variables that are used to predict the torque and power output. For various positions of the rotor, a fixed number of flux paths is assumed. These flux paths are obtained from flux maps derived by two-dimensional FEM calculations. The equations derived apply to all levels of excitation under the following assumptions:

(1)   The flux lines enter and leave the iron surface perpendicularly.

(2)   The flux lines in the stator and rotor poles are parallel to the pole axis.

(3)   The windings are assumed to be rectangular blocks; the stator inter polar space is only partially filled with windings.

(4)   The flux lines in the stator and rotor yoke are concentric.

(5)   The air gap flux lines consist of concentric arcs and straight-line segments.

(6)   The shaft consists of purely non-magnetic material.

(7)   The calculations are done for the complete q-phase machine with $p = |N_s - N_r| / 2$ pole pairs in order to achieve high universality and flexibility of the derivations.

(8)   Tapered (trapezoidal) pole profiles are considered.

Calculation of aligned inductance

For determining the maximum inductance at the aligned position, an 8/6- SRM is considered for example. A certain stator pole flux density is assumed, giving a stator pole flux by multiplying with the stator pole cross section area. The flux densities in other machine parts (rotor pole, stator and rotor yoke and air gap) are derived from the machine geometry and the assumed stator pole flux density. From the flux densities in various machine parts and the B(H) characteristic of the lamination material, the corresponding magnetic field strengths are obtained. Given the magnetic field strengths and the length of the flux path in each part, their product gives the magnetomotive force mmf. The mmf's for various parts are likewise obtained, and for the magnetic equivalent circuit and stator excitation the AMPERE'S circuital law is applied. The error between the applied stator mmf and that given equivalently by various machine parts is used to adjust the assumed flux density in the stator pole. The entire iteration continuous until the error is reduced to a fixed tolerance value.

Considering the complete aligned position, two main flux paths are shown in Fig. 3.4. The presented flux map is obtained by a previous two-dimensional FEM calculation. It was found that about 90% to 98% of the flux lines pass the air gap between the stator and rotor, identified as flux path 1. There is only a small flux due to leakage between adjacent poles, identified as flux path 2. The derivations for these two flux paths are given separately.
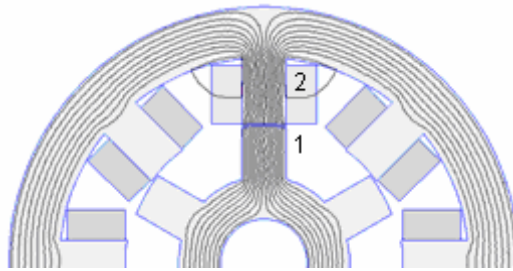

Fig. 3.4   Two flux path for calculation of aligned inductance, obtained by FEM computation

Aligned inductance - flux path 1

The flux distribution is symmetric with respect to the centre line of the excited stator pole. The magnetic equivalent circuit of one phase is shown in Fig. 3.5a in terms of reluctances $\mathfrak{R}$ and stator-mmf F_1. From F_1, the flux Φ_1 in each segment of the magnetic circuit is known and accordingly the flux densities for these segments are evaluated. In the maximum inductance position the field pattern is symmetrically about the axis of the excited phase and therefore

only *one half of the magnetic circuit* which carries one half of the magnetic flux, need to be considered, resulting in the magnetic equivalent circuit in Fig. 3.5b.
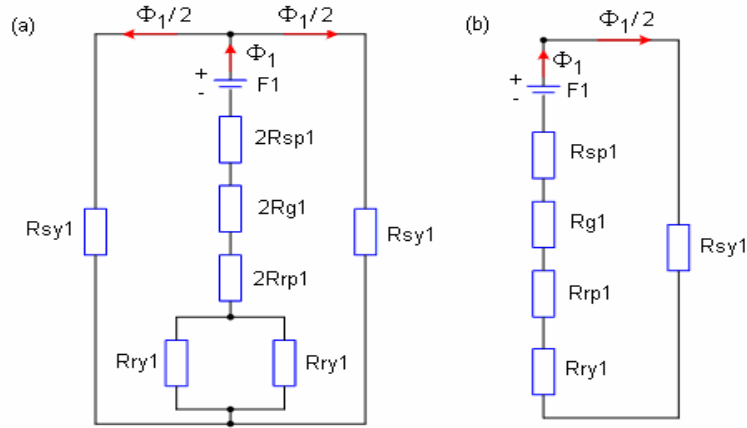

Fig. 3.5   Magnetic equivalent circuit for flux path 1 a) one pole pair; b) half of magnetic circuit

The stator and rotor poles are assumed to be tapered (trapezoidal) as shown in Fig. 3.6a. The 'degree' of tapering is defined by the pole shape angle γ_s and γ_r respectively. Therefore, concerning SIMPSON'S law (3.5), the cross section area must be calculated at the pole base (index *b*), the middle of the pole height (index *m*) and at the pole tip (index *t*):

Pole base:
$$A_{sp1,b} = \left(\left(D\sin\left(\frac{\beta_s}{2}\right) + 2h_s \tan(\gamma_s) \right) \cdot l_{Fe} \right) \cdot \frac{1}{2} = \frac{1}{2} t_{sp1,b} l_{Fe} \tag{3.9}$$

Pole middle:
$$A_{sp1,m} = \left(\left(D\sin\left(\frac{\beta_s}{2}\right) + h_s \tan(\gamma_s) \right) \cdot l_{Fe} \right) \cdot \frac{1}{2} = \frac{1}{2} t_{sp1,m} l_{Fe} \tag{3.10}$$

Pole tip:
$$A_{sp1,t} = \left(D\sin\left(\frac{\beta_s}{2}\right) \cdot l_{Fe} \right) \cdot \frac{1}{2} = \frac{1}{2} t_{sp1,t} l_{Fe} \tag{3.11}$$

Pole length:
$$l_{sp1} = 2p \cdot h_s \tag{3.12}$$

Reluctance:
$$\Re_{sp1} = \frac{1}{6} \left(\frac{H_{sp1,b}}{B_{sp1,b} A_{sp1,b}} + 4 \frac{H_{sp1,m}}{B_{sp1,m} A_{sp1,m}} + \frac{H_{sp1,t}}{B_{sp1,t} A_{sp1,t}} \right) l_{sp1} \tag{3.13}$$

where l_{Fe} is the iron length which is assumed with the stack length l_{stk} and the lamination fill factor φ_{Fe} to be $l_{Fe} = l_{stk}\varphi_{Fe}$. In order to concern the magnetic disburdening of the stator pole in the aligned position for flux density values B>1.7T with reference to (3.6), the cross section area of the air parallel to the main flux path (A_1) must be calculated by applying (3.7), assuming that it is equal to half of the cross section area of the stator interpolar space plus half of the cross section of the lamination insulation. There are no ventilation channels supposed. The same is true for the rotor poles. Their reluctance can be similarly calculated with:

Pole base:
$$A_{rp1,b} = \left(\left((D - 2g) \cdot \sin\left(\frac{\beta_r}{2}\right) + 2h_r \tan(\gamma_r) \right) \cdot l_{Fe} \right) \cdot \frac{1}{2} = \frac{1}{2} t_{rp1,b} l_{Fe} \tag{3.14}$$

Pole middle: $A_{rp1,m} = \left(\left((D - 2g) \cdot \sin\left(\frac{\beta_r}{2}\right) + h_r \tan(\gamma_r) \right) \cdot l_{Fe} \right) \cdot \frac{1}{2} = \frac{1}{2} t_{rp1,m} l_{Fe}$ (3.15)

Pole tip: $A_{rp1,t} = \left((D - 2g) \cdot \sin\left(\frac{\beta_r}{2}\right) \cdot l_{Fe} \right) \cdot \frac{1}{2} = \frac{1}{2} t_{rp1,t} l_{Fe}$ (3.16)

Pole length: $l_{rp1} = 2p \cdot h_r$ (3.17)

Reluctance: $\Re_{rp1} = \frac{1}{6} \left(\frac{H_{rp1,b}}{B_{rp1,b} A_{rp1,b}} + 4 \frac{H_{rp1,m}}{B_{rp1,m} A_{rp1,m}} + \frac{H_{rp1,t}}{B_{rp1,t} A_{rp1,t}} \right) l_{rp1}$ (3.18)

The flux path in the air gap is considered now. Its length is assumed to be:

$$l_{g1} = 2p \cdot g$$ (3.19)

Due to fringing effects the effective cross section in the air gap is bigger than the stator pole cross section area. In order to make some allowance for this the air gap cross section A_{g1} is increased by introducing CARTER's coefficient σ [64]:

$$A_{g1} = \left[\frac{1}{2} D \sin\left(\frac{\beta_s}{2}\right) + (1 - \sigma) \cdot u \right] l_{Fe}$$ (3.20)

with $\quad u = \frac{1}{2}\left(\frac{D}{2} - g\right) \sin\left(\frac{\beta_r - \beta_s}{2}\right)$ (3.21)

and $\quad \sigma = \frac{2}{\pi}\left[\arctan\left(\frac{u}{g}\right) - \frac{g}{2u} \ln\left(1 + \left(\frac{u}{g}\right)^2\right) \right]$ (3.22)

$$\Re_{g1} = \frac{l_{g1}}{\mu_0 A_{g1}}$$ (3.23)

The cross section, length of the flux path and resulting reluctance in the stator yoke (half of the magnetic circuit) is obtained by assuming the flux path in the middle of the yoke:

$$l_{sy1} = \frac{\pi}{2}(D_s - y_s)$$ (3.24)

$$A_{sy1} = y_s l_{Fe}$$ (3.25)

$$\Re_{sy1} = \frac{H_{sy1} \cdot l_{sy1}}{B_{sy1} A_{sy1}}$$ (3.26)

Similarly, the length of the flux path in the rotor yoke and its cross section are determined:

$$l_{ry1} = \frac{\pi}{2}(D - 2g - 2h_r - y_r)$$ (3.27)

$$A_{ry1} = y_r l_{Fe}$$ (3.28)

$$\Re_{ry1} = \frac{H_{ry1} \cdot l_{ry1}}{B_{ry1} A_{ry1}}$$ (3.29)

From the final flux densities in the various segments of the flux path and the magnetic field strengths, the reluctances are calculated. With them the Ampere circuital equation for one side of the magnetic circuit can be written as

$$F_1 = N_{ph}i = \phi_1 \cdot \left(\mathfrak{R}_{g1} + \mathfrak{R}_{sp1} + \mathfrak{R}_{rp1} + \mathfrak{R}_{ry1} + \mathfrak{R}_{sy1} \right) \tag{3.30}$$

If the calculated right-hand mmf is not equal to the applied mmf, F_1, the error between them can be reduced by an iterative adjustment of the stator pole flux density B_{sp}, and then recalculating all other parameters. The error mmf is defined as

$$\Delta F_1 = F_1 - \sum Hl = N_{ph}i - \sum Hl \tag{3.31}$$

Finally, the phase inductance contributed by the flux path 1 at aligned position is determined. For both sides of the magnetic circuit flux path 1 contributes to the inductance L_{a1}:

$$L_{a1} = 2 \frac{N_{ph}\phi_1}{i} \tag{3.32}$$

Aligned inductance - flux path 2

Flux path 2 in Fig. 3.6a represents the leakage flux in the aligned position. The flux-linkage of path 2 is small in comparison to path 1 because the linked amp-turns become smaller. The magnetic equivalent circuit of path 2 is presented in Fig. 3.6b.
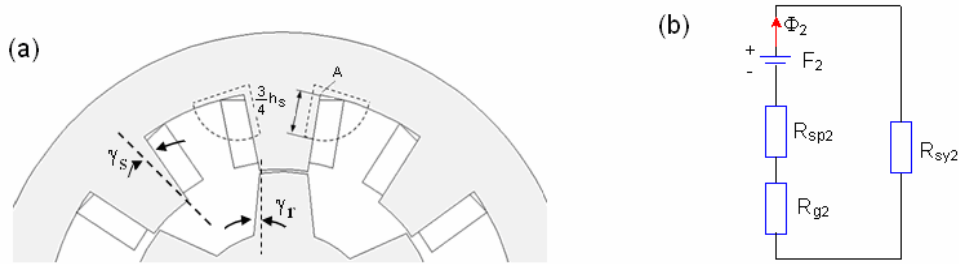

Fig. 3.6   a) Detail with flux path 2 in aligned position; b) magnetic equivalent circuit for a half pole

The flux lines are assumed to be linked with 3/4 of the stator turns. Thus, the mmf equation is

$$F_2 = \frac{3}{4} N_{ph}i = \phi_2 \cdot \left(\mathfrak{R}_{sp2} + \mathfrak{R}_{g2} + \mathfrak{R}_{sy2} \right) \tag{3.33}$$

For the calculation of flux path length, the flux path is assumed to be centred at point A in Fig. 3.6a, with a radius of $3/4h_s$ and an angle of $\pi/2$. The various lengths and cross section areas of the segments are then:

Stator pole: $l_{sp2} = \left(\frac{3}{4}h_s + \frac{y_s}{2} \right)$ (3.34)

$$A_{sp2} = \frac{1}{2}\left(\frac{3}{4}h_s \right) \cdot l_{Fe} \tag{3.35}$$

Air gap: $l_{g2} = \left(\frac{3}{4}h_s \cdot \frac{\pi}{2} \right)$ (3.36)

$$A_{g2} = \frac{3}{4} h_s l_{Fe} \qquad (3.37)$$

Stator yoke: $l_{sy2} \approx l_{sp2}$ (3.38)

$$A_{sy2} = y_s l_{Fe} \qquad (3.39)$$

The inductance contributed by the 2(2p) flux paths 2 is calculated as

$$L_{a2} = 2(2p) \cdot \frac{\frac{3}{4} N_{ph} \phi_2}{i} = p \frac{3 N_{ph} \phi_2}{i} \qquad (3.40)$$

The total aligned inductance L_a is the sum of the inductance of flux path 1 and 2:

$$L_a = L_{a1} + L_{a2} \qquad (3.41)$$

Calculation of unaligned inductance

Although [29], [30], [64], [135] and [150]-[152] give equations for calculating minimum inductance, the equations cannot be easily verified. The best way to determine the minimum inductance is to plot the equiflux lines for a test machine in the completely unaligned position and calculate the lengths of the equiflux lines in the air gap and then account for the paths in the iron sections, as proposed in [4] and [128]. Fig. 3.7 shows the equiflux lines in the unaligned position for the example of a 4-phase 8/6-machine, obtained by FEM computation.
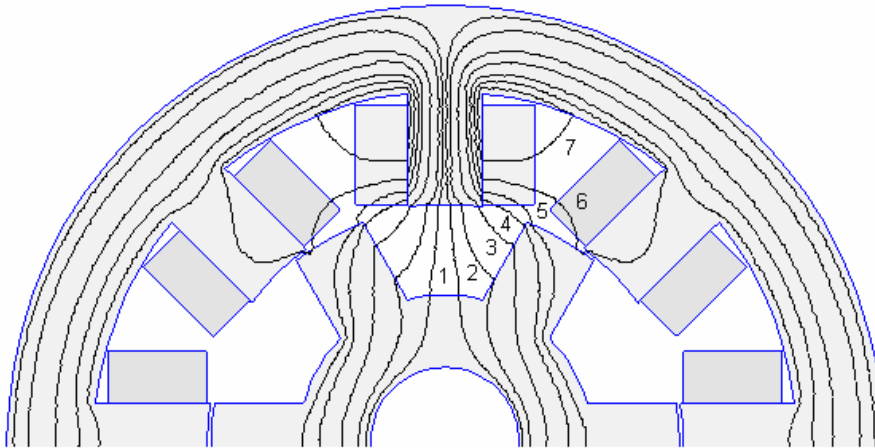

Fig. 3.7 Identification of 7 flux paths for analytical calculation of unaligned inductance

Unaligned inductance – Flux path 1

The field lines of path 1 in Fig. 3.8a lead from the stator pole face to the rotor interpolar face. They are assumed to be linked with all turns. Path 1 encloses one quarter of the stator pole arc, as proposed in [64]. Note, for the case of trapezoidal poles, the cross section area of the poles is calculated at the base, the middle and the tip to obtain the mmf drop in this sections according to SIMPSON'S law. In order to calculate easily the inductance for machines with a pole pair number p>1 it is favourable to calculate firstly one half of the magnetic circuit for

the flux path. That is justified if it is assumed that the field pattern is symmetrical about the axis of the excited phase. Hence, the cross section of path 1 in the stator pole is halved.
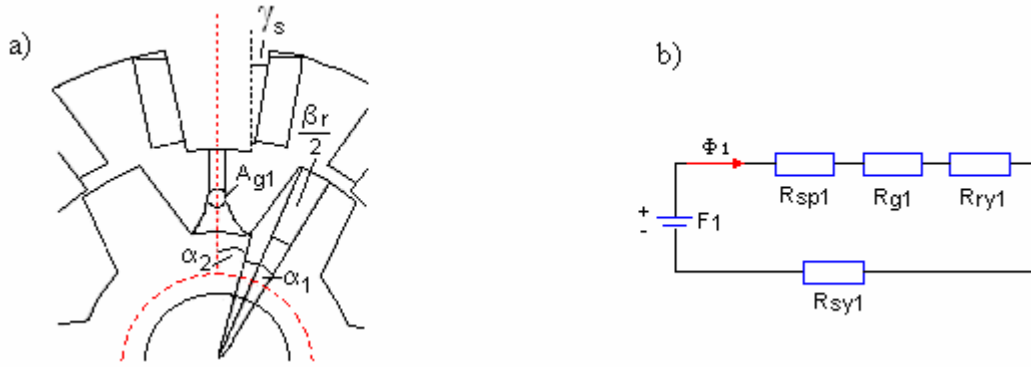

Fig. 3.8   a) Detail with flux path 1 in unaligned position; b) magnetic equivalent circuit

The reluctance for path 1 in the stator pole is derived as follows:

Pole base:
$$A_{sp1,b} = \left(\frac{1}{4}\left(D\sin\left(\frac{\beta_s}{2}\right) + 2h_s \tan(\gamma_s)\right)\cdot l_{Fe}\right)\cdot\frac{1}{2} \tag{3.42}$$

Pole middle:
$$A_{sp1,m} = \left(\frac{1}{4}\left(D\sin\left(\frac{\beta_s}{2}\right) + h_s \tan(\gamma_s)\right)\cdot l_{Fe}\right)\cdot\frac{1}{2} \tag{3.43}$$

Pole tip:
$$A_{sp1,t} = \left(\frac{1}{4} D\sin\left(\frac{\beta_s}{2}\right)\cdot l_{Fe}\right)\cdot\frac{1}{2} \tag{3.44}$$

Pole length: $\quad l_{sp1} = 2p\cdot h_s \quad$ (where $\quad p = |N_s - N_r|/2$)
$$\tag{3.45}$$

Reluctance:
$$\mathfrak{R}_{sp1} = \frac{1}{6}\left(\frac{H_{sp1,b}}{B_{sp1,b}A_{sp1,b}} + 4\frac{H_{sp1,m}}{B_{sp1,m}A_{sp1,m}} + \frac{H_{sp1,t}}{B_{sp1,t}A_{sp1,t}}\right) l_{sp1} \tag{3.46}$$

The length of the flux path in the air gap l_{g1} is

$$l_{g1} = 2p(h_r + g) \tag{3.47}$$

The area of cross section of path 1 in the air gap varies throughout the air gap, therefore its mean is considered for calculation. It is obtained with respect to Fig. 3.8a:

$$A_{r1} = \left(2\left(\frac{D}{2} - g - h_r\right)\sin(\alpha_2)\cdot l_{Fe}\right)\cdot\frac{1}{2} \tag{3.48}$$

with
$$\alpha_1 = \arcsin\left[\frac{\frac{1}{2}\left((D - 2g)\sin\left(\frac{\beta_r}{2}\right) + 2h_r \tan(\gamma_r)\right)}{\frac{D}{2} - g - h_r}\right] \tag{3.49}$$

and
$$\alpha_2 = \frac{1}{2}\left(\frac{2\pi}{N_r}\right) - \alpha_1 = \frac{\tau_r}{2} - \alpha_1 \tag{3.50}$$

The average cross section area of path 1 in the air gap is

$$A_{g1} = \frac{A_{sp1} + A_{r1}}{2} \tag{3.51}$$

The length of path 1 in the rotor yoke is assumed to be the average of the shaft periphery with the shaft diameter D_{sh} and the inner rotor pole base periphery.

$$l_{ry1} = \frac{1}{2}\left[\frac{D_{sh}\pi}{2} + (D - 2g - 2h_r)\frac{\pi}{2} \right] \tag{3.52}$$

$$A_{ry1} = y_r \cdot l_{Fe} = \left(\frac{D}{2} - g - h_r - \frac{D_{sh}}{2} \right) l_{Fe} \tag{3.53}$$

$$\Re_{ry1} = \frac{H_{ry1} \cdot l_{ry1}}{B_{ry1} A_{ry1}} \tag{3.54}$$

The length and cross section area of the flux path in the stator yoke completes the relevant parameters for the reluctance calculation of path 1:

$$l_{sy1} = \frac{\pi}{2}(D_s - y_s) \tag{3.55}$$

$$A_{sy1} = y_s l_{Fe} \tag{3.56}$$

$$\Re_{sy1} = \frac{H_{sy1} \cdot l_{sy1}}{B_{sy1} A_{sy1}} \tag{3.57}$$

The AMPERE'S circuital equation and the inductance contributed by flux path 1 for both sides of the magnetic circuit can be determined from the magnetic equivalent circuit in Fig. 3.8b:

$$F_1 = N_{ph}i = \phi_1 \cdot \left(\Re_{sp1} + \Re_{g1} + \Re_{sy1} + \Re_{ry1} \right) \tag{3.58}$$

$$L_{u1} = 2\frac{N_{ph} \cdot \phi_1}{i} \tag{3.59}$$

Unaligned inductance – Flux path 2

The details of the magnetic configuration for flux path 2 in the unaligned position are presented in Fig. 3.9a. Fig. 3.9b shows the magnetic equivalent circuit for one side of the machine. The flux lines are assumed to be linked with all turns. Further it is supposed that the flux enters at $h_r/4$ from the inner rotor pole radius [4], [38]. The area of the flux path is estimated to be one quarter of the entire stator pole cross section area. Accounting tapered poles, the areas and length for the reluctance of the stator poles $\Re_{sp2}$ are calculated (with reference to (3.13)) for one side of the machine similarly to path 1:

Pole base: $$A_{sp2,b} = \frac{1}{2}\left[\frac{1}{4}\left(D\sin\left(\frac{\beta_s}{2}\right) + 2h_s \tan(\gamma_s) \right) \right] l_{Fe} \tag{3.60}$$

Pole middle:
$$A_{sp2,m} = \frac{1}{2}\left[\frac{1}{4}\left(D\sin\left(\frac{\beta_s}{2}\right) + h_s \tan(\gamma_s)\right)\right]l_{Fe} \tag{3.61}$$

Pole tip:
$$A_{sp2,t} = \frac{1}{2}\left(\frac{1}{4}D\sin\left(\frac{\beta_s}{2}\right)\right)l_{Fe} = \frac{1}{8}D\sin\left(\frac{\beta_s}{2}\right)l_{Fe} \tag{3.62}$$

Pole length: $l_{sp2} = 2p \cdot h_s$ $\tag{3.63}$

For calculating the reluctance $\Re_{rp2}$, the length and cross section of flux path 2 are

$$A_{rp2} = \left(\frac{h_r}{4}\right)l_{Fe} \tag{3.64}$$

$$l_{rp2} = 2p \cdot \frac{h_r}{4} \tag{3.65}$$
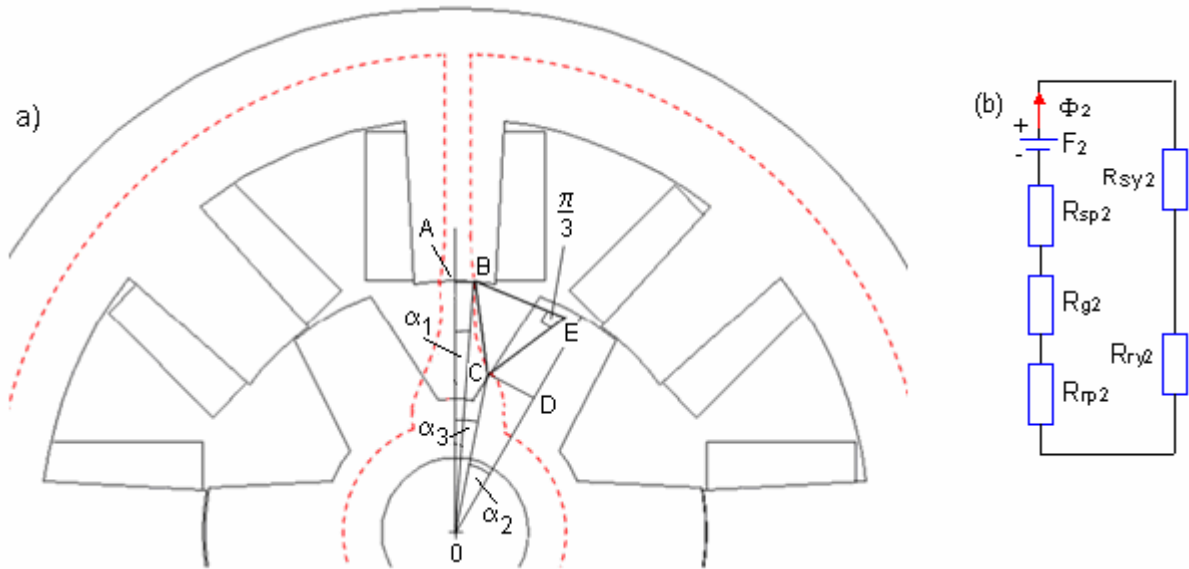
Fig. 3.9   a) Detail with flux path 2 in unaligned position; b) magnetic equivalent circuit

The area of cross section of path 2 in the air gap is approximately the average of stator and rotor pole. Attention is now turned on the estimation of the path length in the air gap by means of Fig. 3.9a. The angle α_1 is assumed to be $\beta_s/4$. The length of AB is referred with x_1 and the length OA with y_1. Point C is found in coordinate form (x_2, y_2) with respect to point 0:

$$(x_1, y_1) = \left[\frac{D}{2}\sin(\alpha_1), \frac{D}{2}\cos(\alpha_1)\right] \tag{3.66}$$

$$(x_2, y_2) = [OD \cdot \sin(\alpha_3), OD \cdot \cos(\alpha_3)] \tag{3.67}$$

with $\quad \alpha_2 = \arctan\left(\dfrac{CD}{OD}\right) = \arctan\left(\dfrac{\left(\dfrac{D}{2} - g\right)\sin\left(\dfrac{\beta_r}{3}\right) + \dfrac{3h_r}{4}\tan(\gamma_r)}{\dfrac{D}{2} - g - \dfrac{3}{4}h_r}\right) \tag{3.68}$

and $\alpha_3 = \angle COA = \dfrac{\tau_r}{2} - \alpha_2$ (3.69)

The linear distance between the points B and C is assumed to be one side of an equilateral triangle and represents the radius of the arc formed by path 2. The length BC is

$$BC = l_{x2} = \sqrt{(x_2 - x_1)^2 + (y_2 - y_1)^2}$$ (3.70)

The arc is part of the circle centered at point E. The reluctance $\mathfrak{R}_{g2}$ (ref. equation (3.23)) can be calculated with length of flux path 2 in the air gap:

$$l_{g2} = (2p) \cdot l_{x2} \frac{\pi}{3}$$ (3.71)

The length and cross section of the flux path in the stator yoke are equal to flux path 1 in the unaligned position, thus $A_{sy2}=A_{sy1}$ and $l_{sy2}=l_{sy1}$, respectively. The same is true for the area in the rotor yoke, so $A_{ry2}=A_{ry1}$. The length of path 2 in the rotor yoke is assumed to be 2/3 of that from path 1 in the unaligned position, thus $l_{ry2} = 2/3\, l_{ry1}$. The corresponding reluctances are calculated similarly to (3.26) and (3.29). Finally, the AMPERE'S circuital equation for path 2 and the inductance can be determined from the magnetic equivalent circuit in Fig. 3.9b:

$$F_2 = N_{ph} i = \phi_2 \cdot \left(\mathfrak{R}_{sp2} + \mathfrak{R}_{g2} + \mathfrak{R}_{rp2} + \mathfrak{R}_{sy2} + \mathfrak{R}_{ry2} \right)$$ (3.72)

$$L_{u2} = 2 \frac{N_{ph} \cdot \phi_2}{i} \quad (\textit{whole machine})$$ (3.73)

Unaligned inductance – Flux path 3

Details of flux path 3 in the unaligned position are shown in Fig. 3.10. The magnetic equivalent circuit is similar to that of flux path 2 and therefore not shown here. The flux lines are assumed to be linked with all turns. Krishnan [4] advises to assume that the flux enters the rotor pole at $h_r/4$ from top and leaves the stator pole at $5/64\beta_s$ from the tips. Further, the width of path 3 in one side of the stator pole is assumed to be 3/32 of the stator pole width. Concerning tapered poles, the reluctance $\mathfrak{R}_{sp3}$ of the stator pole for path 3 is determined with

Pole base: $A_{sp3,b} = \dfrac{3}{32} \left(D \sin\left(\dfrac{\beta_s}{2} \right) + 2h_s \tan(\gamma_s) \right) l_{Fe}$ (3.74)

Pole middle: $A_{sp3,m} = \dfrac{3}{32} \left(D \sin\left(\dfrac{\beta_s}{2} \right) + h_s \tan(\gamma_s) \right) l_{Fe}$ (3.75)

Pole tip: $A_{sp3,t} = \dfrac{3}{32} D \sin\left(\dfrac{\beta_s}{2} \right) \cdot l_{Fe}$ (3.76)

Pole length: $l_{sp3} \approx h_s$ (3.77)

The reluctance $\mathfrak{R}_{rp3}$ is obtained from the length and area of cross section in the rotor pole:

$$l_{rp3} \approx (2p)\frac{3}{4}h_r \tag{3.78}$$
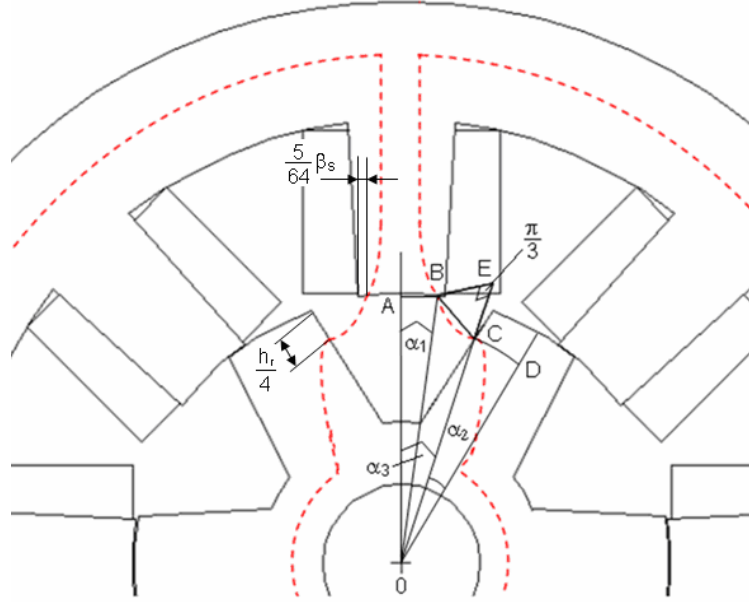
$$A_{rp3} = \frac{h_r}{4}l_{Fe} \tag{3.79}$$

Fig. 3.10   Detail with flux path 3 in unaligned position

The area of cross section in the air gap is assumed to be the average of stator and rotor pole. The length of the flux path 3 in the air gap is calculated by means of a similar procedure as it was used for path 2. The coordinates of B and C with point 0 as origin can be calculated and the flux path length in the air gap for obtaining $\mathfrak{R}_{g3}$ is derived as follows:

$$\alpha_1 = \frac{\beta_s}{2} - \frac{5}{64}\beta_s = \frac{27}{64}\beta_s \tag{3.80}$$

$$B = (x_1, y_1) = \left[\frac{D}{2}\sin(\alpha_1), \frac{D}{2}\cos(\alpha_1)\right] \tag{3.81}$$

$$OD = \frac{D}{2} - g - \frac{h_r}{4} \tag{3.82}$$

$$CD = \left(\frac{D}{2} - g\right)\sin\left(\frac{\beta_r}{2}\right) + \frac{h_r}{4}\tan(\gamma_r) \tag{3.83}$$

$$\alpha_2 = \arctan\left(\frac{CD}{OD}\right) \tag{3.84}$$

$$\alpha_3 = \frac{\tau_r}{2} - \alpha_2 \tag{3.85}$$

$$C = (x_2, y_2) = [OD \cdot \sin(\alpha_3), OD \cdot \cos(\alpha_3)] \tag{3.86}$$

$$l_{x3} = \sqrt{(x_2 - x_1)^2 + (y_2 - y_1)^2} \tag{3.87}$$

$$l_{g3} = (2p) \cdot l_{x3} \frac{\pi}{3} \tag{3.88}$$

The length and cross section of the flux path in the stator yoke are equal to flux path 1 in the unaligned position, thus $A_{sy3}=A_{sy1}$ and $l_{sy3}=l_{sy1}$, respectively. The same is valid for the area in the rotor yoke, so $A_{ry3}=A_{ry1}$. The length of path 3 in the rotor yoke is assumed to be equal to that of path 2, thus $l_{ry3}=l_{ry2}$. AMPERE'S circuital equation and the inductance contributed by flux path 3 for the complete machine can be written as

$$F_3 = N_{ph}i = \phi_3 \cdot \left(\Re_{sp3} + \Re_{g3} + \Re_{rp3} + \Re_{ry3} + \Re_{sy3} \right) \tag{3.89}$$

$$L_{u3} = 2 \frac{N_{ph} \cdot \phi_3}{i} \tag{3.90}$$

Unaligned inductance – Flux path 4

The magnetic equivalent circuit for flux path 4 is similar to that of flux path 2. In contrast to path 3 the flux lines leave the stator at the pole tips and enter the rotor pole at $7/8h_r$ from the pole base. The width of the path in one side of the stator pole is assumed to be $1/32$ of the pole width plus one quarter of $h_s/4$ [4]. With these assumptions, the reluctance $\Re_{sp4}$ of the stator pole is calculated using Fig. 3.10, since the general geometric relationships are similar.

Pole base: $\quad A_{sp4,b} = \left[\frac{1}{32} \left(D \sin\left(\frac{\beta_s}{2} \right) + 2h_s \tan(\gamma_s) \right) + \frac{1}{16} h_s \right] l_{Fe}$ $\tag{3.91}$

Pole middle: $A_{sp4,m} = \left[\frac{1}{32} \left(D \sin\left(\frac{\beta_s}{2} \right) + h_s \tan(\gamma_s) \right) + \frac{1}{16} h_s \right] l_{Fe}$ $\tag{3.92}$

Pole tip: $\quad A_{sp4,t} = \left[\frac{1}{32} D \sin\left(\frac{\beta_s}{2} \right) + \frac{1}{16} h_s \right] l_{Fe}$ $\tag{3.93}$

Pole length: $\; l_{sp4} \approx (2p) \cdot h_s$ $\tag{3.94}$

The rotor pole and air gap reluctance for path 4 are obtained with

$$l_{rp4} = (2p) \frac{7}{8} h_r \tag{3.95}$$

$$A_{rp4} = \frac{h_r}{4} l_{Fe} \tag{3.96}$$

$$\alpha_1 = \frac{\beta_s}{2} \tag{3.97}$$

$$\alpha_2 = \arcsin\left(\frac{\left(\frac{D}{2} - g \right) \sin\left(\frac{\beta_r}{2} \right) + \frac{h_r}{8} \tan(\gamma_r)}{\frac{D}{2} - g - \frac{h_r}{8}} \right) \tag{3.98}$$

$$\alpha_3 = \frac{\tau_r}{2} - \alpha_2 = \frac{\pi}{N_r} - \alpha_2 \tag{3.99}$$

$$B = (x_1, y_1) = \left[\frac{D}{2} \sin\left(\frac{\beta_s}{2}\right), \frac{D}{2} \cos\left(\frac{\beta_s}{2}\right) \right] \tag{3.100}$$

$$C = (x_2, y_2) = [OC \sin(\alpha_3), OC \cos(\alpha_3)] \tag{3.101}$$

where $OC = \dfrac{D}{2} - g - \dfrac{h_r}{8}$ (3.102)

$$l_{g4} = (2p) \cdot \sqrt{(x_2 - x_1)^2 + (y_2 - y_1)^2} \tag{3.103}$$

$$A_{g4} = \frac{A_{sp4,t} + A_{rp4}}{2} \tag{3.104}$$

The magnetic equivalent circuit is similar to that of flux path 3. Hence, AMPERE'S circuital equation and the inductance contributed by the two flux paths of each pole pair is calculated for the whole machine similarly, assuming that the flux lines are linked with all turns:

$$F_4 = N_{ph} i = \phi_4 \cdot \left(\mathfrak{R}_{sp4} + \mathfrak{R}_{g4} + \mathfrak{R}_{rp4} + \mathfrak{R}_{sy4} + \mathfrak{R}_{ry4} \right) \tag{3.105}$$

$$L_{u4} = 2 \frac{N_{ph} \cdot \phi_4}{i} \tag{3.106}$$

Unaligned inductance – Flux path 5

The width of flux path 5 in the stator pole is assumed to be $3/4(h_s/4)$ on exit at the stator pole at $5/32 h_s$ [4]. All flux lines shown in Fig. 3.11 are assumed to be linked with all turns.
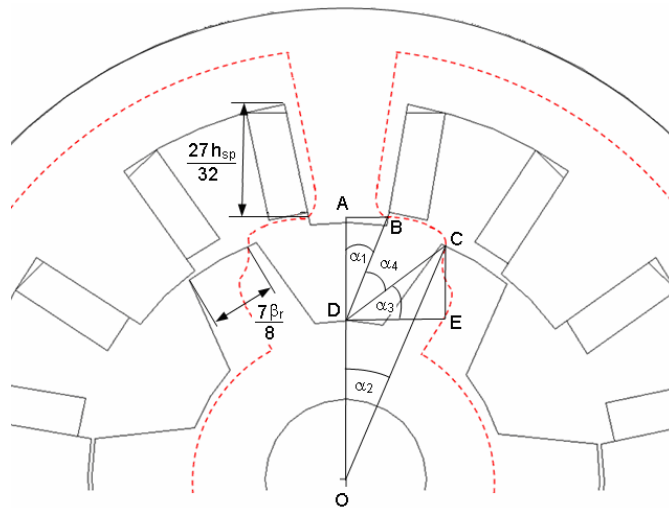

Fig. 3.11   Detail with flux path 5 in unaligned position

The magnetic equivalent circuit is similar to that of path 2 and therefore not shown here. The cross section area and the length of flux path 5 in the stator pole are

$$A_{sp5} = \frac{3}{4} \frac{h_s}{4} l_{Fe} \tag{3.107}$$

$$l_{sp5} \approx (2p)\frac{27}{32}h_s \tag{3.108}$$

For the rotor pole the reluctance $\mathfrak{R}_{rp5}$ is obtained concerning the assumptions above:

Pole base: $\quad A_{rp5,b} = \frac{1}{8}\left[(D-2g)\sin\left(\frac{\beta_r}{2}\right) + 2h_r\tan(\gamma_r)\right]\cdot l_{Fe}$ (3.109)

Pole middle: $A_{rp5,m} = \frac{1}{8}\left[(D-2g)\sin\left(\frac{\beta_r}{2}\right) + h_r\tan(\gamma_r)\right]\cdot l_{Fe}$ (3.110)

Pole tip: $\quad A_{rp5,t} = \frac{1}{8}(D-2g)\sin\left(\frac{\beta_r}{2}\right)\cdot l_{Fe}$ (3.111)

Pole length: $l_{rp5} \approx (2p)h_r$ (3.112)

The area of flux path 5 is the average of the cross section area in stator and rotor pole. The reluctance $\mathfrak{R}_{g5}$ in the air gap for flux path 5 is obtained assuming that the length of the path is an arc of circle with an average radius of DB and DC and subtended by α_4:

$$B = (x_1, y_1) = (AB, AO) \tag{3.113}$$

with $\quad AB = \frac{D}{2}\sin\left(\frac{\beta_s}{2}\right) + \frac{5h_s}{32}\tan(\gamma_s)$ (3.114)

and $\quad OA = \frac{D}{2}\cos\left(\frac{\beta_s}{2}\right) + \frac{5h_s}{32}$ (3.115)

$$\alpha_2 = \frac{\tau_r}{2} - \frac{3\beta_r}{8} \tag{3.116}$$

$$\alpha_1 = \arctan\left(\frac{AB}{AD}\right) = \arctan\left(\frac{\frac{D}{2}\sin\left(\frac{\beta_s}{2}\right) + \frac{5h_s}{32}\tan(\gamma_s)}{\left(\frac{D}{2}\cos\left(\frac{\beta_s}{2}\right) + \frac{5h_s}{32}\right) - \left(\frac{D}{2} - g - h_r\right)}\right) \tag{3.117}$$

$$C = (x_2, y_2) = \left[\left(\frac{D}{2}-g\right)\sin(\alpha_2), \left(\frac{D}{2}-g\right)\cos(\alpha_2)\right] \tag{3.118}$$

$$D = (x_3, y_3) = \left[0, \frac{D}{2}-g-h_r\right] \tag{3.119}$$

$$DC = \sqrt{(x_3-x_2)^2 + (y_3-y_2)^2} \tag{3.120}$$

$$DB = \sqrt{(x_3-x_1)^2 + (y_3-y_1)^2} \tag{3.121}$$

$$\alpha_3 = \angle CDE = \arctan\left(\frac{CE}{DE}\right) = \arctan\left(\frac{y_2-y_3}{x_2}\right) \tag{3.122}$$

$$\alpha_4 = \frac{\pi}{2} - \alpha_1 - \alpha_3 \tag{3.123}$$

$$l_{g5} = (2p)\frac{DB + DC}{2}\alpha_4 \qquad (3.124)$$

The length and cross section area for flux path 5 in the stator and rotor yoke are approximately equal to them of flux path 2. Finally, AMPERE'S circuital equation and the inductance contributed by the two flux paths of each pole pair are calculated:

$$F_5 = N_{ph}i = \phi_5 \cdot \left(\Re_{sp5} + \Re_{g5} + \Re_{rp5} + \Re_{ry5} + \Re_{sy5}\right) \qquad (3.125)$$

$$L_{u5} = 2\frac{N_{ph} \cdot \phi_5}{i} \qquad (3.126)$$

Unaligned inductance – Flux path 6

The enlarged magnetic configuration for flux path 6 is shown in Fig. 3.12a. Fig. 3.12b shows the magnetic equivalent circuit. The path is assumed to be an arc centered at the midpoint of the shaft. A further assumption is a path width of $h_s/4$. The flux leaves respectively enters the stator pole side at $5/8h_s$ [4]. The length and cross section area in the stator pole and yoke are:

$$l_{sp6} \approx \frac{5}{8}h_s \qquad (3.127)$$

$$A_{g6} \approx A_{sp6} = \frac{h_s}{4}l_{Fe} \qquad (3.128)$$

$$AC = x_1 = \frac{D}{2}\sin\left(\frac{\beta_s}{2}\right) + \frac{3h_s}{8}\tan\gamma_s \qquad (3.129)$$

$$AO = y_1 = \frac{D}{2}\cos\left(\frac{\beta_s}{2}\right) + \frac{3h_s}{8} \qquad (3.130)$$

$$\alpha_1 = \arctan\left(\frac{x_1}{y_1}\right) \qquad (3.131)$$

$$\alpha_2 = \tau_s - 2\alpha_1 = \frac{2\pi}{N_s} - \alpha_1 \qquad (3.132)$$

$$CO = \left(\frac{x_1}{\sin(\alpha_1)}\right) = \sqrt{(x_1 + y_1)^2} \qquad (3.133)$$

$$l_{g6} = (CO)\cdot\alpha_2 \qquad (3.134)$$

$$l_{sy6} \approx \left(\frac{D}{2} + h_s + \frac{y_s}{4}\right)\cdot(\tau_s - 2\alpha_1) \qquad (3.135)$$

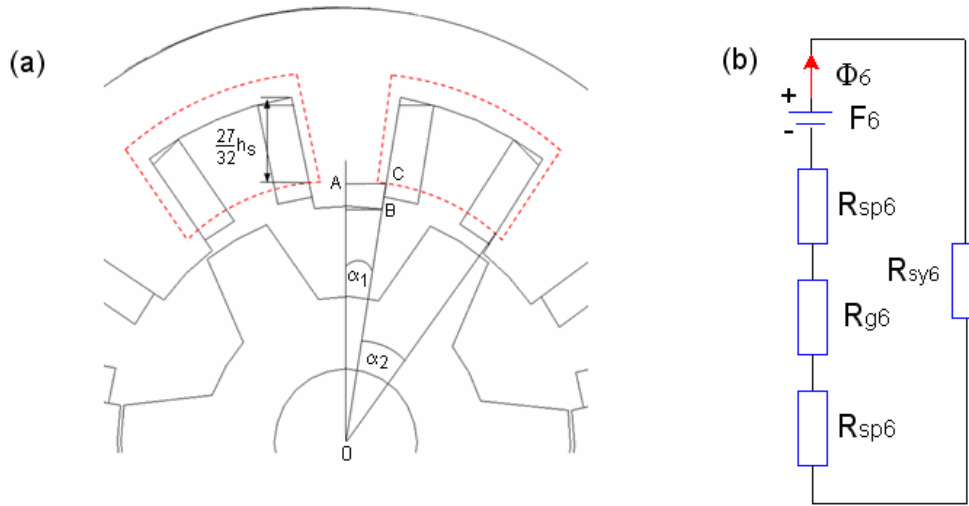$$A_{sy6} \approx A_{sy1} = y_s l_{Fe} \qquad (3.136)$$

Fig. 3.12   a) Detail with flux path 6 in unaligned position; b) magnetic equivalent circuit

The magnetic equivalent circuit for flux path 6 is shown in Fig. 3.12b. It contains reluctances due to the stator poles, air gap and stator yoke. Note that there are in total 2(2p) flux paths 6 in the complete machine. It is assumed that the flux encloses only three eights of the stator turns, hence the mmf equation and resulting inductance contributed by the 2(2p) flux paths 6 are

$$F_6 = \frac{3}{8} N_{ph} i = \phi_6 \cdot \left(2 \Re_{sp6} + \Re_{g6} + \Re_{sy6} \right) \tag{3.137}$$

$$L_{u6} = 2(2p) \cdot \left[\frac{\frac{3}{8} N_{ph.} \phi_6}{i} \right] = (2p) \cdot \left[\frac{\frac{3}{4} N_{ph.} \phi_6}{i} \right] \tag{3.138}$$

Unaligned inductance – Flux path 7

Flux path 7 in Fig. 3.13a is assumed to be an arc centered about point B with a radius of $\pi/2$.
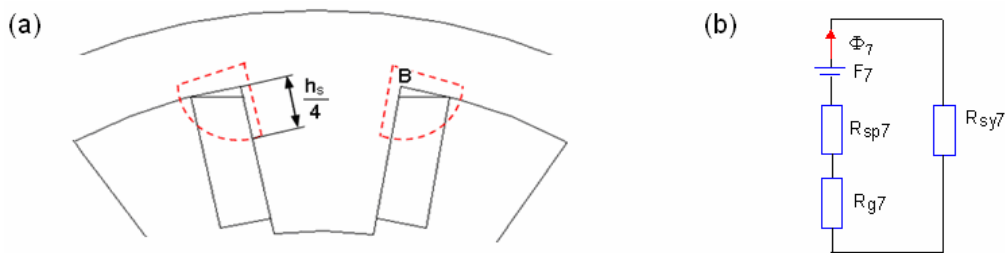

Fig. 3.13   a) Detail with flux path 7 in unaligned position; b) magnetic equivalent circuit

For calculating the reluctances, the length and cross section areas are

$$l_{sp7} \approx \frac{h_s}{4} \tag{3.139}$$

$$A_{g7} \approx A_{sp7} = \frac{h_s}{2} l_{Fe} \tag{3.140}$$

$$l_{g7} \approx \frac{\pi}{2}\frac{h_s}{4} \tag{3.141}$$

$$l_{sy7} \approx \frac{1}{2}\frac{h_s}{2} + \frac{y_s}{2} \tag{3.142}$$

$$A_{sy7} = A_{sy1} \tag{3.143}$$

Concerning the magnetic equivalent circuit for flux path 7, there are in total 2(2p) paths in the complete machine. It is assumed that the flux encloses only 1/4 of the stator turns; hence the mmf equation and inductance contributed for path 7 are as follows, referring Fig. 3.13b:

$$F_7 = \frac{1}{4}N_{ph}i = \phi_7 \cdot \left(\Re_{sp7} + \Re_{g7} + \Re_{sy7}\right) \tag{3.144}$$

$$L_{u7} = 2(2p) \cdot \left[\frac{\frac{1}{4}N_{ph\cdot}\phi_7}{i}\right] = (2p) \cdot \left[\frac{\frac{1}{2}N_{ph\cdot}\phi_7}{i}\right] \tag{3.145}$$

The *total unaligned inductance* is the sum of all inductances contributed by the 7 flux paths:

$$L_u = \sum_{s=1}^{7} L_{us} \tag{3.146}$$

Fringe flux at the end of the core

In order to consider the inductance component due to the field at the ends of core of the SRM, a simple method for making a rough estimation of the contribution to the minimum inductance by the fringing flux was firstly proposed by [64]. The mathematical treatment of the fringe flux at the ends of core is very complicated, particularly for doubly salient machines, and would normally require a 3-dimensional numerical field solution. J. Corda [64] suggests representing the stator and rotor poles by a pair of opposing faces with flanks extending to infinity and with a fictitious uniform air gap, g_f, as shown in Fig. 3.14a.
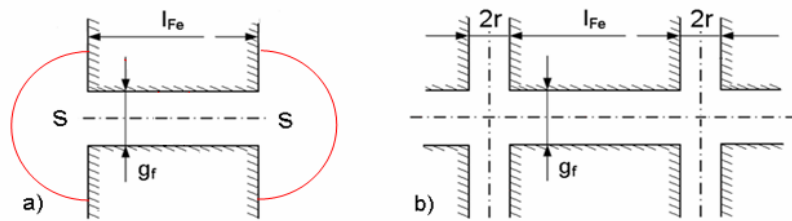

Fig. 3.14 a) Axial model of the fictitious air gap; b) approximated model

Its length is assumed to be equal to the mean length of the flux path 1-5 used for the unaligned inductance calculation where the fringing is most pronounced:

$$g_f = \frac{1}{5}\left(l_{g1} + l_{g2} + l_{g3} + l_{g4} + l_{g5}\right) \tag{3.147}$$

It is supposed that the air gap flux is uniform to the end of the core and the fringe flux at the ends of the core is linked with all turns. If the red field line in Fig. 3.14a from the stator pole end to the rotor pole end is approximated by a semi-circle with the radius equal to r, then the model may be approximated by the model shown in Fig. 3.14b. With it, an effective core length is defined by [64], taking into account fringe flux:

$$l_{eff} = (l_{Fe} + 2r)\sigma - 2r = l_{Fe} + 2r(1 - \sigma) \tag{3.148}$$

with
$$\sigma = \frac{2}{\pi} \left[\arctan\left(\frac{2r}{g_f}\right) - \frac{g_f}{4r} \ln\left[1 + \left(\frac{2r}{g_f}\right)^2\right] \right] \tag{3.149}$$

and
$$r = h_1 + h_2 \tag{3.150}$$

$$h_1 = \frac{D}{2} - \left[\left(\frac{D}{2} - g\right)\cos\left(\frac{\tau_r + \beta_r}{2}\right)\right] \tag{3.151}$$

$$h_2 \approx \frac{h_c}{2} \tag{3.152}$$

where h_c is the height of an assumed rectangular stator coil. Using these empirically found factors the corrected value of the unaligned inductance is

$$L_u' = L_u + 2L_f = L_u + 2\left(\frac{l_{eff}}{l_{Fe}} L_u - L_u\right) \tag{3.153}$$

where L_u is the estimated value of minimum inductance when the fringe flux is excluded; L_f is the estimated value of inductance component due to fringe flux.

3.3   Estimation of flux-linkage characteristics for all rotor positions

To predict the performance characteristics of the SRM the knowledge about the relationship $\psi(i,\Theta)$ is required. A very smart approach to estimate the $\psi(i,\Theta)$-characteristics is to use a model that bases on the magnetic characteristics in the aligned and unaligned position. The values for intermediate rotor positions are determined by 'gage curves' which represent the magnetisation curves as ψ vs. Θ at constant current relationships, as shown in Fig. 3.15a. The curve on the right hand side is a scaleable 'gage' that fits between the unaligned and aligned curves in the left-hand graph. The gage curves are normalized in such a way that if there were no magnetic saturation, there would be only one normalized curve for all current levels. The gage curve changes shape with saturation and can model both pole-corner saturation and bulk-saturation of the poles and yokes.

A machine model that works with such a set of analytical equations instead of look-up tables (e.g. in [26], [86], [168], [171]) can offer significant improvements. By choosing an appropriate approach, it is possible to avoid any problems with differentiability of the desired

values. This approach can be finally used in a very flexible way for the simulation of the drive performance as well as for real online drive control. The procedure proposed in this thesis is based on the work of Miller at al. [134] and M. Hiller [97].
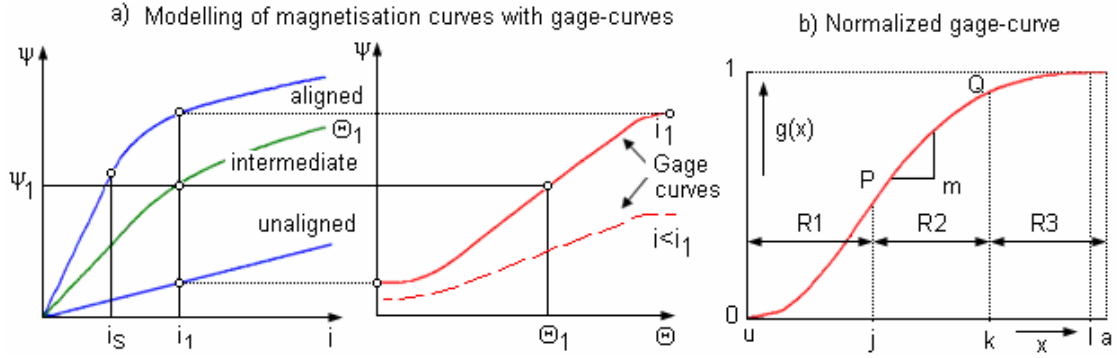

Fig. 3.15 a) Modelling of magnetisation curves with gage-curves, b) gage curve with normalized flux linkage g(x) vs. normalized rotor position x (i=const.)

A gage curve value represents the ratio of the distance $g_1(\Theta)$ between the actual flux $\psi(i_1,\Theta)$ and the unaligned flux $\psi_u(i_1)$ at a given current i_1 versus the distance between the aligned and the unaligned flux linkage $\psi_a(i_1)$ and $\psi_u(i_1)$ at this certain current i_1:

$$g_1(x) = \frac{\psi(i_1, x) - \psi_q(i)}{\psi_d(i) - \psi_q(i)}$$

(3.154)

with

$$x = \frac{\Theta - \Theta_u}{\Theta_a - \Theta_u} = \frac{\Theta - \Theta_u}{\Theta_{au}}$$

(3.155)

where Θ_u is the unaligned position angle, corresponding to $\Theta=0°$; Θ_a is the angle of aligned position and Θ_{au} is generally half of the rotor pole pitch. Thus x =1 corresponds to the aligned position and x=0 to the unaligned position. To define the gage curve, the basic structure of the normalized phase angle sections u, j, c, k, l and a (see Fig. 3.15b) must be determined. Region R1 extends from unaligned position *u* to the 'corner point' *j* where the approaching corners of stator and rotor poles start to overlap:

$$x_u \le x \le x_j$$

(3.156)

with

$$u = 0 \Rightarrow x_u = 0$$

(3.157)

$$j = \Theta_a - \frac{\beta_r + \beta_s}{2} = \frac{\pi}{N_r} - \frac{\beta_r + \beta_s}{2} \Rightarrow x_j = \frac{j - \Theta_u}{\Theta_{au}} \approx 0.3...0.4$$

(3.158)

The overlap region is divided into regions R2 and R3, with the dividing point k between the angle of maximum stator-rotor pole overlap l and j:

$$x_j < x \le x_k$$

(3.159)

with

$$l = \Theta_a - \frac{|\beta_r - \beta_s|}{2} = \frac{\pi}{N_r} - \frac{\beta_r - \beta_s}{2} \Rightarrow x_l = \frac{l - \Theta_u}{\Theta_{au}} \approx 0.95...1$$

(3.160)

$$k = \frac{j+l}{2} \Rightarrow x_k = \frac{x_j + x_l}{2} \approx 0.6...0.7 \tag{3.161}$$

Hence, the width of Region R2 is equal to the smaller pole angle min(β_r,β_s). That agrees with the fact that torque can be produced only while the stator-rotor-pole-overlap is changing. Region R3 extends from k to the aligned position a:

$$x_k < x \le x_a \tag{3.162}$$

with $a = \Theta_a \Rightarrow x_a = 1$ (3.163)

For the red curve in Fig. 3.15b it is assumed that there are no rotor positions near the aligned or unaligned position where the machine produces no output torque. Hence, the gage-curve in section R1 ($x_u \le x \le x_j$) is a trigonometric function as proposed in [134]:

$$g_1(x) = \frac{m_P}{2}\left[\varphi_u - \frac{\sin(q \cdot \varphi_u)}{q}\right] \tag{3.164}$$

with $\varphi_u = x - x_u$ (3.165)

$$q = \frac{\pi}{x_j} \tag{3.166}$$

$$m_P = \frac{2}{x_j + c(1+\mu) + 4k \cdot \mu/\pi} \tag{3.167}$$

$$c = x_k - x_j \tag{3.168}$$

At the end of section R1 (point j) the first order derivate of the gage reaches its maximum value, i.e. as well the maximum value of the output torque. In the central region R2 ($x_j < x \le x_k$) it is an observed fact that the static torque curve tends not to be flat and that there is a maximum torque/ampere arising very shortly after the *j*-position. After this when the rotor moves towards the *k*-position, the torque/ampere declines slowly at first, and then more rapidly as the overlap increases toward the maximum as the *k*-position is approached. In order to represent this variation of torque/ampere while retaining the assumption that the torque is proportion to dg(x)/dx, then the gage curve function $g_2(x)$ in region R2 must be at least a second-order parabolic function [134]:

$$g_2(x) = a_0 + a_1\varphi_k - a_2\varphi_k^2 \tag{3.169}$$

with $\varphi_k = x - x_j$ (3.170)

$$a_0 = m_P \frac{x_j}{2} \tag{3.171}$$

$$a_1 = m_P \tag{3.172}$$

$$a_2 = \frac{m_P - m_Q}{2c} \tag{3.173}$$

At the transition from region R1 to region R2 the model still ensures that no discontinuity occurs in the output torque course since $dg_2(x=x_j)/dx=dg_1(x=x_j)/dx=m_p$. This is also true for the region R3 ($x_k > x \leq x_a$), where the gage curve function $g_3(x)$ is given by a similar complex trigonometric expression as for region R1 that satisfies continuity conditions at the end points x_k and x_a.

$$g_3(x) = 1 - \frac{2x_k}{\pi} m_Q \left[1 - \sin(r \cdot \varphi_z) \right] \tag{3.174}$$

with $\varphi_z = x - x_k$ (3.175)

$$r = \frac{\pi}{2x_k} \tag{3.176}$$

$$m_Q = \mu \cdot m_P \tag{3.177}$$

The constant $\mu = m_Q/m_P$ is the ratio of the gradients at points P and Q (see Fig. 3.15b). Generally, $\mu < 1$ and a typical value might be 0.95 [134]. Finally, the flux linkage $\psi_n(i_1, x_n)$ for the n-regions for the current i_1 can be found:

$$\psi_n(i_1, x_n) = g_1(x) \cdot \left(\psi_d(i_1) - \psi_q(i_1) \right) + \psi_q(i_1) \tag{3.178}$$

Fig. 3.16 shows for the example the calculated $\psi(i,\Theta)$ curves and their first-order derivates for different phase currents of the 6/4- SRM II. There are no discontinuities in these curves and their rate of change resulting in a smooth calculated torque. As reference, data obtained by FEM calculation are shown (dotted lines). The analytical calculation error is about 5 - 7%.
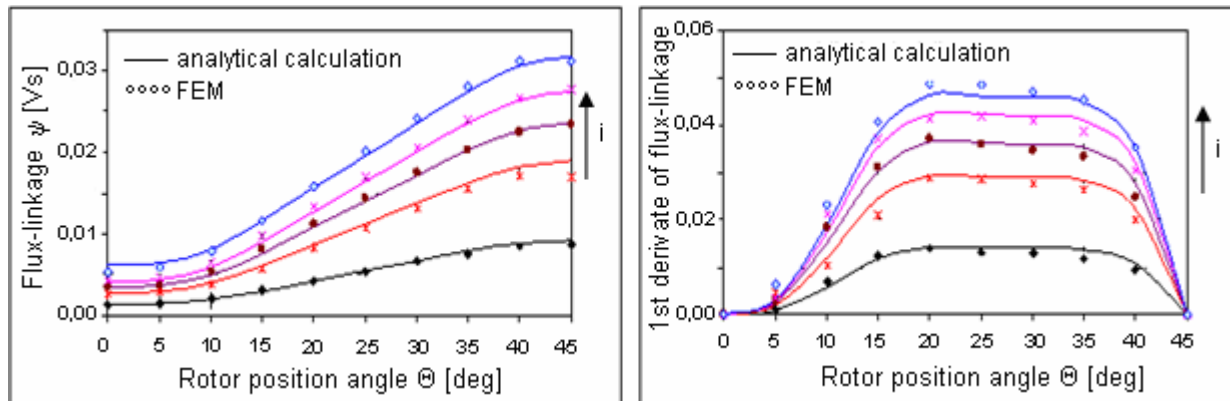

Fig. 3.16   Flux-linkage (left) and their first-order derivates (right) for different currents

3.4   Calculation of static torque characteristics

Simulation of the SRM operational behaviour is essential for an accurate dimensioning of the entire drive system. Following a procedure is presented which determines in a first 'static' step the torque characteristics $T(i,\Theta)$ by means of an iterative coenergy calculation using the $\psi(i,\Theta)$-curves. The magnetization curves, the coenergy and the obtained static torque values are stored as discrete data points in a two-dimensional data field. For the analytical

calculation of phase currents and -torques in a second 'dynamic' step these data fields are used. Intermediate values are approximated by linear interpolation. The first 'static' part must be executed only one time when a new ψ-i-data set hast to be prepared. The 'dynamic' part must be executed for each new operating point. After the analytical calculation of the magnetic circuit with the procedure outlined in the previous sub-chapters, the magnetization curves are point wise available as a two-dimensional data field as shown in Fig. 3.17a.
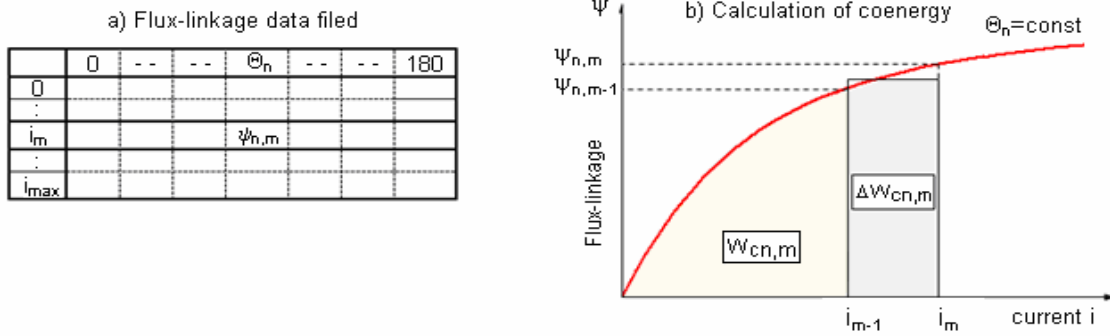

Fig. 3.17   a) Structure of the $\psi(I,\Theta)$-data set; b) calculation of the $W_c(i,\Theta)$ data set

The values of the rotor position angle Θ_{el} (in el. degree) must be available from the aligned ($\Theta_{el}=0°$) to the unaligned position ($\Theta_{el}=180°$) with an arbitrary increment, equidistance is not required. Note, the *electrical angle* is the mechanical rotor position angle Θ_{mech} multiplied with the number of rotor poles: $\Theta_{el}=N_r\Theta_{mech}$. For angle values from the aligned to the next unaligned position the data field is mirrored at $\Theta_{el}=180°$. Also for the current data points equidistance is not required, however it is favourable to work with a higher density of the data point in the range of small currents and at beginning iron saturation.

The instantaneous torque T of a SRM is given by the rate of change of the coenergy W_c with the angle Θ at constant phase current i, referring to equation (1.28). Therefore it is useful to generate first of all a $W_c(i,\Theta)$ data field:

$$\Delta W_{cn,m} = \frac{\psi_{n,m} + \psi_{n,m-1}}{2}\left(i_m - i_{m-1}\right) \tag{3.179}$$

$$W_{cn,m} = W_{cn,m-1} + \Delta W_{cn,m} \tag{3.180}$$

where n is the interval between the grid points and m is the index of the current. The calculation procedure approximates the increase of the area corresponding to the coenergy $\Delta W_{cn,m}$ by a rectangular area. Now, a further data set can be obtained which contains for each point of the $W_c(i,\Theta)$ data field the instantaneous torque T. For this reason (1.28) is approximated with the difference quotient

$$T = \frac{\Delta W_c}{\Delta \Theta}\bigg|_{i=konst} \tag{3.181}$$

With a sufficient fine resolution of the rotor position angle these approximations give accurate results as the comparison of the calculated torque characteristic with them obtained by FEM computation shows for the example of the three manufactured prototypes, presented in Chapter 5. Additionally, Chapter 6 gives a comparison with measurement results.

3.5 Calculation of Switched Reluctance Motor drive losses

Since the SRM is an electromechanical energy converter it produces losses as well as the power electronic converter belonging to the drive system. SRM losses can be subdivided into copper-, core-, mechanical- and additional losses. Hysteresis and eddy currents in the iron material are responsible for the core losses. Mechanical losses consist of friction losses with the air and inside the bearings. Additional losses include mechanically and electrically caused losses which can a priori not measured and localized exactly [16]. Finally, in the converter occur conduction and switching losses of the diodes and switches. Additional losses in the converter, for example in the dc-link capacitors or in the control electronics are neglected in this thesis in the style of [33] and [34]. For both SRM and converter separate efficiencies can be defined and multiplied to obtain system efficiency:

$$\eta_{sys} = \eta_{Conv} \cdot \eta_{SRM} = \frac{P_{Conv}}{P_{el}} \cdot \frac{P_{mech}}{P_{Conv}} = \frac{P_{mech}}{P_{el}} \tag{3.182}$$

where P_{mech} is the mechanical output power, P_{el} is the electrical input power supplied by the dc-link and P_{Conv} is the output power of the converter.

3.5.1 Copper losses

Accurate calculation of SRM copper losses at all speeds is complicated by the fact that the current waveform in the SRM is not sinusoidal. Further, the waveform is dependent on operating conditions, particularly the excitation current, speed and the switching strategy. For the case of flat- topped currents, the current waveform can be approximated by a rectangular block and it has been shown among others by [120] and [117] that the r.m.s. current per phase, assuming unity duty cycle, can be calculated with the peak value I_p as

$$I_{rms} = \frac{I_p}{\sqrt{q}} \qquad (q\text{- }number\text{ }of\text{ }phases) \tag{3.183}$$

However, in praxis, the phase current is usually not flat-topped, thus, for a precise prediction of copper losses the r.m.s. current must be accurately determined by

$$I_{rms} = \sqrt{\frac{1}{T_{el}} \int_{t}^{t+T_e} i_{ph}^{2}(t)dt} \tag{3.184}$$

where T_{el} is the electrical time period of the phase. The copper losses are then:

$$P_{cu} = q I_{rms}^2 R_{ph} \tag{3.185}$$

In order to predict the dc resistance R_{ph} of the phase winding, the average length l_w of one single winding around a stator pole is assumed to be approximately

$$l_w \approx 2 \cdot l_{stk} + 4 \cdot l_{oh} \tag{3.186}$$

with the stack length l_{stk} and the overhang length at each end of the winding l_{oh}. It can be roughly estimated as $l_{oh} \approx 1.2 t_s$, where t_s is the stator pole width [8]. The dc-resistance of the winding per phase with p pole pairs is then [16]

$$R_{ph} = \frac{2p \cdot N_p \cdot l_w}{\chi_{Cu} \cdot A_w} \quad \text{with} \quad \chi_{Cu} = \chi_{Cu,20} \cdot \left(1 + \alpha_{Cu} \cdot \left(\vartheta - \vartheta_0\right)\right) \tag{3.187}$$

A_w is the wire cross-section area, N_p is the number of turns per pole and χ_{Cu} is the specific conductivity of copper at the temperature ϑ. The specific conductivity of copper is $\chi_{Cu,20}$=58000S/mm at ϑ_0=20°C; α_{Cu}=39·10^{-4} K.

A time-variable magnetic field induces eddy currents in an electric conductor which is situated in this field [13], [16]. From the superposition of the current in an electric wire and the eddy-current due to the time-variable magnetic field results an unevenly distributed current density across the wire cross section. That leads to the 'SKIN-Effect' and an increase of the wire resistance. The penetration depth (also 'skin-depth') of the magnetic field in the wire depends on the frequency, the specific conductivity χ_{Cu} and the permeability μ of the wire material. In the framework of this thesis the SKIN-effect is not considered. It is assumed that the SKIN-depth is small compared to the wire diameter. Hence the phase resistance is frequency-independent. SKIN-effect occurs in very high-speed motors wound with small numbers of turns. It may be necessary in such cases to use stranded conductors or Litz wire. Detailed investigation to the influence of the SKIN-effect on copper losses in SRMs can be found in [33] where J. Reinert proposes a procedure transferring round wires in a first step into equivalent rectangular wires with the same cross section. In the second step the serial connected adjacent rectangular wires are transferred into one single strip conductor.

3.5.2 Core losses - new calculation method

Flux-linkage waveforms in various parts of the magnetic circuit

Energizing a phase winding of the SRM by a positive voltage pulse at turn-on angle Θ_{on} leads to the built up of flux-linkage according to FARADAY's Law. At constant angular velocity ω the flux-linkage is

$$\psi = \int_{\Theta_{on}}^{\Theta_{off}} \frac{(V_s - Ri)}{\omega} d\Theta + \psi_0 \qquad (3.188)$$

The pre-existing flux-linkage ψ_0 at the turn-on angle is assumed to be zero, which is usually the case. The commutation angle Θ_{off} occurs when a negative voltage applies to decay the current and hence the flux-linkage back to zero. Above equation can be written as

$$\psi = \frac{V_s - Ri}{\omega} \left(\Theta_{off} - \Theta_{on} \right) \qquad (3.189)$$

The angle (Θ_{off} - Θ_{on}) is also called "dwell-angle" Θ_d [8]. Neglecting the voltage-drop due to winding resistance in the fluxing and de-fluxing period, the flux-linkage varies linearly with the rotor position angle. If the absolute value of supply voltage is the same during fluxing and de-fluxing period and if it is further assumed that these periods have approximately the same duration, the flux-linkage vs. angle characteristic has a triangular form. It occurs in the poles and the yoke parts between the poles of stator and rotor when one phase is energized.
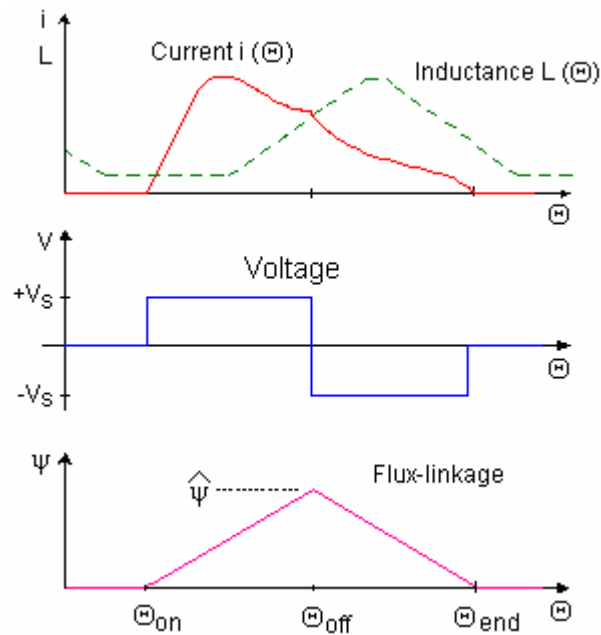

Fig. 3.18 Current-, voltage-, and flux waveform for single pulse operation

Depending from the motor speed, turn-on and commutation angle, there is usually an overlapping of the flux-linkage waveforms of the phases in the stator and rotor yokes. Hence the period and form of the flux-waveform in the iron vary between the different parts of the magnetic circuit, and can be deduced by superposition of separate waveforms. In Fig. 3.19 the flux-linkage waveforms of a 4-phase 8/6-SRM are presented for one electrical period. The flux-pulses are shown by closed magnetic field lines as a vector plot. One mechanical revolution of the rotor is achieved after N_r electrical pulses. Hence, the 8/6-SRM with N_r=6 requires 24 current pulses per revolution. Fig. 3.20 shows the flux-density waveform as a function of time in the different machine parts for a dwell-angle Θ_d=10°.
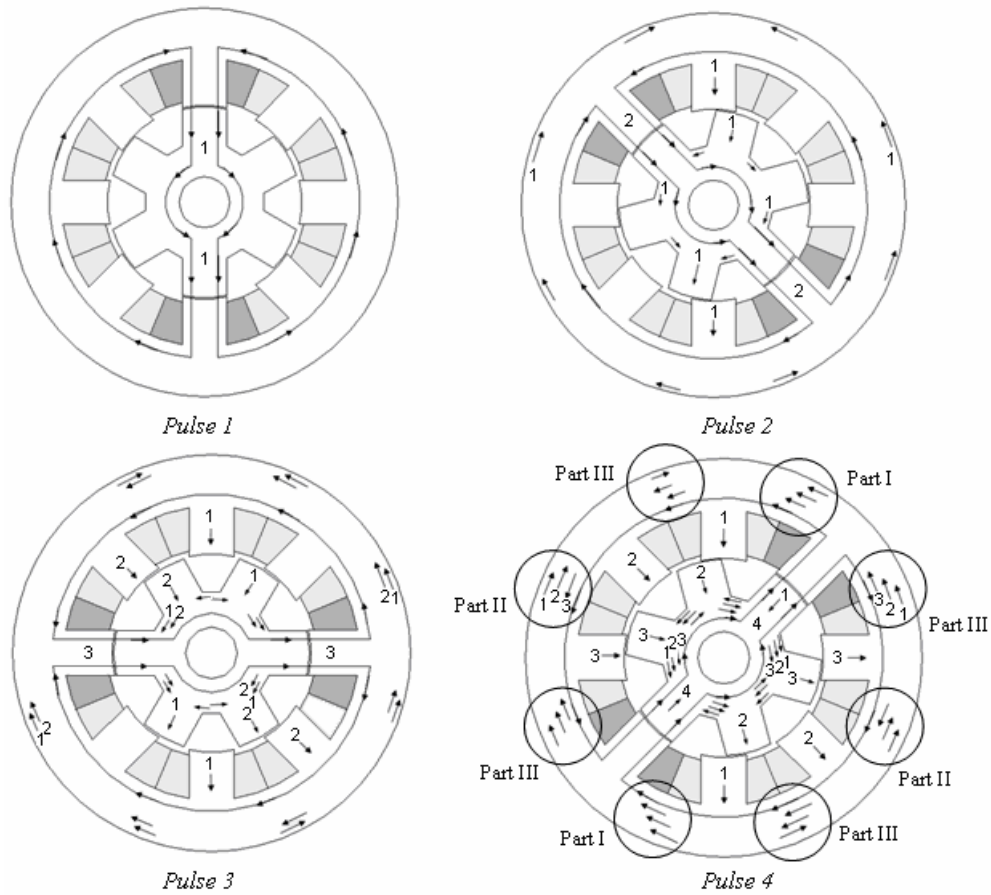
Fig. 3.19   Vector plot of magnetic flux in an 8/6-SRM for one electrical period

The flux in the stator and rotor yoke parts is often composed of the flux of two phases resulting in a doubled alternation speed compared to the pole flux. With a dwell less than 7.5° no flux-overlapping occurs in the 8/6-SRM. On the other hand, a dwell greater than 15° results in a tripled alternation speed of the flux, because in that case the flux in the yokes consist partially of the flux of three different phases! Referring to Fig. 3.19, an unipolar flux density waveform occurs in the stator parts I, a bipolar symmetrical flux density waveform in the parts II. Both appear two times. An unsymmetrical waveform occurs four times in the parts III. Especially the bipolar flux density produces high core losses due to its high frequency. The flux-density waveform in the rotor yoke is the same in all parts. The remagnetization frequencies in stator f_S and rotor f_R are

$$f_s = n \cdot N_r \tag{3.190}$$

$$f_R = n \cdot \frac{N_s}{2q} \quad \text{with mechanical rotor speed n in 1/s} \tag{3.191}$$
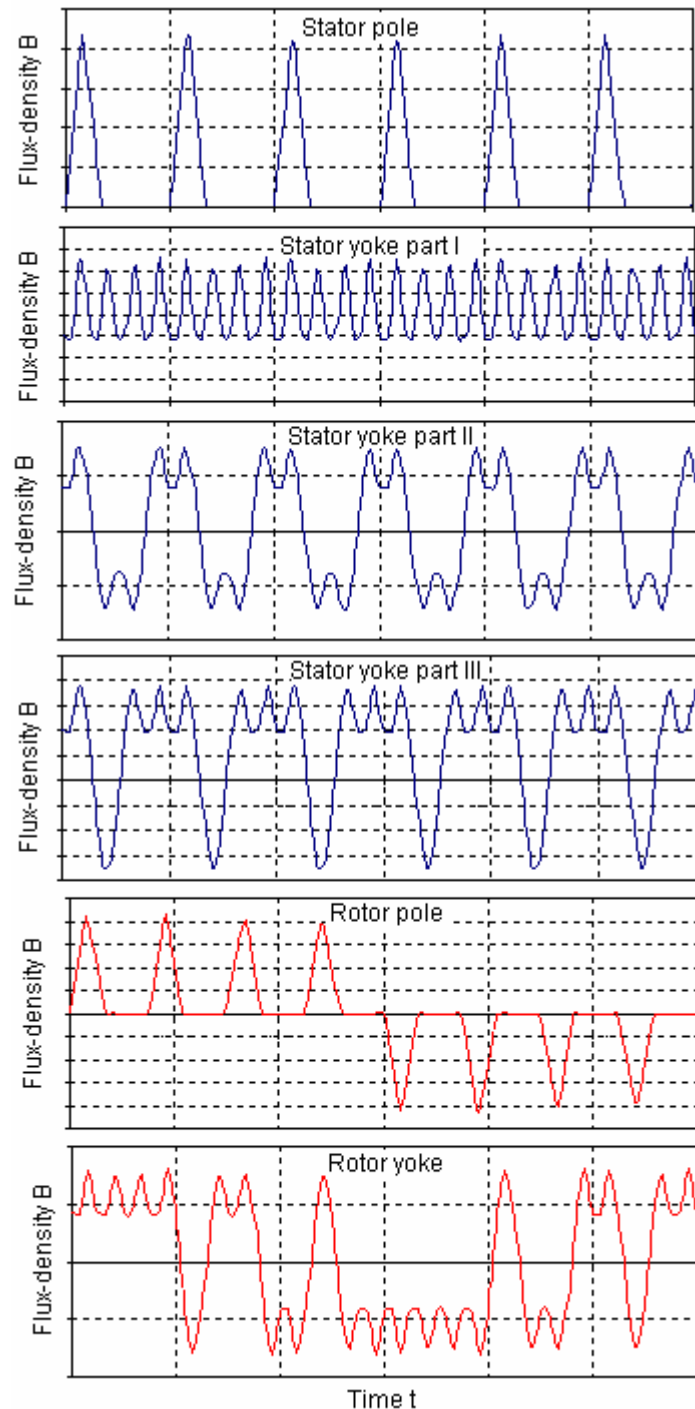
Fig. 3.20   Flux density waveforms for one mechanical period in different parts of an 8/6-SRM

Physical principle of remagnetization losses

It is known that ferro- and ferrimagnetic materials have a domain structure. The magnetization of this internal structure is not uniform but subdivided into more or less saturated domains, which differ from each other by the orientation of their magnetization vectors. Domain walls, so called 'BLOCH-walls', separate the magnetic domains from each other. A magnetization of the firstly uneven organised domains is achieved by an external magnetic field. At complete alignment the material is totally saturated. A change of total

material magnetization can only be achieved by movement of the domain walls. Therefore, the magnetization is discrete in terms of space. It is important to know that the magnetization changes in a highly localized way, rather than uniformly through the material. Impurities and imperfections inside the material hinder the domain wall movement and cause rapid movements of the domain walls at a sufficient high field strength. That effect is also known as BARKHAUSEN-jumps. Hence, the movement of the domains is not regular. The local velocity of the BLOCH-walls is not equal to the change of rate of the external field. Therefore, the magnetization change is also discrete in terms of time. The results of changes of magnetization are local energy losses caused by eddy currents and by spin relaxation. There is no physical difference between "hysteresis" losses and "eddy-current" losses and the only physical origin of remagnetization losses is the damping of domain wall movement by eddy currents and spin relaxation [18], [33], [34], [47] [51], [58].

Known calculation methods for Switched Reluctance Machines

Only a few approaches can be found in the bibliography for determining core losses during non-sinusoidal remagnetization processes [33], [42], [47], [72], [164]. First investigations based on a harmonic analysis of the triangular flux-density waveform in the stator poles by a FOURIER series [34], [47], [129]. After the discretization and calculation of the absolute coefficients also the FOURIER-coefficients for the stator- and rotor yoke parts can be determined by the lag theorem of the discrete FOURIER transformation. A similar approach is developed by Gradzki [91] and Severns [164]. To each single Fourier component the empirical STEINMETZ equation from 1891 is applied:

$$p_{Fe} = C_m f^\alpha \hat{B}^\beta \tag{3.192}$$

Finally, the individual losses of the fundamental and all harmonics are superimposed and summarized to calculate the total losses. The calculation procedure bases on material characteristics given by the manufactures. However, the fact that the flux-density exponent of the STEINMETZ-equation has a typical value of $\beta=2.5$ indicates that there is an extremely nonlinear relation between losses and peak flux density. The method of superposition is mathematically only applicable for linear or piecewise linear systems [47]. In the case of non-linear magnetic materials its application is not valid and the results of this procedure are invalid [41], [42], [58]. Another method to calculate core losses in SRMs is presented by Miller [8]. He proposes to subdivide the losses corresponding to Jordan [108].

$$p_{Fe} = C_h f \hat{B}^{a+b\hat{B}} + C_e f^2 \hat{B}^2 = C_h f \hat{B}^{a+b\hat{B}} + \frac{C_e}{2\pi^2} \left(\frac{dB}{dt}\right)^2 \tag{3.193}$$

The second right-hand term, corresponding to the eddy-current losses, shall consider the non-sinusoidal flux-waveform. A quiet difficult problem is the estimation of the four coefficients

for which a complicated curve-fitting procedure is necessary. This can lead to the fact that the material constants are adapted only to one particular operating point and causes large errors in other operating points since non-sinusoidal processes and high modulation-levels can not be considered correctly [33]. A very detailed investigation of core losses in SRMs can be found in Boivie [55], [56]. Also in these works the losses are subdivided into a static hysteresis and a dynamic eddy-current part. By means of experimental verifications Boivie calculated a maximum error of 14% and therefore a dramatic improvement in accuracy compared to calculations with (3.193). However, Boivie concedes that a strict partitioning of the losses in the ferromagnetic material into a hysteresis- and eddy-current part is such a difficult task that he also needed some correction factors. As a conclusion, the results of Miller and Boivie confirm the statement that the losses during quasi-static remagnetization are the result of eddy currents as well as losses during high-frequency remagnetization. There is a lack of physical foundation for the classification of core losses into hysteresis- and eddy-current losses.

New calculation method using a modified STEINMETZ-equation

Since the known methods to calculate core losses do not fulfil the specific properties and requirements of SRMs, a new approach must be found. This can be made on the basis of the work of [33], [34], [47], [59] and [70]. A modified STEINMETZ-equation which uses common material characteristics given by the manufactures and determines the remagnetization losses for any flux-density waveforms forms the starting point of this calculation method.

In this thesis the method proposed in [33] for the example of an 8/6-SRM is generalized on various machine types with different numbers of phases and poles. Influence of geometric machine modifications, actual operating conditions and the mode of control are regarded now already during the design stage of the motor to be developed. The proposed calculation procedure is more complex as presented in [33] since all required flux-density waveforms and corresponding frequencies are calculated analytically, not as described in [33] by the exclusive way of FEM calculations. The procedure is finally implemented in the program "DesignSRM", presented at the end of this chapter. Actually, the empirical STEINMETZ-equation has proven to be the most useful tool for the calculation of remagnetization losses in bibliography. For sinusoidal flux waveforms it provides a high accuracy and is quite simple to use. Therefore, it should be extended to non-sinusoidal problems. The flux density rate of change dB/dt is averaged in a first step over a complete remagnetization cycle, i.e. from maximum flux density value B_{max} down to its minimum B_{min} and back [59]:

$$\dot{B} = \frac{1}{\Delta B} \oint \frac{dB}{dT} dB \quad \text{with} \quad \Delta B = B_{max} - B_{min} \tag{3.194}$$

$$\dot{B} = \frac{1}{\Delta B} \int_0^T \left(\frac{dB}{dt} \right)^2 dt \tag{3.195}$$

It was found in [72] that (3.195) can be normalized with respect to a sinusoidal case. Therefore, in order to find a relationship between the remagnetization frequency f and the averaged remagnetization rate dB/dt, an equivalent frequency f_{eq} can be calculated from the averaged remagnetization rate, using the constant $2/(\Delta B \pi)^2$:

$$f_{eq} = \frac{2}{\pi^2} \frac{1}{\Delta B^2} \int_0^T \left(\frac{dB}{dt} \right)^2 dt \qquad (3.196)$$

For k piece wise linear waveforms in the different parts of the SRM, f_{eq} can be simplified:

$$f_{eq} = \frac{2}{\pi^2} \cdot \sum_{k=2}^K \left(\frac{B_k - B_{k-1}}{B_{max} - B_{min}} \right)^2 \cdot \frac{1}{t_k - t_{k-1}} \qquad (3.197)$$

Similar to the empirical formula of STEINMETZ the specific energy losses w of every remagnetization cycle can now be determined using this equivalent frequency [59]:

$$w = C_m \cdot f_{eq}^{\alpha-1} \cdot \hat{B}^{\beta} \quad \text{with} \quad \hat{B} = \frac{\Delta B}{2} \qquad (3.198)$$

If the remagnetization is repeated with the frequency f_T, the specific core losses in W/kg are

$$p_{Fe} = f_T \cdot \left(C_m \cdot f_{eq}^{(\alpha-1)} \hat{B}^{\beta} \right) \qquad (3.199)$$

The coefficients C_m, α and β are empirically extracted from loss curves of the iron given by manufactures with a curve fitting procedure. By means of consequent using (3.197) and (3.199) the core losses in different parts of the SRM can be calculated as follows:

The flux-density in the *stator poles* has a triangular waveform, as shown above. The equivalent specific core losses $p_{Fe,SP}$ are therefore calculated as

$$p_{Fe,SP} = \frac{N_r}{T_{mech}} \cdot C_m \cdot \left(\frac{2}{\pi^2} \cdot \left[\frac{1}{\Delta t_r} + \frac{1}{\Delta t_f} \right] \right)^{(\alpha-1)} \cdot \left(\frac{\hat{B}}{2} \right)^{\beta} \qquad (3.200)$$

where Δt_r and Δt_f are the rice and fall time of the stator pole flux density; T_{mech} is the duration for one rotor revolution in seconds.
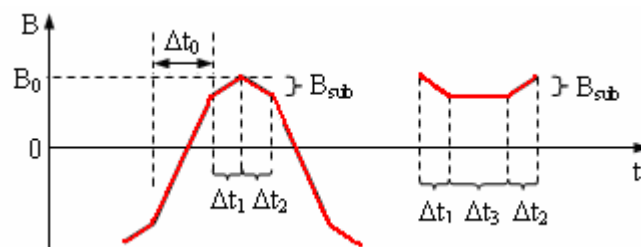

Fig. 3.21   Splitting the stator- and rotor yoke flux density waveform into two basic figures

The estimation of core losses in the stator- and rotor yoke is more complicated since the flux waveforms in these segments are a sum of stator- and rotor pole flux-density waveforms.

They can be subdivided into two basic figures shown in Fig. 3.21, whose equivalent frequency can be obtained with (3.197). With it the specific core losses in the other parts of the magnetic circuit can be calculated now.

For the *stator yoke segments with bipolar flux waveform* the specific core losses are

$$p_{Fe,SJ1} = \frac{N_r C_m}{T_{mech}} \left\{ \begin{array}{l} s \left(\frac{2}{\pi^2} \left[\frac{1}{\Delta t_1} + \frac{1}{\Delta t_2} \right] \right)^{(\alpha-1)} \left(\frac{B_{sub}}{2} \right)^{\beta} + \\ \left[\frac{2}{\pi^2} \left(\frac{1}{2B_0} \right)^2 \left[2\frac{B^2_{sub}}{\Delta t_1} + 2 \cdot \frac{B^2_{sub}}{\Delta t_2} + \\ 2\frac{(2(B_0 - B_{sub}))^2}{\Delta t_0} \right] \right]^{(\alpha-1)} B_0^{\beta} \end{array} \right\} \quad (3.201)$$

The parameter *s* describes the number of the small figures according to Fig. 3.21. A value s=1 is valid for a three-phase machine, s=2 in the case of a 4-phase machine. For the parts of the *stator yoke with unipolar flux waveform* the specific core losses are

$$p_{Fe,SJ2} = \frac{1}{T_{mech}} \cdot C_m \cdot \left\{ q \cdot N_r \cdot \left(\frac{2}{\pi^2} \cdot \left[\frac{1}{\Delta t_1} + \frac{1}{\Delta t_2} \right] \right)^{(\alpha-1)} \cdot \left(\frac{B_{sub}}{2} \right)^{\beta} \right\} \quad (3.202)$$

where $T_{mech} = \dfrac{1}{n/60}$ with *n* in 1/min $\quad (3.203)$

In (3.202) it is favourable to use the repeating frequency of a mechanical rotor revolution T_{mech} where the small basic figure occurs qN_r-times. Each rotor pole passes an excited stator pole N_s-times during one rotor revolution. Similarly to the stator poles, the flux-waveform in the *rotor poles* can be assumed to be triangular during single pulse operation:

$$p_{Fe,RP} = \frac{N_s}{T_{mech}} C_m \left(\frac{2}{\pi^2} \left[\frac{1}{\Delta t_r} + \frac{1}{\Delta t_f} \right] \right)^{(\alpha-1)} \left(\frac{\hat{B}}{2} \right)^{\beta} \quad (3.204)$$

The flux in the *rotor yoke* is bipolar, thus core losses are obtained similarly to the stator yoke:

$$p_{Fe,RJ} = \frac{pC_m}{T_{mech}} \left\{ \begin{array}{l} s_1 \left(\frac{2}{\pi^2} \left[\frac{1}{\Delta t_1} + \frac{1}{\Delta t_2} \right] \right)^{(\alpha-1)} \left(\frac{B_{sub}}{2} \right)^{\beta} + \\ s_2 \left[\frac{2}{\pi^2} \left(\frac{1}{2B_0} \right)^2 \left[2\frac{B^2_{sub}}{\Delta t_1} + 2\frac{B^2_{sub}}{\Delta t_2} + \\ 2\frac{(2(B_0 - B_{sub}))^2}{\Delta t_0} \right] \right]^{(\alpha-1)} B_0^{\beta} \end{array} \right\} \quad (3.205)$$

The small sub-figure in Fig. 3.21 occurs s_1-times and the large figure s_2-times. If p is the number of pole pairs, values for s_1 and s_2 are given in Table 3.1 for common SRM designs.

Table 3.1 Number of basic figures in the rotor yoke flux waveform for different SRM geometries

N_s/p	N_r/p	s_1	s_2
6	4	6	3
6	8	14	5
8	6	14	5
10	8	24	8

Once the specific iron losses $p_{Fe,k}$ and the iron weights m_k for each part k of the magnetic circuit are known, the total core losses P_{Fe} are calculated according to

$$P_{Fe} = N_s \cdot m_{sp} \cdot p_{Fe,SP} + \left(1 - \frac{2p}{N_s}\right) m_{SJ} \cdot p_{Fe,SJ1} + \frac{2p}{N_s} m_{SJ} \cdot p_{Fe,SJ2} +$$
$$N_r \cdot m_{RP} \cdot p_{Fe,RP} + m_{RJ} \cdot p_{Fe,RJ}$$

(3.206)

In (3.206) it is assumed with respect to Fig. 3.20 that the unipolar flux-waveform occurs in approximately $2p/N_s$ of the entire stator yoke volume.

The investigations so far are valid only for the case that the conduction (dwell-) angle of the energized phase is less or equal to the stroke angle Θ_{sk} when the flux of maximum two phases overlaps during the commutation. However, for 3- or 4-phase machines (and higher phase numbers) it is usual to choose a dwell angle $\Theta_d > \Theta_{sk}$. For the 4-phase machine it leads to the effect that for some short instants the flux in the stator yoke consist of three different pole fluxes which overlap during the commutation, hence the remagnetization frequency is three-times of that in the poles. This is shown in Fig. 3.22a for the example of the 8/6-SRM III. The stroke angle is $\Theta_{sk}=15°$, the turn-on angle $\Theta_{on}=0°$ and the turn-off angle $\Theta_{off}=20°$ (mech. deg.). It is very impressive to see that the bipolar flux-density waveform in the stator yoke has now a significant steady component which increases with the conduction angle.
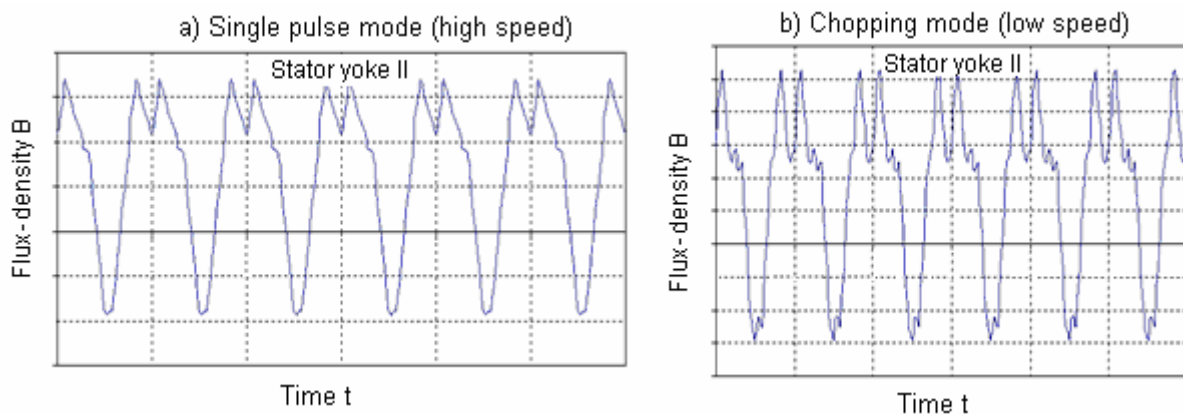
Fig. 3.22 Flux-density in the stator yoke of 8/6-SRM for $\Theta_d=20°$ a) single pulse, b) chopping mode

Approaches for calculation SRM core losses which can be found in the bibliography mostly concern the single pulse operation at higher speed since it results in a triangular flux-density waveform. The proposed method in this thesis can also be used for a low-speed current control mode by means of a hysteresis band controller. In comparison to the single pulse

mode, Fig. 3.22b shows the bipolar flux-density waveform in one part of the stator yoke for chopping mode. It can be clearly seen from the flux-density waveforms for $\Theta_d > \Theta_{sk}$ with chopping- and single pulse control mode, that for operating points with two or more phases simultaneously conducting or with an active tolerance band current control mode the flux-density waveform cannot be subdivided into some few basic figures. Therefore, the determination of the equivalent frequency occurs for constant time-steps Δt:

$$f_{eq} = \frac{2}{\pi^2} \frac{1}{(B_{max} - B_{min})^2} \cdot \sum_{t=0}^{T-\Delta t} \frac{(B(t+\Delta t) - B(t))^2}{\Delta t} \qquad (3.207)$$

3.5.3   Mechanical and additional losses

The *mechanical losses* in the SRM consist of friction and windage losses which are independent of the load. Friction losses occur in the machine bearings. If the bearings are anti-friction bearings, then this component is very small [2], [60], [153]. Windage losses represent the power dissipated in the machine due to friction with air. They depend on the rotor speed, air gap- and the stack length. A general formulation is given by V. Raulin [155]:

$$P_{fr} = a_w V_{air} \omega^m \qquad (3.208)$$

where a_w is called a windage coefficient, V_{air} is the volume of air in the motor considering that the stator is full, and m is a curve-fitting parameter. The coefficients of the equation are usually derived from experiments with the motor. The analytical calculation is quiet difficult and due to complex laminar airflow-conditions or lubricant friction in the bearings relatively unreliable. An empirically expression for determining friction and windage losses P_{fr} in [kW] for rotating electrical machines with salient poles is given by Wiedmann [17]:

$$\frac{P_{fr}}{kW} = k \cdot 10^{-6} \cdot \left(\frac{D_r}{m}\right)^{3.6} \cdot \left(\frac{l_r}{m}\right)^{0.6} \cdot \left(\frac{n}{\min^{-1}}\right)^{2.3} \text{(kW – kilo Watt)} \qquad (3.209)$$

with the rotor length l_r and the outer rotor diameter D_r. The constant k=1.8 for n<200rpm and k=2.0 for n>200rpm. Another empirically formula is given in [16] for the friction losses:

$$P_{fr} = k_{fr} \cdot D_r \cdot (l_r + 0.6 \cdot \tau_p) \cdot v_r^2 \qquad \text{(for } k_r \text{ see in Table 3.2)} \qquad (3.210)$$

where $v_r = D_r \cdot \pi \cdot n$ is the circumferential speed of the rotor and τ_p is the stator pole pitch.

Table 3.2   Friction coefficient for electrical machines with different cooling systems

Cooling system	K_{fr} [Ws^2/m^4]
Surface-cooled machines	15
Open-circuit ventilated machines	8 ... 10
Turbo generators with air-cooling	5
Turbo generators with water-cooling	<3

Additional losses (often called 'stray load losses') in electrical machines are very difficult to measure and to localize. They vary with the load and are approximately proportional to the square of the machine's r.m.s. current. Additional losses are for example losses produced by harmonics of the magnetic field or remagnetization losses in constructional parts of the stator (e.g. housing) due to end winding effects [13], [16], [34]. The amount of additional losses in electrical machines can be assumed to be 1% of the effective input power [16], which will be taken over in this thesis.

3.5.4 Converter losses

Forward losses

If one phase in the converter is in the conducting state, a forward voltage drop occurs due to the finitely resistance of the power electronic devices. The resulting losses depend on the forward voltage V_F and the junction temperature of the semiconductors, represented by the bulk resistance r_F. The average conducting losses P_{Fa} of diodes and transistors are [5]

$$P_{Fa} = \frac{1}{\Delta t} \int_{t_0}^{t_1} p_F(t) dt \qquad (3.211)$$

$$p_F(t) = V_F \cdot i(t) + r_F \cdot i^2(t) \qquad (3.212)$$

$$P_{Fa} = V_F I_{av} + r_F I_{rms}^2 \qquad (3.213)$$

The time $\Delta t = t_1 - t_0$ is the conducting time, I_{av} is the mean value of the current and I_{rms} the r.m.s current through the semiconductor. Three different switching states can be distinguished for the power electronic devices assuming an asymmetric half bridge supplying the SRM:

(1) energizing a phase means two switches conducting;
(2) during de-energizing two diodes are conducting;
(3) with soft-chopping, one diode and one switch are conducting at the same time.

It is assumed that always one diode and one switch are conducting at the same time. Then, the conducting losses produced in all q-phases of the converter are

$$P_{Fa,Conv} = q \cdot \left(P_{Fa,switch} + P_{Fa,diode} \right) \qquad (3.214)$$

Switching losses

In praxis, current and voltage edges during a switching process of a semiconductor have a finitely slope. For example, during a turn-on, current increases firstly from zero to the final value before the voltage falls from the cut-off voltage down to the forward voltage. During this time switching losses are produced. The voltage to switch by a power electronic device V_{sw} is usually the dc-supply voltage reduced by the voltage drop over the phase resistance. Assuming IGBTs for switching devices, their turn-on power losses $P_{s,on,IGBT}$ are

$$P_{s,on,IGBT} = \int_{t=0}^{t_r} i_c(t) \cdot v(t) \cdot dt \qquad (3.215)$$

where $i_c(t)$ is the collector current and t_r is the current rise time [5]. If a linear current rise-up is assumed then the average turn-on power losses are approximately:

$$P_{s,on,IGBT} \approx \frac{1}{6} \cdot f_{sw} \cdot V_{sw} \cdot I_c \cdot t_r \qquad (3.216)$$

where f_{sw} is the average switching frequency. Considerable turn-on power losses occur almost exclusive in IGBTs. Measurements have shown that turn-on processes with diodes are finished extremely fast so that turn-on power losses are negligible [5], [33]. Similarly to the turn on, the turn-off power losses for an IGBT can be calculated with the fall-time t_f of the current from the maximum value I_C to zero:

$$P_{s,off,IGBT} \approx \frac{1}{6} \cdot f_{sw} \cdot V_{sw} \cdot I_c \cdot t_f \qquad (3.217)$$

The turn-off power losses of a diode dominate its turn-on losses [5]. They are calculated by

$$P_{s,off,diode} = f_{sw} \cdot \int_{(t_{rr})} V_{sw}(t) \cdot i(t) dt \qquad (3.218)$$

The reverse recovery time t_{rr} is the time which is necessary to remove the recovery charge Q_{rr} until the diode can overtake the cut-off voltage V_{sw} again. Solving (3.218) gives [5], [163]:

$$P_{s,off,diode} = f_{sw} \cdot V_{sw} \cdot Q_{rr} \qquad (3.219)$$

Finally, the total switching losses of the q-phase-converter can be determined assuming one diode and one IGBT take part in the commutation:

$$P_{s,Conv} = q \cdot \left(P_{s,on,IGBT} + P_{s,off,IGBT} + P_{s,off,diode} \right) \qquad (3.220)$$

The total converter losses P_{Conv} consist of conducting and switching losses:

$$P_{Conv} = P_{Fa,Conv} + P_{s,Conv} \qquad (3.221)$$

3.6 Dynamic calculations

Following the instantaneous current and torque values will be calculated for one phase. In order to obtain the resulting torque of all phases, the calculated torque waveform of one phase is shifted and added to the next phase with respect to the phase number.

Calculation of current waveform

The starting point for the calculation of the current waveform of one phase forms the voltage equation, given in the form

$$v = Ri + \omega \frac{d\psi(i,\Theta)}{d\Theta} \quad \text{with} \quad d\Theta = \omega \cdot dt \qquad (3.222)$$

where i is the instantaneous phase current and v is the actual phase voltage neglecting the voltage drop over the power electronic devices. It is assumed to be either $+V_s$, 0 or $-V_s$ when V_s is the dc-supply voltage. Rearranging of the voltage equation gives

$$\frac{d\psi}{d\Theta} = \frac{1}{\omega}(v - iR) \tag{3.223}$$

$$\psi = \frac{1}{\omega}\int (v - iR)d\Theta + \psi_0 \tag{3.224}$$

with the initial flux-linkage ψ_0. For the i-th integration step with the finite step width $\Delta\psi$ the change of flux-linkage is given by

$$\Delta\psi_i = \frac{1}{\omega}(v_i - i_iR)\Delta\psi_i \ , \tag{3.225}$$

hence $\psi_i = \psi_{i-1} + \Delta\psi_i$. $\tag{3.226}$

For each angle step the corresponding phase current is determined from the ψ-i-characteristics by searching the calculated flux ψ_i for the actual rotor position Θ_i and selecting the corresponding current i_i. For intermediate rotor positions between the grid points Θ_n and Θ_{n+1} the line index *m* for the phase current is interpolated firstly. After that the corresponding current value is determined by a further linear interpolation between i_m and i_{m+1}. This procedure is graphically shown in the $\psi-\Theta$-plane in Fig. 3.23.
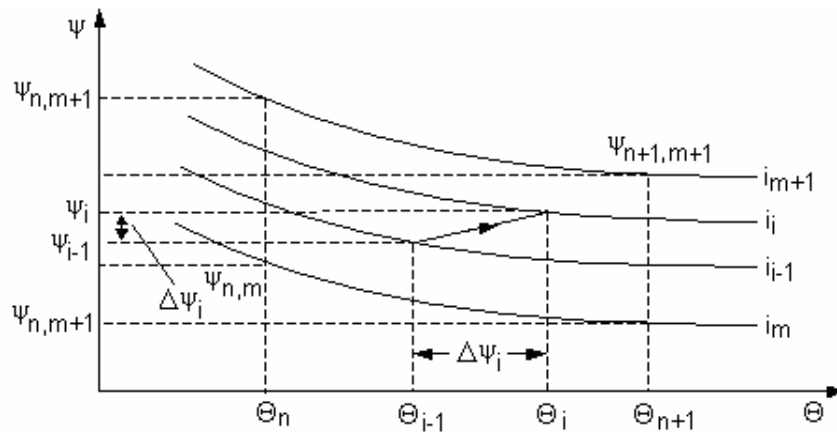
Fig. 3.23 Determination of the phase current in the $\psi-\Theta$-plane

As initial condition the flux linkage ψ_0 and the current i_0 is assumed to be 0 at $\Theta=\Theta_{on}$. The iteration is finished when the current is reduced to 0 again at Θ_{end}. Fig. 3.24 shows the calculated current waveform of SRM II for two operating points with $\Theta_{on}=0°$ and $\Theta_{off}=160°$ (electrical degree): chopping mode at low speed (n=1000rpm) and single pulse mode during high speed (n=6000rpm). Note, at high speed operation the motor back-emf is such as high that the current cannot achieve its reference value of $I_{ref}=6A$.
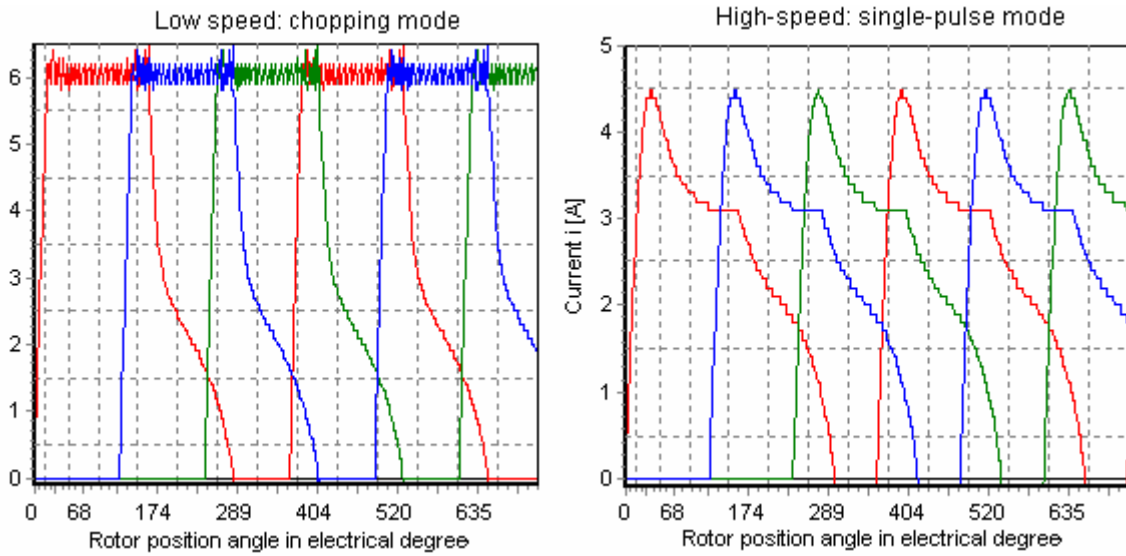
Fig. 3.24 Calculated phase current waveforms for typical operating points of SRM II

Calculation of instantaneous and average torque

The instantaneous torque value for each (i_i, Θ_i)-data pair is calculated by finding the corresponding value from the $T(i, \Theta)$ data field, determined by static calculations before. Intermediate values are obtained by linear interpolation. Fig. 3.25 shows the calculated torque waveforms for the two operating points presented in Fig. 3.24. At high-speed operation, the motor produces remarkable negative torque due to the large turn-off angle. The commutated current is not reduced to zero when the rotor passes the aligned position.
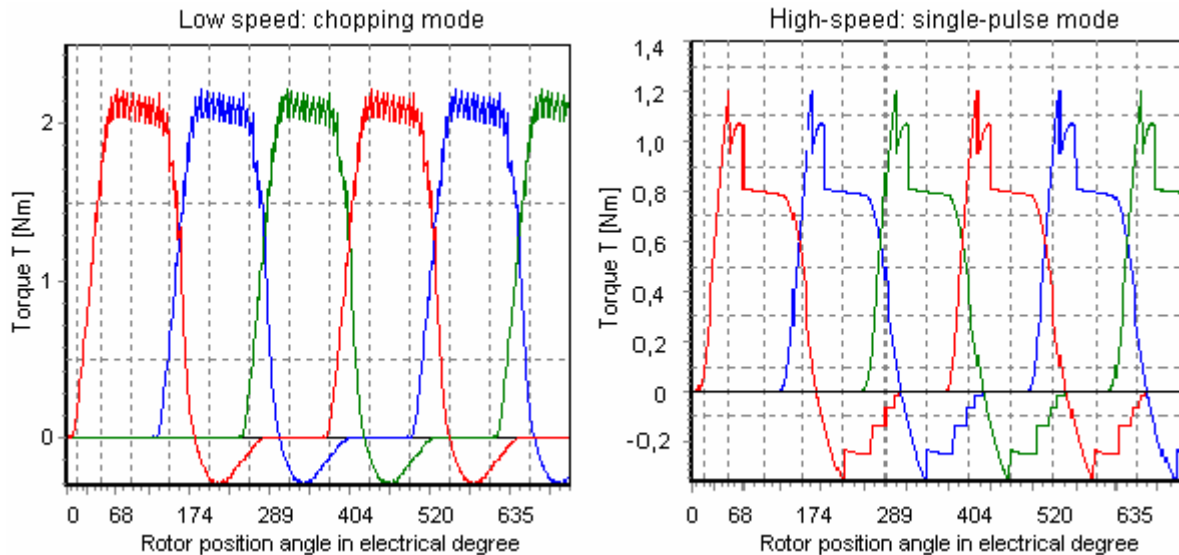
Fig. 3.25 Calculated phase torque waveforms for typical operating points of SRM II

The average torque can be calculated in two different ways. The first one deals with the determination of the enclosed area ΔW^* of the magnetisation curve which the phase current circles during one electrical period in the ψ-i-plane. It is

$$\Delta W^* = T_{av} \frac{2\pi}{N_r} \tag{3.227}$$

69

Such area is shown in Fig. 3.26 for the case of a) chopping mode and b) single pulse mode. In order to calculate the area ΔW^*, for each angle step $\Delta\Theta_i$ between Θ_{on} and Θ_{end} (when the commutated phase current is reduced to zero) the change of current $\Delta i_i = i_i - i_{i-1}$ is multiplied with the average value of the corresponding flux-linkages ψ_{i-1} and ψ_i and subsequent added up. Under the condition of *chopping mode* the area ΔW^* is calculated as follows:

$$\Delta W_1^* = \sum_{\Theta=\Theta_{on}}^{\Theta_1} (i_{i+1} - i_i) \cdot \frac{1}{2}(\psi_{i+1} + \psi_i) \tag{3.228}$$

$$\Delta W_2^* = \sum_{\Theta=\Theta_{off}}^{\Theta_{end}} (i_{i-1} - i_i) \cdot \frac{1}{2}(\psi_{i-1} + \psi_i) \tag{3.229}$$

$$\Delta W_3^* \approx \frac{1}{2}\left(\Delta i_{hys}\left(\psi_{off} - \psi_1\right)\right) \tag{3.230}$$

$$\Delta W^* = \Delta W_2^* - \Delta W_1^* - \Delta W_3^* \tag{3.231}$$

where Δi_{hys} is the wide of the hysteresis band and Θ_1 is the angle when current achieves the first time its reference value and $\psi=\psi_1$. For *single pulse mode*, the area ΔW^* is

$$\Delta W_1^* = \sum_{\Theta=\Theta_{on}}^{\Theta_1} (i_{i+1} - i_i) \cdot \frac{1}{2}(\psi_{i+1} + \psi_i) \tag{3.232}$$

$$\Delta W_2^* = \sum_{\Theta=\Theta_1}^{\Theta_{end}} (i_{i-1} - i_i) \cdot \frac{1}{2}(\psi_{i-1} + \psi_i) \tag{3.233}$$

$$\Delta W^* = \Delta W_2^* - \Delta W_1^* \tag{3.234}$$

The average torque per phase is than

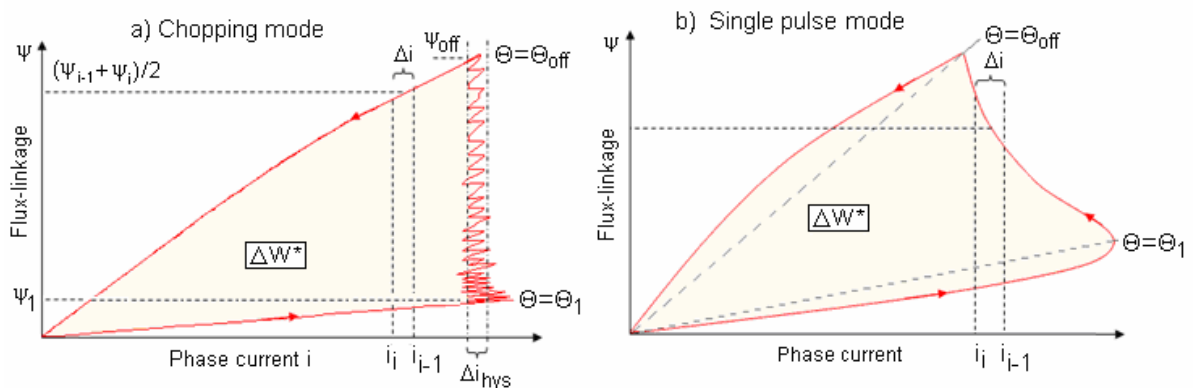$$T_{av} = \Delta W^* \cdot \frac{N_r}{2\pi} \tag{3.235}$$

Fig. 3.26 Magnetisation curve during a) current regulation and b) single pulse mode

The second possibility for calculation the average torque of one phase during one electrical period ($\Theta_{el}=360°$) is the direct calculation of the average value of the torque waveform. Since the first calculation method determines the average torque in terms of the ψ-i-trajectory and the second one uses the torque waveform $T(i,\Theta)$, the comparison of the results obtained by

both methods can give a statement about the quality of the approximation. For the operational points shown in Fig. 3.25 the average torque (one phase) determined from the ψ-i-plane is T_{av}=0.56Nm for chopping mode and T_{av}=0.287Nm for single pulse mode. The average torque directly determined from the torque waveform shows a good agreement with T_{av}=0.61Nm for chopping mode and T_{av}=0.299Nm for single pulse mode, respectively.

3.7   Influence of saturation

Actually, SRMs can perform well only when they work in saturated regime. The flux density in the area where the stator and rotor poles overlap commonly approaches two teslas. To understand the electromagnetical energy conversion properly, a nonlinear analysis is needed that takes account of the saturation of the magnetic circuit. Such an analysis is based on magnetization curves. Fig. 3.27 shows a set of these curves for a typical machine constructed from real iron, together with a ψ(i) trajectory at different rotor position angles for an idealised 'flat topped' current i as shown in Fig. 3.28.
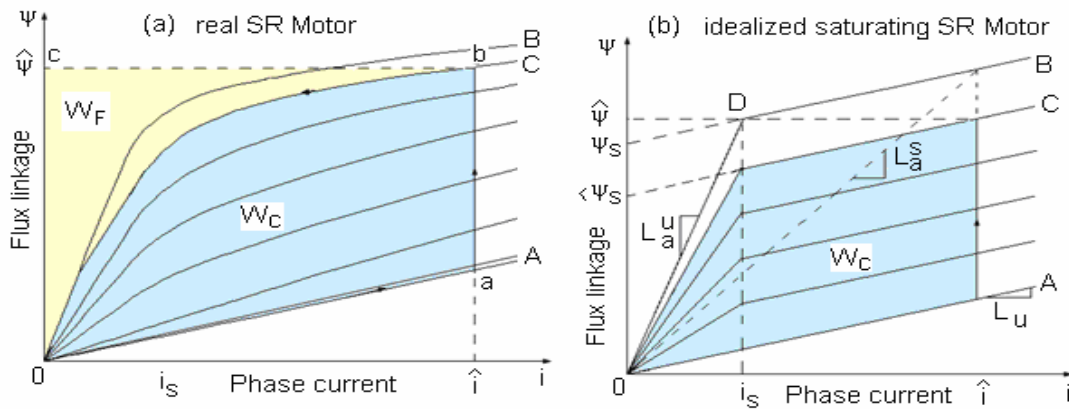

Fig. 3.27   Energy conversion loop: a) real saturating motor; b) idealized ψ(i) trajectory

A constant current is established very quickly after the turn-on angle near the minimum inductance position A, and remains constant until the turn-off angle at position C is reached, when the commutation occurs. Due to the larger inductance around the aligned position the de-energizing of the commutated current takes a certain time and the rotor moves some degree before the current is dropped off. Thus, a part of magnetic energy is additionally converted into mechanical work.
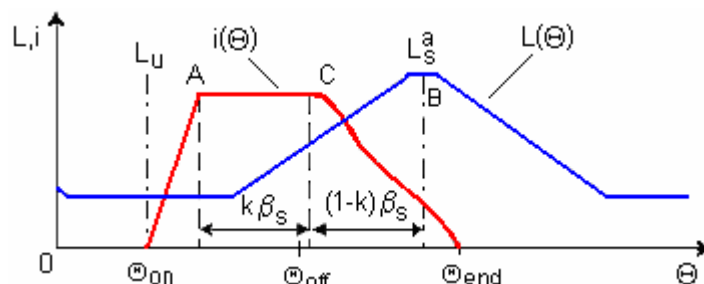

Fig. 3.28   Flat-topped current waveform of SR Motor

The energy supplied by the inverter (area *oabco*) can be divided into two parts: the stored field energy W_F (area *obco*) which is returned except hysteresis losses to the supply during commutation, and the coenergy W_C (area *oabo*) that is available to be converted into mechanical work. Following assumptions are embodied in the structure of Fig. 3.27:

- The minimum inductance L_u occurs in the unaligned position and remains constant.
- The magnetization curve for the aligned position is linear up to point D with unsaturated aligned inductance L_a^u. Thereafter it continues with the slope L_u, so DC is parallel to 0A and separated from it by the flux linkage ψ_s.
- The saturated inductance in the aligned position is L_a^s, which is a function of current.
- The operation point trajectory reaches the end of its flat topped current i interval at the commutation point C such that $AC = k \cdot AB = k \cdot \psi_s$ where k<1 (early commutation before reaching the aligned position in order to avoid negative torque generation).

An aligned saturation factor σ_a and an unsaturated inductance ratio λ_u is defined [132] as

$$\sigma_a = \frac{L_a^s}{L_a^u} \qquad and \qquad \sigma_a < 1 \tag{3.236}$$

$$\lambda_u = \frac{L_a^u}{L_u} \qquad and \qquad \lambda_u > 1 \tag{3.237}$$

Studying simplified ψ-i-trajectories in Fig. 3.27b gives after some simple derivations an analytical expression for the coenergy and the average electromagnetic power P:

$$W_c = V_s \frac{\beta_s}{\omega} \cdot k \cdot i \left[1 - \frac{1}{2} \frac{k}{s} \right] \tag{3.238}$$

with $\quad s = \dfrac{\lambda_u - 1}{\lambda_u \cdot \sigma_a - 1}$ $\hfill (3.239)$

$$P = W_c \frac{qN_r}{2\pi} = V_s i \frac{\beta_s qN_r}{4\pi} \cdot k \left[2 - \frac{k}{s} \right] = V_s i \frac{\beta_s qN_r}{4\pi} \cdot Q \tag{3.240}$$

Linear (non-saturated) motor

A SRM constructed of infinitely permeable iron will be referred to as a *linear machine*. The aligned and unaligned ψ-i-curves are straight lines without saturation. In the case of no saturation σ_a=1, hence s=1. If also k=1, the expressions for W_k, W_F and EC are

$$W_c = \frac{1}{2} V_s \frac{\beta_s}{\omega} i \tag{3.241}$$

$$W_F = \frac{1}{2} L_a^u \cdot i^2 \tag{3.242}$$

$$EC = \frac{W_c}{W_c + W_F} = \frac{\lambda_u - 1}{2\lambda_u - 1} \tag{3.243}$$

Saturated Motor

The introduction of saturating material (real steel) in the magnetic circuit of the linear machine will produce a saturating SRM. That machine is identical to the linear one in all geometric aspects and in the linear zone of the B(H) magnetisation curve of the iron up to the saturation flux density. Fig. 3.29b presents the linearized ψ-i-characteristic of such a saturated motor with the same unsaturated inductance ratio λ_u and energy conversion W_c (hence the same torque output) compared to the linear non-saturating SRM. Saturation now limits the maximum flux-linkage to a smaller value ($\psi_a < \psi_b$). If the rotor displacement between A and C is unchanged, then the supply voltage must be reduced to the unsaturated case. In other words, the saturated motor cannot accept as large as voltage impulse (volt-time integral) as the non-saturated motor. However, for the same energy conversion W_c, the maximum current must now be greater for the same output torque. On the other hand, it is easy to see in Fig. 3.30a that for the same current the linear machine has much more output torque capability by allowing the linear machine to exploit its true nature and carry higher flux densities. The graphic shows the aligned and unaligned flux-linkage curves for both linear and saturated machine having the same air gap length, same number of turns, and identical geometry. Note that the output torque of both machines increases if the air gap is reduced, but the linear machine by much more (Fig. 3.30b).
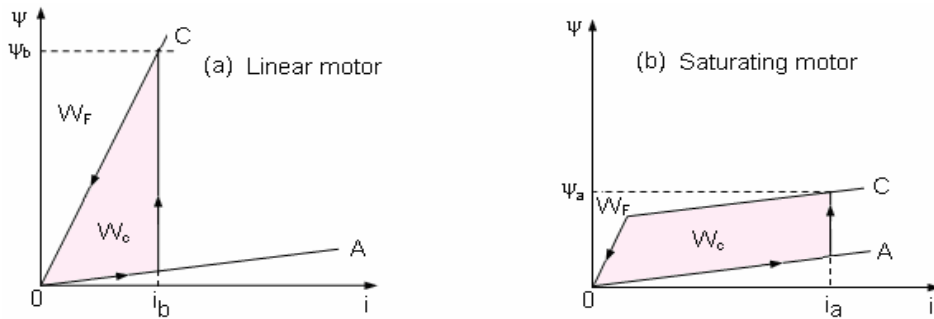

Fig. 3.29   Idealized ψ-i-curves: a) linear and b) saturating SRM for the same torque
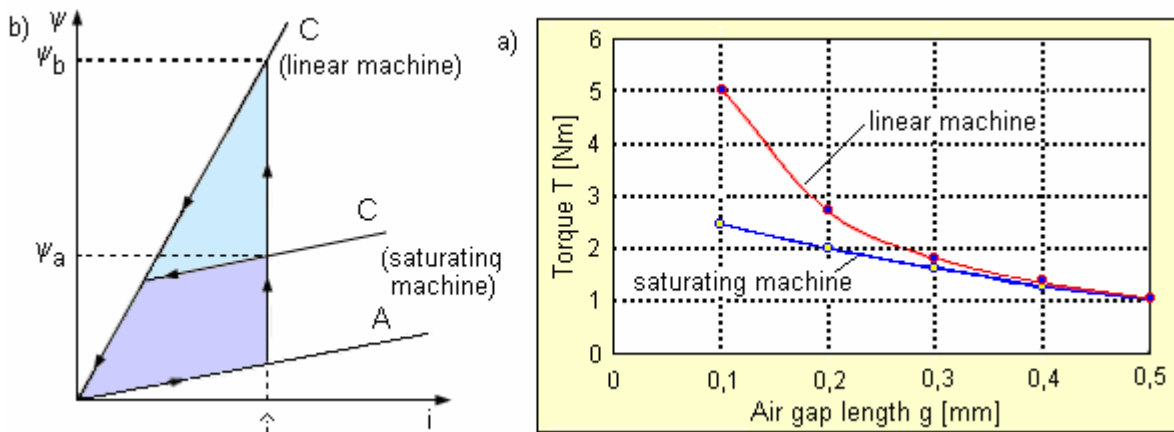

Fig. 3.30   a) idealized ψ-i-curves of linear saturating SRM with the same maximum current;
b) influence of the air gap on torque output for constant current

Volt-ampere requirement and energy ratio for ideal current feeding

The ratio of the maximum current i and voltage v for the saturated (subscript *a*) and unsaturated (subscript *b*) motor can be obtained from Fig. 3.27b for the case of the same enclosed area of the ψ-i-curves and hence the same output torque [132]:

$$\frac{i_a}{i_b} = \frac{s \cdot \sqrt{2-k}}{\sqrt{2s-k}} \tag{3.244}$$

$$\frac{v_a}{v_b} = \frac{\sqrt{2-k}}{\sqrt{2s-k}} \tag{3.245}$$

Fig. 3.31a presents the current and voltage ratio as a function of the aligned saturation factor, starting with $\sigma_a=0.3$ for the example of a real (saturating) motor, increasing up to $\sigma_a=1$ for the ideal non-saturating motor. Both machines operate with the same torque and speed and have an unsaturated inductance ratio $\lambda_u=12.5$. Further it is assumed that the phase inductance is restricted to an angular rotation of the stator pole arc β_s, hence, k=1. It is found that the real saturating motor SRM II (k=1, $\sigma_a=0.6$, $\lambda_u=11.6$, s=1.83 for I=6A) requires a maximum current of 1.12 times that of the ideal non-saturating motor. However, its voltage requirement is lower by a greater factor. In the example with s=1.83, $v_a/v_b=0.61$. The *vi*-products, which are particularly meaningful for transistor inverters since they are sensitive to peak currents, are in the ratio 1.12*0.61=0.74, i.e. the saturating motor requires only 74% of the volt-ampere compared to the linear machine for the same enclosed area W_c! In the general case the ratio of the volt-ampere requirements can be determined from (3.244) and (3.245):

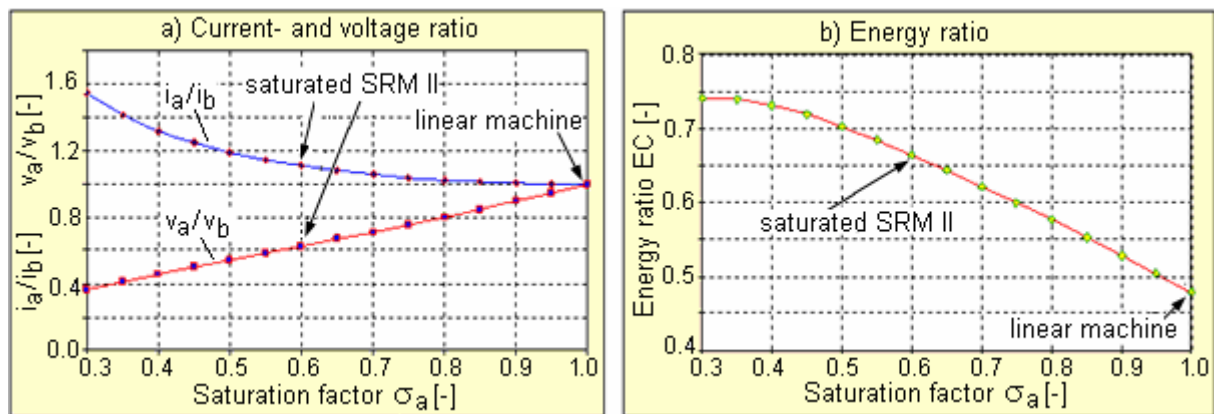$$r = \frac{(vi)_a}{(vi)_b} = \frac{s(2-k)}{2s-k} \tag{3.246}$$

Fig. 3.31   a) Current and voltage ratio and b) energy ratio vs. saturation factor

Note that these results say nothing about the motor size. They only mention that the vi product of a saturating motor will be smaller than for a non-saturating motor with the same values of L_a^u and L_u for a given output torque and speed. Saturation is beneficial from this

point of view. Fig. 3.31b shows the corresponding energy ratio, which is with EC=0.66 much higher for the saturated SRM II compared to the linear motor with EC=0.48. Generally, the energy ratio for the saturating motor can be written as

$$EC = \frac{c(2s-c)(\lambda_u \sigma_a - 1)}{s + 2c(\lambda_u - 1)} \tag{3.247}$$

Practical current feeding

a) Chopping mode

The analyses so far were made under the condition of an idealized flat-topped current. In practice, a chopper is usually used to realize the current-fed excitation at low speed. Since the incremental inductance of the real saturating SRM is very small compared to the linear SRM, the average chopping frequency is much higher for the same tolerance band wide.

It is important to know that the energy conversion capability (EC) of a SRM under hysteresis current control is essentially influenced by the mode of control. It must be distinguished between hard- and soft- shopping mode. Assuming an asymmetric bridge converter as shown in Fig. 1.7a, both transistors T1 and T2 are opened and closed together in *hard chopping mode*. When they are opened, the stored magnetic energy causes the current to flow through the diodes, thus negative supply voltage is applied to the winding. The flux ramps down and energy is returned to the supply. During *soft-chopping mode*, freewheeling is employed, i.e. only one transistor is opened (except at the end of a phase period) and the current circulates with zero applied voltage through one diode and the closed switch. The flux only decays due to winding resistance and device voltage drops, which are usually small. When the supply voltage is off, most of the stored magnetic energy is converted into mechanical work, instead of being returned to the supply, which increases the EC. The current rise time is the same with or without freewheeling, but the decay rate is slower with freewheeling, reducing switching frequency of the converter and therefore switching losses of the power electronic devices. In Fig. 3.32 the ψ-i- trajectories are shown for a real saturating machine with a) hard chopping and b) soft chopping mode. The switch-on occurs in the unaligned position, whereas the switch-off occurs before the aligned position so that zero current is reached at the maximum inductance. In Fig. 3.32a, the coloured area represents the amount of energy circulated by the chopper action and therefore reducing the EC. With soft chopping introducing freewheeling, this energy circulation does not occur, as shown in Fig. 3.32b. Hence, the EC will be higher for soft chopping mode. It is very interesting to see that the EC for both operation modes can be made higher than 0.5, even for the non-saturating machine, if the following condition is satisfied: $W_2 > W_4 + \sum_{k=1}^{N_c} \Delta W_k$, where N_c is the number of chops per working stroke. That can be achieved by

(1)   a machine design with small unaligned inductance L_u,

(2)   using a small tolerance band width Δi,

(3)   switching off earlier than the aligned position in order to enable the stored magnetic energy at the turn-off angle to be removed as mechanical output
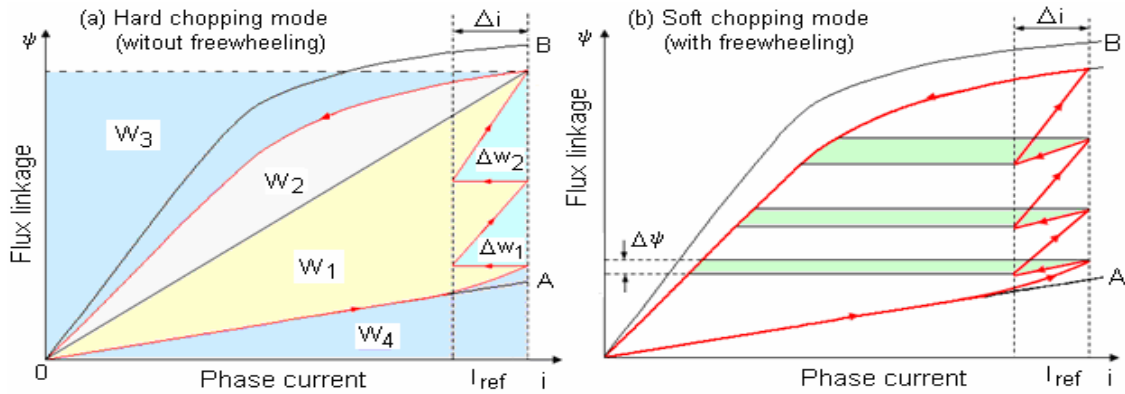

Fig. 3.32 ψ-i- trajectory for saturating machine: a) hard chopping, b) soft chopping mode

A computer study has been carried out based on the original saturated motor SRM I desired for vacuum cleaner application with 3000rpm. Iron losses are neglected throughout. The linear non-saturation machine was modelled by replacing the real steel with infinity permeable iron. The aligned unsaturated inductance is the same for both SRMs as well as the geometric dimensions. The reference current was adjusted firstly such that the average torque and therefore the output power was the same for both machines; secondly the reference current was the same for both machines. Table 3.3 summarises the results.

Table 3.3   Comparison of chopping parameters for saturated and non-saturated motor SRM I

SRM type	chopping mode	I_{ref} [A]	Δi [A]	I_{rms} [A]	EC	f_s [kHz]	P_{out} [W]
saturated	soft	8.0	0.5	5.3	0.787	13.5	940
saturated	hard	8.0	0.5	5.2	0.254	22.8	940
non-saturated	soft	6.6	0.5	4.4	0.576	5.1	940
non-saturated	hard	6.3	0.5	4.3	0.286	7.7	940
non-saturated	soft	8.0	0.5	5.2	0.563	3.1	1460
non-saturated	hard	8.0	0.5	5.2	0.383	5.7	1460

It was found that

- for the same output power of approx. P_{out}=940W the non-saturated machine has significant lower peak and r.m.s current values than the real saturating machine;
- the linear machine has approx. 55% more output power for the same r.m.s current of I_{rms}=5.2A, i.e. the same temperature rise;
- the energy conversion capability EC is much higher for both machines for the soft-chopping mode employing freewheeling; the saturating motor has highest EC;
- by satisfying the early turn-off condition (Θ_{off}=150° electric degree) the EC of the non-saturated motor can be higher than 0.5 in soft chopping mode at low speed.

b) Single pulse mode

At higher speeds, a practical SRM drive is operated in the single pulse mode, i.e. the two transistors T1 and T2 in Fig. 1.7a are closed together at a particular rotor position angle Θ_{on} and opened together at the end of conduction period at the turn-off angle Θ_{off}. Unlike the chopping mode this occurs only once in each phase induction cycle. Each phase is energized with a constant positive voltage pulse through its conduction period. The stored magnetic field energy causes current to flow through the diodes at turn-off, applying the dc supply voltage to the winding with opposite polarity. The actual current value at any rotor position angle is that which is necessary to establish the impressed flux through the reluctance of the magnetic circuit at the particular angle. The current waveform can be determined by solving the voltage equation during both the conduction period, and the turn-off period. At a given speed and torque, different current waveforms can be produced by varying both the turn-on angle and the turn-off angle. Switching angles are therefore the main control parameters in single pulse operation, and good design practice of SR motor drives is very much concerned with the optimum choice of these angles. A computer study for the same machines introduced in the previous section for chopping mode operation has been made. The control parameters of the non-linear machine were first modified to produce the same rated output power of 2kW at the same r.m.s. current. The calculation results are summarized in Table 3.4. Note that the linear motor can match the output of the saturating motor on a thermal basis only, at the expense of a 1.5-times higher peak volt-ampere product. The very high rate of rise of inductance in the linear machine causes the current to fall very rapidly. Hence, to develop the required torque, a high peak current must be established before the poles start to overlap.

Table 3.4   Comparison between saturated and linear motor for the same r.m.s. current with 6000rpm

Motor type	P_{out} [kW]	I_{max} [A]	I_{rms} [A]	Θ_{on} [el.°]	Θ_{off} [el.°]	V_s [V]	EC	$I_{max}*V_{dc}$ [kVA]
saturated	2.0	9.5	5.30	0	140	310	0.74	2.95
non-saturated	2.0	9.6	5.26	0	160	470	0.45	4.51

Conclusions for the machine design

The object of the previous studies was to compare a real saturating with an idealized non-saturating (linear) SR motor. Starting from a first linear approach, expressions for the energy conversion capability and volt-ampere demand respectively the ratio of these values for saturating and unsaturating machine were derived for the case of ideal current feeding. It was shown that the effect of saturation is to reduce the torque generating capability of a motor of given dimensions, but at the same time it reduces the inverter volt-ampere-requirement for a given torque and speed. Thus, the degree of saturation will influence the balance between motor and inverter size. Saturation is desirable from this point of view, but must be localized on the pole tips, for instance by a trapezoidal shape of the teeth, since the electromagnetic

energy conversion occurs in the air gap [18], [33], [39], [170]. Consequently, the demand to operate the SRM partially in the range of saturation is not in the contradiction to the common procedure to avoid the nonlinear operation at electrical machines.

In a second analysis the machine properties were investigated under practical operation conditions. Chopping control mode is used at low-speed with and without freewheeling, and single-pulse operation is used for high speed. The conclusions must distinguish between the goal of maximum output power from a given machine size, volt-ampere requirement and energy conversion capability EC. In order to achieve a maximum output power from a given machine size, it is desirable to use infinitely permeable, non-saturating iron for the machine design and to make the air gap as small as practicable. Such a linear machine can have many times the output power of a real saturating motor, for the same r.m.s current in low-speed chopping or high-speed single pulse operation. The penalty is a much higher voltage which is necessary to achieve the same r.m.s current; hence the volt-ampere requirement increases rapidly. It was found that:

- With single-pulse operation mode at high speed the EC of the linear machine can significantly increase the value of 0.5 under the condition of an early current turn off.
- Generally, switching off earlier than the maximum inductance at aligned position increases the EC since stored magnetic energy is converted into mechanical output.
- Operating of the linear motor with single pulse mode at the same output power and r.m.s current as the saturated motor with the same dimensions requires much more converter peak volt-ampere demand, leading to a larger inverter size.
- Introducing a freewheeling period at chopping mode (soft chopping) dramatically increases the EC compared to the hard chopping mode without freewheeling.

Finally, to achieve maximum specific output power, ideal iron is beneficial. The price paid is a high volt-ampere requirement from the electronic converter. In praxis, the machine design should have magnetic circuits of low reluctance in order to have a high ratio of maximum to minimum inductance. To minimize the size of both the motor and the inverter, the coenergy W_c should be maximized and the magnetic field energy W_F minimized. This requires a small air gap and iron with very high permeability.

3.8   Hybrid Design Program

3.8.1   *Structure of hybrid design method*

The complex design procedures of the SRM's taking into account the another elements of the whole drive system as supply device, electronics and control are the subject of the presented dissertation. Therefore, this thesis is proposed to make a contribution to the hybrid design of

complete SRM drive systems. Actually, it is beyond controversy that the design of SRMs by numeric methods with FEM-programs provides the most precise and proof results. However, FEM calculations require expensive software tools, are relatively complicated and time consuming in spite of modern and fast computer systems. Consequently, for a complete design of new type series of machines with different dimension's variants the way of using only FEM is not practicable in an industrial situation. Therefore software is necessary that can

- abbreviate considerably the preparation time for the following FEM-calculation and
- research the dynamic operational behaviour and the combination of the electric machine with other electrical and mechanical components of the complex drive system.

Meeting these requirements for an effective machine design requires a new hybrid time-economic design-, calculation- and simulation procedure which is presented in this thesis. The structure is presented on Fig. 3.33, including at first analytical and then numerical calculation methods and finally dynamic simulations.
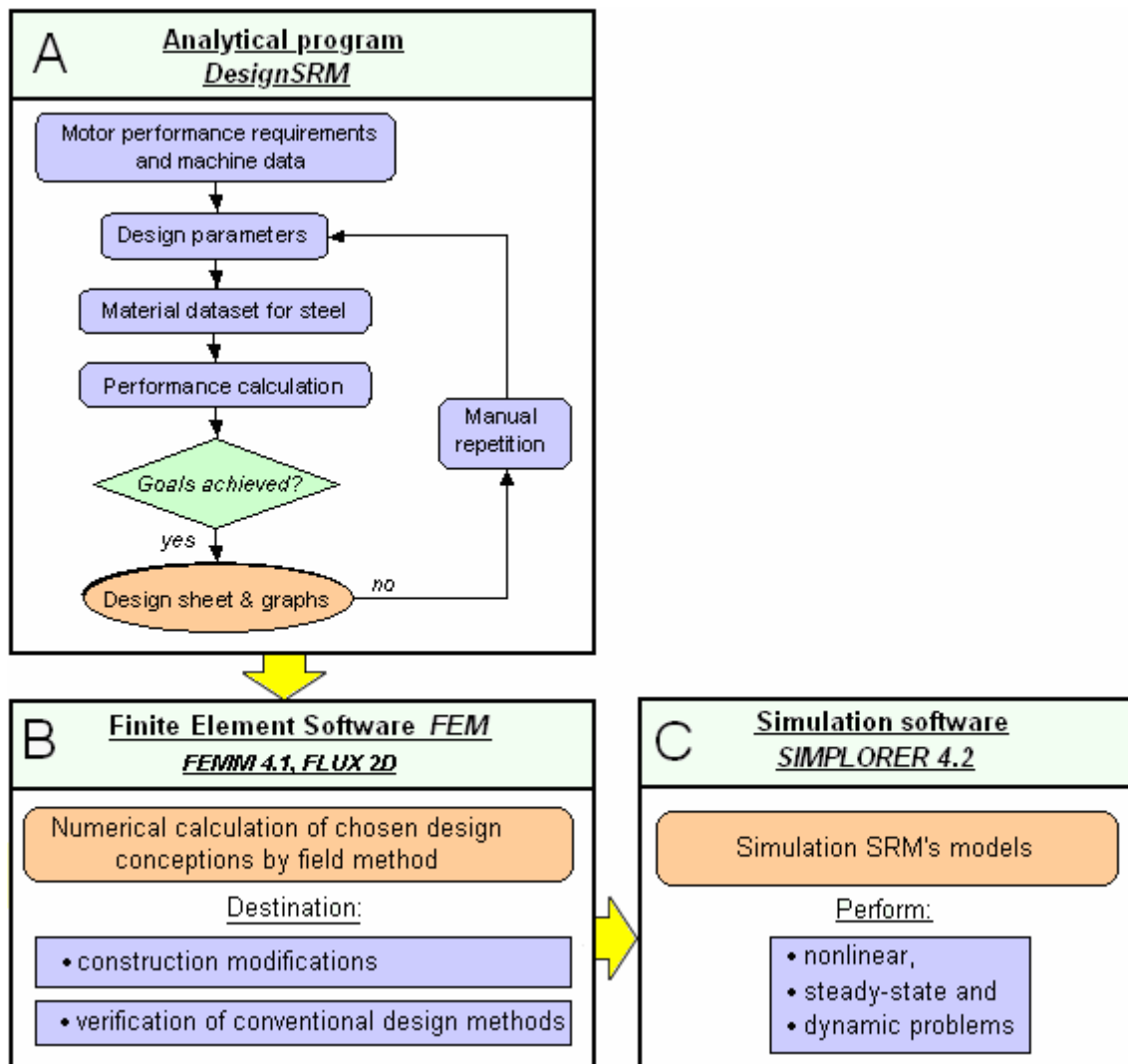

Fig. 3.33 Structure of the hybrid design program

The algorithms and the structure of the Finite Element Method (see Fig. 3.33-Block B) are known very well in the large bibliography (e.g. [79], [112], [137], [140], [177]) and thus will be not presented in this thesis. Some informations are given in the sub-chapter 5.1.2. Simulation SRM's models with application of SIMPLORER 4.2 software (see Fig. 3.33-Bloch C) are the subject of the next chapter.

3.8.2 *Analytical program DesignSRM*

In order to fulfil the requirements in a time-effective machine design the analytical computer program "DesignSRM" was developed by author as an very important result of this dissertation. That is a special software tool for designing SRMs of various constructions, basing on analytical calculation and design methods proposed in the previous sections of this work. It is developed with the programming language Delphi/Pascal. The program is designed to be fast in operation, with an efficient user interface. Its main use is

- a totally free new machine design or a similar machine design with the same construction starting with a standard geometry proposed by the program;
- winding design;
- calculation of the magnetic circuit, considering non-linear magnetization characteristics and saturation effects;
- calculation of motor and converter losses as well as system efficiency in dependence of different control modes and control parameters;
- calculation and sizing of various steady-state characteristics, e.g. $\psi(i,\Theta)$, $L(i,\Theta)$, $T(i,\Theta)$
- dynamic calculations like instantaneous current and torque waveforms;
- studying and learning SRM drives.

Fig. 3.34 shows a desktop view of the program. Starting from a performance requirement or after loading machine data the computation of all results follows in seconds. A control window shows the program progress and guides the user through the design.
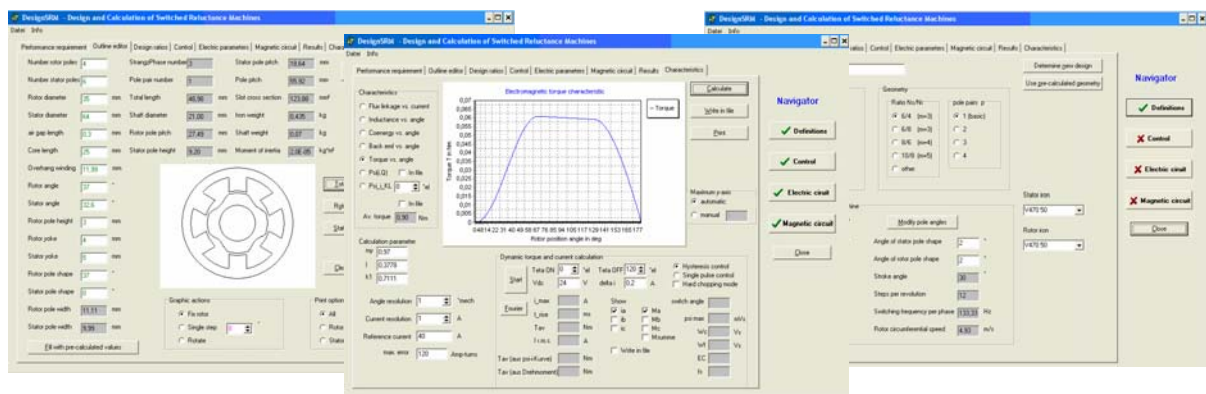

Fig. 3.34   Program "DesignSRM"

The general calculating procedure shows Fig. 3.33-block A. The motor design is found by calculating its various performance parameters using the calculation methods developed in this thesis. The process is repeated manually until the design objectives like efficiency, torque-speed-characteristics etc. are achieved. The program provides an outline editor for modifying the cross section. Electrical parameters, control values and many other inputs can be made in further tab sheets of the program panel. A material data base includes magnetization and loss characteristics of various steels and also a linear non-saturating (ideal) material. Analysis and performance calculations can be either at a specific operating point or over a whole speed-, current-, or torque range to obtain typical machine characteristics. Further, the program contains a discrete time-stepping model to obtain current and torque waveforms with different modes of control. Finally, at the end of the design stage a design sheet and all graphs of interest can be printed and stored in separate data-files.

The design procedure with "DesignSRM" occurs step-by-step using several tab sheets. These tab sheets are shortly introduced below in their logical order for an accurate motor design.

Tab sheet 1: *Performance requirement*

In this first tab sheet shown in Fig. A.1 in the Appendix, the user defines the performance requirements of the motor by typing the desired speed, torque and torque density from which the motor main dimensions can be determined using equation (2.2). Further, the general geometric structure can be specified by choosing the number of rotor and stator poles with their corresponding angles β_s and β_r, respectively. Useful values for β_s and β_r will be proposed by the program to start with. The user has the choice between standard N_s/N_r-ratios multiplied with the number of pole pairs or a totally new N_s/N_r ratio which will be checked automatically for validity. Another important option is the choice of the core material for the stator and rotor laminations. After pushing the button "Determine new design" a first rough motor geometry will be calculated using special *design ratios* for the internal motor geometry.

Tab sheet 2: *Design ratios*

Beside the air gap length the user can choose here suitable design ratios for sizing the internal motor geometry like

    (a) core length/rotor diameter l_{Fe}/D_r;

    (b) outer rotor diameter/outer stator diameter D_r/D_s;

    (c) length of the overhang winding/stator pole width l_{oh}/t_s;

    (d) rotor yoke thickness/rotor pole width y_r/t_r;

    (e) stator yoke thickness/stator pole width y_s/t_s and

    (f) the rotor pole height/air gap length h_r/g.

There is the choice between some different pre-defined datasets obtained from various well working SRMs published in bibliography or of course self defined values. The desktop of tab sheet 2 can be found in Fig. A.2 in the Appendix.

Tab sheet 3: *Outline editor*

The outline editor presented in Fig. A.3 in the Appendix is for editing the motor cross section which is graphically shown to the user. It is advisable to proceed cautiously with careful changes, starting with a valid design. The motor cross section can be stored and printed out.

Tab sheet 4: *Control parameter*

This tab sheet (see Fig. A.4 in the Appendix) has two important tasks. The first is to give suitable advises for the user concerning switching angles for the current (useful for a following simulation program or prototype tests to start with). The second is to type electrical parameter of the power electronic devices which are necessary to calculate converter losses.

Tab sheet 5: *Electric parameters*

The winding design is made in this sheet (see Fig. A.5 in the Appendix) as well as the calculation of copper losses, current density and the average electromagnetic torque. The number of turns per phase can be chosen either manually (option "*choose number of turns per phase*") or determined automatically (option "*determine number of phases*") using equations (2.30) and (2.31). In the first case, the necessary dc supply voltage for achieving the required current at given speed and saturating flux density will be calculated by rearranging equation (2.31). In the latter case, the input parameters are the dc supply voltage and the saturation flux density in the stator pole. The wire diameter of the winding depends on the available slot area and the slot fill factor which must be chosen with respect to manufacturing capabilities. Determining copper losses, current density and electromagnetic torque requires the current value to be known. By choosing the option "*use current for rated torque*" an idealised flat-topped phase current will be calculated iteratively which produces the required rated main torque. The other (faster) possibility is to preset a flat topped current value and calculate the resulting average electromagnetic torque (option "*choose current*"). The copper losses are determined by using the temperature dependent phase resistance and the r.m.s. value of the current, estimated with equation (3.183). Also current density is calculated with r.m.s. current.

Tab sheet 6: *Magnetic circuit*

After determining the electrical parameters and winding design, the calculation of core losses can occur. Tab sheet 6 in Fig. A.6 in the Appendix shows the results for calculating the magnetic circuit and core losses. Important values like aligned and unaligned inductance or

flux-density, magnetic field strength and specific core losses in each part of the magnetic circuit are given to the user. All results can be printed out and stored in a separate data file.

Tab sheet 7: *Characteristics*

Tab sheet 7 is desired for the graphical output of motor characteristics and waveforms. The corresponding desktop is presented in Fig. A.7 in the Appendix. By means of the developed machine design and calculation methods, the program "DesignSRM" is able to calculate and size the most important SRM characteristics like

- flux-linkage $\psi(i,\Theta)$ and inductance $L(i,\Theta)$,
- coenergy $W_c(i,\Theta)$ and back-emf $e(i,\Theta)$,
- electromagnetic torque $T(i,\Theta)$

Further, dynamic current-, flux- and torque waveforms can be calculated for different modes of control by a discrete time-stepping model proposed in Chapter 3.6. The user can adjust

- single pulse mode or chopping mode with hard or soft chopping,
- turn-on and turn-off angle of phase current,
- rotor speed and dc supply voltage,
- hysteresis band width of the current controller and
- current- and angle resolution of the calculation.

Additionally to the calculation with "idealized" flat-topped current the converter-, core- and copper losses can be calculated as well as the energy ratio with the "real" current waveform and corresponding r.m.s. value (3.184) for the sake of comparison with the idealized case. Also current rise- and fall times and the average switching frequency of the hysteresis current controller are calculated. Each waveform or motor characteristic is graphically shown on the desktop, can be printed out and of course stored in a separate data file.

Tab sheet 8: *Results*

All calculation results for the investigated operating point and the motor geometry parameter are summarized here (see Fig. A.8 in the Appendix for the desktop print). The sheet includes motor and converter losses, efficiencies, iron and copper weight, winding parameter and electrical operating conditions. All results can be printed and stored in a design sheet. Fig. A.9 in the Appendix shows a typical output of a designed SRM for the example of SRM II for the use as textile spindle drive. Further, a motor data file can be applied from which the program can load all informations of the machine to start calculations again after closing and restarting the software.

4 Simulation model of the SRM with SIMPLORER®

4.1 General remarks

This chapter describes a simulation model of a 6/4 - SR Motor for the example of SRM I for vacuum cleaner. With only a few extensions which will be shown it is suitable for SRMs of any phase numbers. The model is developed in the framework of the presented thesis by means of the simulation software SIMPLORER® 4.2 from ANSOFT Corporation. It considers the non-linear characteristics of the SRM as well as the steady-state and dynamic behaviour with different modes of control. Also a sensorless control scheme is presented. The entire drive, including power converter, SRM, mechanical load and control are included in one complex simulation model using electric networks, block diagrams and Petri-nets.

4.2 Non-linear SRM model

The mathematical model of a SRM is highly nonlinear due to magnetic saturation. Assuming that there is no mutual coupling to other phases, the instantaneous voltage of one phase of the SRM windings is given in equation (1.12). Theoretically the electromagnetic torque T_e produced by each particular phase can be calculated using the well known relationship between flux-linkage ψ, current i and rotor position angle Θ:

$$T_e = \frac{\partial \int_0^i \psi(i,\Theta)\partial i}{\partial \Theta} \tag{4.1}$$

However, due to the summation of numerical inaccuracies, the torque calculation with (4.1) is inapplicable [125]. The key to achieve an accurate simulation of SRMs is to use a mythology that permits to take account the non-linearity of its magnetic characteristic while minimizing the simulation time. Such feature offers the method using 3-dimensional look-up-tables which approximate the relations $L(i,\Theta)$ and $T(i,\Theta)$ shown in Fig. 4.1 for the example of the 6/4-SRM I. They are obtainable either by previous FEM calculation, analytical calculations or measurements. In this case they were obtained by analytical calculation methods.
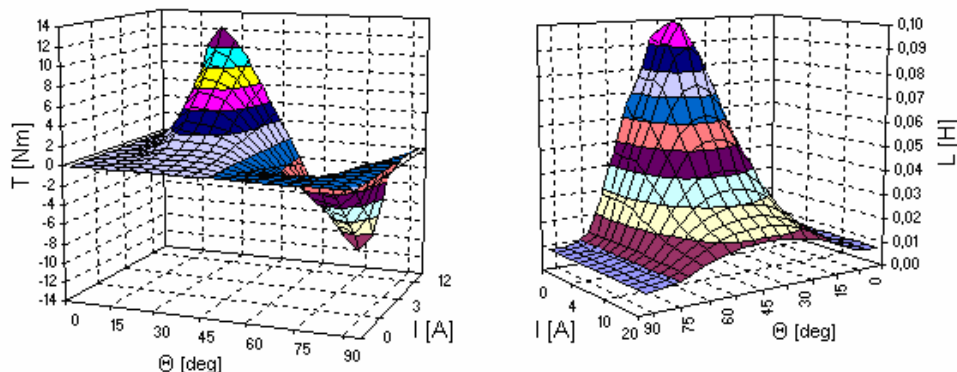

Fig. 4.1 3D-torque and inductance characteristic as a function of phase current and position angle

The proposed SRM simulation model can be subdivided into two parts: a mechanical and an electrical part. They are realized as follows:

Mechanical simulation part

The differential equations (1.33) and (1.34) describing the dynamics of the mechanical part are modelled by a block diagram shown in Fig. 4.2 for one phase. The electromagnetic torque corresponding to the actual rotor position and phase current is obtained using the 3D-look-up-table where the data field is stored. Intermediate values are automatically approximated by cubic splines. An initial angle Θ_0 is added to the actual position angle defining the rotor position at the simulation start for time t=0. The block diagrams for the other motor phases are similarly to phase a.
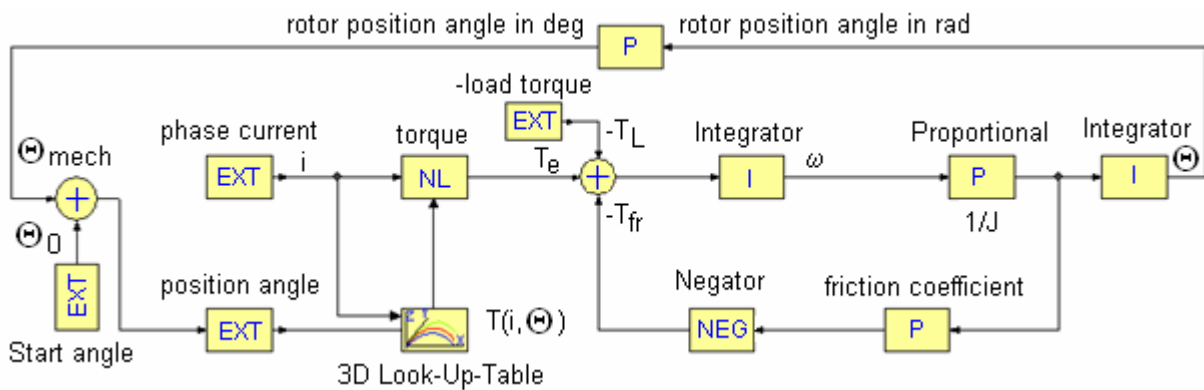
Fig. 4.2   One phase of the mechanical SRM model part in SIMPLORER

Electrical simulation part

The electrical part is modelled in circuit model as shown in Fig. 4.3 for all 3 phases. It is the equivalent circuit corresponding to the SRM voltage equation. Each machine phase is represented by its phase resistance R, the non-linear inductivity $L(i,\Theta)$ and the motor back-emf, modelled as an extern controlled voltage source with reference to equation (1.13). An extension for more phases can be easily achieved by adding the corresponding circuit and adjust the control parameter for the converter. The inductance characteristics $L(i,\Theta)$ are available in form of a 3-dimensional data field which is stored in a look-up-table similarly to the torque characteristics. The motor is supplied by an asymmetric bridge converter providing freewheeling and regeneration capability. Such a converter topology represents an appropriate solution for high performance and high power applications. However, also other converter configurations such as C-Dump converter can be implemented in the simulation model relatively easy. The simulation program SIMPLORER® 4.2 has specialized models for semiconductor switches and diodes, which require a minimum of simulation time.
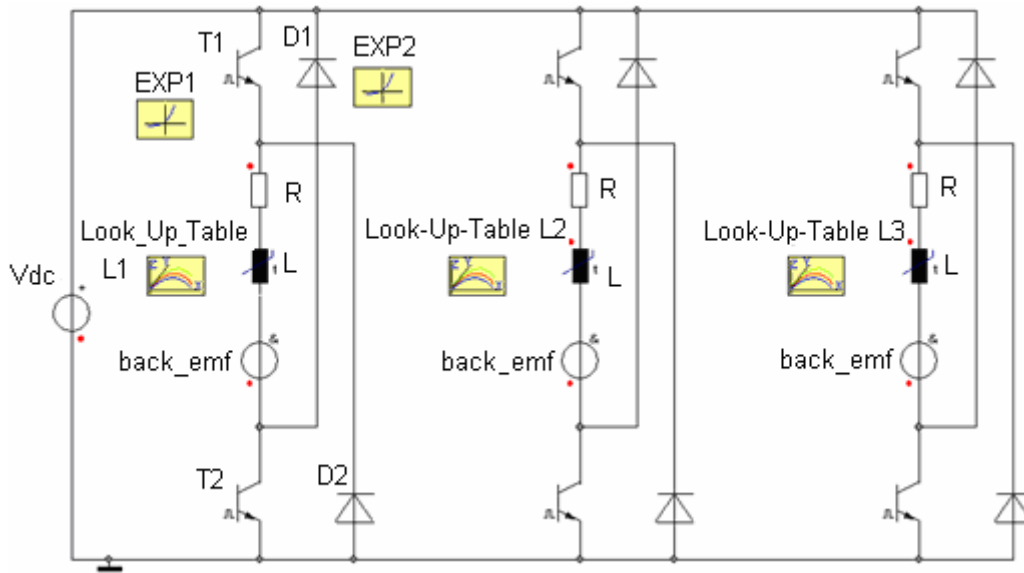
Fig. 4.3 Electrical SRM model in SIMPLORER, supplied by an asymmetric bridge converter

4.3   Implementation of current and single pulse control mode

The control for the SRM drive is described using state diagrams or rather Petri-nets to define different states and transition conditions from one state to the next. The firing of the switches in the power converter occurs in dependence of the rotor position and actual current value in each phase in order to achieve either a chopping or single pulse control mode. Concerning chopping mode, hard- and soft chopping control can be chosen. Fig. 4.4 shows the hysteresis type current controller of one phase using Petri-nets. The commands *T1:=1*, *T2:=1* and *T1:=0*, *T2:=0* turn on and off the transistor T1 and T2, respectively. Further, *ia* is the actual and *is* the desired phase current. The width of the hysteresis band is *di* and the actual rotor position angle is *teta*. The switching angles are referred as *teta_ON* and *teta_OFF*.
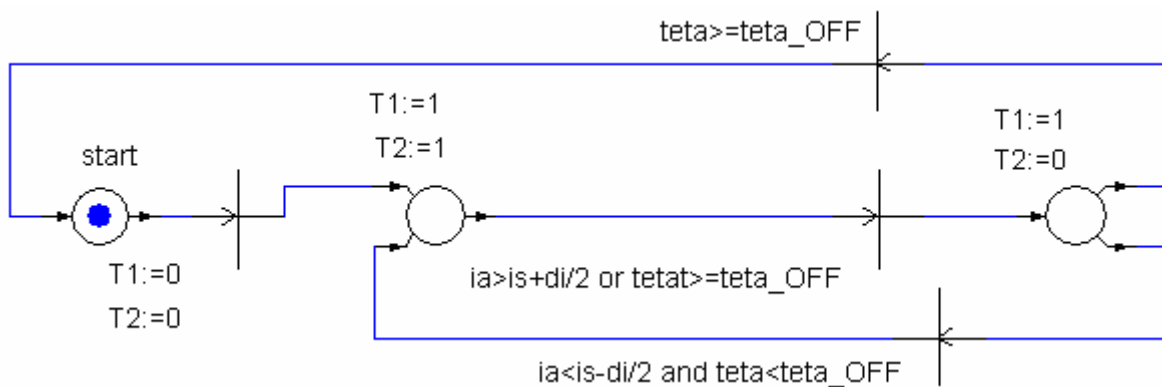

Fig. 4.4   State diagram of hysteresis type current controller for one motor phase

The rotor position angle for each phase is prepared in form of a triangular function which repeats periodically with the aligned position (90°), as shown in Fig. 4.5. The shift angle between two adjacent phases Θ_s is

$$\Theta_s = 2\pi \cdot \left| \left(\frac{1}{N_s} - \frac{1}{N_r} \right) \right|$$
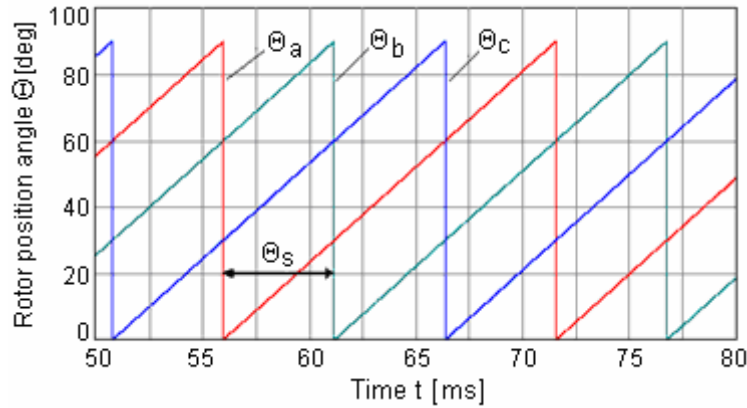(4.2)

Fig. 4.5 Triangular rotor position signal in mech. degree for the three motor phases

Following the simulated current and torque waveforms for each phase are shown for SRM I. Fig. 4.6a presents the results for low speed (n=1000rpm) operation with chopping control; in Fig. 4.6b the motor operates at high speed (n=6000rpm) with single pulse control mode. The turn-on and turn off angle can be adjusted manually. For high speed operation, both switching angles must be preceded in order to energize the phase winding in a zone of low inductance and to decay the current to zero again before the rotor passes the aligned position since the motor back-emf increases with the speed and hinders the current feeding.
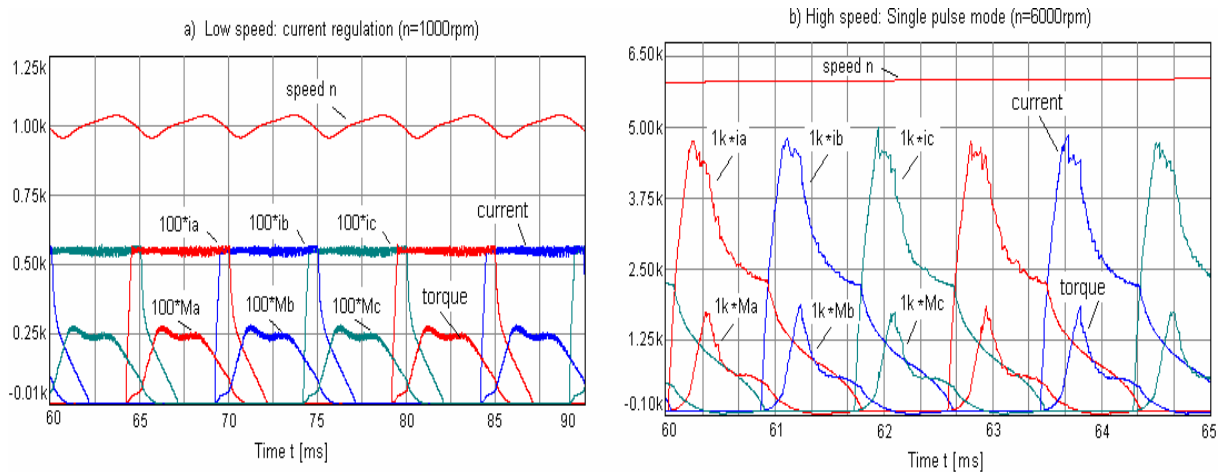

Fig. 4.6 Simulated current and torque waveforms of the 6/4-SRM I for a) 1000rpm; b) 6000rpm

4.4 Influence of mutual couplings on accuracy of the SRM model

For the case of 3-phase SRM structures mutual couplings are relatively small between the phases [57], [98], [120] and [125]. Even though, they shall be considered in the simulation model since they can influence the current waveform considerable at high speed operation and during extended overlap of adjacent phase excitation [33], [68], [120], [131], [138], [152]. In the presented simulation model a constant mean mutual inductance M is assumed.
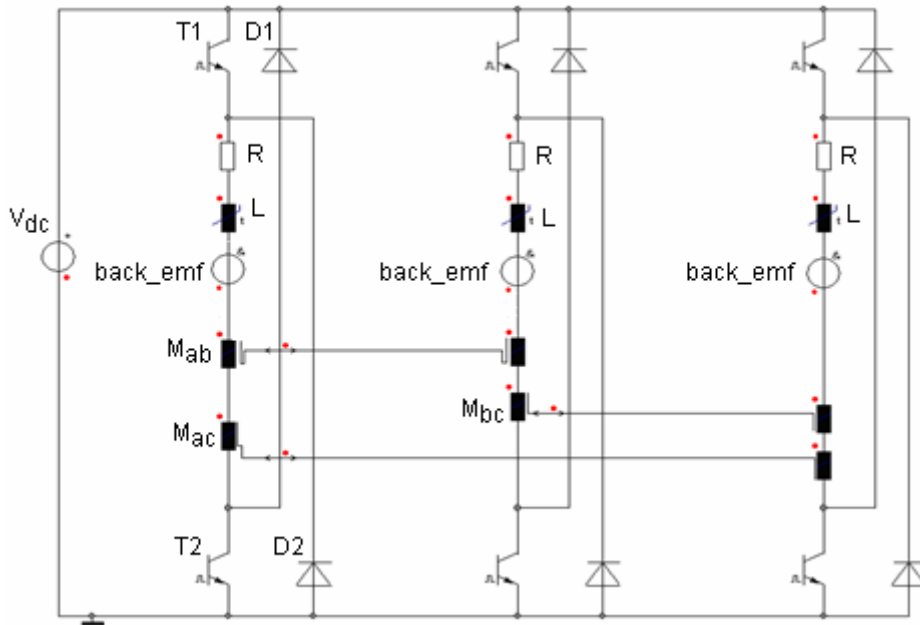
Fig. 4.7 SRM simulation model including mutual inductances

In analogy to the work of F. Laube [120] it is chosen to be approximately one order of magnitude smaller than the phase self inductance. However it must be regarded that similarly to the phase self inductances also mutual inductances are in praxis a function of both, rotor position angle and current! Approaches for determining mutual inductances in detail can be found in [68], [131], [138] and [147]. The simulation program SIMPLORER$^{®}$ provides the virtual device 'extern controlled mutual inductance' for investigating the influence of mutual inductances on the operating performance. The implementation is shown in the extended circuit model in Fig. 4.7
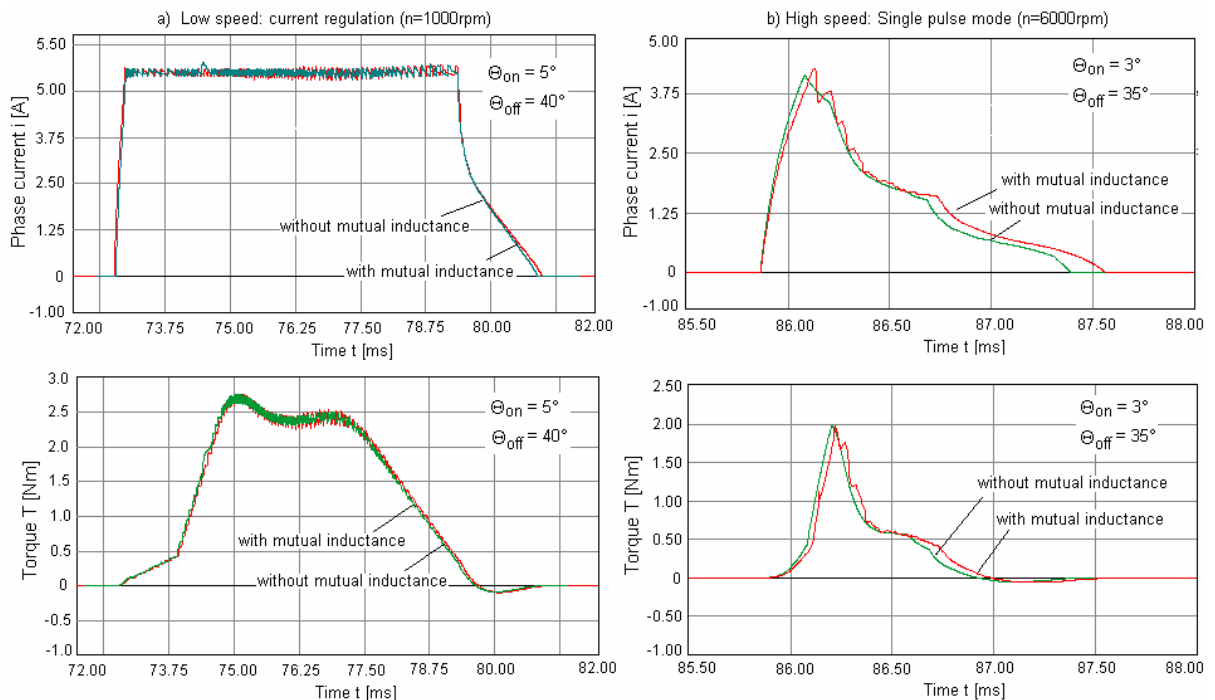

Fig. 4.8 Phase current and torque waveform: a) with and b) without mutual inductances

88

Fig. 4.8 shows the current waveform for high- and low speed operation with and without accounting mutual inductances. The reference value for current regulation is I_{ref}=5.5A with Δi=0.15A. At low speed, very few differences are observed. However, for the case where mutual inductance is considered, there is a longer current signal in the phase winding which produces a small negative torque when the rotor passes the aligned position. This effect enhances with the rotor speed. Therefore, the hypothesis made in [57] to say that mutual inductances are negligible in the case of 6/4 SRMs is verified only for low speed operation because the influence increases with the rotor speed and the number of phases, as reported also in [33], [131], [138] and [147]. As a conclusion, mutual couplings between the motor phases must be considered in the simulation model which occurs in this dissertation by the simplified assumption of a constant mutual inductance, chosen in agreement with [98], [121], [125] to be one order of magnitude smaller than the phase self inductance.

4.5   Sensorless control procedure based on flux-linkage-current method

The control of SRM drives depends on the phase current, rotor position and rotor speed signals to obtain closed-loop control of current, torque and speed. Concerning the feedback signals for the control, current and rotor position can be physically measured with good accuracy using the present sensor technology. One note, the rotor position is definitely needed for the commutation control. However, the position sensor has many demerits due to high cost, installation expense and system reliability reduction. Using a position sensor could be a decisive drawback in applications, where cost and reliability play a crucial role. There have been many attempts in the past to eliminate the position sensor by applying indirect position estimation techniques instead of encoders and resolvers. Comprehensive overviews of published works concerning rotor position estimating methods and sensorless control techniques are summarized in [4], [8], [9], [22] and [74]. Nevertheless, the sensorless operation often has a degraded drive performance and requires more complexity of the control, which is the price to be paid for eliminating position sensor.

For the position sensorless operation, an instantaneous torque control as it is used in the presented simulation model should operate on the basis of measured electrical terminal quantities i.e. current and voltage. From the phase voltage v_{ph}, the flux-linkage can be indirectly determined by rearranging the voltage equation:

$$\psi_{ph}(t) = \int \left(v_{ph}(t) - R_{ph}(t)i_{ph}(t) \right) dt \tag{4.3}$$

Since the phase current and flux-linkage are available, the position estimation is developed on the current-flux-linkage method. Due to its simplicity, this method can be implemented with a short computation time. A potential error source is the unknown phase resistance R_{ph} in (4.3).

In praxis, its value varies with temperature and losses during operation. Despite this fact, most of the flux-linkage estimations in literature were implemented by assuming a constant phase resistance [76], [89], [99], [109] and [130]. With the assumption that the flux-linkage reaches zero at the end of the phase excitation as the current reaches zero at time t_0, (4.3) can be used for online phase resistance estimation [86]:

$$\psi_{ph}(t = t_0) = 0 = \int_0^{t_0} v_{ph}(t)dt - R_{ph} \cdot \int_0^{t_0} i_{ph}(t)dt \tag{4.4}$$

$$R_{ph} = \frac{\int_0^{t_0} v_{ph}(t)dt}{\int_0^{t_0} i_{ph}(t)dt} \tag{4.5}$$

Implementing this procedure into an analog circuit and a Digital Signal Processor (DSP) platform requires generating a reset signal for the integrators at the end of the stroke excitation by a phase active period signal. At the same instant, the values of voltage and current integral must be sampled and phase resistance is determined by the DSP. It is expected that the variation of R_{ph} can be compensated by this method and the accuracy of the flux-linkage is improved. From the predicted or measured machine characteristics it is possible to determine the rotor position by using current and flux-linkage. Derived from the relationships $\psi(i,\Theta)$ and $T(i,\Theta)$, a rotor position characteristic as a function current and flux-linkage $\Theta(i,\psi)$ can be obtained, which is shown in Fig. 4.9. Using this $\Theta(i,\psi)$ curves the rotor position can be indirectly estimated with a sufficient accuracy in a wide operating range.
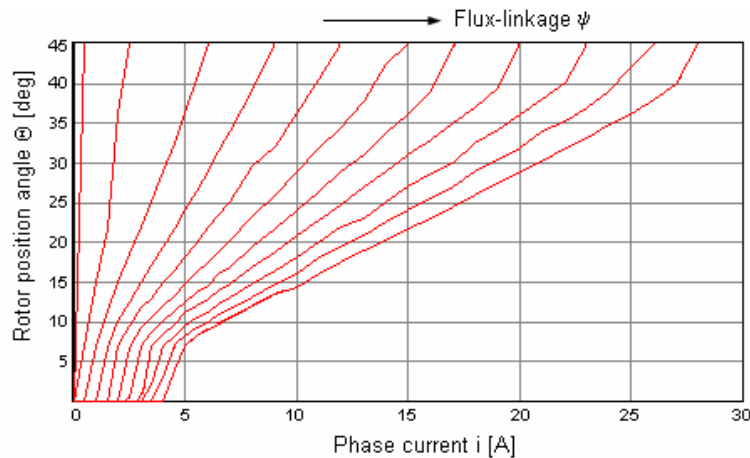

Fig. 4.9   Machine characteristics: rotor position vs. current for various flux levels $\Theta(i,\psi)$

Fig. 4.10 shows the block diagram of the sensorless control strategy using flux-linkage-current method and storing these characteristics in a look-up-table. It was shown by J.P. Lyons in [126] that the accuracy of the position estimation depends on the output gradient of the $\Theta(i,\psi)$ characteristic, especially in the range of aligned and unaligned position. That's why during commutation a selecting function chooses the phase with the lowest gradient on

the $\Theta(i,\psi)$-plane which will contribute to the absolute rotor position angle from all phases in order to minimize the output error.
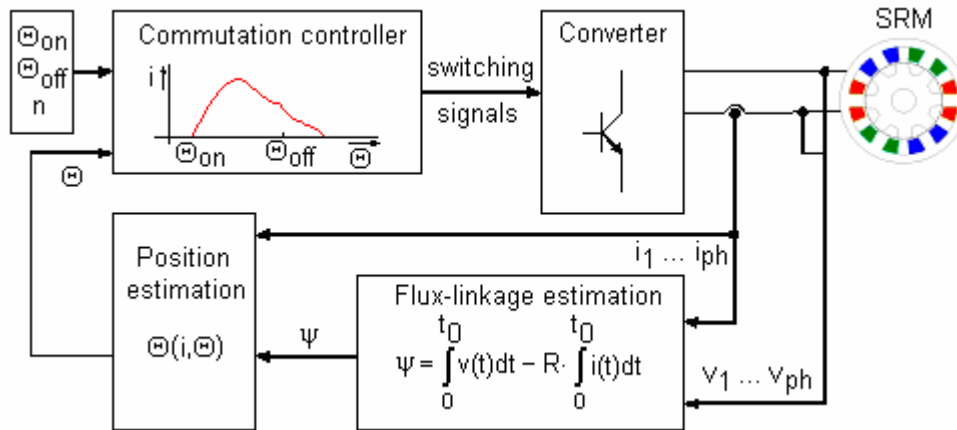

Fig. 4.10   Function block diagram of position sensorless SRM control

For small angles near the unaligned position the $\Theta(i,\psi)$ curves are bunched very tightly in the lower left-hand corner of the graph in Fig. 4.9. Therefore, under the condition of low current and near the unaligned position, small errors in current or flux input values result in large errors in the angle estimation. Likewise, at large angles near alignment the curves are nearly vertical. Thus, near the aligned position, small errors in current input values can also cause large errors in the angle estimation. In order to overcome these problems, the resolution of the look-up table should be higher near the aligned and unaligned position. Alternatively, the position estimation on any phase should be restricted to the central region of these curves, as proposed in [126].

To determine the sensitivity of the position accuracy the position error was calculated between the 'true' position angle computed by means of the mechanical equation $\Theta = d\omega/dt$ and the total estimated angle Θ_{est}. It is shown in Fig. 4.11 with the factor 2 for the sake of clarity. In the middle period of the phase excitation the difference between the estimated and 'true' position angle is near zero. However there are still noticeable errors at the beginning and the end of excitation. These errors can be reasoned by two main points: The first point is that the gradient of the current in these positions is relatively high, on the other hand the resolution of the $\Theta(i,\psi)$ characteristic is insufficient near aligned and unaligned position as explained above. Hence the accuracy of the position estimation is very sensitive to interpolation errors of flux and current between the mesh points in the look-up-table. The second error source is the magnetic coupling between phases during commutation. Since the measured (or calculated) flux-linkage in the static ψ-i-characteristics neglects magnetic coupling effects, mutual coupling in the 'real' operation can affect the measured flux-linkage. However, after a series of simulation experiments it was found that these small estimation

errors have only small effect on the performance of the current and torque control for SRM I under the condition of a sufficient fine resolution in the $\Theta(i,\psi)$-plane.
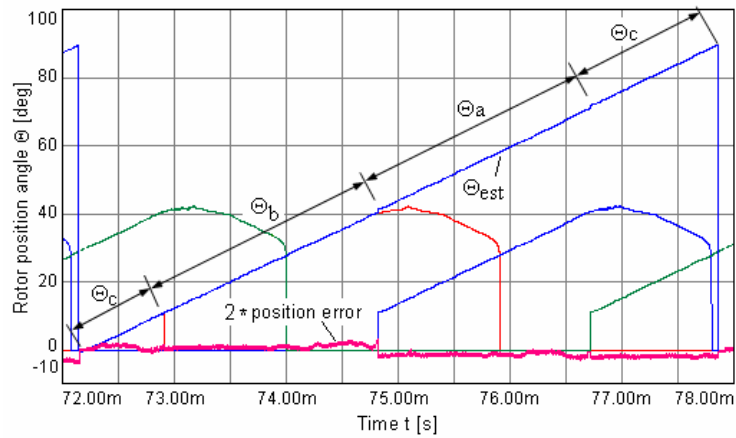

Fig. 4.11 Absolute estimated position angle constructed of estimated angle from each active phase

5   Design examples of industrial prototypes

5.1   Prototype I: 6/4-SRM for vacuum cleaner

5.1.1   Introduction

The rotor geometry of a 6/4-SRM desired for vacuum cleaner has to be modified in order to improve torque characteristics, i.e. reducing torque ripples and increase the average torque. Further, the operational behaviour with a common angle control strategy (chopping mode or single pulse operation with variable turn-on and turn-off angle of phase current) shall be improved. In Chapter 6, the calculation results will be verified by laboratory tests. The cross section of the original SRM I geometry is shown in Fig. 5.1 [52], [53]. The motor rating speed is n_n=6000rpm with rated torque of T_n=1Nm.
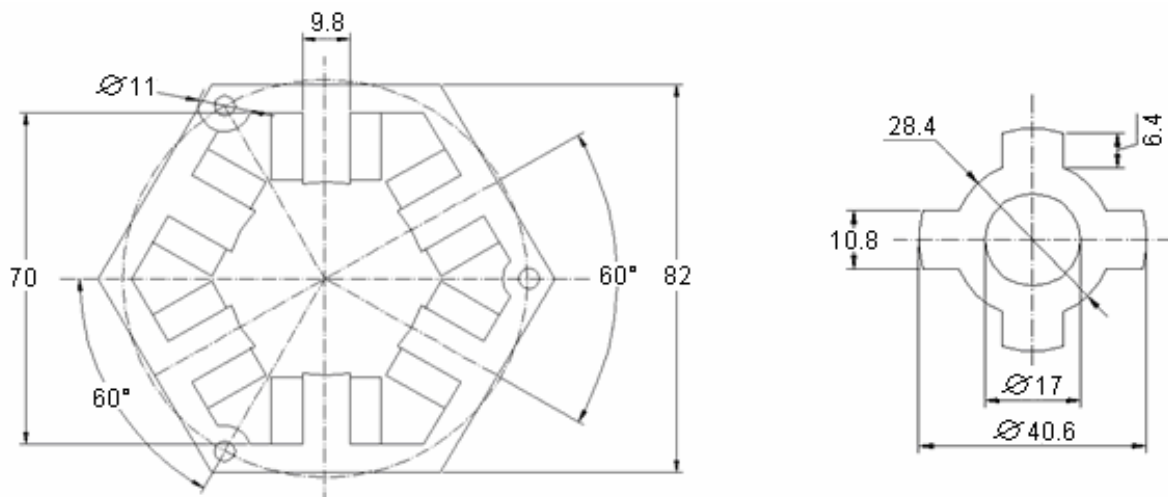

Fig. 5.1   Stator and rotor geometry dimensions of the original 6/4- SRM I

It is observed in many publications ([4], [8], [44], [73], [103], [136]) that the average torque is mostly affected by changes that alter the dominant radial flux components, such as changes of air gap length. Further, an increase of average torque can be obtained by a favourable shift in the torque vs. rotor position angle characteristic by relatively simple changes of the rotor pole profile. An important element of these studies is to determine the extent that slanting the rotor pole sides might have on the average torque and torque ripple. Other variations such as iterative changing the rotor pole width and air gap length are also included for completeness. During changing of one parameter the other parameters are assumed to be the values from the original construction. The stator geometry and core length of the laminations remains unchanged as well as the shaft diameter during changing the rotor parameters. Both, FEM calculations and analytical calculations have been used for determining the SRM characteristics in order to compare the results of the different machine models.

5.1.2   FEM model

To develop a FEM model for the SRM as the complimentary tool in respect to the analytical models the software FEMM 4.0 (Finite Elements Method Magnetics) [7] is used. It allows the distribution of the vector potential and the post-processor submits the processing of the data and calculation of interesting physical values, such as torque or flux density.
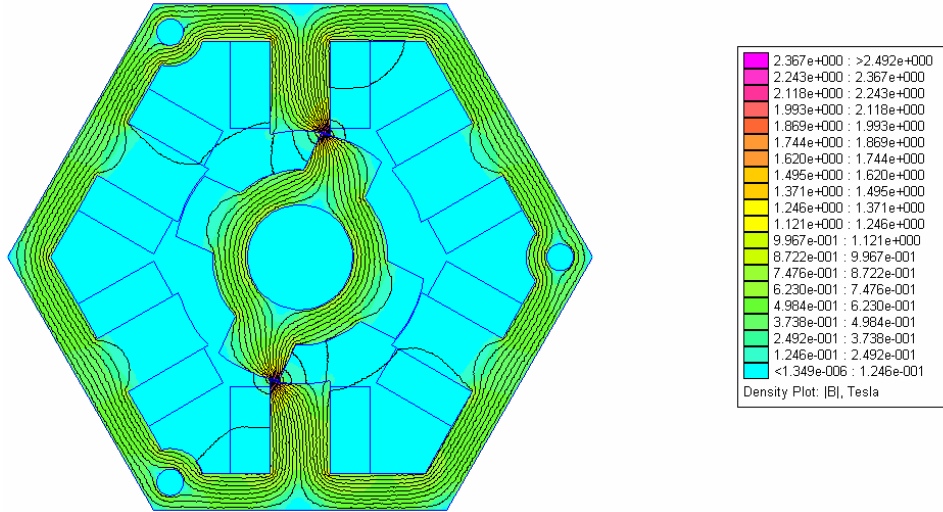

Fig. 5.2   Field distribution of researched SRM I for Θ=20°

Determination of the torque vs. rotor position angle characteristics requires the calculation of a set of values of electromagnetic torque for given set of angular position of the rotor. A single value of torque T at fixed rotor position angle Θ can be calculated by integrating of Maxwell stress tensor in the air gap region. The simplifying assumption of constant magnetic flux distribution along the length of the core leads to solution of the two-dimensional magnetostatic problem. The electromagnetic torque can therefore be calculated by [7], [52]:

$$T = r^2 \cdot l \int_0^{2\pi} \frac{B_r B_t}{\mu_0} d\alpha \tag{5.1}$$

where r describes the radius of the air gap circle, α the angle, l is the length of the core and B_t, B_r are the tangential and radial flux density components, respectively. The FEM magnetic flux is obtained only in k nodes of the mesh, therefore (5.1) has the form

$$T = r^2 \cdot l \cdot \frac{2\pi}{k} \sum_{i=1}^{k} \frac{(B_r B_t)_i}{\mu_0} \tag{5.2}$$

The above torque expression shows that the magnitude of the electromagnetic torque is proportional to the magnitude of both the radial and tangential components of the flux density, whereas the radial flux component in the overlapping region of the excited stator and rotor poles is in most situations the dominant component [136].

5.1.3   Rotor modifications

Selected rotor parameters will be modified in the following in order to investigate the effect of different rotor geometries on the electromagnetic torque: air gap length g, rotor pole height h_r, rotor pole width t_r and a trapezoidal rotor pole shape.

Air gap length

Fig. 5.3a presents the static torque profile of the researched motor for different air gap values. It clearly shows the strong influence on the maximum torque as well as the flat torque range on the characteristics. Hence the machine with the smallest air gap length, subject to acceptable manufacturing tolerances, will produce the highest average torque. The torque ripples referring to (1.8) can be slightly reduced by growing air gap length (see Fig. 5.3b). However, the original air gap length of *g=0.2mm* and therefore the rotor outer diameter remain unchanged due to manufacturing tolerances.
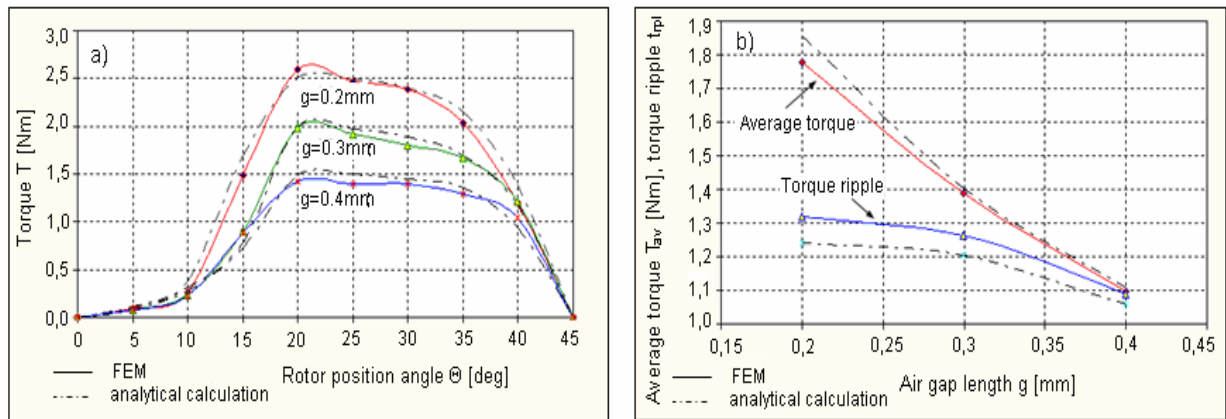

Fig. 5.3   Effect of air gap length on a) torque characteristic and b) average torque and torque ripple

Rotor pole height

The influence of rotor pole height on the maximum torque value is presented in Fig. 5.4a.
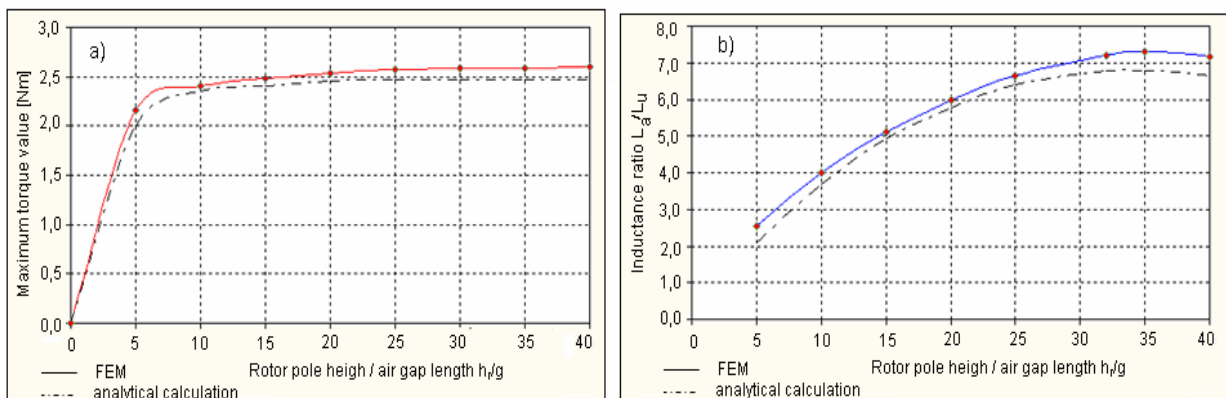

Fig. 5.4   a) Maximum torque vs. rotor pole heights b) inductance ratio vs. rotor pole height

There are shown the maximum torque values T_{max} versus rotor pole height/air gap length h_r/g since increasing the rotor pole's height practically does not influence the rotor position angle

with maximum of torque. The shape of this curve is similar to the material magnetization characteristic in examined range. Height of pole increasing from 0 to 12g caused torque increasing from 0 to 2.5Nm. Enlarging h_r above 30-35g is practically not justified for the researched motor. The maximum torque value mainly depends from the ratio of aligned and unaligned inductance L_a/L_u [8], [80]. Fig. 5.4b indicates a maximum of the inductance ratio vs. rotor pole height characteristic at *$h_r=35g$*, which was chosen for the new rotor design.

Rotor pole width

The influence of the rotor pole width t_r on the torque profile is presented in Fig. 5.5a. A change of t_r practically does not influence the maximum torque value and causes only change of maximum torque rotor position. On the other hand, considering the operational behaviour with the usual angle control mode, the shift characterized by higher torque towards the unaligned position and lower torque near the aligned position is beneficial [136]. For motoring operations, such skewing corresponds to having most of the torque developed at the early stage of rotor-stator poles overlapping.
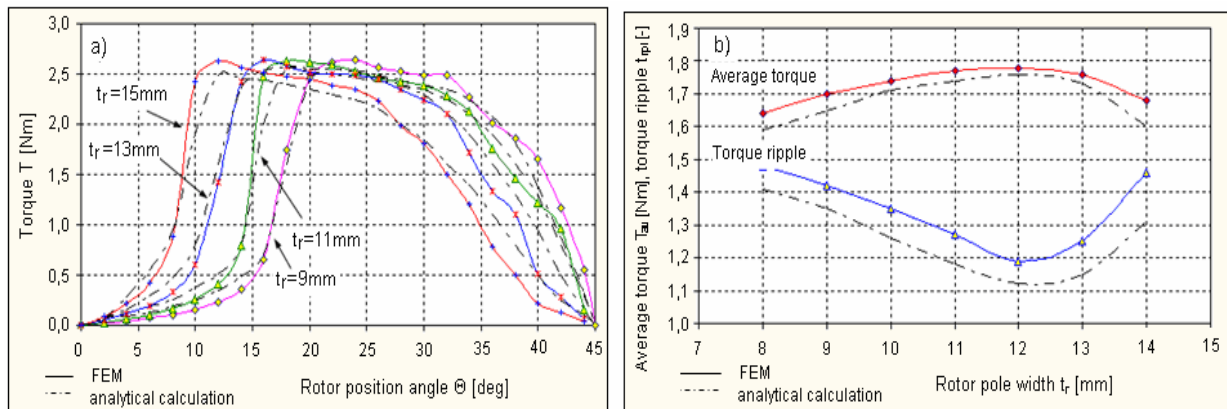

Fig. 5.5   Effect of changing rotor pole width: a) torque curves, b) average torque and torque ripple

Breadth of rotor pole has significantly influence on the average torque and torque ripple, as it can be seen in Fig. 5.5b. The torque ripples coefficient (1.8) decreases with increasing rotor pole width up to a minimum at $t_r=12mm$. The average torque can be increased by growing breadth of stator pole up to $t_r=12…13mm$. A wider rotor pole width is practically not justified.

Worth mentioning is the fact that there exists an optimum value of rotor pole width which causes maximum energy conversion during phase band operating cycle which is assumed to be half of the rotor pole pitch τ_r, as presented in Fig. 5.6. That optimum can be found by determining maximum of the magnetic coenergy W_c:

$$W_c = \int_0^{\tau_r/2} T(\Theta) \cdot d\Theta \quad \text{[with } \Theta \text{ in rad]} \tag{5.3}$$

96

The modified motor has its maximum energy conversion capability with a rotor pole width of approximately $t_r=12mm$, which corresponds to the ratio $t_r/\tau_r=0.38$. Therefore, and in order to make the rotor pole wide slightly greater than the stator pole width to produce a 'dead zone' in the inductance profile $L(i,\Theta)$ with all it's benefits mentioned in Chapter 2.5, that value is chosen for the new rotor design.
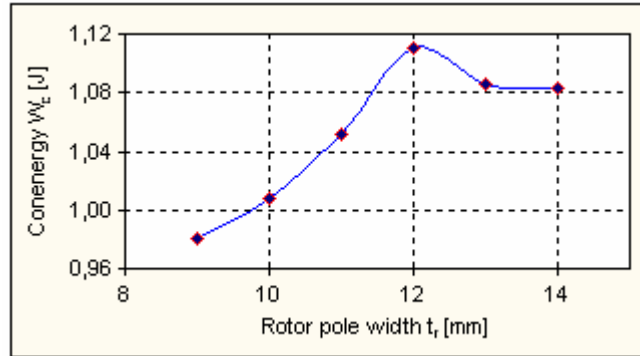

Fig. 5.6   Maximum energy conversion capability of SRM I with different rotor pole widths

Trapezoidal rotor pole shape

The magnetic flux in the rotor pole base consists of main and fringing flux components and is therefore higher than in the top of the pole. Tapering the poles (trapezoidal pole shape) avoids that the corresponding magnetisation requirement increases and magnetically 'releases' the pole base. Assuming that the mmf remains unchanged, that results in a higher flux linkage towards the aligned position, hence higher average torque and reduced torque ripples [18], [33], [159], [160]. The trapezoidal rotor pole is characterized by the pole wide at the top t_{r1}, at the base t_{r2} and the pole height h_r. Goal of the following calculations is finding the optimal rotor pole base width t_{r2} with respect to the torque ripples coefficient and average torque. The other parameters were determined in the previous calculations and remain unchanged during changing t_{r2}. The researches are carried out with changing the vector $t_{r2}=[13,14,15,16]mm$.
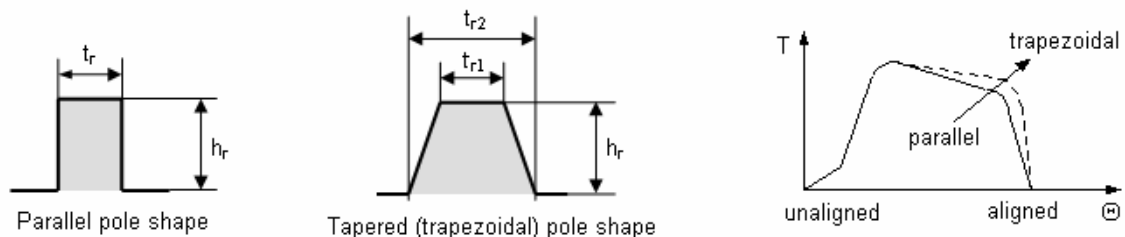

Fig. 5.7   Parallel and trapezoidal pole shapes and their influence on static torque characteristic

Making $t_{r2}>t_{r1}$ practically does not effect the maximum torque value, but the shape of torque characteristic. It is an observed fact that torque curves $T(i,\Theta)$ tend not to be flat topped and there is a maximum torque value arising very shortly after beginning of stator-rotor pole overlapping. Thereafter, as the rotor moves towards the aligned position, the torque curve declines slowly at first, and than more rapidly as the overlap increases due to increasing

saturation of stator and rotor poles. At higher excitation, also stator and rotor yokes tend to saturate. The torque decrementing can be reduced by tapering the rotor poles; hence the torque curve is flatter, especially for higher excitation current values. The wider pole base enables higher flux values at given mmf in the direction of aligned position without saturation, resulting in smoother and to average higher torque waveform. The calculations results shown in Fig. 5.8a and b agree with these considerations.
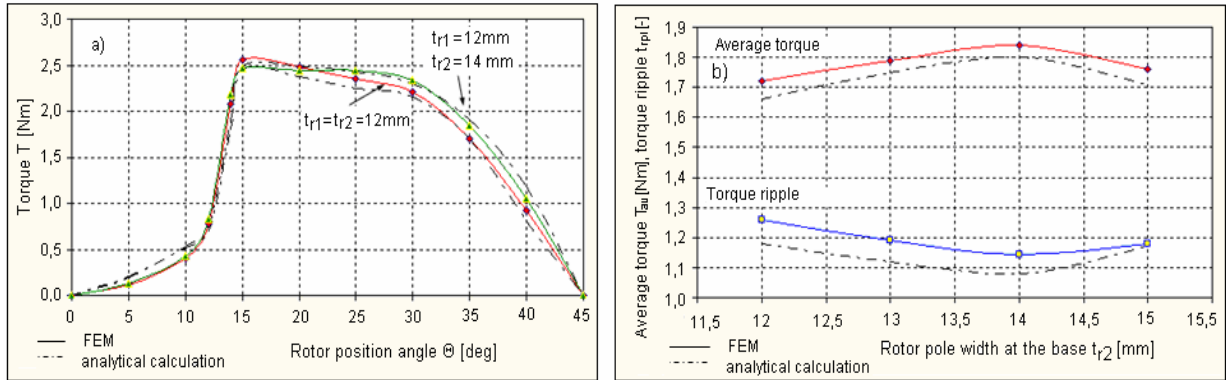

Fig. 5.8 Influence of trapezoidal rotor poles on a) torque curve b) average torque and torque ripple

A slightly increase of average torque is notable for the transition from parallel to trapezoidal pole geometry. A maximum value is found at t_{r2}=14mm. At the same time, the torque ripple can be slightly reduced. Therefore, the rotor pole width at the base is chosen to be *$t_{r2}=14mm$* corresponding to the ratio *$t_{r2}/t_{r1}=1.17$*. Finally, the obtained modified rotor geometry is presented in Fig. 5.9. Table 5.1 compares important parameter with the original rotor design. Note the good agreement of analytical calculations and numerical results obtained by FEM.
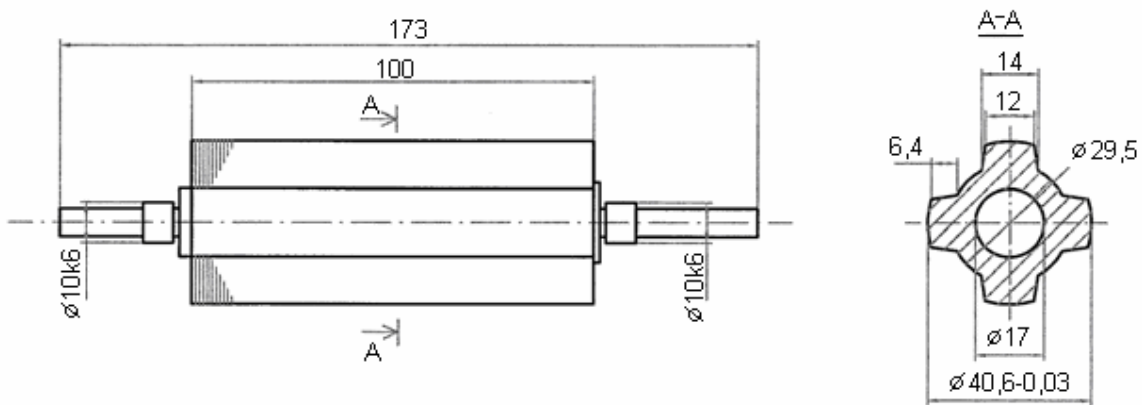
Fig. 5.9 Modified rotor design with wider and trapezoidal poles

Table 5.1 Motor parameters of the original and the new SRM I with modified rotor construction

	Symbol	Unit	Original SRM	Modified SRM	Improvement
Rotor pole width at the top	t_{r1}	mm	10.8	12	
Rotor pole width at the base	t_{r2}	mm	10.8	14	
Rotor pole height	h_r	mm	6.4	6.4	
Rotor yoke thickness	y_r	mm	5.7	6.3	
Shaft diameter	D_{sh}	mm	17	17	

Air gap length	g	mm	0.2	0.2	
Turns per phase	N_{ph}	-	180	180	
Phase current (constant value)	I	A	5.5	5.5	
Average torque by FEM (analytical calculation)	T_{av}	Nm	1.77 (1.74)	1.84 (1.81)	3.96% (4.02%)
Torque ripple coefficient by FEM (analytical calculation)	t_{rpl}	-	1.27 (1.18)	1.14 (1.08)	10.24% (8.47%)
Energy conversion capability by FEM (analytical calculation)	W_m	J	1.05 (1.03)	1.09 (1.07)	3.81% (3.88%)
Aligned inductance by FEM (analytical calculation)	L_a	mH	57.73 (56.96)	58.25 (57.48)	
Unaligned inductance by FEM (analytical calculation)	L_u	mH	8.02 (7.53)	8.72 (7.98)	

5.1.4 Simulation results

The operational behaviour of the original SRM and the motor with modified rotor pole profile was investigated by means of the SIMPLORER® simulation model proposed in Chapter 4. Following, the influence of the turn-on and turn-off angles on the average torque and torque ripple is presented for both rotor constructions. The motor operates with chopping mode; the maximum current and width of the tolerance band are constant as well as the rotor speed. The average torque and torque ripple are shown in Fig. 5.10a and b for the case of the modified rotor construction. Compared to the original motor a higher average torque can be achieved in the operational range of the phase band with effective torque generating (between 5° and 42°) due to the wider 'death zone' around the aligned position (45°) and the shift of static torque vs. angle characteristic through the unaligned position. Such a shift that reduces the slope of the T(i,Θ)-characteristics by skewing the curve towards the unaligned position has two positive effects. The first is that the phase inductance is at its maximum positive slope and therefore maximum torque when the phase is energized. The second one is that the flatter phase inductance profile near the aligned position allows a faster drop off of the commutated current, thus smaller negative torque, resulting in a higher average torque. The optimum turn-on and turn-off angle and corresponding values of torque ripple and average torque summarizes Table 5.2 for both rotor variants.
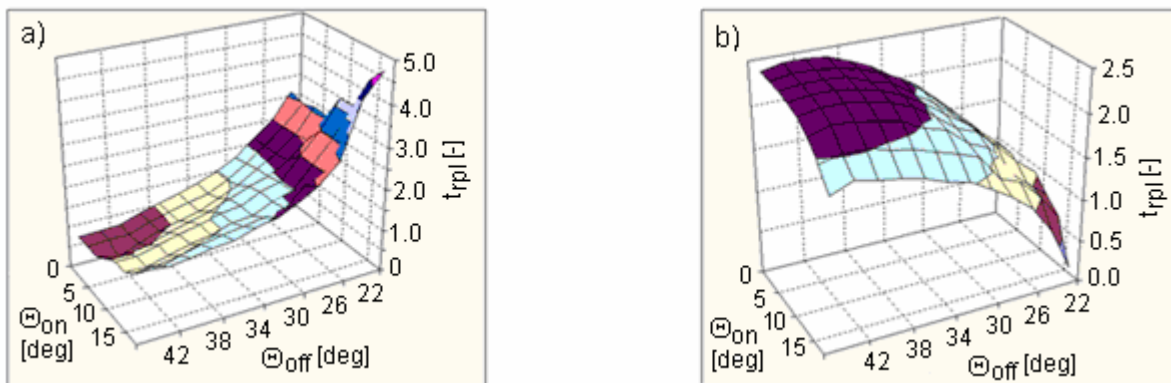

Fig. 5.10 Influence of Θ_{on} and Θ_{off} on average torque and torque ripple of modified SRM I

Table 5.2 Optimum control parameters for both rotor designs (I_{ref}=6A, n=1000rpm)

Parameter	Symbol	SRM (original)	SRM2 (modified)	Improvement
Turn-on angle	Θ_{on}	5°	2°	
Turn-off angle	Θ_{off}	40°	42°	
Average torque	T_{av}	2.31 Nm	2.42 Nm	4.8%
Torque ripple	t_{rpl}	0.75	0.71	5.3%

5.2   Prototype II: 6/4-SRM for an electric textile spindle drive

5.2.1   Introduction

Target of the research project in cooperation with the German machine building factory 'Mechanik Leisnig GmbH' and textile machine manufacture CETEX ('Chemnitzer Textilmaschinenentwicklung') gGmbH is a new innovative generation of spindle elements for twist and yarn producing machines in the textile industry. Those new spindle elements include electric single drives which shall replace the conventional belt drive systems in spinning machines where mechanic components like belts, cogwheels and gears transmit and distribute the mechanic energy from a central energy source [21], [118], [156]. The technical progress for today's spinning machines is characterized by an increase in performance, quality and ergonomics. Beside the adherence of technological requirements the electrical machines to be developed must fulfil the demand on an efficiency η≥80% in the preferred operational point, which is quiet high for small electrical machines in the desired power range. SRMs are considered for this application since the various advantages of this machine type have made them an attractive alternative to conventional induction and synchronous machines in adjustable speed drives. Particularly for the application in textile spinning machines, SRMs offer a number of advantages like

- constant speed without mechanic slip due to the synchronous operating principle,
- short end-windings since concentrated windings can be easily mounted on the stator poles; that enables short machine lengths and reduces copper material,
- low manufacturing costs in serial production,
- low moment of inertia and high starting torque and
- easy realisation of a holding torque at zero speed which is a technological need.

Fig. 5.11 shows the principle design for a single spindle drive with SRM. Table 5.3 summarizes the most important machine parameters required by the industrial user. The electric spindle drive with SRM shall fulfil the high demands by the following features:

- simple and robust construction of the SRM for an almost maintenance free machine and low manufacturing costs,
- optimum rotor design for small torque ripple, reduced air friction and noise generation,
- low losses to achieve high efficiency ≥80%,
- simple control method to reduce cost for control electronics and
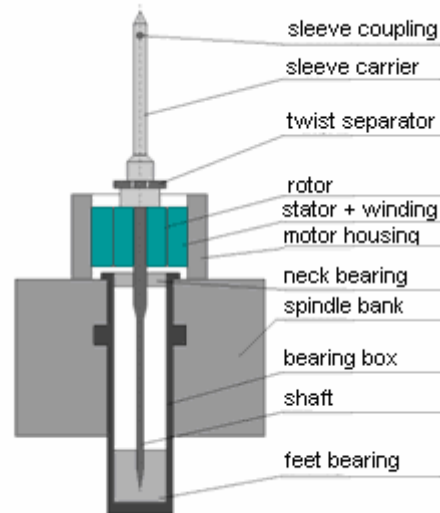- for future a sensorless control procedure to eliminate rotor position sensor

Fig. 5.11 Single textile spindle drive with SRM [118]

Table 5.3   Required spindle motor parameter and operating points

Parameter		Value
Stator outer diameter D_s		64 mm
Shaft diameter D_{sh}		21 mm
Stack length l_{stk}		25 mm
Power range		20 ... 120 W
Speed range		5000 ... 30000 /min
Moment of inertia of the load		60 ... 80 kgmm²
Operational points		
Preferred operation point	1	n = 24000 /min (T = 0.03 Nm) P = 80 W
Maximum efficiency; rated operating point	2	n = 20000 /min (T = 0.04 Nm) (P = 80 W)

5.2.2   Geometry

High efficiency is one of the most important requirements for the SRM to be developed. The motor must run with high speed up to 30000rpm. Therefore it is expected that especially core losses will dominate compared to copper losses. It is known that the magnetization frequency which influences the core losses grows with the number of phases q. Therefore q was chosen to be 3. That is the smallest possible phase number allowing self-starting in both directions and a 4-quadrant operation [8]. To minimize core- and converter losses at high speed, a 6/4-SRM was designed. That makes also a great contribution to the desired low-cost SRM drive since converter costs will be small. The stator outer diameter $D_s=64mm$ was constrained beside the restricted putting in place space for the motor into the existing spinning machine by the technological spinning process. The same is true for the shaft diameter with $D_{sh}=21mm$

and the stack length $l_{stk}=25mm$. The optimal internal stator diameter D and the stator pole width t_s were chosen with respect to

(1) high average torque and small torque ripple,

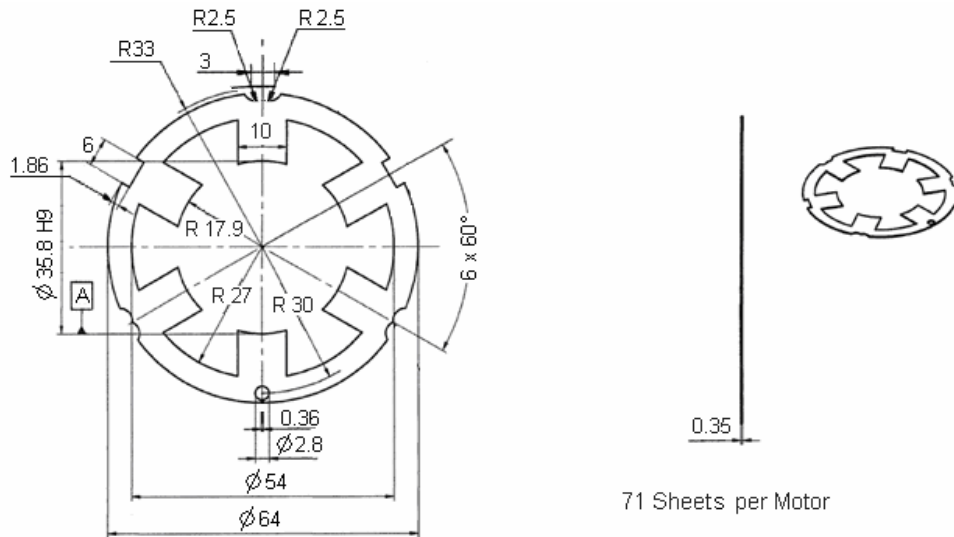(2) small copper losses and maximum current density S≤4A/mm^2

Fig. 5.12 Stator geometry of the SRM II for textile spindle drive

Meeting the first demand requires wider stator poles. On the other hand, making the stator poles to wide reduces the slot area and therefore increases the copper losses. Hence a compromise must be found in order to meet both demands. Further and more detailed calculations to the stator dimensioning can be found in a paper publication which is actually in preparation and will be published following this dissertation. The final stator geometry shows Fig. 5.12. Laminated steel is used with a thickness of 0.35mm. The core material is *M250-35A* (STAPOLIT 60). The stator pole edges are parallel for maximum winding space.

Considering researches in Chapter 2, the air gap should be chosen as small as possible, regarding technological constrains like manufacturing tolerances or deformations of the rotor because of heating or harmonic oscillations at high speed. On the other hand, the technological spinning process requires a flexible, slightly elastic bearing of the shaft in order to produce high quality textile twists and to avoid ripping of the yarn in error cases. As a result of these competing requirements the choice of the air gap is a compromise between technological and electromagnetic demands and was selected to be *g=0.35mm*.

The rotor outer diameter was chosen with the goal to produce a maximum output torque. With respect to the previous calculations of the stator geometry it is *D_r=35.1mm*. In order to find the optimum rotor pole geometry, in a first step parallel shaped poles are assumed. The shaft diameter is fixed with D_{sh}=21mm. Similarly to the rotor dimensioning of the SRM I for the vacuum cleaner proposed in Chapter 5.1, the rotor design of SRM II is determined. The results are summarized here in short form. More detailed researches can be found in [118]. The influence of constructional rotor parameter on average torque and torque ripple was

investigated. These parameter were changed in the range of rotor pole height h_r=[2,3,4]mm and rotor pole width t_r=[10,11,12,13,14]mm. Analytical calculations have been made as well as FEM calculations for comparison and to verify the different machine models. The SRM is assumed to be excited by mmf=400Amp-turns.
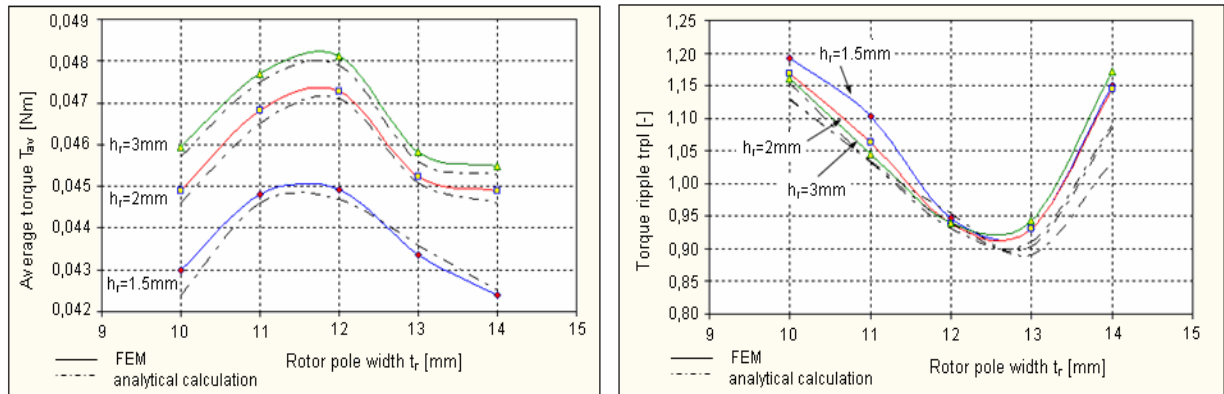

Fig. 5.13 Average torque and torque ripple of SRM II for different rotor pole widths and heights

Referring to Fig. 5.13 it is found that the optimum rotor pole parameters are *t_r=12mm* and *h_r=3mm*. Note the good agreement of the calculation results obtained by FEM and by analytical methods. That shows the high accuracy of the developed calculation procedures and mathematical models which provide quiet reliable results. The results for the first SRM version with parallel rotor poles summarizes Table 5.4 for the optimum geometric parameters.

Table 5.4   Parameter of SRM II with parallel rotor poles

Rotor pole width	Rotor pole height	Average torque	Torque ripple
12mm	3mm	0.0481 (FEM) 0.0477 (analytical)	0.947 (FEM) 0.93 (analytical)

5.2.3   *Construction modifications for noise reducing*

Reducing acoustic noise during high speed operation requires a modified rotor design which decreases the air friction and gives the poles higher mechanical stiffness. Therefore many different rotor geometries have been investigated by author which will be published in a separate paper following this thesis. As a result of these researches a new rotor geometry was found which promises the best results with respect to the average torque, torque ripple and acoustic noise. This rotor variant was manufactured by the German factory 'Mechanic Leisnig GmbH' and will be introduced shortly in the following. The idea is to increase the rotor pole width at the pole base in such a way that the rotor surface becomes more 'round' and 'smoother' compared to the conventional geometry with straight parallel poles. But note that making the rotor poles wider at the bottom increases the unaligned inductance [8] and therefore the torque producing capability of the SRM. Hence, the final rotor design is a

compromise between various competing effects like reduced average torque but decreased torque ripple and noise generation! Three important modifications have been made:

- the rotor pole width at the base is equal to the rotor pole pitch,
- the edges at the rotor pole tips are slightly rounded with a radius of r=2mm and
- the transition from the rotor pole to the rotor yoke is also rounded with r=2mm.

Fig. 5.14 presents the new rotor design with the corresponding geometric parameters. The manufactured prototype for the textile spinning machine is presented in Fig. 5.15.
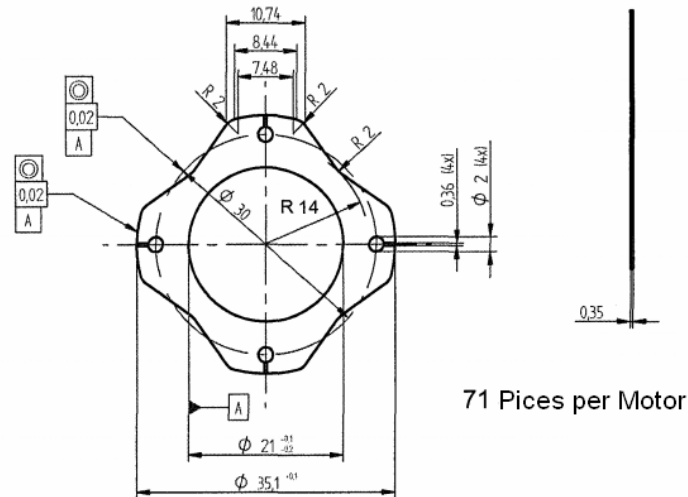

Fig. 5.14   Rotor geometry of SRM II

Fig. 5.15   Manufactured prototype of SRM II

The calculation results have shown that the torque characteristics of the new rotor geometry don't vary very wide from the first variant with parallel poles, an important positive fact to meet the demands from the industrial partner! Due to the flatter pole faces of the modified rotor construction the rate of change of torque is smaller when the stator and rotor poles start overlapping and before complete alignment. The maximum torque is slightly decreased. However, it was found that particularly the flatter rising and falling edges of the torque characteristics lead to a reduced noise generation since the radial forces on the stator and rotor poles are reduced, which agrees with investigations made by [45], [78], [160] and [175]. Further, air friction and the well known 'sirens-effect' for SRMs are reduced by a favourable aerodynamic rotor design, which was also described in [2], [26] and [27].

5.2.4   Winding design

Using equation (2.23) the slot area of the designed spindle SRM is calculated to be $A_{slot}=120mm^2$. The winding shall be designed for a dc supply voltage in the range of $V_s=150...170V$ (available dc bus voltage in the spinning machine) and a rated speed of $n_n=20000rpm$. With (2.31) the number of turns per phase is determined to be $N_{ph}=100$. Two coils of opposite stator poles are series connected. Since no particularly cooling system is desired for the application, the maximum current density of the motor is constrained on $J_{max}=4A/mm^2$ (r.m.s. value). Assuming an idealized flat-topped current, a magneto motive force of mmF=400Amp-turns is necessary to generate the rated torque of $T_n=0.04Nm$. That value is determined iteratively by analytical calculations (program "DesignSRM") and verified by FEM calculation. With $N_{ph}=100$ an (idealized) peak current value of $I_p=4A$ is required. Using equation (3.183) gives $I_{rms} \approx 2.3A$. Now, the conductor bare diameter is calculated with (2.32) to be $D_w=0.86mm$, a value of $D_w=0.9mm$ is chosen. The wire cross section assuming a lacquered round wire is $A_w=0.74mm^2$. The winding cross sectional area is then $A_{wc}=37.1mm^2$ (2.33). That requires a slot fill factor of $\varphi_{slot}=0.6$ (2.34).
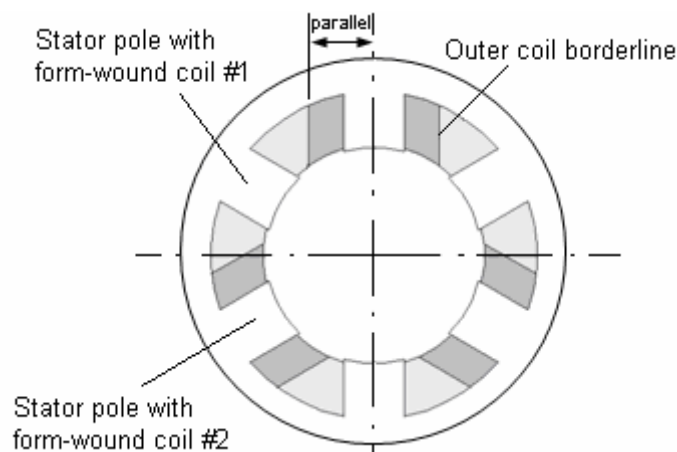

Fig. 5.16   Geometry of the stator windings of SRM II

To insert the windings into the stator slots, a winding design with two different form-wounded coils is proposed which was firstly presented in [18] for a 16/12 SRM. These coils only differ with respect to their geometry. The number of turns and the wire diameter are the same. The coils can be wounded easily with suitable wounding machines. Thereafter, firstly pre-wounded coils #1 are placed around the stator poles, followed by coils #2. The coils are alternated placed like 'wedges' on the poles. Both outer lines of coils #2 trend parallel to the pole middle. Therefore also the last coil can be placed quiet easily. If the wire diameter is relatively large, the border line between the coils has a slightly stepping form, thus, the shown straight lines between coils #1 and #2 in Fig. 5.16 must be understood as a principle course. Both coils in the slot must be isolated against each other.

5.3 Prototype III: 8/6-SRM for an automatic truck gear

5.3.1 Introduction

The inherent qualities of the SRM make it an ideal solution for an electrically assisted automotive gear for cars and trucks [23], [25]. The rotor inertia is low, allowing precise, and high-bandwidth steering control. Further, the motor has no electrical failures that can cause unwanted torque when it is in an unpowered state.

In cooperation with the German gear manufacture 'ZF Friedrichshafen AG' a SRM was developed for the use as a short-time actuator in an automatic truck gear. Fig. 5.17 shows the general arrangement of the electrical assisted gear, consisting of a choice-shaft with several blocking elements, gearwheels and the SR Motor. The gear is much like a classic rack-and-pinion assist gear except that the hydraulic assist function is replaced with a SRM.
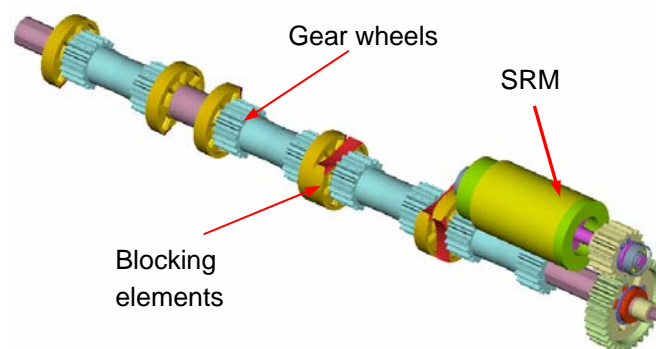
Fig. 5.17   Electrically assisted gear with SRM

The task of the SRM is to turn the tappet elements in a 6-gear shift for multiples of 45° in order to choose the lane of a selector fork. At the same time unused selector forks are blocked. Thereby a precision of 0.5° is required. A further important demand is the trouble-free adjusting process within a temperature range between -30 to 110°C which can occur in the gear. Additionally possible fluctuation of the vehicle electrical distribution system must be

regarded. Conventional servo motors, e.g. permanent excited synchronous machines (PMSM) or dc machines often require an expensive control system which leads in many cases to high costs due to a complex sensor system. Moreover that produces an additionally error source! The SRM offers similarly to stepping motors pre-defined rotor positions (aligned and unaligned), which can be easily used for an adjusting process. Target of the researches is to develop a suitable SRM design for the desired automotive gear within the frame work of the research project [119]. The outer dimensions are constrained by the application, and the generated torque must be maximised. Further, material demand and manufacturing costs in serial production have to be as small as possible. Efficiency plays a secondary role.

5.3.2 Motor design

Essential criteria for an optimized rotor design with maximum torque output are:
- core material with high saturation flux-density,
- operating in a saturated regime to maximise the utilization of the magnetic circuit,
- N_s/N_r-combination providing a smooth torque characteristic and low torque ripple

With respect to manufacturing costs, robustness and positional accuracy, a 4-phase SRM with 8 stator poles and 6 rotor poles was chosen with a rated speed of n_n=1000rpm and a rated torque of T_n=1Nm. Fig. 5.18 shows the cross section of the developed motor geometry. It was found that the 8/6-SRM has several advantages compared to a 6/4-machine with respect to the torque characteristic for the desired application [28], [119]. Higher core losses due to the higher switching frequency are marginal for this application since the motor works in short-time operation mode with only 1000rpm.
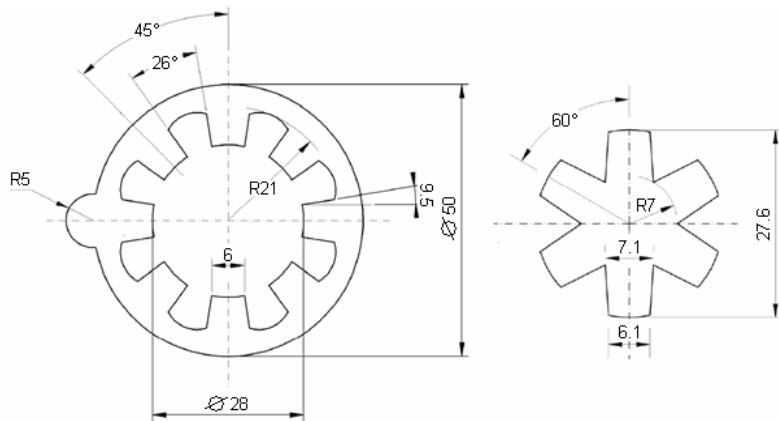

Fig. 5.18 Geometry of the 8/6-SRM for automatic gear application

The geometric parameters of the developed machine design are:
- large rotor outer diameter for maximum torque output,
- air gap g=0.2mm,
- stack length l_{stk}=50mm; core material of the stator laminations: M400
- trapezoidal stator and rotor pole profiles to reduce saturation effects and torque ripples,

- larger radius in the stator slots to increase the winding area,

- massive rotor design without laminations; rotor material: 430 Stainless Steel

Fig. 5.19   8/6-SRM III for automatic truck gear, manufactured by the ZF Friedrichshafen AG

The vehicle electrical distribution system voltage is V_s=24V. Concerning the specific application area of the SRM in a truck gear, a 'worst-case' voltage of V_s=18V must be assumed since voltage fluctuations in the board net can occur. For mounting the winding a 'coil-body' is used on which the stator laminations are pushed on. That is shown on the right-hand side of Fig. 5.19. The number of turns per phase (series connected) is chosen with respect to equation (2.31) to be N_{ph}=40. The wire diameter is D_w=0.45mm.

5.3.3   Calculation results

At first, the electromagnetic torque is presented as a function of the rotor position angle for different current values. It can be seen in Fig. 5.20 that the desired value of approx. T=1Nm can be achieved with a current of I=40A. *The greatest contribution to increase the torque producing capability is making a larger radius in the stator slots to increase the winding area.* Of course, that leads to a higher flux density in the stator core where the radius is increased (see Fig. 5.22) and therefore higher core losses and local heat sources, but since the motor just works in short time operation the heating is controllable, as laboratory tests have shown [119]. Another critical fact could be the high current level of I=40A, leading to high current density in the windings. But note, the phase is energized very short with that high current value. Since a heat resistant coil body of PA66 (Polyamid) is used, the heating of the winding is acceptable and will not destroy the machine, as it was proven by measurements [119]. The developed torque is nearly constant in the range between 6 and 25° up to a current of approximately I=10A. For higher current values, the iron starts to saturate, which leads to a stronger decrease of the torque characteristic towards the aligned position (Θ=30°). Note, in order to achieve an acceptable torque waveform for high currents, the firing angles of the phase currents must be adjusted carefully.

The effect of saturation can be seen obviously in the flux-linkage vs. current characteristics for different rotor position angles, presented in Fig. 5.21a. Up to 10A the SRM operates in the

linear range. For higher current values, iron saturation occurs with an increasing stator-rotor pole overlapping.
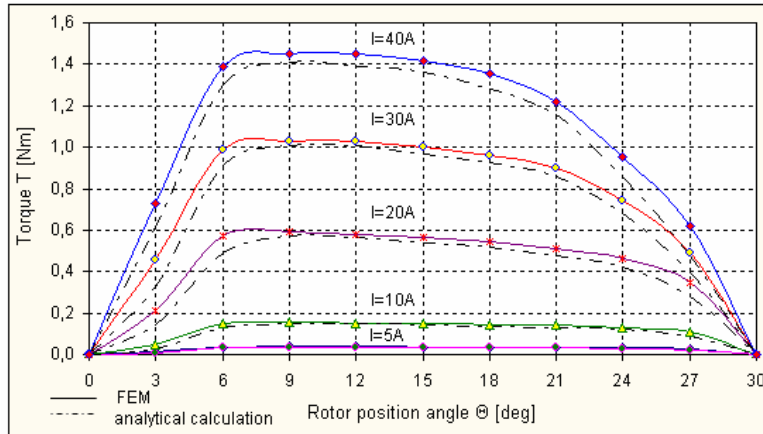
Fig. 5.20   Torque characteristics of the gear SRMIII for different current values

Fig. 5.21b shows the phase inductance vs. rotor position angle for different current values. Note the good agreement of the analytical calculated values with that obtained by FEM.

Fig. 5.21   a) $\psi(i,\Theta)$-characteristics and b) $L(i,\Theta)$-characteristics of the gear SRM III

The distribution of the magnetic field is shown in Fig. 5.22 for the aligned position with maximum current I=40A. The motor operates here in high saturation regime.

Fig. 5.22   Field distribution and flux-density of SRM III for I=40A (FEM calculation)

6 Experimental verification

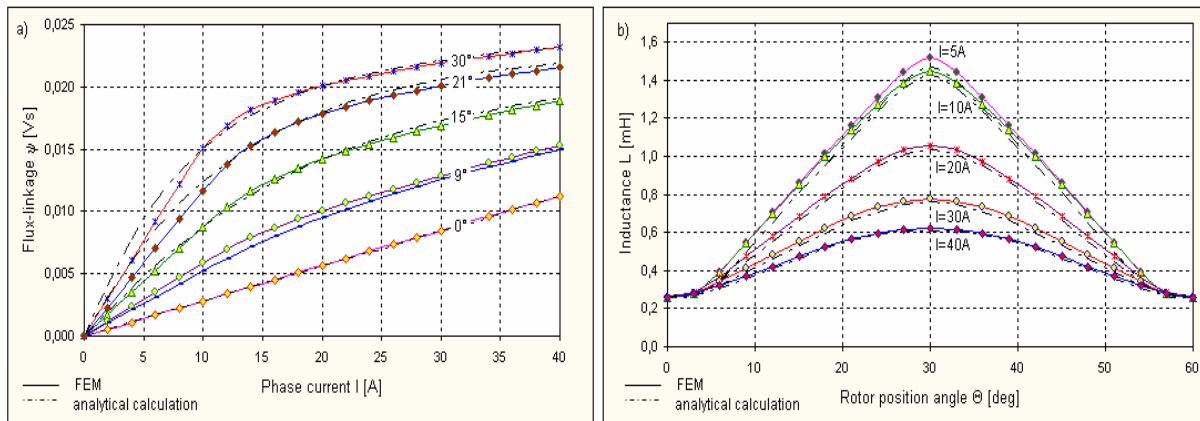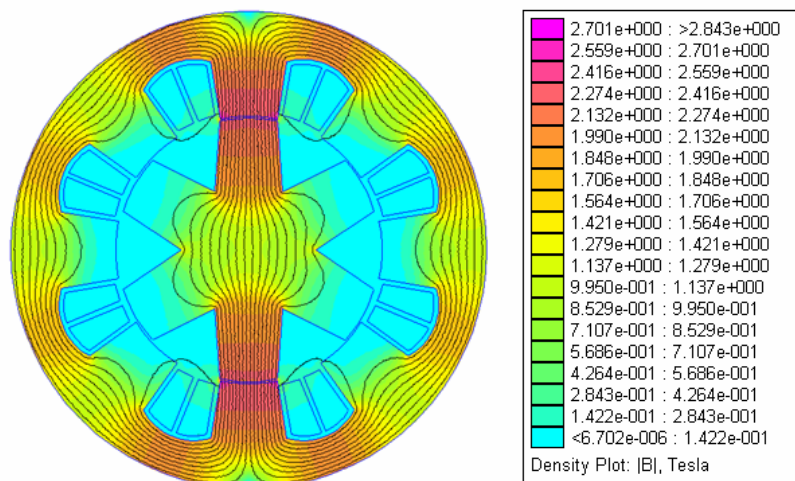To verify the developed design- and calculation methods for SRMs proposed in this thesis, experimental results of the three manufactured prototypes are necessary. The measurement results are therefore compared to the analytical and finite element analysis predictions.

6.1 Comparative laboratory tests of SRM prototype I with original and modified rotor

The laboratory tests of SRM prototype I for the use in vacuum cleaners are divided into two parts. Firstly, characteristics of the original motor were measured. Thereafter, the measurements have been repeated for SRM I with the new modified rotor geometry. The results are compared in order to research the influence of constructional rotor parameters on steady-state and performance parameters and to verify the previous calculations.

6.1.1 Inductance measurement with 50Hz method

Due to the non-linear operation and doubly salient structure of SRMs, the inductance profile is a function of both the rotor position and excitation current. That makes the measurement of this parameter difficult. Various techniques are known in bibliography for measuring the SRM inductance for any rotor position and level of excitation [63], [83], [114], [154], [165]. A simple and efficient procedure to measure $L(i,\Theta)$-characteristics is the '50Hz method'. The corresponding experimental setup shows Fig. 6.1.
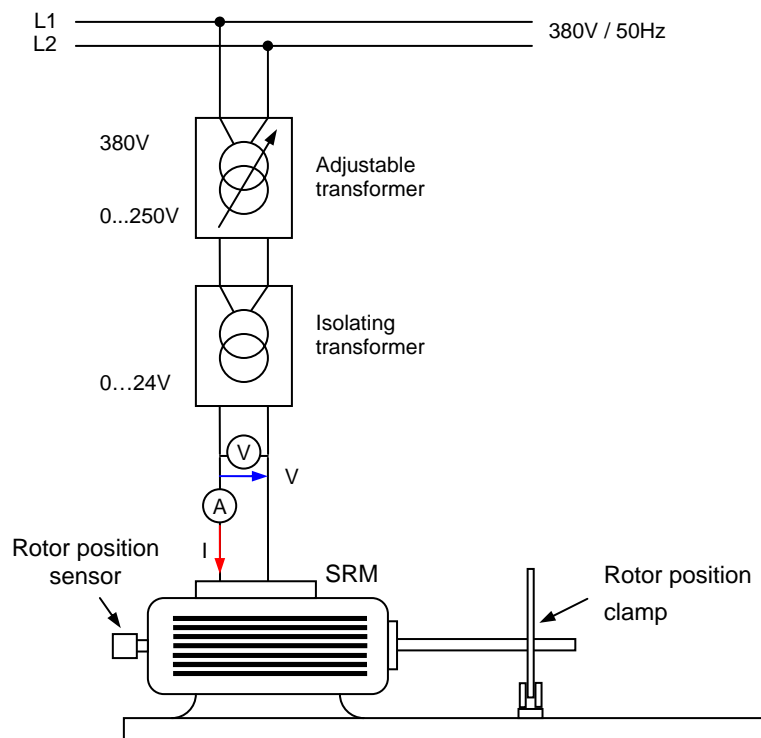

Fig. 6.1 Experimental setup for measuring $L(i,\Theta)$-characteristics with 50Hz method (TUW)

110

The measurement sequence is as follows. The rotor is fixed to the desired rotor position angle by mechanical means, the phase winding is energized with a 50Hz excitation current. The r.m.s. value of the phase voltage V and current I are measured simultaneously (Fig. 6.1). Knowing the (warm) phase resistance R, the phase inductance is obtained with

$$L(I,\Theta) = \sqrt{\left.\frac{\left(\frac{V}{I}\right)^2 - R^2}{2\pi \cdot f}\right|_{\Theta=const}} \qquad \text{with f=50Hz and R=1.44}\Omega \qquad (6.1)$$

The r.m.s value of the sinusoidal 50Hz voltage is adjusted manually with the transformer to maintain a constant current I for various rotor position angles. The measurements were repeated for both rotor variants within a current range of I=[1...6]A and a rotor position angle of Θ=[0...90]°. Fig. 6.2a and b present the measurement results for the original and modified SRM I, respectively. For comparison, the predicted results obtained by analytical calculations with the method proposed in this thesis are shown with broken lines.
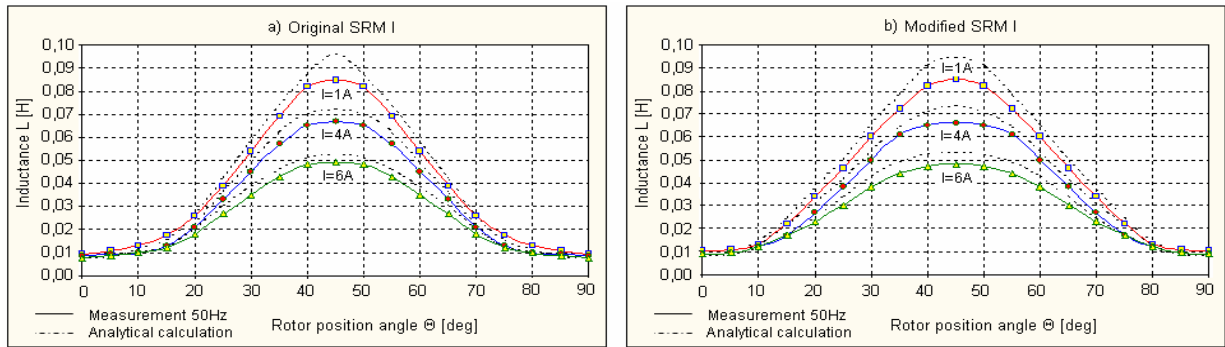
Fig. 6.2 Predicted and measured L(i,Θ) curves with 50HZ for SRM I: a) original, b) modified rotor

The measured inductance values are smaller than the predicted ones. Obviously, measuring the r.m.s. values of current and voltage and calculating the inductance with (6.1) leads to considerable mistakes due to two reasons.

(1) Equation (6.1) is obtained from the general theory of a.c. current which is valid only for sinusoidal values. For distorted non-sinusoidal measured values with many harmonics, (6.1) should be applied on each harmonic. This is obviously not very useful. The inductance calculation only for the 50Hz- fundamental harmonic gives a wrong result.

(2) For r.m.s. measurements the measured values are quadratic-weighted and integrated over one period. Therefore, r.m.s. measurements of non-sinusoidal values including many harmonics yield to results which can differ in a wide range in dependence of the 'degree' of distortion, even if the fundamental harmonic is equal.

As a consequence, the inductance should be measured additionally by an alternative method for comparison which concerns the non-linear magnetisation characteristics of the SRM. Such a feature offers the dynamic di/dt method proposed in the following.

6.1.2   Measurement of dynamic inductance

The rotor is fixed to the desired angle by mechanical means. A rectangular voltage pulse energizes the phase winding. The resulting current waveform and its rate of rise di/dt in the coil depend beside the phase resistance R on the inductance L(i,Θ). The corresponding experimental setup presents Fig. 6.3. Instead of the pulse generator and inverter also a simple mechanical switch can be used to connect and disconnect a phase winding with the dc-link. Rearranging the voltage equation gives an expression for the phase inductance:

$$L(i,\Theta) = (V - Ri) \cdot \frac{dt}{di}\bigg|_{\Theta=const.} \tag{6.2}$$

Important measurement devices:

- 2-channel oscilloscope HP5460 A
- Position sensor RENISHAW RE36 encoder
- DC Supply MERATRONIC TYPE P322 (rectifier)
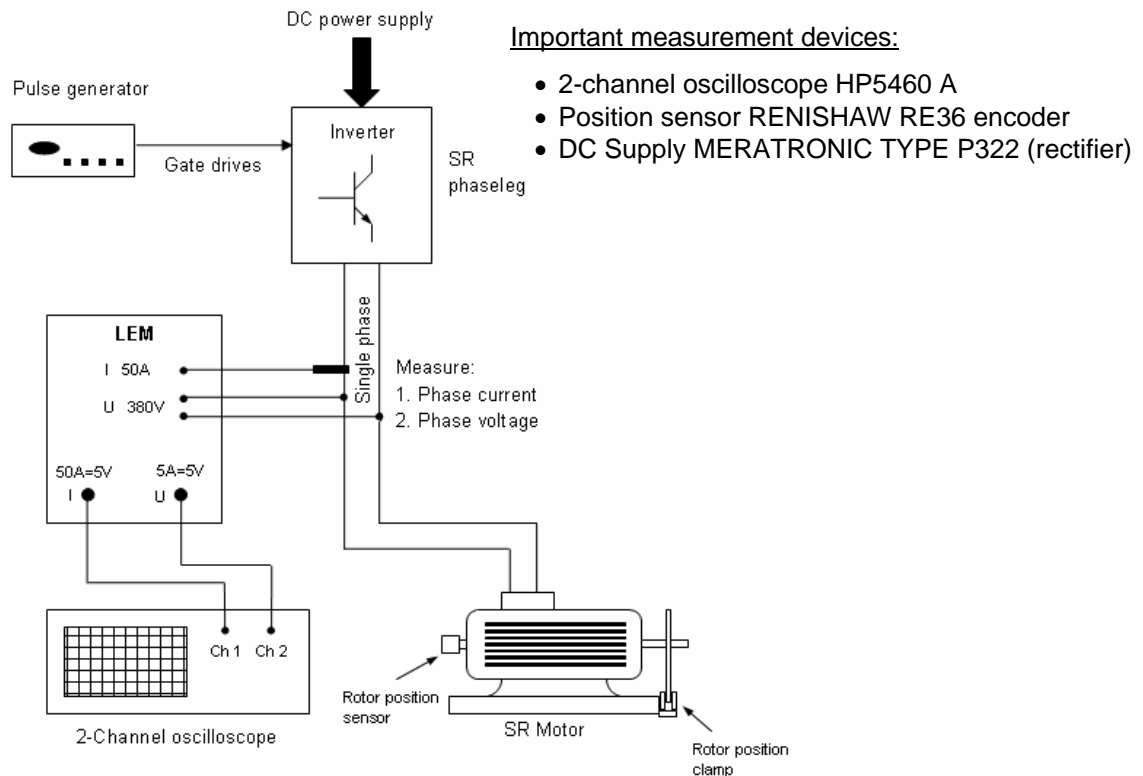
Fig. 6.3   Experimental setup for measuring L(i,Θ)-characteristics with di/dt method

When the desired maximum current is achieved, the voltage pulse is turned off. By the evaluation of the current rate of change di/dt the complete inductance characteristic can be obtained for the winding with only one single measurement at a fixed rotor position angle. The influence of the extremely non-linear magnetisation characteristics of the core material on the inductance is considered by calculating the differential inductance for each discrete time step Δt. The measured inductance as a function of rotor position angle for different current level is shown in Fig. 6.4. Compared to Fig. 6.2, only in the range of unaligned position when saturation is negligible, the 50Hz method gives accurate results. In the near of aligned position the error increases since saturation occurs. The difference for inductance values in the aligned position is in the range of 10-20%. The dynamic inductance can be

measured very well and the results confirm with the predicted characteristics. The error for aligned position is less than 6% for both FEM and analytical calculation. In the unaligned position, the maximum errors are 16% and 10%, respectively (see also Table 6.1).
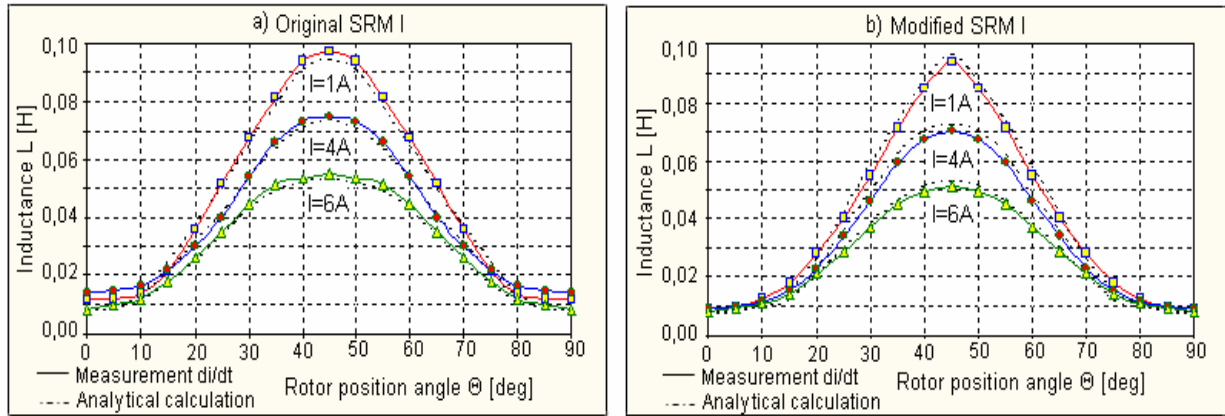

Fig. 6.4 Dynamic inductance profiles predicted and measured for: a) original, b) modified SRM

Table 6.1 Comparison of measured and predicted inductance values for SRMI

		I=2A				I=6A			
	Inductance	Analytical calculation	FEM	Measurement 50Hz	Measurement di/dt	Analytical calculation	FEM	Measurement 50Hz	Measurement di/dt
original SRM	aligned	96,1mH	99,1mH	85,2mH	95,3mH	52,2mH	53,7mH	49,3mH	51,3mH
	unaligned	7,64mH	8,2mH	9,5mH	9,1mH	7,24mH	8,3mH	7,5mH	8,1mH
modified SRM	aligned	94,5mH	96,2mH	77,1mH	96,1mH	53,1mH	54,2mH	48,4mH	55,2mH
	unaligned	8,3mH	8,8mH	10,2mH	9,4mH	7,5mH	8,7mH	8,9mH	8,3mH

6.1.3   *Measurement of characteristics torque vs. angle*

The test setup used to measure the torque characteristics as a function of current and rotor position angle consists of the SRM, a rotor clamping and positioning device, the rotor position sensor, a mechanical lever arm, a digital balance, a variable ac voltage source and a rectifier. As shown in Fig. 6.5, the motor clamping and positioning device consists of a rack wheel with an adjusting screw, attached to the motor's shaft. This arrangement is used for fixing the rotor position to a desired angle, measured by the rotor position sensor. Note that the rotor positioning device must be carefully designed and assembled so that errors in rotor position are minimized. In addition, the clamping by the rack wheel and adjusting screw must be strong enough to hold the rotor through the impulse torque, attempting to align the rotor pole with the nearest excited stator pole, when current is applied. The dc-breaker is turned off for that measurement. The generated torque is transmitted by the lever arm which presses on the digital weight. By measuring the weight m_l, the corresponding torque can be determined as:

$$T(i,\Theta) = m_l \cdot a \cdot l_l \big|_{i=const} \tag{6.3}$$

where l_l is the length of the lever arm and a is the gravity ($a=9.81 m/s^2$).
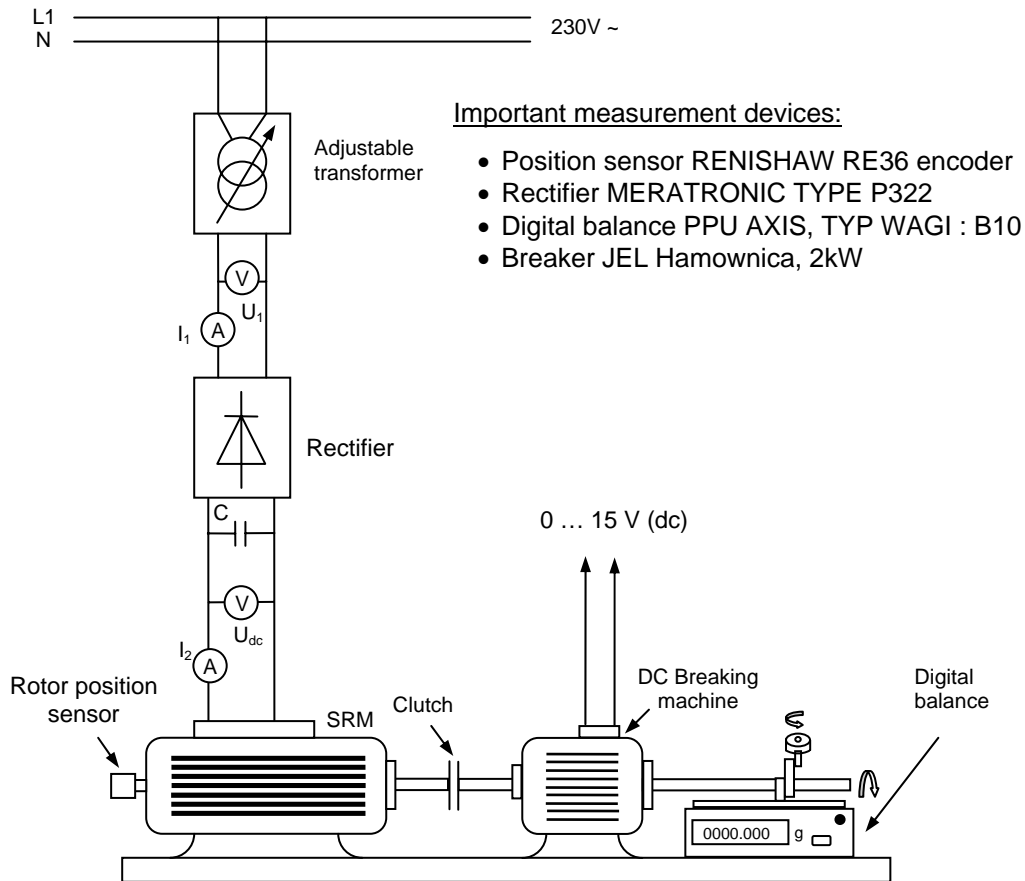
Fig. 6.5   Experimental setup for measuring $T(i,\Theta)$-characteristics

Fig. 6.6 shows a photo of the corresponding laboratory test arrangement for static torque measuring. It is recorded in the laboratory of the University of Technology in Warsaw.
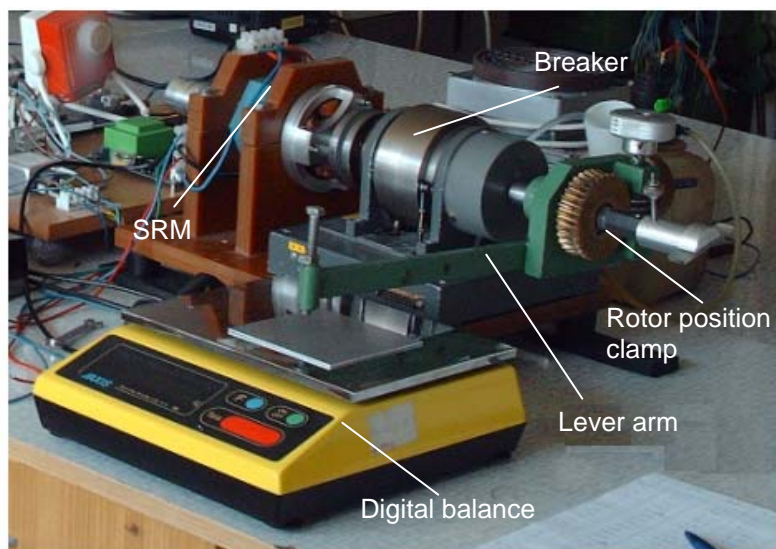
Fig. 6.6   Photography of the laboratory test arrangement for torque measurement of the SRM

The measured torque characteristics for different current values are presented in Fig. 6.7a and b for the original and the modified SRM I, respectively. The effect of the trapezoidal rotor pole profile on torque can be seen impressively.
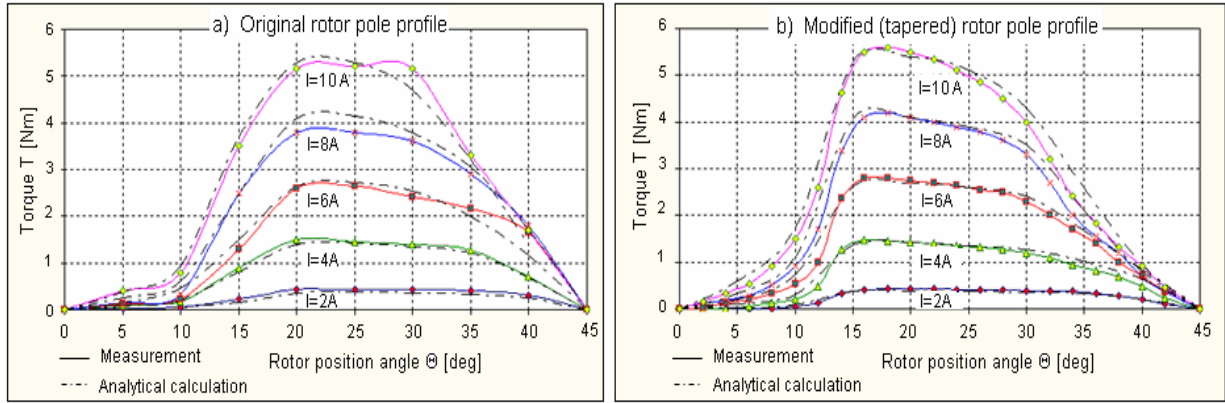
Fig. 6.7 Comparison of predicted and measured T(i,Θ)-characteristics for SRM I: a) original (parallel) and b) modified (trapezoidal) rotor pole profile

As predicted, the torque characteristic of the modified SRM I is shifted toward the unaligned position. The maximum torque values are nearly the same for both rotor constructions. However, the higher torque towards the unaligned position and the smaller torque near the aligned position are beneficial with respect to the average torque and torque ripple during common angle controlled operation as it will be shown below in Chapter 6.1.4.

Table 6.2 Measured and calculated torque parameter for both variants of SRM I

|		I=6A			I=10A		
		analytical calculation	FEM	Measurement	analytical calculation	FEM	Measurement
Original SRM I	Average torque [Nm]	1.71Nm	1.69Nm	1.64Nm	3.11Nm	3.27Nm	3.15Nm
	Torque ripple [-]	1.55	1.59	1.54	1.57	1.62	1.52
Modified SRM I	Average torque [Nm]	1.74Nm	1.77Nm	1.79Nm	3.24Nm	3.34Nm	3.37Nm
	Torque ripple [-]	1.45	1.51	1.56	1.51	1.54	1.49

Table 6.2 summarizes the most important torque parameters for both motor variants and compares with analytical calculation results. The measured average torque is increased with the trapezoidal rotor pole design for about 9% with I=6A and 6.9% with I=10A. At the same time the torque ripple (1.8) is reduced for 1.3% and 1.97%, respectively. The results show that with relative small changes in the rotor geometry the torque characteristics can be considerably improved. The pre-calculated values match very well with the measurements, the difference for average torque and torque ripple is in the range of 5-10%.

6.1.4   Measurement of characteristics speed vs. torque

The speed-torque characteristics have been measured for SRM I with both rotor pole profiles as a function of the turn-on and turn-off angle of the phase currents. The experimental setup is shown in Fig. 6.8 and consists of a variable ac voltage source (1-phase mains, adjustable transformer and isolating transformer), a rectifier, a dc link, a transistor C-Dump converter, the SRM with rotor position sensor, control electronics, driver for the power electronic

devices, and a dc breaker coupled with the SRM at the shaft via a clutch. The breaking torque is proportional to the dc-supply voltage of the breaker. The turn-on and turn-off angle of the current can be manually adjusted by the user as well as the current level for hysteresis control.
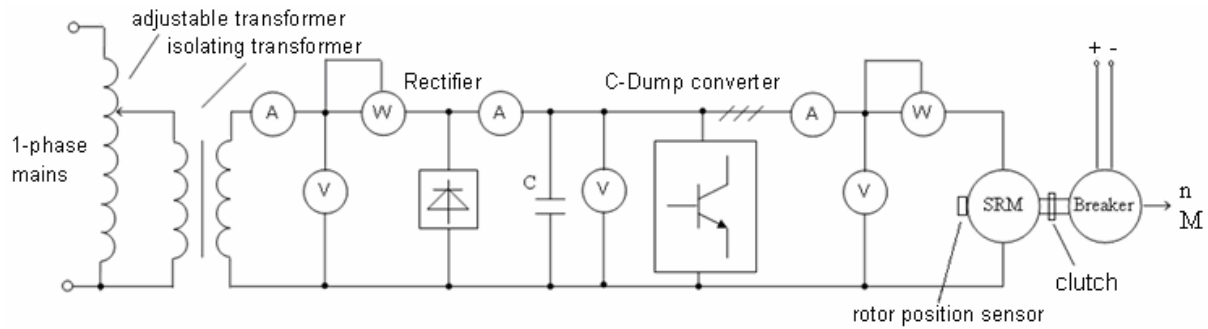
Fig. 6.8   Experimental setup for measuring speed-torque-characteristics

The measured T-n-characteristics for different turn-on angles of both the original and modified SRM with trapezoidal and wider rotor poles are shown in Fig. 6.9. The turn-off angles were chosen to be 38° and 42°. The Maximum current value was chosen to be I_{max}=4A with a dc supply voltage of V_s=400V. Generally, for the same torque, the turn-on and turn-off angle must be preceded for some degree in order to energize the phase winding in an area of low inductance and to give the commutating current enough time for decaying to zero before the rotor passes the aligned position, which would generate negative torque. Note, the back-emf increases in proportion with the speed and embarrasses the current feeding of the SRM!
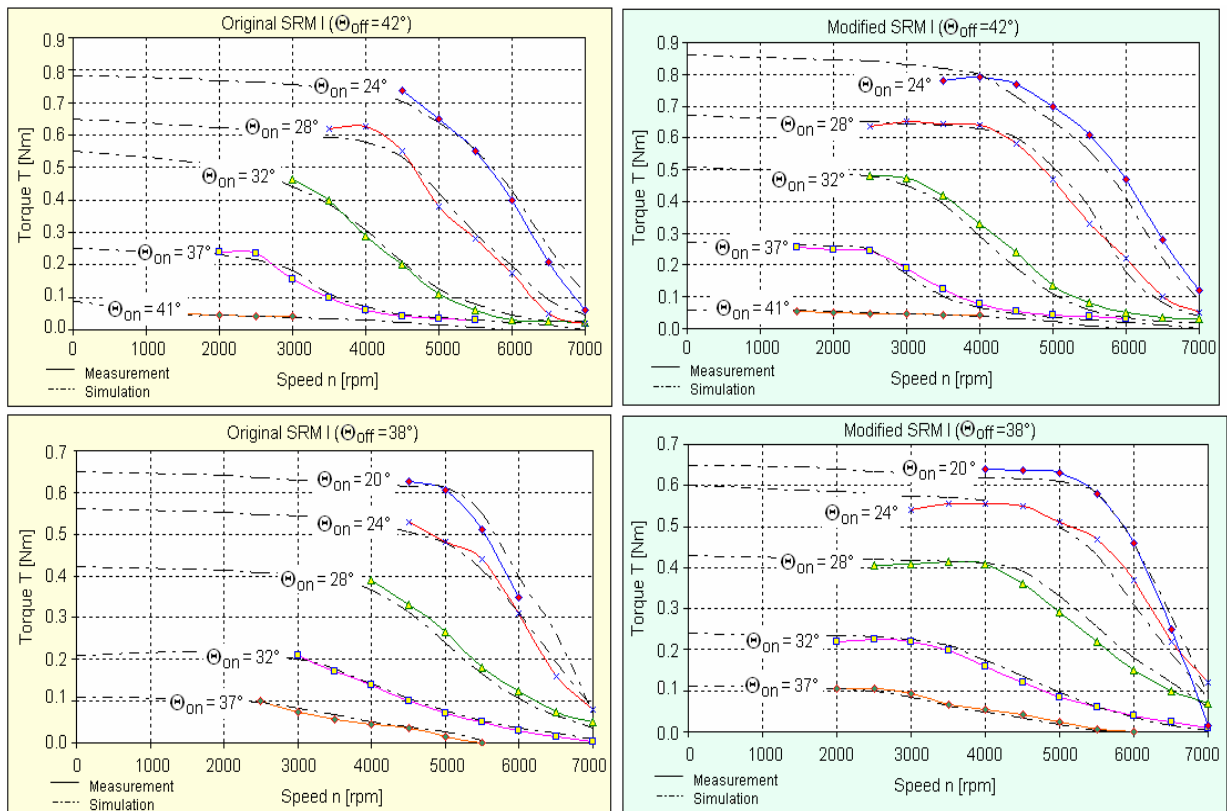
Fig. 6.9   Measured and simulated speed-torque-characteristics of original and modified SRM I for different turn-on and turn-off angles

116

In comparison to the original motor, the SRM with the modified rotor construction achieves a slightly higher torque for the same speed since the turn-on can occur earlier and the turn-off occurs later without negative torque production. That results from the modified inductance and torque characteristics by the new rotor design, as described in Chapter 5.1.

The measured maximum speed is limited to n_{max}=7000rpm due to the speed limit of the dc breaking machine and the switching frequency of the controller. The minimum measured speed is constrained by torque ripples which strongly increase at low speed. For the sake of comparison, the simulated speed-torque-characteristics are shown with dotted lines. These simulation results have been obtained by means of the SIMPLORER® simulation model introduced in Chapter 4. The measurements confirm the preliminary considerations that with the trapezoidal rotor pole profile the average torque can be increased and the torque ripple reduced. That could be physically realized by an obviously smoother operation of the entire drive system and a reduced audible noise level. Table 6.3 summarizes the measurement results for both motor variants. The values given in brackets are simulation results.

Table 6.3 n-T- parameter of the original and modified SRM I (measurement and simulation)

speed n	Θ_{on}	Average torque T_{av} for Θ_{off}=42°		Average torque T_{av} for Θ_{off}=38°	
		original SRM I	modified SRM I	original SRM I	modified SRM I
4000rpm	24°	0.73 (0.71)Nm	0.79 (0.81)Nm	0.49 (0.52)Nm	0.56 (0.57)Nm
	28°	0.63 (0.58)Nm	0.64 (0.63)Nm	0.39 (0.37)Nm	0.41 (0.42)Nm
	37°	0.06 (0.073)Nm	0.069 (0.075)Nm	0.045 (0.05)Nm	0.055 (0.049)Nm
5000rpm	24°	0.65 (0.63)Nm	0.7 (0.65)Nm	0.48 (0.47)Nm	0.51 (0.5)Nm
	28°	0.38 (0.42)Nm	0.47 (0.51)Nm	0.27 (0.24)Nm	0.29 (0.33)Nm
	37°	0.03 (0.04)Nm	0.042 (0.037)Nm	0.016 (0.025)Nm	0.025 (0.018)Nm
7000rpm	24°	0.06 (0.08)Nm	0.12 (0.09)Nm	0.08 (0.083)Nm	0.12 (0.08)Nm
	28°	0.02 (0.045)Nm	0.05 (0.04)Nm	0.05 (0.035)Nm	0.07 (0.06)Nm

6.2 Laboratory tests of SRM prototype II for textile spindle drive

The prototype of the 6/4-SRM II for the use as a textile spindle drive was measured similarly SRM I in the laboratory of the Warsaw University of Technology. Goal of measurements was to verify first principle functionalities and predicted operational steady state characteristics:

- characteristics inductance vs. angle for different current values L(i,Θ),
- characteristics torque vs. angle for different current values T(i,Θ),
- core- and copper losses,
- motor efficiency and
- torque-speed-characteristics.

More complex measurements concerning the operational behaviour during high speed dynamics, e.g. noise measurements and mechanical rotor stress will follow in future researches. Fig. 6.10 shows a photo of the experimental setup with SRM II on the test bench.
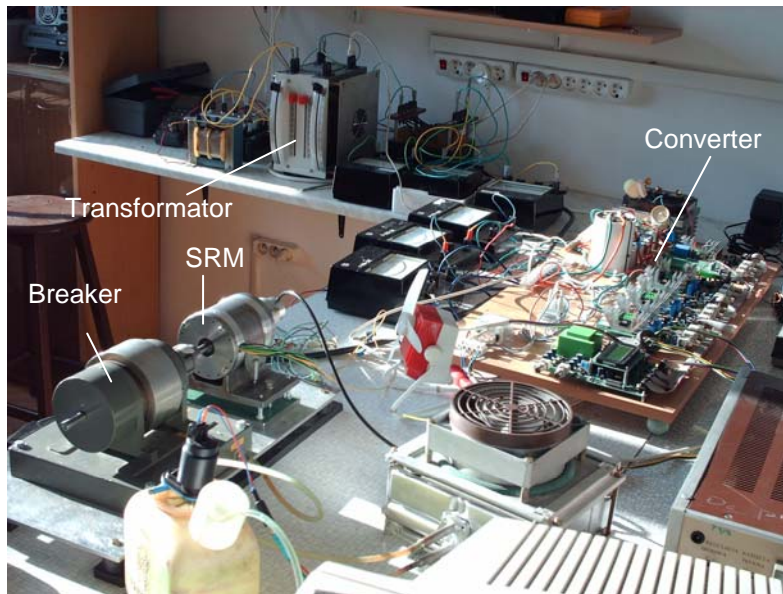
Fig. 6.10 Photo of the test bench with SRM II in the laboratory of the TU Warsaw

6.2.1 *Measurement of characteristics inductance vs. angle*

It was found in Chapter 6.1.2 that measuring dynamic inductance gives more accurate results compared to the 50Hz-method. Therefore, the inductance characteristics of SRM II have been measured by the same way using the identical experimental setup shown in Fig. 6.3. The results are presented in Fig. 6.11. The errors between analytically predicted and measured inductance values for I=2A are 3.9% and 10.3% for aligned and unaligned inductance, respectively. The error increases with current up to 5.3% and 13.6% for I=6A since saturation and end winding effects occur. However, in general, it is found that calculation results match very well with the measurements in the entire researched current range which emphases the high accuracy of the developed calculation models. Table 6.4 summarizes the results for the inductance measurement of SRM II. The values in brackets are the calculation errors.

Fig. 6.11 Comparison of predicted and measured inductance characteristics L(i,Θ) for SRM II

118

Table 6.4 Predicted and measured inductance values for different current levels of SRM II

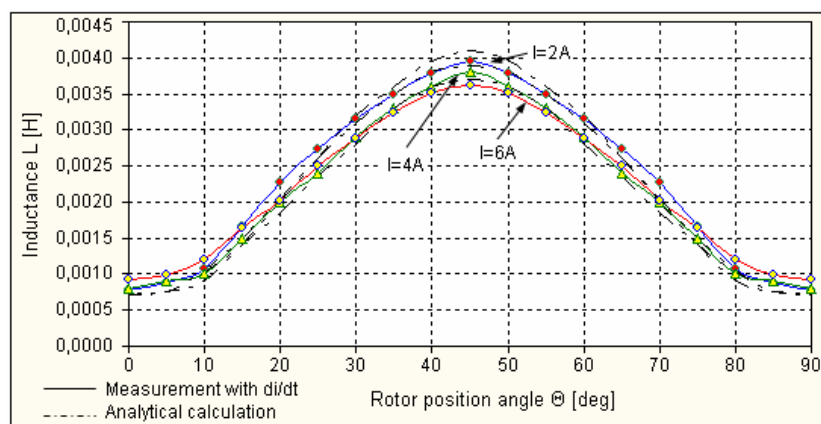|	I=2A			I=6A		
	Measurement	Analytical	FEM	Measurement	Analytical	FEM
Aligned inductance L_a [mH]	3.87	4.02 (3.9%)	3.98 (2.8%)	3.62	3.81 (5.3%)	3.73 (3,0%)
Unaligned inductance L_u [mH]	0.78	0.7 (10.3%)	0.83 (6.4%)	0.88	0.76 (13.6%)	0.94 (6.8%)

6.2.2   *Measurement of characteristics torque vs. angle*

To measure $T(i,\Theta)$-characteristics of SRM II, the same test setup as shown in Fig. 6.5 has been used. The researched current range was between I=[1…10]A. Fig. 6.12 presents the measured torque characteristics compared with the analytically calculated ones. The measured and predicted values match very well. The error between them slightly increases with the current level since the saturation effect leads to a stronger decrease of torque then predicted. Particularly the narrow rotor yoke saturates even at low currents (5-6A) what influences the calculation accuracy.
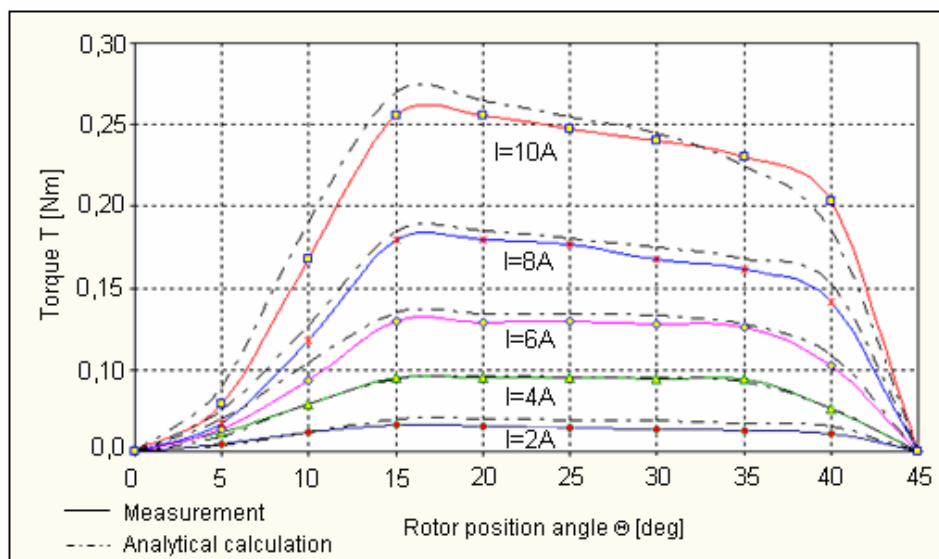
Fig. 6.12 Comparison of predicted and measured torque characteristics $T(i,\Theta)$ for SRM II

Table 6.5 summarizes the measured and calculated average torque and torque ripple values for SRM II. The values in brackets represent the calculation error.

Table 6.5 Predicted and measured torque parameter for SRM II

	I=4A			I=10A		
	Measurement	Analytical	FEM	Measurement	Analytical	FEM
Average torque T_{av}	0.043Nm	0.047Nm (9.3%)	0.045Nm (4.7%)	0.17Nm	0.19Nm (11.7%)	0.16Nm (6.8%)
Torque ripple t_{rpl}	0.92	0.86 (6.5%)	0.89 (3.3%)	1.1	1.01 (8.2%)	1.14 (3.6%)

6.2.3   *Measurement of characteristics speed vs. torque*

According to SRM I, the speed-torque characteristics of SRM II were measured using the test equipment shown in Fig. 6.8. The maximum current value, firing angles of phase current and dc-link voltage can be adjusted. Firstly, the idle speed was measured under the condition of various turn-on and turn-off angles. The dc-link voltage was chosen to be V_s=100V; the maximum current is I_{max}=4A. It was found that the maximum speed is limited to approx. n_{max}=7200rpm, which is constrained by four major facts of the actual test bench:

- maximum speed of the dc breaking machine,
- clock frequency of the controller,
- maximum permissible current and voltage of the power electronic devices and
- maximum dc link voltage constrained by the intermediate circuit capacitor.

However, the achieved maximum speed is sufficient to investigate performance parameters as well as losses and efficiency. As it can be seen in Fig. 6.13, the optimum firing angles for high speed are Θ_{on}=22° and Θ_{off}=31° which gives the current enough time for rising and decaying without negative torque production. Up to 3000rpm the controller works in chopping mode with the given dc-link voltage (hysteresis control of maximum current); for higher speed the motor operates in single pulse mode.
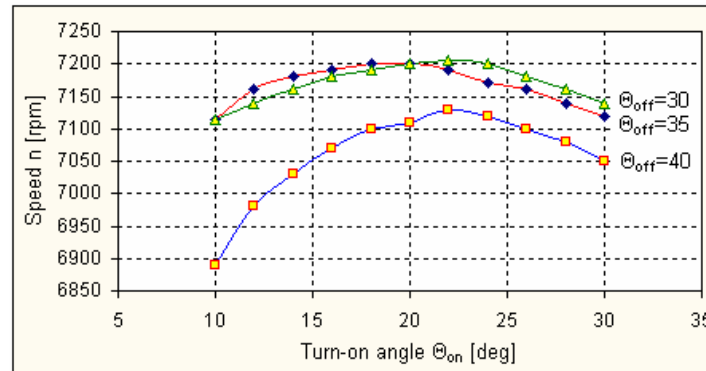
Fig. 6.13 Measured idle speed of SRM II as a function of current turn-on and turn-off angle

The measured speed-torque characteristics of SRM II are presented in Fig. 6.14. The dc-link voltage remains unchanged as well as the maximum current level compared to the idle run. For comparison, the required torque-speed characteristic from the spindle application is shown with broken lines. Within the researched speed range the motor fulfils the industrial demands. The produced torque increases with the dwell-angle, i.e. as earlier the phase is energized and as later the phase current is commutated, as higher is the torque for a given speed. On the other hand, at high speed, the turn-off angle of current must be preceded for some degrees to avoid negative torque production. Derived from measuring results, the optimum firing angles within the investigated torque-speed range to produce maximum torque are Θ_{on}=10° and Θ_{off}=35°.
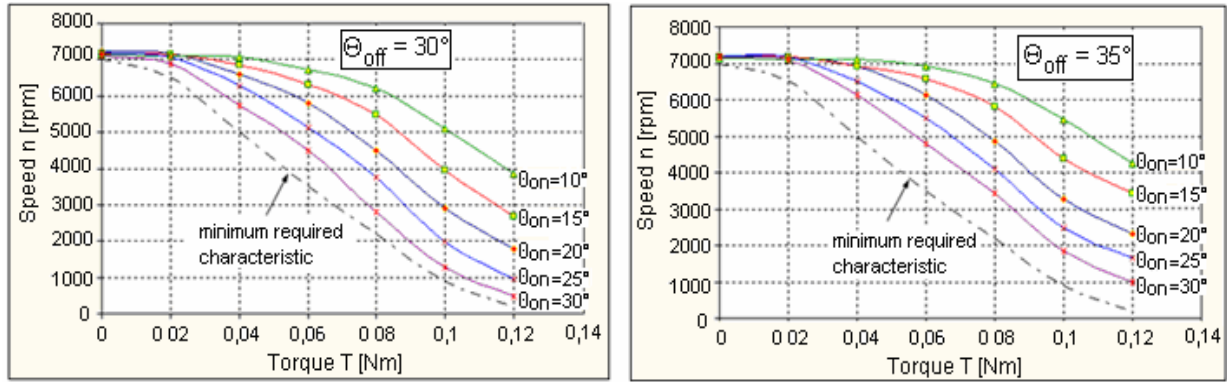
Fig. 6.14 Measured speed-torque characteristics of SRM II for different turn-on and turn-off angles

6.2.4   Measurement of motor losses and efficiency

In order to measure the motor losses, the same experimental setup shown in Fig. 6.8 is used. Copper- and core losses P_{Cu} and P_{Fe} must be determined to obtain the motor efficiency η_{Mot}. The motor runs under the conditions of I_{max}=4A, V_s=100V, Θ_{on}=10° and Θ_{off}=35°. The friction losses P_{fr} have been measured as a function of speed by driving a dc-machine in idle run and thereafter coupled with the non-excited SRM. For both cases the input power of the dc machine was measured, and the difference corresponds to the friction losses of the SRM including windage and bearing losses. The copper losses of the (warm) winding are determined by measuring the r.m.s phase current and using equation (3.185). The warm phase resistance is R_{ph}=0.46Ω. The core losses are determined indirectly by measuring the electrical input active power P_{el}, the mechanical output power P_{mech}, and the friction- and copper losses. A balance of power gives the core losses and the motor efficiency η_{Mot}:

$$P_{Fe} = P_{el} - P_{mech} - P_{Cu} - P_{fr} \tag{6.4}$$

$$\eta_{Mot} = \frac{P_{mech}}{P_{el}} = \frac{P_{mech}}{P_{mech} + P_{Cu} + P_{Fe} + P_{fr}} \tag{6.5}$$

Fig. 6.15 presents the measured core and copper losses vs. motor speed. To verify the analytical calculation methods, the predicted loss curves are shown with broken lines. The rated load torque is T_n=0.04Nm and remains constant as well as the current firing angles. The predicted and measured copper losses match very well since the r.m.s. current remains nearly constant. The motor operates in the researched speed range up to 7000rpm with single pulse mode. For an exact determination of the r.m.s. current referring to (3.184) the phase current is calculated from an oscilloscope plot. For analytically calculation, the current waveform for each operating point is determined with the procedure proposed in Chapter 3.6. However, due to the increase of friction and core losses, the temperature of the winding and therefore the phase resistance increases in praxis, which leads to the slightly increase of the copper losses with the speed. Further, the SKIN-effect, which is not considered by the analytical

calculations, slightly increases the phase resistance with speed. Nevertheless, the maximum calculation error is between 5-7% for the researched speed range. With I_{rms}=2.9A, the measured copper losses of the warm windings are approximately $P_{Cu}=3.9W$ at 7000rpm.
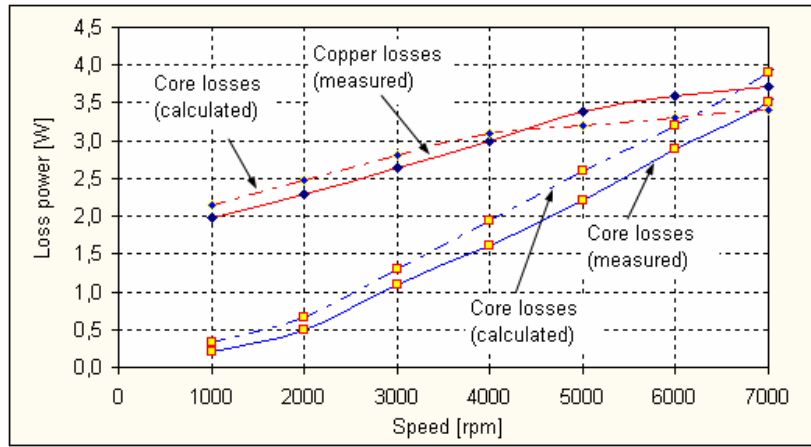
Fig. 6.15 Measured and calculated copper and core losses as a function of motor speed

The switching frequency of the 6/4-SRM from phase to phase is f_s=467Hz for n=7000rpm. Therefore, the core losses contribute with a substantive proportion to the entire motor losses. Up to 7000rpm the copper losses are dominating, but core losses increase much faster with speed and will dominate for higher speed. Compared with the calculation results, the measured core losses are a little smaller. The reason is that the real flux waveform in the magnetic circuit differs from the idealized one which is assumed for calculation. As Fig. 6.16a shows for the unaligned position, the flux lines (determined by FEM) enter the core material after crossing the air gap by using two rotor pole edges and the rotor yoke. Hence, different lengths of the flux path in the iron and the air are passed what is not considered in the analytical calculation. Further, in the aligned position the magnetic flux lines partially cross the magnetically not-loaded stator poles, which can be seen in Fig. 6.16b. Both effects lead to a smaller reluctance of the magnetic circuit than predicted. That reduces the flux density and therefore the core losses compared calculations.
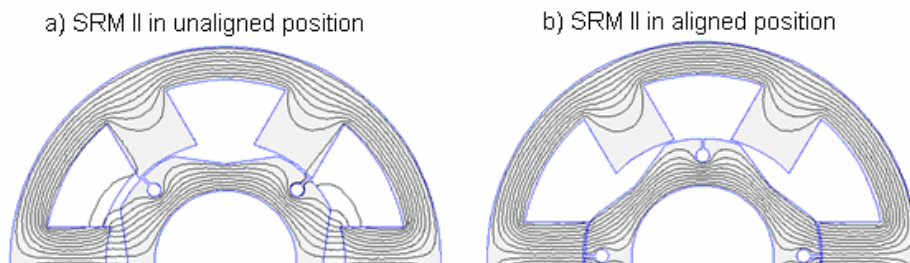
Fig. 6.16 FEM calculation of the field distribution in SRM II a) aligned; b) unaligned position

The maximum calculation error is in the range of 10-17% for the researched speed range, which is a quiet accurate result and allows a reliable optimization of the motor efficiency. Derived from the measured losses the motor efficiency can be calculated with respect to (6.5).

Fig. 6.17 presents the efficiency as a function of speed. The load torque remains constant and is equal to the rated torque of T_n=0.04Nm. The predicted efficiency is presented with broken lines and shows a good agreement. The measured efficiency at 7000rpm is η_{Mot}=80.3% compared to 79.8% which was calculated. That fulfils the demand of the desired application ($\eta_{ref} \geq 80\%$). One note, the desired rated speed of n_n=20000rpm could not achieved with the actual test equipment. However, the calculations match very well within the researched speed range and have the same tendency. Therefore it is expected that the predicted values for losses and efficiency for higher speed can be achieved with the prototype under the condition of a modified test bench. Such a new test bench is at present under construction and measurement results for higher speed up to n_{max}=30000rpm will be presented in a separate publication after finishing this thesis.
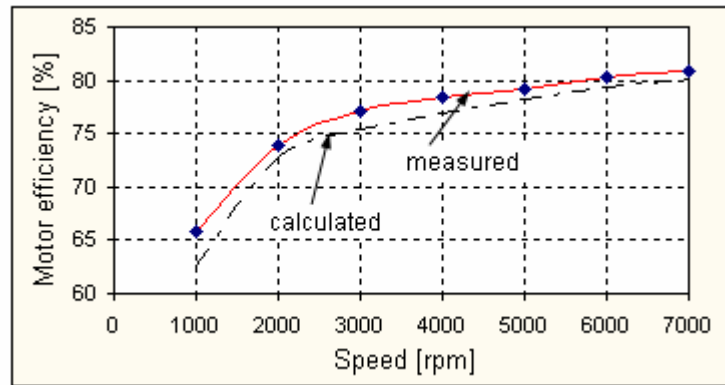
Fig. 6.17 Measured and calculated motor efficiency as a function of speed (I_{max}=4A, V_s=100V)

Table 6.6 summarizes the measured and predicted losses and efficiency for two different operating points. The torque remains constant with T_n=0.04Nm. All measurement results proof that the designed and manufactured SRM II fulfils the requirements from the desired spindle application within the investigated speed and torque range.

Table 6.6   Measured and predicted motor losses and efficiency of SRM II

	n=3000rpm			n=7000rpm		
	Measurement	Analytical	Error	Measurement	Analytical	Error
Copper losses P_{Cu}	2.6W	2.8W	7.7%	3.7W	3.5W	5.4%
Core losses P_{Fe}	1.2W	1.4W	16.7%	3.5W	3.9W	11.4%
Motor efficiency η	77.1%	75.4%	2.20%	80.3%	79.8%	0.6%

6.3   Laboratory tests of SRM prototype III for automatic truck gear

The experimental tests of SRM III which is desired for the use in an automatic truck gear were made by author on the test bench of the company 'ZF Friedrichshafen AG' in Friedrichshafen, Germany. Following, the experimental setup is presented and measurements of the T(i,Θ)-characteristics are summarized and compared with calculation results.

6.3.1 Experimental setup

For measuring the static torque characteristics T(i,Θ), the experimental setup shown in Fig. 6.18 was used. Here, the induction machine (ASM) works as the driving machine which is coupled via a worm gear with the SRM. The induction machine is supplied by the three-phase mains and runs with constant (rated) speed during the measurements. For measuring static torque values a small rotational speed was necessary in order to avoid the influence of SRM's core losses since the rotor consists of massive steel (not laminated!). Therefore, the gear between ASM and SRM was implemented. By means of a specific torque measuring shaft the static torque values of the SRM can be obtained as a function of rotor position angle.
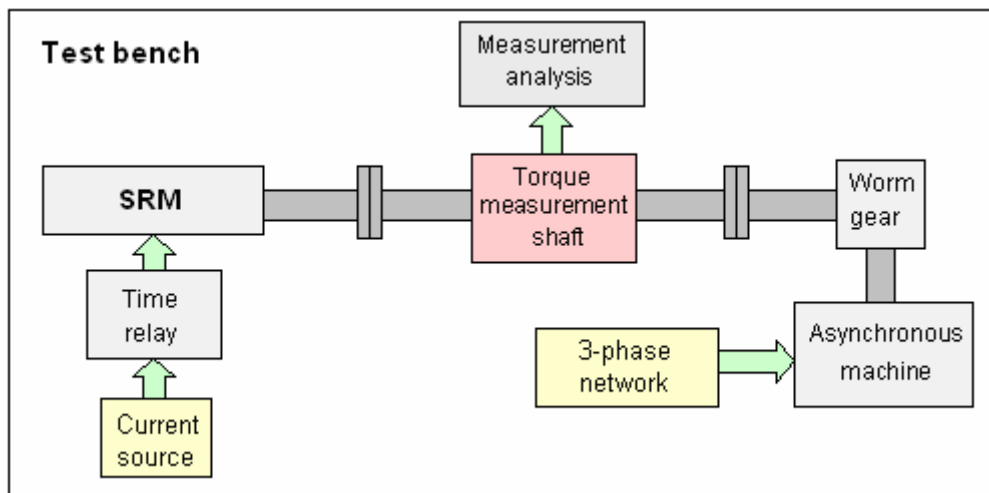
Fig. 6.18 Schematic of the experimental setup for static torque measuring of SRM III

A current source feeds the SRM with a constant current in the range of I=[1…40]A. Due to the rotation, the rotor poles move under the excited stator poles and produce a positive torque towards the aligned position and thereafter a negative torque when the rotor moves from the aligned into the unaligned position. The resulting counter torque is measured by the torque-measuring shaft. Fig. 6.19 presents a picture of the complete test bench.

Fig. 6.19 Test bench with SRM III in the laboratory of the ZF Friedrichshafen AG

6.3.2 Comparison of calculated and measured torque characteristics

In Fig. 6.20 measured (straight lines) and analytically calculated (broken lines) torque values are compared. The torque characteristics for small currents are approximately identical. The calculation error increases with current values higher than I=30A. Nevertheless, comparing the characteristics for the investigated current range it is found that the maximum calculation error is less than 10%.
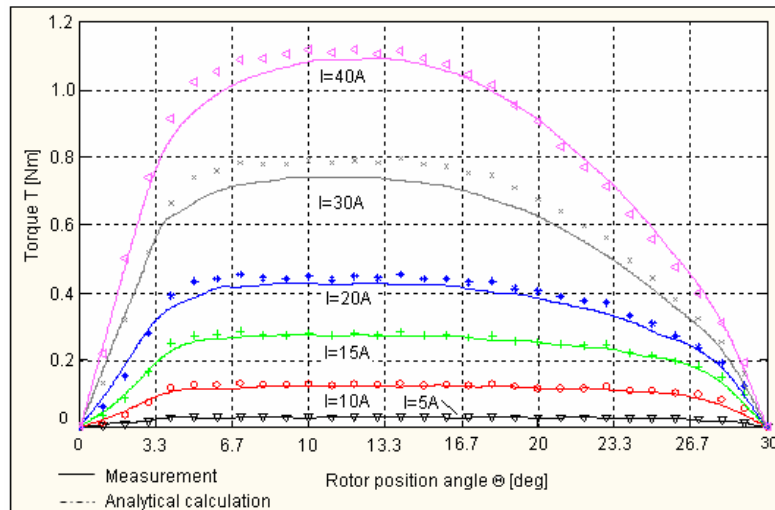
Fig. 6.20 Comparison of measured and predicted torque characteristics for SRM III

An interesting result during the researches was found by calculating the torque characteristics for another core material. After manufacturing of the prototype the information about the B-H-curve was incorrect which caused high calculation errors since a wrong stator core material was assumed (M19 stainless steel instead of M400; American notation). In this case the predicted torque was about 20% smaller than the measured! That shows the strong influence of the core material on the torque production capability of the SRM. Therefore, the simple way of choosing a higher quality of the iron leads to a remarkable increasing of the generated torque, without any modifications of the motor geometry or winding design! Of course, like with all industrial applications, the costs must be considered.

6.4   Error's analysis

Usually, inaccuracies are inevitably during measurements of any kind. The reason for the development of measurement errors are very manifoldy, thus it is necessary to analyse the process of obtaining measurement results in order to find the causes of error. The measuring process and therefore also the origins of measurement errors depend on the following points and are objectively influenced by them:

(1.) the characteristics of the measuring object itself,

(2.) the used measurement devices and their error classes,

(3.) the applied measuring method,

(4.) the personal characteristics and skills of the people performing the measurement and

(5.) environmental conditions.

It is normally the case that for the development of a measurement error not only one single reason is responsible, but it is the result of a combination of many different error parts with different kinds of causales. Reducing the measurement error requires a quantitative description of error sources, a sufficient metrological experiences and the knowledge about the random or systematically character of errors. Three different kinds can be distinguished:

1. rough errors,
2. random errors,
3. systematic errors

Rough errors can occur because of inadvertence, wrong handling, incorrect readings or damaged measuring devices. Generally, rough errors are avoidable and easy to identify. During the laboratory tests of the three SRM prototypes, rough measuring errors can be excluded since all measurement devices have been checked and certificated; all measurements have been multiple repeated and then averaged.

Random errors can appear for a number of different reasons. They lead to a statistical distribution of the results, indifferent the source of errors can be described physically. But even if a measured value is reproducible, it can differ considerably from the true value. Random errors occur due to the influence of many different stochastic events. They can not be corrected or 'switched off'. They lead to statistical fluctuations (in either direction) in the measured data due to the precision limitations of the measurement device. The influence on the measurement result can be reduced by means of multiple repeated measurements and averaging. Systematic errors, by contrast, are reproducible inaccuracies that are consistently in the same direction. Systematic errors are often due to a problem which persists throughout the entire experiment. The main casuals for such systematically errors are:

- The devices used for the measurement are calibrated wrongly.
- Problems during the applied method of measurement.

Since systematic errors occur with a specific regularity, they are in principle controllable, allocateable and correctable. However, spotting and correcting for systematic error takes a lot of care. In the following, a structural error's analyses researches measurement errors compared to analytical and numerical calculations. Concerning the above presented laboratory test results for the three SRM prototypes, reasons for the variation measurement results from calculations will be pointed out for

a.) Dynamic inductance measurement

b.) Measurement of characteristics torque vs. angle

c.) Measurement of characteristics speed vs. torque

d.) Measurement of iron- and copper losses

a) Dynamic inductance measurement

The difference between measuring inductance by means of 50Hz-method and dynamic inductance was described in Chapter 6.1.1 and 6.1.2. It was found that measuring dynamic inductance by di/dt-method is preferable since it considers saturation effects of the iron and the non-sinusoidal current feeding. The difference between both methods for inductance values in the aligned position is in the range of 10-20%. Compared to calculation results, the error of dynamic inductance is less than 6% (aligned position) for both FEM and analytical calculation. The maximum errors in unaligned position are 16% and 10% for analytical and numerical calculation, respectively (see also Table 6.1). The main reasons for those errors are

- simplification of analytical magnetic flux path calculation,
- end-winding effects which are not considered by FEM and only rough considered in analytical inductance calculation,
- bouncing of the mechanical switch for turning on- and off the phase current,
- inaccuracies during reading the graphics on the oscilloscope (reading error) and
- fluctuations and small break-in of the dc-link voltage at the instant of current switch-on.

In order to minimize the measuring errors, all measurements have been multiple repeated and averaged. Thus, measurement- and calculation results match very well and the maximum error does not increase 16% for both SRM I and II, which is a quiet good result!

b) Measurement of characteristics torque vs. angle

The measurement procedure for determining torque vs. angle characteristics are the same for both SRM I and II, thus the same reasons for measurement errors are assumed. In the presented laboratory test results, a maximal error of 12% occurs compared to analytical calculations, and 7% compared to FEM. Reasons for that differences are very manifoldy; the most important ones can be summarized as follows:

- Calculation of torque vs. angle characteristics bases on inductance calculation and therefore includes the same systematically error as described above since the mathematical inductance model involves various simplifications with respect to determining flux paths, saturation- and end-winding effects.
- The dc supply voltage provided by the 2-pulse rectifier is not totally smooth in spite of a large dc-link capacitor, leading to high-frequency oscillations of the torque during a fixed rotor position angle (the lever arm which presses on the digital weight is slightly 'buzzing' especially at high current).
- The rotor position sensor RENISHAW RE36 has a resolution of 360deg/(255steps)≈1,41deg/step. The digital display only shows full steps with integer number. Therefore the rotor position angle can not be exactly determined since rounding errors occur. Note, the same is true for the inductance measurement. However, repeating and averaging the measurement results minimizes that error.

Comparing measurement and calculation results shows: the measurement error is quiet small, the analytical and numerical SRM models provide very accurate and reliable results. The analytical calculation error is in the range of 10% and slightly increases for very high current level when the iron is strongly saturated. That is true for SRM I, II and III. The major error source of torque measurement for SRM III is the resolution of the torque measuring shaft since the torque values to measure are very small. Mechanical friction and vibrations quiet complicates determination of T(i,Θ) characteristics. An accurate calibration of the entire measurement system is absolutely essential.

c) Measurement of characteristics speed vs. torque

For SRM I and II speed vs. torque characteristics have been measured as a function of the current switching angles and a comparison to simulation results obtained with the program SIMPLORER® 4.2 was shown. The results match very well, however a principle calculation error occurs since the simulation model uses static torque- and inductance characteristics as a function of angle and current. Those characteristics were determined by means of static analytical calculations respectively magnetostatic FEM computations and it is problematic to transfer these static calculations on dynamic measurements when the motor runs with high speed where among others mutual couplings play an important role. Nevertheless, the calculation error is less than 10% showing the high accuracy of the developed SRM models.

d) Measurement of iron- and copper losses

Loss calculation- and measurement is one of the most difficult tasks during researching SRMs since saturation effects occur and the motor is supplied by non-sinusoidal current waveforms, leading among others to non-sinusoidal magnetic flux-waveforms with different frequencies in different parts of the magnetic circuit. Further, overlapping of phase currents during commutation and high frequency harmonics of the current waveform complicate the investigation and the determination of iron and copper losses. The following error sources must be recognized when measurement results are analysed and compared to calculations:

- Reading error from the oscilloscope for calculating the r.m.s. current from the real current waveform referring to (3.184) to determine the copper losses with (3.185).

- The SKIN-effect occurring at high current frequencies is not considered in analytical calculations of copper losses and increases the phase resistance. Therefore measured copper losses rise stronger with the motor speed then predicted.

- Calculation of core losses bases on analytical inductance calculation with all the simplifications mentioned above and also described in Chapter 3 (e.g. end winding effects, saturation, etc.), leading to a systematic error.

128

- The flux waveform in the different machine parts can differ from the idealized waveform shown in Chapter 3.5.2 due to overlapping of phase currents or high frequency harmonic oscillations of the phase current.

- Thermal effects are not considered in numerical and analytical calculations. However, all measurements have been performed with operating temperature of the prototype SRMs. The phase resistance is of course also calculated assuming a warm winding. A further warming of SRM II during high speed where friction in the bearings produced unexpected much heat is not considered in calculations.

In spite of these error sources, the measurement results are quiet accurate and match well with the predicted values showing once again that the developed hybrid design- and calculation procedure proposed in this thesis gives reliable results, how simple it may be. The calculation error of copper losses of SRM II is in the range of 5-7% for the researched torque-speed range. The core losses have an error of 10-17% compared to the analytical calculation results. These are very accurate results and allow a realistic determination of motor efficiency.

7   Contributions and future works

The quickly received, complex information on the quantitative relationships between constructional parameters and machine performance characteristics is very useful and advantageous for a machine and drive system designer. Therefore, the need for improved effective hybrid calculation program for motor and drive system design, capable for predicting of these relationships exists. Thus, the most general intention of this thesis is the fulfilment of this demand. The thesis is intended also to develop the necessary tools for determination of most convenient motor's construction regarding the application requirements.

In this context, the main contributions and original elements in the presented dissertation are summarized as follows:

(1)   Elaboration of hybrid effective 3-parts program for SRM design calculation (Ch.3, p.3.8 and Ch.4, p.4.1-4.5)

         First part of this program "Design SRM" is the original conception of methodical approach for design SRM's using a quick analytical methods. This part enables the realization of multiple, effective design calculations. The analysis of chosen constructional versions of machine by finite element method is realized in second part of the program. This part can be considered as the complimentary design tool. Third part concerns of simulation and motor dynamic behavior analysis, what is useful for appreciation of whole drive system dynamic properties. Application of proposed hybrid program by users requires only a little theoretical background knowledge. Finally, very effective and reliable design tools have been developed in this thesis in order to find optimum solutions for sophisticated drive applications within shortest time.

(2)   Proposition of „DesignSRM" subprogram which enables the easy modifications of the input data e.g. geometric motor parameters and the immediate receiving of the results of investigation using analytical methods concerning the influence of these input data on the operational motor behaviour (Ch.3, p.3.2-3.8).

         That offers the possibility to obtain new knowledge about SRM characteristics and to develop a modified motor design on the basis of those new findings for a specific application.

(3)   Procedure for calculation the unaligned inductance based on the principles of electromagnetics and conventional methods of circuit analysis (Ch.3, p.3.2).

         Proposed procedure is easy to application and characterised by only a small error when compared to the Finite Element and measurement results and allows users to develop their own procedures with minor modifications.

(4)   Detailed procedure for calculation the core losses (Ch.3, p.3.5.2)

         The determination of core losses is preceded by accurate analysis of flux plots obtained from analytical calculations and evaluation of the real flux-waveforms in the

various parts of the magnetic circuit. The method determines the core losses in dependence of the actual mode of control and corresponding current waveform, no matter if single pulse or chopping mode. The procedure works with a modified STEINMETZ-equation and uses material characteristics given by the manufactures. The accuracy of the calculation method is verified by laboratory tests.

(5)   Demonstration of the relation between constructional motor parameters, control parameters and inner phenomena like iron losses and saturation effects (Ch.3, p.3.7).

(6)   Presentation of the correlation between the saturation level of motor magnetic circuit and Volts/Ampers requirements of inverter (Ch.3, p.3.7)

In terms of saturation theory it was shown that for the same torque and speed of motor, the Volts/Ampers requirements of a non-saturating motor are quiet higher than that of a saturating motor with the same dimensions. That leads to a larger inverter size.

(7)   Application of hybrid 3-parts program, point (1), for design calculation of three different SRM's destined for three different kinds of industrial drives (Ch.5).

(8)   Proposition of the modified 6/4-SRM I construction with new trapezoidal rotor pole (Ch.5, p.5.1).

The new proposed trapezoidal rotor design has wider poles at the base than at the tip. The wider pole base is able to carry higher flux values in the direction of aligned position without saturation, resulting in smoother and to average higher torque waveform.

(9)   Proposition of the innovative 6/4-SRM II construction with new trapezoidal rotor pole for reduced level of the noise (Ch.5, p.5.2).

The proposed 6/4-SRM construction is characterised by the new trapezoidal shape of the rotor pole with rounded edges and a rotor pole wide at the base equal to the rotor pole pitch. That leads to an in average higher torque, reduced torque ripple and therefore a reduced noise level compared to rotor pole with parallel sides. The design procedure was verified by FEM calculations and simulations, and finally by measurement results.

(10) Proposition of a new 8/6-SRM III with trapezoidal stator and rotor pole profiles and larger radius in the stator slots to increase the winding area and torque (Ch.5, p.5.3).

The new proposed 8/6-SRM construction is characterised by trapezoidal stator and rotor pole profiles to reduce saturation effects and torque ripples, a larger radius in the stator slots to increase the winding area and maximize torque and a massive rotor design without laminations to minimize manufacturing costs in serial production.

(11) Elaboration of laboratory stands and realization of experimental tests of three industrial SRM prototypes for verification the presented design and calculation algorithms (Ch.6, p.6.1-6.4).

(12) The proposed hybrid design program for SRM's enables the effective and more complex motor design from the point of view of considered drive requirements, in comparison with proposals published up to now and known by author from the bibliography.

The hybrid design program includes at first analytical and then field calculation methods. Finally dynamic simulations have been developed. The program can perform

1. Machine and winding design
2. Steady-state calculations like
   - torque-, flux- and inductance characteristics vs. rotor position and current,
   - copper and core losses of the motor and converter losses; efficiency
3. Verification of the projects by application of numerical field method (FEM)
4. Dynamic calculations like current and torque waveform in dependence of speed and mode of control

The future research following this dissertation could be outlined as follows:

(1) There is a need for a more detailed experimental verification of the calculated core losses for all three prototypes under the condition of different control modes. Therefore an efficient measurement method has to be developed.

(2) The mechanical design and acoustic noise reduction of SRMs, particularly for high-speed operation, will be very useful.

This vast topic has only started in this thesis. There is a strong need to relate the geometric machine parameters to the acoustic noise by refining the design procedure in order to develop quieter machines.

(3) Further theoretical and practical investigations concerning typical problems with high-speed drives should be performed.

The theory and experimental tests of SRM II made in this thesis involve only steady-state operation. Typical effects which occur in high-speed drives are among other harmonics rotor oscillations, radial and tangential stress on the rotor laminations, loading of the bearings, core losses, mutual couplings between motor phases and noise generation. These questions must be investigated in the future.

(4) Thermal models must be developed for SRMs and the temperature rise of the manufactured prototypes should be calculated.

The research is necessary for a better understanding of the requirements for the cooling system. The methods for loss calculation which were developed in this thesis will help to refine the model for future research interested in thermal modelling.

(5) A low cost converter must be developed for the SRM II desired for the high speed application. Therefore researches are necessary for designing an open-loop control system with an asymmetric half bridge. Such an open loop control system does not require any rotor positioning system which is an essential demand on the drive system.

8   Summary

This PhD thesis deals with the design, calculation and optimization of Switched Reluctance Machines (SRM) and has the typical complete scheme of scientific technical research. The initial part presents a general introduction in SRM drives including a short review on the development history and the motivation for this work.

The **OBJECTIVE** of the thesis is:

1. **Elaboration of effective hybrid design program for SRM's taking into account all losses in drive system, field verification and modeling of dynamic operation as well.**
2. **Application of this program to the design calculation of three different SRM's destined to concrete industrial drives.**
3. **Demonstration of the correctness of proposed program by comparison of the calculation and measurement results made for three prototypes of SRM's manufactured in industry.**

Results of the research evaluated from the point of view of the presented above objective enable the formulation of the **THESIS TO BE PROVED** related to the PhD thesis:

The proposed in the thesis hybrid design program for SRM's enables the effective and more complex motor design from the point of view of considered drive requirements, in comparison with proposals published up to now and known by author from the bibliography.

In the proposed hybrid design program at first analytical and then field calculation methods and finally dynamic simulations have been developed. This program can perform:

1. Machine and winding design
2. Steady-state calculations like torque-, flux- and inductance characteristics, copper and core losses of the motor and converter losses and finally system efficiency.
3. Verification of the projects by application of numerical field method (FEM).
4. Dynamic calculations like current waveform in dependence of speed and control mode.

Synthetic informations on conventional design procedures for these SRMs with common operating principles, structures and the mathematical model of a SRM are given in Chapter 1. Also principle of energy conversion, elementary types of converter topologies and general modes of control are introduced in context of the large world wide bibliography.

A principle design procedure of Switched Reluctance Motors which allows meeting the manufacturer's requirement while helping a machine manufacturer with no background in SRM design to built and test prototypes is proposed in Chapter 2. Machine's main dimensions calculation, number of poles and air-gap determination, correlation of dimensions in pole zone and principles of winding design are discussed in this part as well.

Chapter 3 represents the most important part of this thesis. Here, the main calculation models, design algorithms and programs applied by author are presented. Algorithms of calculation of parameters and operation SRM characteristics are described as well as the method of winding inductance and static torque characteristic calculation. The analysis and the methods of determination of motor and converter losses are the very important parts of the research. The new calculation method of SRM's iron losses on the basis of a modified STEINMETZ equation is developed. The influence of magnetic circuit saturation on motor operation characteristics with different modes of control is discussed. Also the model of motor dynamic behaviour is presented. Based on proposed calculation algorithms the hybrid 3-parts effective design program for SRM's is finally introduced. The first part of this program "DesignSRM" enables the realization of numerous effective design calculations using analytical quick methods. The second part of the program performs the field analysis of chosen construction version of the machine by numerical calculation of electromagnetic circuit using Finite Element Method. This part is the complimentary tool for evaluation of machine construction during design procedure and can be used in case when the construction modifications are considered for improvement of machine parameters and characteristics. The third part of hybrid design program refers to the simulation of the drive dynamics, which is presented in detail in Chapter 4. These problems are useful for evaluation of the properties of whole drive system. The model of motor dynamics is elaborated using Simplorer$^{®}$ 4.2 software. The motor parameters calculated in earlier design procedures are used in this model. The modelling of dynamics takes into account the different methods of motor control and the influence of mutual couplings between motor phases. Also a sensorless control procedure based on flux-linkage-current method is proposed.

Design examples of three industrial SRM prototypes made by factories are sown in Chapter 5. The prototypes of a 6/4-SRM for vacuum cleaner (conventional and modified versions), a 6/4-SRM for an electric spindle drive for a spinning machine in textile industry, and an 8/6-SRM for an automatic truck gear are presented.

After calculation models and design procedures give in final solution the concrete machine constructions described by calculation parameters and operation characteristics, the experimental verification and error's analysis follows in Chapter 6. Laboratory tests are made for all SRM's constructions. The comparison of both calculation and experimental results was made. All SRM prototypes fulfil the high demands of their explicit industrial application.

Personal contributions of author in presented elaboration together with indication for future investigations are the subject of the Chapters 7. Important bibliography (182 positions) is presented at the end of the thesis.

The **JUSTIFICATION OF THESIS TO BE PROVED** results from following considerations:

Effectiveness of the proposed in the thesis hybrid design program results from application of block "Design SRM" (Fig. 3.2.9, part a) which enables the realization of the quick, effective, multiple design calculations using the analytical methods. In this block the "parametric models" of the designed motors are applied. The parametric analytical models in form of large equations contain inside dimension's and material's parameters as simple factors. Thus the quickness of calculations results from fact that the parametric models can be solved by quick analytical methods.

More complex character of proposed hybrid design program is justified by:

- Application of field analysis (Finite Element Method), Fig. 3.2.9, part b, for chosen, quickly earlier calculated in block a, motor construction. This additional numerical analysis gives the possibility of more complex evaluation of the motor construction, enables the calculation of chosen motor parameters and characteristics from field theory and can be useful for next eventual construction modifications and optimizations as well.
- Procurement of data on motor dynamic operation, which gives the possibility of more complex evaluation of the motor properties from the point of view of whole drive system requirements.

The design procedures of the SRMs are widely described in different fragments in numerous bibliography positions. However, there no exists, according to knowledge of author, the complex design procedure in form presented in this thesis. The proposed hybrid design program has been successfully applied for design calculation of three SRM's. Calculation parameters and characteristics of proposed SRM's constructions have been successfully verified by laboratory tests. The correctness of the proposed design program and the rightness of the thesis to be proved are also confirmed in this PhD by the questions presented above.

The main **CONTRIBUTIONS** and original elements can be formulated in short form as:

1. Elaboration of hybrid effective 3-parts program for SRM design calculation.
2. Proposition of „DesignSRM" subprogram which enables the easy modifications of the input data e.g. geometric motor parameters and the immediate receiving of the results of investigation using analytical methods concerning the influence of these input data on the operational motor behaviour.
3. Procedure for calculation the unaligned inductance based on the principles of electromagnetics and conventional methods of circuit analysis.
4. New detailed procedure for calculation the core losses.
5. Demonstration of the relation between constructional motor parameters, control parameters and inner phenomena like iron losses and saturation effects.

6. Presentation of the correlation between the saturation level of motor magnetic circuit and Volts/Ampers requirements of inverter.

7. Application of hybrid 3-parts program for design calculation of three different SRM's destined for three different kinds of industrial drives.

8. Proposition of the modified 6/4-SRM I construction with new trapezoidal rotor poles.

9. Proposition of an innovative rotor construction of SRM II with reduced level of the noise.

10. Proposition of a new 8/6-SRM III with trapezoidal stator and rotor pole profiles and larger radius in the stator slots to increase the winding area and maximize generated torque.

11. Elaboration of laboratory stands and realization of experimental tests of three industrial SRM prototypes

At the end of this summary, the **FINAL CONCLUSIONS** can be formulated:

- All designed and manufactured SRM prototypes fulfill the high demands from the desired industrial application with respect to output torque, efficiency and torque-speed characteristics. Measurement results confirm the previous calculations.

- To achieve maximum specific output power, ideal non-saturating iron is beneficial. The price paid is a high volt-ampere requirement from the electronic converter. In praxis, the machine design should have magnetic circuits of low reluctance in order to have a high ratio of maximum to minimum inductance. Minimizing the size of both the motor and the inverter requires a small air gap and iron with very high permeability.

- In terms of saturation theory it was shown that for the same torque and speed, the VA-requirement of a non-saturating motor is quiet higher than that of a saturating motor with the same dimensions, leading to a larger inverter size.

- Laboratory tests of the three industrial SRM prototypes have proven the high accuracy of the developed hybrid design- and calculation procedure. The errors between calculations and measurements are small and result mainly from simplifications of the mathematical machine models or from the transformation of static analytical or numerical calculation results into dynamic models. Note, magnetostatic FEM problem with more than 6000rpm is very problematic! In order to minimize the measurement error, a careful calibration of all measurement devices is essential necessary as well as a multiple repeating and averaging of the measurements to reduce random and systematic errors.

- The THESIS TO BE PROVED has been justified in this thesis.

- All calculation and experimental results show that the SRM can be a serious alternative to ac machines for many industrial applications.

- The analytical calculation of the iron losses is one of the most difficult tasks of SRM researches due to the non-sinusoidal current feeding and highly saturated core material. Measurement results have proven that the presented new calculation method for predicting SRM's iron losses can solve this problem very successfully. The proposed analytical method bases on a modified STEINMETZ-equation and considers the non-sinusoidal current feeding with different modes of control.

- Researches about SRM's noise generation and noise reducing are very complex and require a lot of mechanical investigations. That would go beyond the scope of this thesis and is therefore researched only very provisionally in context with the rotor-design of SRM II.

- Future researches will deal with the measurement of core losses for all three SRM prototypes, mechanical design and acoustic noise reduction, thermal problems and the development of a low-cost power electronic converter for SRM II without sensor positioning system.

Appendix: Program 'DesignSRM'

In the following, the various tab sheets of the developed program "DesignSRM" are shown.
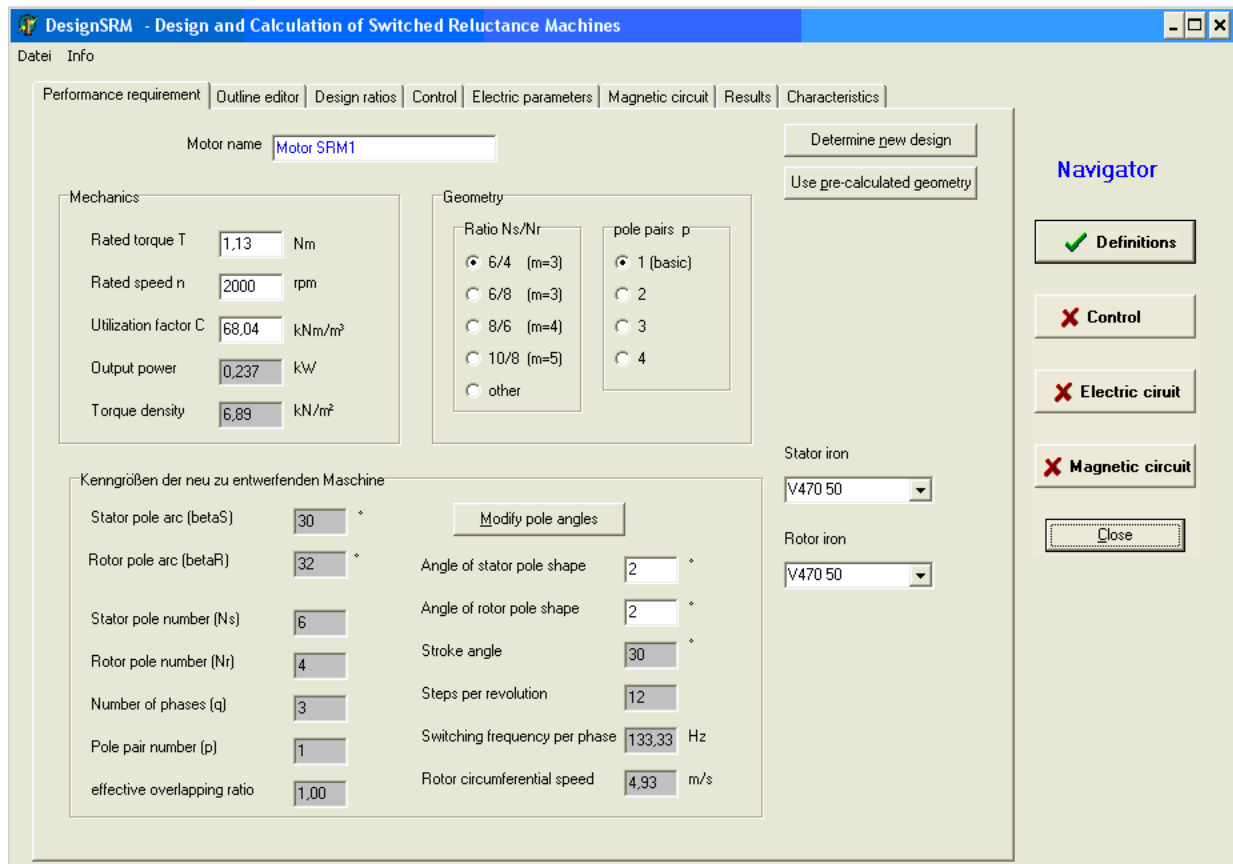
Fig. A.1   DesignSRM- tab sheet 1: *Performance requirement*

Fig. A.2   DesignSRM- tab sheet 2: *Design ratios*

138

Fig. A.3 DesignSRM- tab sheet 3: *Outline editor*

Fig. A.4 DesignSRM- tab sheet 4: *Control parameter*

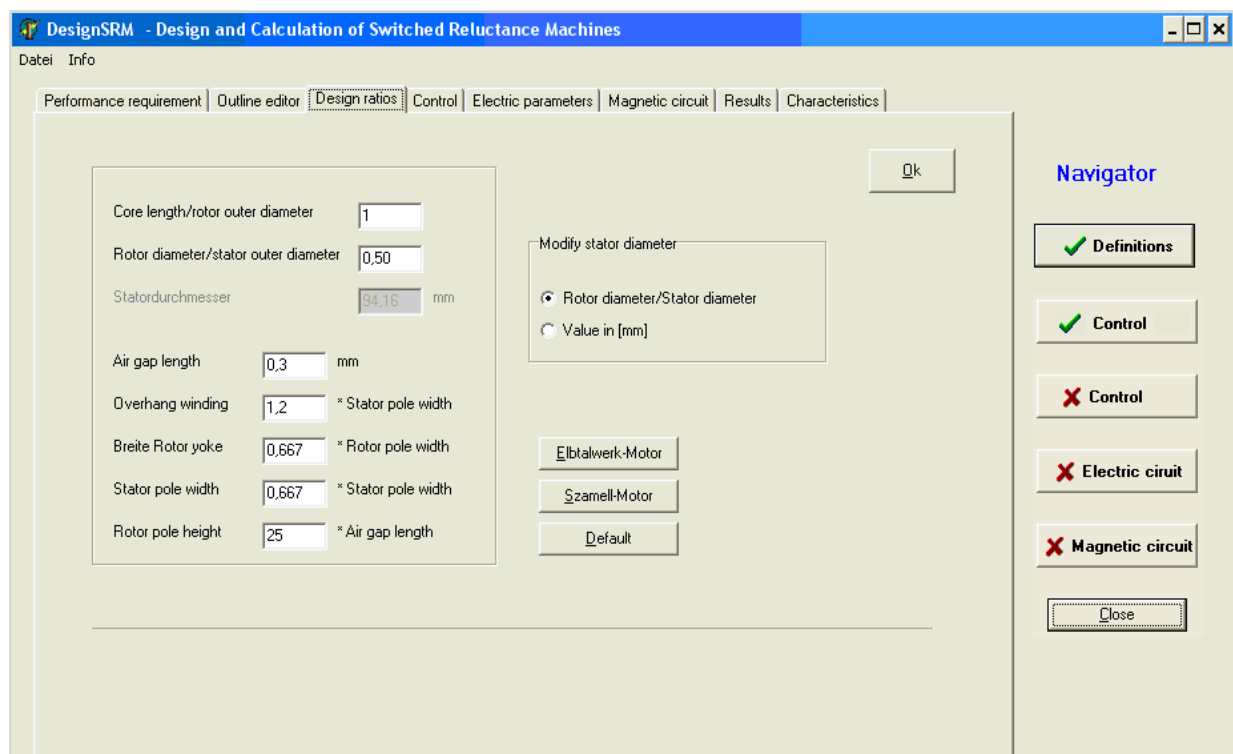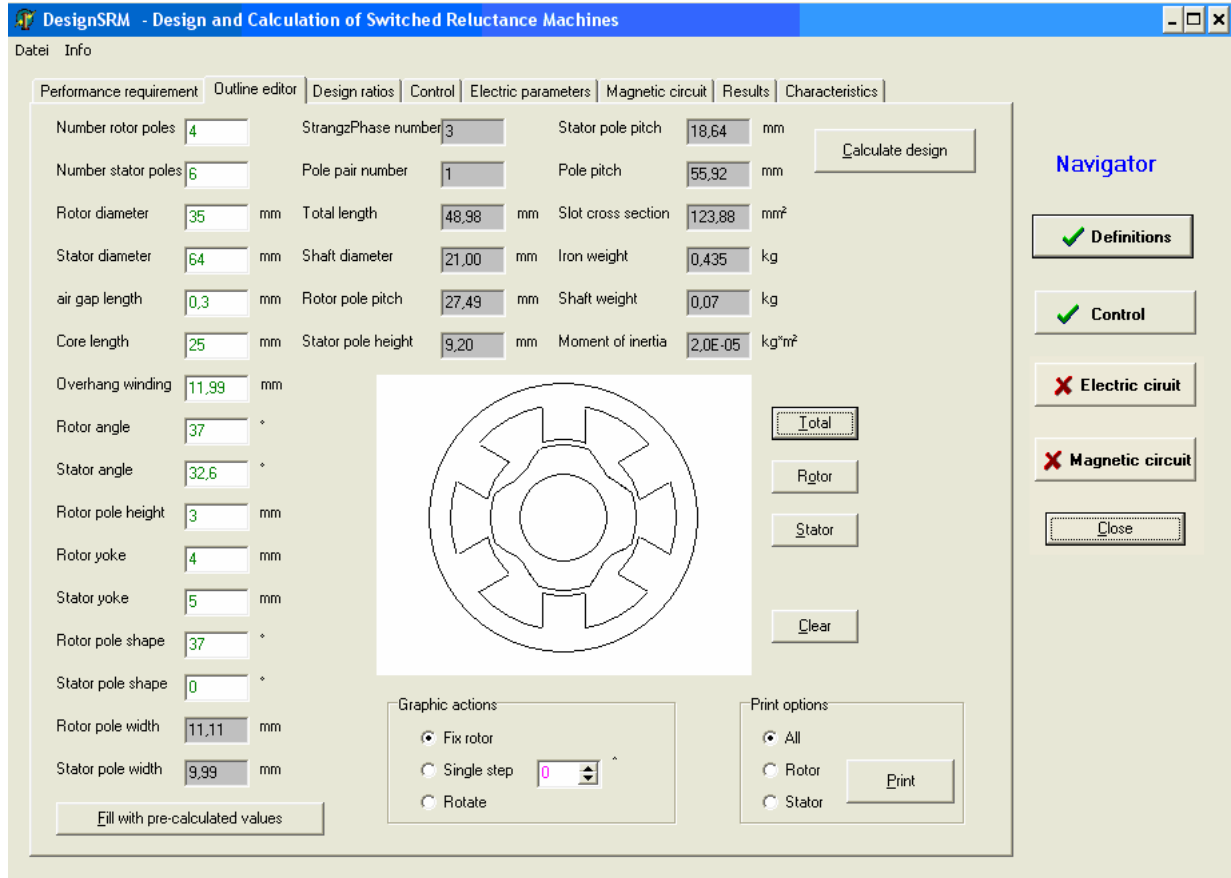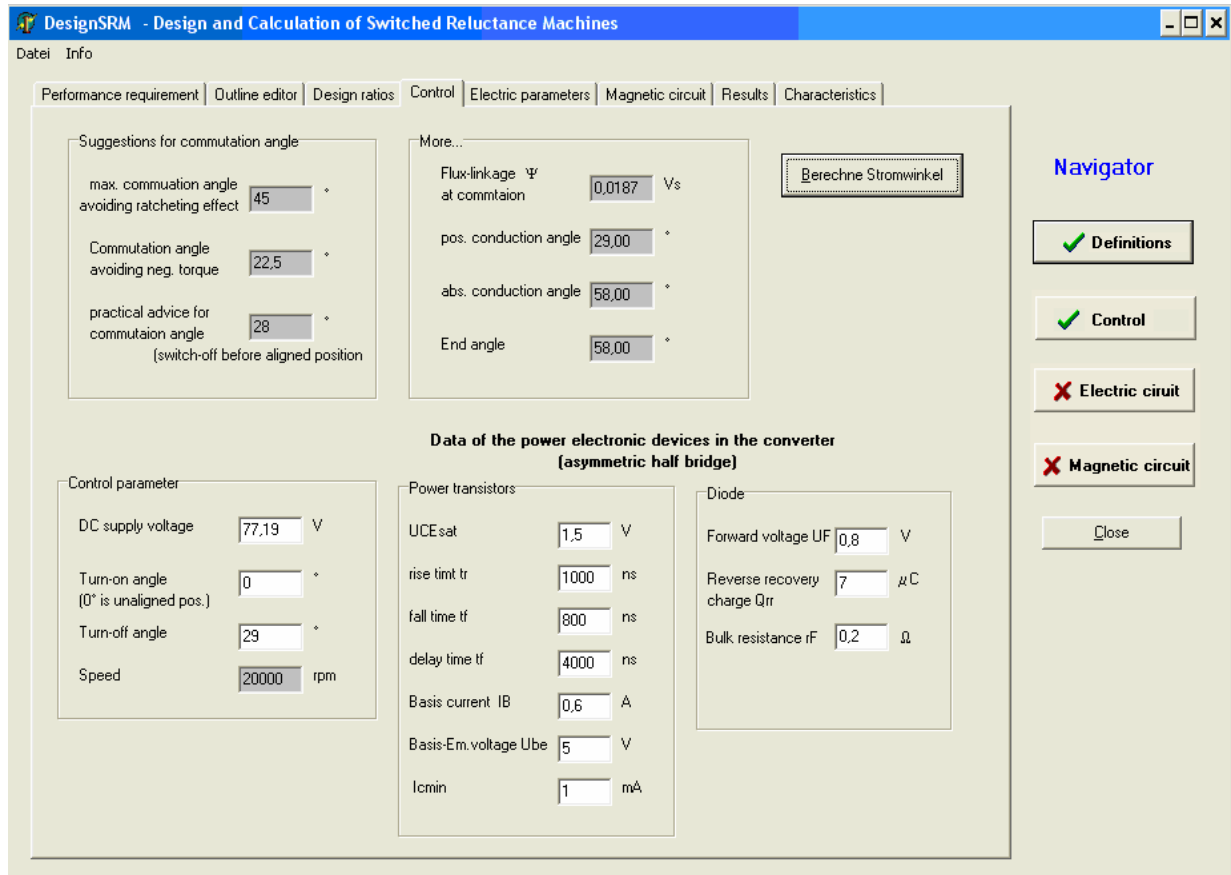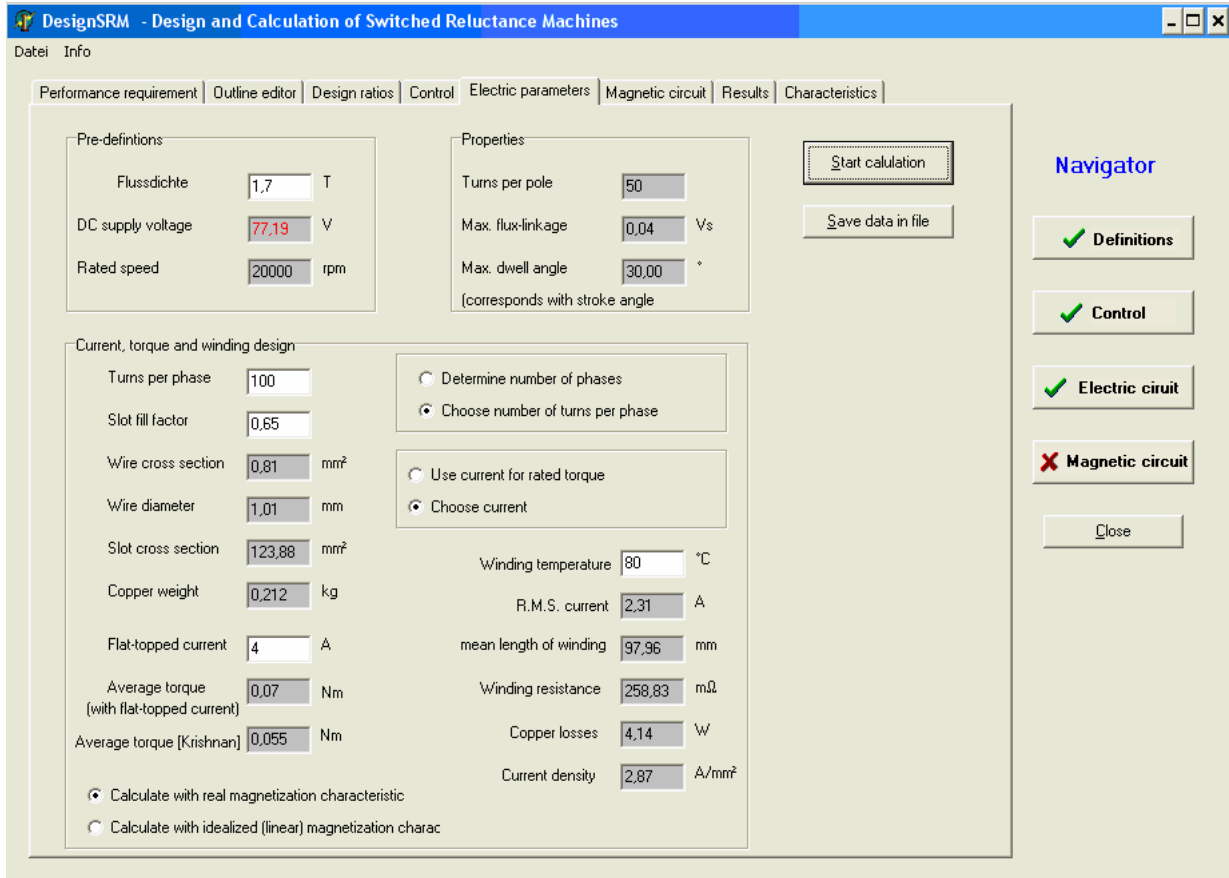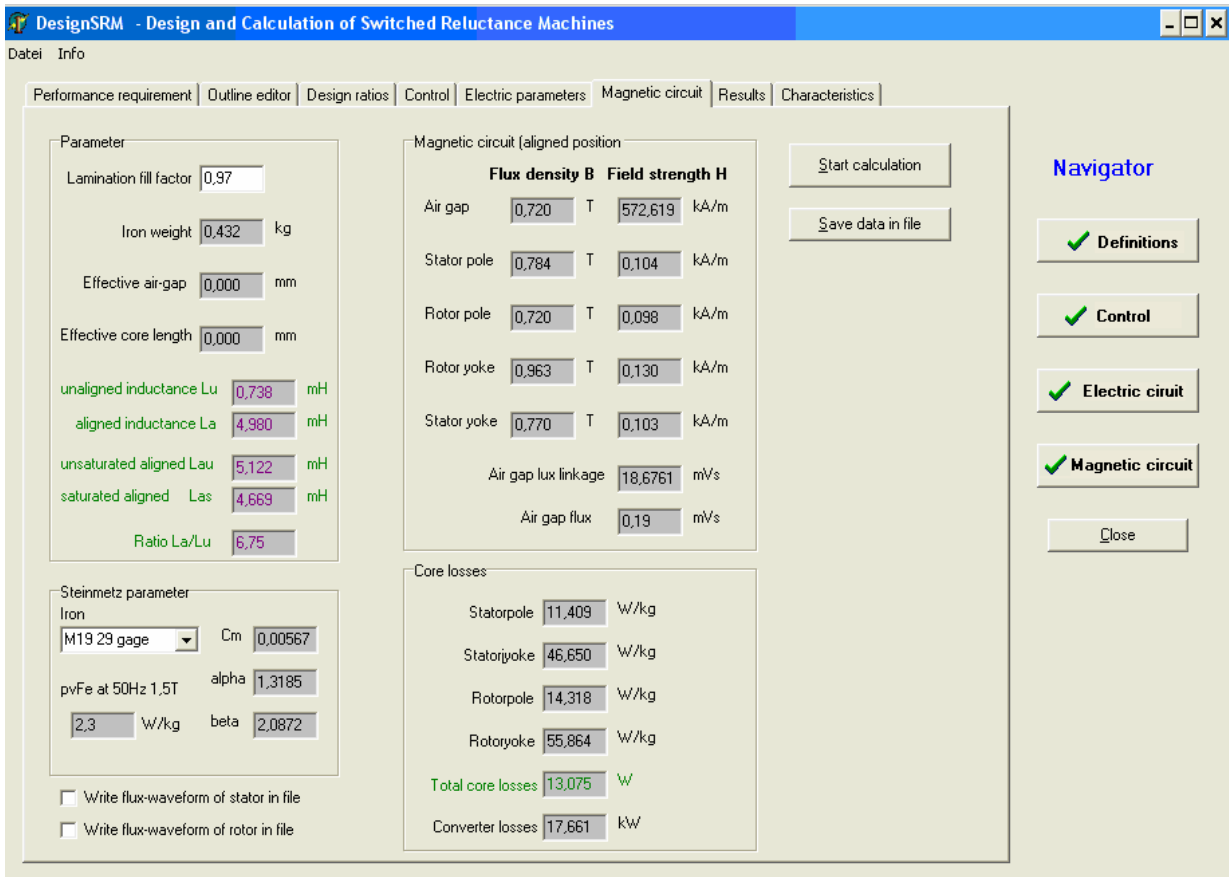**Fig. A.5**   DesignSRM- tab sheet 5: *Electrical parameter*

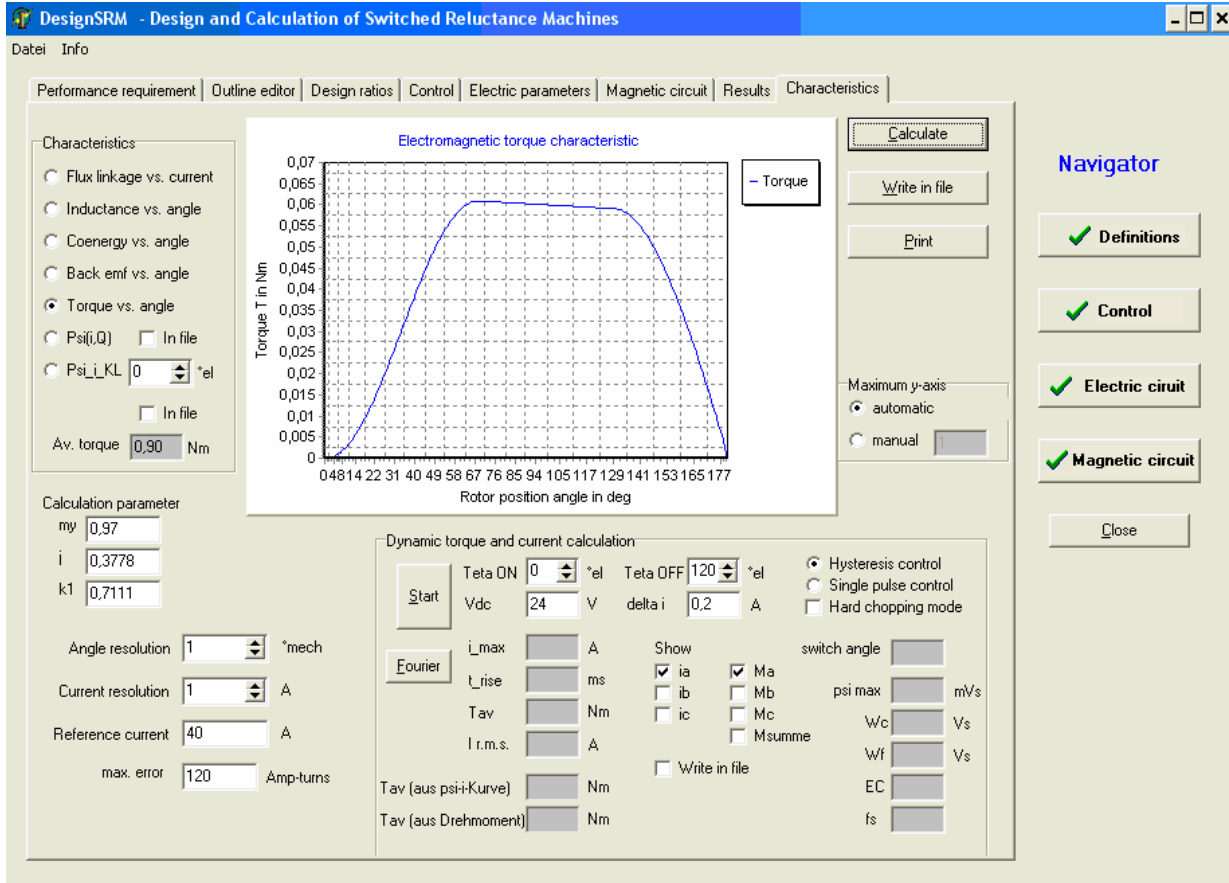**Fig. A.6**   DesignSRM- tab sheet 6: *Magnetic circuit*

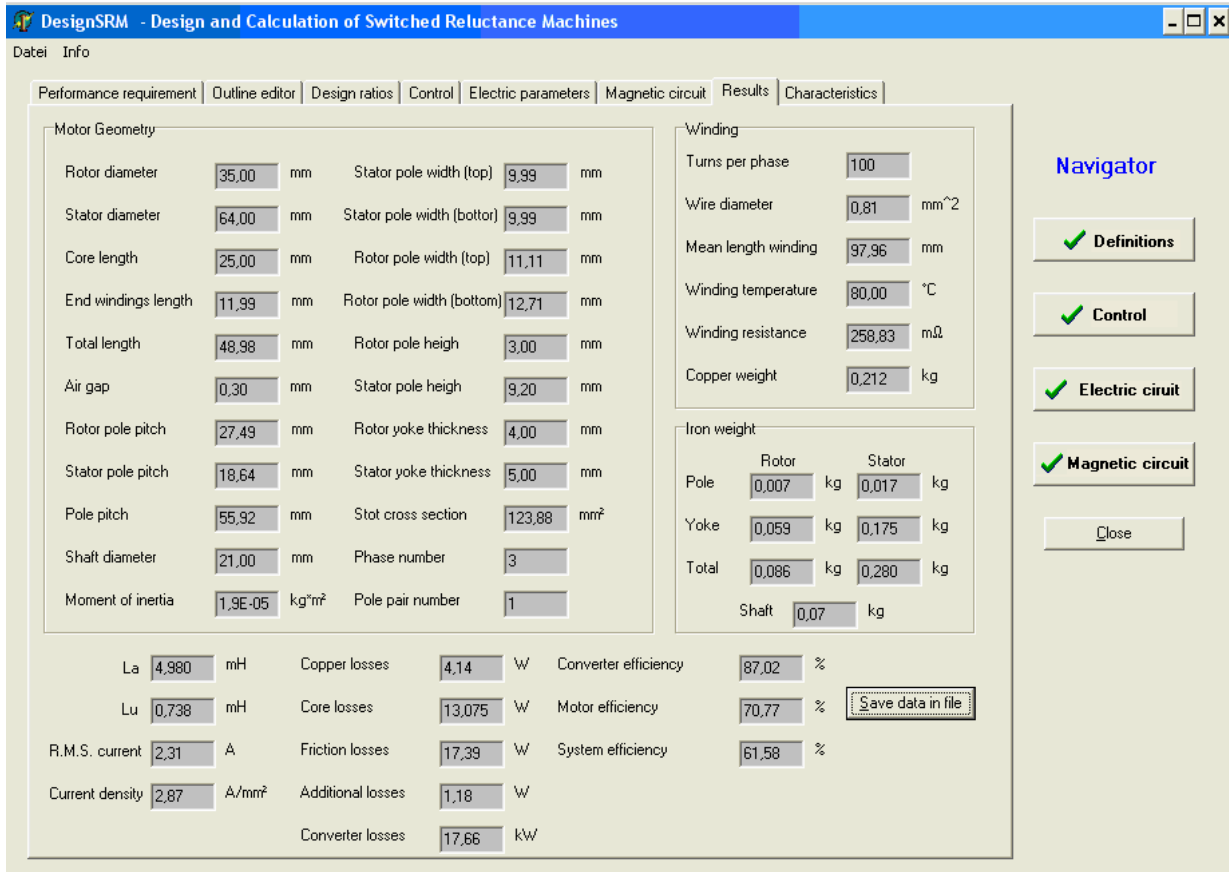**Fig. A.7**   DesignSRM- tab sheet 7: *Characteristics*

Fig. A.8   DesignSRM- tab sheet 8: *Results*

```
C:\Delphi\DesignSRM
******************* Definitions *******************
Torque density: [kN/m^2]:                  0.83
Torque per rotor volume [kNm/m^3]:         8.21
Torque [Nm]:                               0.04
Rotor speed [rpm]:                         20000
Power [kW]:                                0.08
Steps per revolution:                      12
Switching frequency [Hz]:                  1333.33
Rotor circumferential speed [m/s]:         36.65


******************* General data *******************
Number of stator poles:                    6
Number of rotor poles:                     4
Number of phases:                          3
Number of pole pairs:                      1
Stroke angle [°]:                          30
Stator pole angle [°]:                     32.6
Rotor pole angle [°]:                      37
Air gap length [mm]:                       0.30


******************* Geometry *******************
Rotor diameter [mm]:                       35.00
Stack length [mm]:                         25.00
Overhang windings [mm]:                    11.99
Total winding length [mm]:                 48.98
Shaft diameter [mm]:                       21.00
Stator outer diameter [mm]:                64.00
Stator pole width (tip) [mm]:              9.99
Stator pole width (base) [mm]:             9.99
Rotor pole width (tip) [mm]:               11.11
Rotor pole width (base) [mm]:              15.63
Stator pole height [mm]:                   9.20
Rotor pole height [mm]:                    3.00
Stator yoke thickness [mm]:                5.00
Rotor yoke thickness [mm]:                 4.00
Stator pole pitch [mm]:                    18.64
Rotor pole pitch [mm]:                     27.49
Pole pitch [mm]:                           55.92
Slot area [mm^2]:                          123.88
Moment of inertia [kg*m^2]:                2.0E-05


******************* Winding *******************
Turns per phase:                           100
Slot fill factor:                          0.65
Winding cross section [mm^2]:              0.81
Average winding length (1 turn) [mm]:      97.96
Winding temperature [°C]:                  80.00
Resistance per phase [Ohm]:                0.259


******************* Magnetic circuit *******************
Stator iron:                               M250-35A
Rotor iron:                                M250-35A
Flux density air gap [T]:                  0.908
Flux density air stator pole [T]:          0.989
Flux density air stator yoke [T]:          0.972
Flux density air rotor pole [T]:           0.908
Flux density air rotor yoke [T]:           1.214
Field strength air gap [A/m]:              722347.790
Field strength air stator pole [A/m]:      110.518
Field strength air stator yoke:            122.590
Field strength air rotor pole [A/m]:       110.518
Field strength air rotor yoke [A/m]:       213.689
Aligned (saturated) inductance [mH]:       5.02
Unaligned inductance [mH]:                 0.74
Inductance ratio:                          6.80


******************* Weights *******************
Total rotor weight (iron) [kg]:            0.09
Total stator weight (iron) [kg]:           0.28
Total stack weight [kg]:                   0.37
Copper weight [kg]:                        0.21
Shaft weight [kg]:                         0.07

****** Current, Losses & Efficiency ***********
Current (flat topped) [A]:                 4
R.M.S. current [A]:                        2.31
Current density [A/mm^2]:                  2.87
Copper losses [W]:                         4.14
Core losses [W]:                           15.81
Motor efficiency [%]:                      80.77
Converter losses [W]:                      17.68
Converter efficiency [%]:                  88.50
System efficiency [%]:                     71.48
```

Fig. A.9   DesignSRM- output design sheet for SRM II

Bibliography

Books

[1] Bahram, A. "Variable Reluctance Machines-Analysis Design and Control". *Jouve, Paris,* June 2003.

[2] Grote, K.-H., Feldhusen, J.: „Dubbel Taschenbuch für den Maschinenbau". Springer Verlag Berlin, 20. Auflage, 2005

[3] Henneberger, G., Viorel, J.A.: "Variable Reluctance Electrical Machine*s"*. Shaker Verlag, Aachen, 2001

[4] Krishnan R. "Switched Reluctance Motor Drives". CRC Press LLC, Boca Raton, Florida, 2001.

[5] Lappe, R.: „Handbuch Leistungselektronik: Grundlagen, Stromversorgung, Antriebe". Verlag Technik GmbH, Berlin, 5. Aufl., 1994

[6] Kreuth, H. P.: „Schrittmotoren". R. Oldenbourg Verlag GmbH, München, 1988

[7] Meeker, D. "Finite Element Method Magnetics 4.0 - User's Manual". 2004

[8] Miller T.J.E. "Switched Reluctance Motors and their control". Magna Physics Publishing, Hillsboro, 1993.

[9] Miller, T.J.E.: "Electronic Control of Switched Reluctance Machines". Newness Power Engineering Series, Reed Educational and Professional Publishing Ltd, Oxford/UK, 2001

[10] Miller, T.J.E.: "Brushless Permanent Magnet and Reluctance Motor Drives ". Oxford Science Press, 1989

[11] Miller, T.J.E.: "PC-SRD 8". SPEED Consortium, University of Glasgow, 2002

[12] Müller, G, Ponick, B.: „Grundlagen elektrischer Maschinen". WILEY-VCH Verlag GmbH & Co KGaA, Weinheim, 9. Aufl., 2006

[13] Müller, G.: „Theorie elektrischer Maschinen". VCH Verlagsgesellschaft mbH, Weinheim, 1. Aufl., 1995

[14] Richter, R.: „Elektrische Maschinen. Band 4 - Die Induktionsmaschinen". 2. Auflage, Verlag Birkhäuser, Basel/Stuttgart, 1954

[15] Schröder, D.: „Elektrische Antriebe – Regelung von Antriebssystemen". Springer- Verlag, Berlin, Heidelberg, New York, 2. Aufl., 2001

[16] Vogt, K.: „Elektrische Maschinen: Berechnung rotierender elektrischer Maschinen". VEB Verlag Technik, Berlin, 4. Aufl., 1988

[17] Wiedemann, E., Kellenberger, W.: „Konstruktion elektrischer Maschinen". Springer Verlag Berlin/Heidelberg/New York, 1967

[18] Wolff, J.: „Drehzahlveränderbarer Industrieantrieb mit geschaltetem Reluktanzmotor". Verlag Mainz, Wissenschaftsverlag, Aachen, 1. Aufl., 1999

Thesis

[19] Backhaus, K., Reinert, J., Link, L.: „Spannungseinprägendes Direktantriebssystem mit Schnelllaufender geschalteter Reluktanzmaschine". Aachener Beiträge des ISEA Band 14, Dissertation der RWTH Aachen, Verlag der Augustinus Buchhandlung, 1995

[20] Bae, H.K.: "Control of Switched Reluctance Motors Considering Mutual Inductance". Ph.D. thesis, Bradley Department of Electrical and Computer Engineering, Virginia Tech., Blacksburg, VA, 2000

[21] Bosch, V.: „Elektronisch kommutiertes Einzelspindelantriebssystem". D93 (Diss. Universität Stuttgart) Shaker Verlag, Aachen, 2001

[22] Brösse, A.: „Sensorloser Betrieb eines geschalteten Reluktanzmotors mittels Kalman Filter". D 82 Diss. RWTH Aachen, Shaker Verlag, Aachen, 1. Aufl., 1998

[23] Fehn, A.: „Modellierung und Regelung von Stellantrieben mit geschalteten Reluktanzmotoren". VDI Fortschrittsberichte, Bd. 1061, VDI Verlag GmbH, Stuttgart, 2005

[24] Gao, Y.: "Speed Control of Switched Reluctance Motors". Master Thesis, Department of Electrical and Electronic Engineering The Hong Kong University of Science and Technology, 2000

[25] Gotovac, S.: „Geschalteter Reluktanzmotor für Positionierantriebe". Dissertation, TU Berlin, 1994

[26] Greif, A.: „Untersuchung an geschalteten Reluktanzantrieben für Elektrofahrzeuge". Universität der Bundeswehr München, Neubiberg 2000

[27] Güngör, S.: „Ein Verfahren zur Auslegung von geschalteten Reluktanzmaschinen". D 83 Diss. Technische Universität Berlin, Verlag Dr. Köster, 1. Aufl., 2000

[28] Hering, T.: "Switched Reluctance Motor als Stellantrieb (2004)". Masterarbeit HTW Dresden, 2004

[29] Kim, J.: „Entwurf und Bau einer geschalteten Reluktanzmaschine in Außenläuferausführung". D 83 Diss. Technische Universität Berlin, Verlag Dr. Köster, 1. Aufl., 2001

[30] Materu, P.N., "Design and Steady-state Analysis of the Switched Reluctance Motor Drive", Ph.D. Dissertation, Virginia Tech, 1989

[31] Pfeiffer, G.: „Analyse, Berechnung und Betriebsverhalten von permanent-magnetischen Gleichpol-Schrittmotoren". D 17 Diss. Technische Hochschule Darmstadt, 1983

[32] Protiwa, F.: "Vergleich dreiphasiger Resonanzwechselrichter in Simulation und Messung". Aachener Beiträge des ISEA Band 18, Dissertation der RWTH Aachen, Verlag der Augustinus Buchhandlung, 1997

[33] Reinert, J.: „Optimierung der Betriebseigenschaften von Antrieben mit geschalteter Reluktanzmaschine". D 82 Diss. RWTH Aachen, Verlag der Augustinus Buchhandlung im Besitz des Verlags Mainz, 1998

[34] Risse, S.: „Entwicklung einer geschalteten Reluktanzmaschine als Elektrofahrzeugantrieb". D 82 Diss. RWTH Aachen, Shaker Verlag, Aachen, 1. Aufl., 2002

[35] Rolim, L.G.B.: 'Investigation of a drive system: soft-switching converter and switched reluctance motor". Technische Universität Berlin, Dissertation D83, Berlin, 1997

[36] Staley, A. M.: "Design and Implementation of a Novel Single-Phase Switched Reluctance Motor Drive System". Thesis for the degree of Master of Science, Blacksburg, Virginia, 2001

[37] Steiert, U.: „Drehmomentsteuerung einer Reluktanzmaschine mit beidseitig ausgeprägten Polen und geringer Drehmomentwelligkeit". Dissertation TH Karlsruhe, 1992

[38] Vijayraghavan, P.: "Design of Switched Reluctance Motors and Development of a Universal Controller for Switched Reluctance and Permanent Magnet Brushless DC Motor Drives", Dissertation Virginia Polytechnic Institute and State University, Blackburn, Virginia, 2001

[39] Walter, S.: "Entwicklung miniaturisierter elektrodynamischer Energiewandler mit Reluktanzläufer". D 83 Dissertation Technische Universität Berlin, 2004

[40] Yinghui, L.: "Instantaneous torque control of Switched Reluctance Motors". Thesis for the Master of Science degree, University of Tennessee, Knoxville, 2002

Papers and other Publications

[41] Albach, M., Brockmeyer, A., Dürbaum, T. "Remagnetization losses of ferrite materials used in power electronic applications," in Proc PCIM'96, Nurenberg, Germany, 1996.

[42] Albach, M, Dürbaum, T., Brockmeyer, A.: "Calculating core losses in Transformers for arbitrary magnetization currents - A comparison of different approaches," Proceedings of the IEEE PESC'96, vol. 78, pp. 1463–1468, June 1996

[43] Anwar, M.N., Husain, I., Radun, A.V.: "A Comprehensive Design Methodology for Switched Reluctance Machines". IEEE Transactions on Industry Applications, Vol. 37, No. 6, 2001

[44] Anwar, M.N., Husain, I.: "Radial Force Calculation and Acoustic Noise Prediction in Switched Reluctance Machines". IEEE Transactions on Industry Applications, Vol. 36, No. 6, Nov./Dec. 2000

[45] Anwar M.N., Husain I.: "Design Perspectives of a Low Acoustic Noise Switched Reluctance Machine". Industry Applications Conference, 2000. Conference Record of the 2000 IEEE, Rome, Italy

[46] Arumugam, R., Lindsay, J.F., Krishnan, R.: "Sensitivity of Pole Arc/Pole pitch ratio on Switched Reluctance Motor Performance". Proc. IEEE IAS Annual Meeting., Pittsburgh, Oct. 1988.

[47] Backhaus, K., Reinert, J., Link, L.: "Investigations on a High-Speed Switched Reluctance drive Incorporating Amorphous Iron". European Power Electronics Conference (EPE), Vol. 1, 1995

[48] Bahram, A. "Variable Reluctance Machines - Analysis Design and Control". Jouve, Paris, June 2003.

[49] Barnes, M., Pollock, C.: "Power electronic converters for switched reluctance drives". IEEE Transactions on Power Electronics, vol. 13, no. 6, Nov. 1998

[50] Bass, J.T., Ehsani, M., Miller, T.J.E., Steigerwald, R.L.: "Development of a Unipolar Converter for Variable Reluctance Motor Drives". IEEE Transactions on Industry Applications, pp. 1062-1068, 1985

[51] Becker, J.J.: "Magnetization changes and losses in conducting ferromagnetic materials," J. Appl. Phys., vol. 34, pp. 1327–1332, Apr. 1963.

[52] Bienkowski, J., Gajewski, M., Szczypior, J., Rogalski, A.: "Wpływ parametrów konstrukcyjnych na moment obrotowy przełączalnego silnika reluktancyjnego". XXXVIII Miedzynarodowe Sympozjum Maszyn Elektrycznych 18-21 czerwca 2002. Cedzyna-Kielce

[53] Bienkowski, K., Szczypior, J., Bucki, B., Biernat, A., Rogalski, A.: "Influence of geometrical parameters of Switched Reluctance Motor on electromagnetic torque". Berichte und Informationen HTW Dresden, ISSN 1433-4135, 1/2002

[54] Blanqué, B., Perat, J.I., Andrada, P., Torrent, M.: "Improving efficiency in switched reluctance motor drives with online control of turn-on and turn-off angles". EPE 2005, Dresden, Germany 2005

[55] Boivie, J.: "Losses in a small Switched Reluctance Machine". Licentiate-Thesis, KTH Stockholm, 1995

[56] Boivie, J.. "Iron Loss Model and Measurements of the Losses in a Switched Reluctance Motor ". IEEE Sixth International Conference on Electrical Machines and Drives, Publ. No. 376, September 1993

[57] Branco, Costa P.J.: "Influence of Magnetic Nonlinearities on Simulation Accuracy of Switched Reluctance Motor Models". Systems and Control: Theory and Application, pp. 403-408, World Scientific and Engineering Society Press, Danvers, USA, 2000

[58] Brockmeyer, A.: "Dimensionierungswerkzeug für magnetische Bauelemente in Stromrichteranwendungen," Ph.D. Dissertation (in German), Inst. Power Electron., Aachen Univ. Technol., Aachen, Germany, 1997.

[59] Brockmeyer, A, Reinert, J., De Doncker, Rik W.A.A.: "Calculation of Losses in Ferro- and Ferrimagnetic Materials Based on the Modified Steinmetz Equation". IEEE Transactions an Industry Applications, Vol. 37, No. 4, July/August 2001

[60] Chalmers, B.J.: "Electric Motor Handbook". Butterwoth and Co., 1988

[61] Chancharoensook, P., Rahman, M.F.: "A Modified Switching Strategy for Asymmetric Half-Bridge Converters for Switched Reluctance Motor Drives". Proceedings of the Australasian Universities Power Engineering Conference (AUPEC 2003), Christchurch, NEW ZEALAND, Sep. 2003. CD

[62] Chen, D. Y.: "Comparison of high frequency magnetic core losses under two different driving conditions: A sinusoidal voltage and a square wave voltage". IEEE Power Electronics Specialists Conference (PESC) '78, pp. 237-241, 1978

[63] Cheok, D.C., Ertugrul, N.: "Computer-based automated test measurement system for determining magnetization characteristics of Switched Reluctance Motors". IEEE Transaction on Instrumentation and Measurement, Vol. 50, No. 3, June 2001

[64] Corda, J., Stephenson J.M.: "Analytical Estimation of the Minimum and Maximum Inductances of a Double-Salient Motor". Proceedings of the International Conference on Stepping Motors and Systems, University of Leeds, September 1979

[65] Dahmane, M., Meibody-Tabar, F., Sargos, F.-M.: "An adapted converter for switched reluctance motor/generator for high speed Applications". IEEE Transactions on Industry Applications, vol. 3, pp. 1547-1554, October 2000

[66] Davis, R.M.: "Variable Reluctance Rotor Structures - Their Influence on Torque Production". IEEE Transactions on Industrial Electronics, Vol. 39, No. 2, April 1992

[67] Davis, R.M., Ray, W.F., Blake, R.J.: "Inverter drive for switched reluctance motor: circuits and component ratings". IEEE Proceedings, Vol. 128, Pt. B, No. 2, pp. 126-136, 1981

[68] Davis, R.M., Al-Bahadly, I.: "Experimental Evaluation of Mutual Inductances in a Switched Reluctance Motor". Power Electronics and Variable Speed Drives Conference, IEE Conference Publ. No. 324, 1990

[69] Davis, R.M.: "A Comparison of Switched Reluctance Rotor Structures". IEEE Transactions on Industrial Electronics, Vol. 35, No. 4, November 1998

[70] De Doncker, R.W., Reinert, J., Inderka, R.: "A Novel Method for the Prediction of Losses in Switched Reluctance Machines". European Power Electronics (EPE) Conference, Vol. 3, pp. 3608-3612, 1997

[71] De Doncker, R.W., Lyons, J.P.: "An auxiliary Quasi-Resonant DC Link Inverter for Switched Reluctance Machines". European Power Electronics (EPE) Conference, Vol. 4, pp. 4.18-4.23, 1991

[72] Dürbaum, T., Albach, M.: "Core losses in transformers with an arbitrary shape of the magnetization current". Proceedings of the EPE'95, vol. 1, Seville, Spain'95, pp. 1.171–1.176, 1995

[73] Ehsani, M., Husain, I.: "Torque Ripple Minimization in Switched Reluctance Motor Drives by PWM Current Control". IEEE Transactions on Power Electronics, Vol. 11, No. 1, January 1996

[74] Ehsani, M., Fahimi, B.: "Elimination of Position Sensors in Switched Reluctance Motor Drives: State of the Art and Future Trends". IEEE Trans. on Industrial Electronics, Vol. 49, pp.40-47, Feb, 2002

[75] Elliot, C. R., Stephenson, J. M., McClelland, M. L.: "Advances in switched reluctance drive system dynamic simulation". Proceedings of EPE '95, Vol. 3, pp. 622-626, 1995

[76] Ertogrul, N., Cheok, A.D.: "Indirect angle Estimation in Switched Reluctance Motor Drive Using Fuzzy Logic Based Motor Model". IEEE Transactions on Power Electronics, Vol. 15. pp. 1029-1044, Nov. 2000

[77] Ertogrul, N., Cheok, A.D.: "Indirect angle Estimation in Switched Reluctance Motor Drive Using Fuzzy Logic Based Motor Model". IEEE Transactions on Power Electronics, Vol. 15. pp. 1029-1044, Nov. 2000

[78] Fahimi B., Ehsani M.: "Spatial Distribution of Acoustic Noise Caused by Radial Vibration in Switched Reluctance Motors: Application to Design and Control". Conference Record of the 2000 IEEE, Rome

[79] Faiz, J., Harris, M.R., Finch, J.W.: "Two-dimensional finite element analysis of multi-tooth per stator pole switched reluctance motor-four teeth per stator pole". IEEE Transactions on Industry Applications, vol. 1, No. 10, October 1990

[80] Faiz, J., Finch, J.W.: "Aspects of design optimisation for switched reluctance motors". IEEE Transactions on Energy Conversion, Vol. 8, No. 4, December 1993

[81] Faizul, M., Husain, M.I.: "Design and Performance Analysis of a Switched Reluctance Motor for Low Duty Cycle Operation". IEEE Transactions on Industry Applications. Vol. 39, No. 3, May/June 2003

[82] Farzenehfard, H., Krishnan, R.: "A fully controlled converter for switched reluctance motor". Proceedings of the VPEC Ann. Sem., November 1986

[83] Ferrero, A., Raciti, A., Urzi, C.. "An indirect method for the characterization of variable reluctance motors". IEEE Transaction on Instrumentation and Measurement, Vol. 42, No. 6, December 1993

[84] Finch, J.W., Faiz, J., Metwally, H.M.B.: "Design study of switched reluctance motor performance". IEEE Transactions on Industry Applications, vol. 1, pp. 242-248, October 1992

[85] Franceschini, G., Pirani, S., Rinaldi, M., Tassoni, C.: "SPICE-assisted simulation of controlled electric drives: an Application to switched reluctance drives". IEEE Transactions on Industry Applications, Vol. 27, No. 6, November/December 1993

[86] Fuengwarodsakul, H.N., Bauer, S.E., Krane, J., Christian, P.D., De Doncker, R.W.: "Sensorless Direct Instantaneous Torque Control for Switched Reluctance Machines". Proceedings of the EPE 2005, Dresden, Germany 2005

[87] Fuengwarodsakul, N.H., Menne, M., Inderka, R.B., De Doncker, R.W.: "High performance four-quadrant switched reluctance traction drive based on DITC". Industry Applications Conference, 2004. 39th IAS Annual Meeting. Conference Record of the 2004 IEEE, Volume 3, 3-7 Oct. 2004, Page(s):1602 - 1609

[88] Fuengwarodsakul, N.H., Bauer, S., Tsafak, O., De Doncker, R.W.: "Characteristic Measurement System for Automotive Class Switched reluctance Machines". Proceedings of the EPE 2005, Dresden, Germany

[89] Gallegos-Lopez, G., Kjaer, P.C., Miller, T.J.E.: "High-grade Position Estimation for SRM drives using Flux linkage/Current Correction Model". IEEE Transactions on Industry Applications, Vol. 35, pp. 859-869, July/August 1999

[90] Garrigan N.R., Soong W.L., Stephens C.M., Storace A., Lipo T.A.: "Radial force characteristics of a switched reluctance machine". Industry Applications Conference, 1999. Thirty-Fourth IAS Annual Meeting. Conference Record of the 1999 IEEE, Phoenix, AZ, USA

[91] Gradzki, P.M., Jovanovic, M.M., Lee, F.C.: "Computer aided design for high-frequency power transformers". Proceedings of the IEEE APEC'90, pp. 336–343, 1990

[92] Graham, Jr., C.G.: "Physical origin of losses in conducting ferromagnetic materials (invited)," J. Appl. Phys., vol. 53, pp. 8276–8280, Nov. 1982.

[93] Harris, W.A.: "Switched Reluctance Motor Control Circuit with Energy Recovery Capability". U.S. Patent No. 5,075,610, Dec. 24, 1991

[94] Heinze, R.: "Klein- und Kleinstantriebe mit viel drive". Antriebstechnik etz, pp. 14-15, Heft 11-12/2001

[95] Henriques, L. O. P., Rolim L. G. B., Suemitsu, W. I., Branco, P. J. C.: "Proposition of an Offline Learning Current Modulation for Torque-Ripple Reduction in Switched Reluctance Motors: Design and Experimental Evaluation". IEEE Transactions on Industrial Electronics, Vol. 49, No. 3, June 2002

[96] Higuchi, T., Fiedler, J., De Doncker, R.: "On the Design of a Single-phase Switched Reluctance Motor". International Electric Machines and Drives Conference, 2003 (IEMDC03), Madison, WI, USA, 2003

[97] Hiller, M.: "Dynamic Torque Control for Switched Reluctances Drives based on a new Online Machine Model". Proceedings of the EPE 2005, Dresden, Germany 2005

[98] Holub, M.: „Das Matlab/Simulink – Simulationsmodell der Geschalteten Reluktanzmaschine". Aus dem Jahresbericht der Technischen Universität Braunschweig, 2002

[99] Hossain, S., Husain, I., Klode, H., Omekanda, A., Gopalakrishan, S.: "Four quadrant and zero speed sensorless control of a switched reluctance motor". Industry Applications Conference, 2002. 37th IAS Annual Meeting. Conference Record of the Volume 3, 13-18 Oct. 2002 Page(s): 1641 – 1646

[100] Hur, J., Kang, G.H., Lee, J.Y., Hong, J.P., Lee, B.K.: "Design and Optimization of High Torque, Low Ripple Switched Reluctance Motor with Flux Barrier for Direct Drive". IEEE Transactions on Industry Applications. Vol. 39, No. 3, pp. 713-719, May/June 2003

[101] Husain,*I.,* Radun*, A.,* Nairus, J.: "Fault Analysis and Excitation Requirements for Switched Reluctance Generators". IEEE Transactions on energy conversion, Vol. 17, No. 1, March 2002

[102] Husain, I., Radun, A., Nairus, J.: "Unbalanced Force Calculation in Switched-Reluctance Machines". IEEE Transactions on Magnetics, Vol. 36, No. 1, January 2000

[103] Husain, I., Ehsani, M.: "Torque Ripple Minimization in Switched Reluctance Motor Drives by PWM Current Control". IEEE Transactions on Power Electronics, Vol. 11, No. 1, January 1996

[104] Ichinokura, O., Onda, T., Kimura, M., Watanabe, T., Yanada, T., Guo, H. J.: "Analysis of dynamic characteristics of switched reluctance motor based on SPICE". IEEE Transactions on Magnetics, Vol. 34, No. 4, pp. 2147-2149, 1998

[105] IEC International Electrotechnical Commission, "Dimensions and output ratings for rotating electrical machines – Frame numbers 56 to 400 and flange numbers F55 to F1080", Publication 72, Geneva, Switzerland, 1971.

[106] Ilic-Spong, M., Miller, T.J.E., MacMinn, S.R, Thorp, J.S.: "Instantaneous torque control of electric motor drives". IEEE Transactions on Power Electronics, Vol. 2. No. 1, pp. 55-61, 1987

[107] Inderka, R., Menne, M. and De Doncker, R.W.: "Generator operation of a switched reluctance machine drive for electric vehicles". Proceedings of the European Power Electronics and Applications Conference (EPE'99), Lausanne, 1999

[108] Jordan, H.: "Die ferromagnetischen Konstanten für schwache Wechselfelder," Elektr. Nach. Techn., 1924.

[109] Khalil, A., Husain, I., Hossain, S.A., Gopalakrishnan, S., Omekanda, A., Lequesne, B.: "A hybrid sensorless SRM drive with eight- and six-switch converter topologies". Industry Applications Conference, 2004. 39th IAS Annual Meeting. Conference Record of the 2004 IEEE, Volume 3, 3-7 Oct. 2004, Page(s):1618 – 1624

[110] Kim, E.S., Lee, K.C., Rim, W.H.: "A choppingless converter for switched reluctance motor with unity power factor and sinusoidal input current". IEEE PESC, pp. 500-5007, 1994

[111] King-Jet Tseng, Shuyu Cao, Jijiu Wang: "A New Hybrid *C*-Dump and Buck-Fronted Converter for Switched Reluctance Motors". IEEE Transactions on Industrial Electronics, Vol.47, No. 6, December 2000

[112] Koibuchi, K., Ohno, T., Sawa, K.: "An Approach for Optimal Design of Switched Reluctance Motor by Finite Elemet Method". IEEE Conference on Electromagnetic Filed Compuation, pp. 143-147, 1996

[113] Krishnan, R., Bharadwaj, A.S., Materu, P.N.: "Computer-Aided Design of Electrical Machines for Variable Speed Applications". IEEE Transactions on Industrial Electronics, Vol.35, No. 4, November 1988

[114] Krishnan, R., Materu, P.: "Measurement and instrumentation of a Switched Reluctance Motor". IEEE Conferences on Industry Application Society, pp. 116-121, October 1989

[115] Krishnan, R., Materu, P.N.: "Design of a Single-Switch-per-Phase Converter for Switched Reluctance Motor Drives". IEEE Transactions on Industrial Electronics, Vol. 37, No. 6, December 1990

[116] Krishnan, R.: "A novel converter topology for switched reluctance motor drives". Conference Record of the IEEE PESC, Baveno, Italy, pp. 1811-1816, 1996

[117] Krishnan, R., Arumugam, R., Lindsay, F.F.: "Design Procedure for Switched-Reluctance Motors". IEEE Transactions on Industry Applications, Vol.24, No. 3, May/June 1998

[118] Kuß, H., Schuffenhauer, U., Wichert, T.: „Entwicklung einer Spindelmotorbaureihe". Fortschrittsbericht 3, Dresden, Oktober 2006

[119] Lamke, M.: „Technische Anforderungen an ein System zur Automatisierung eines HASG für Nutzfahrzeuge mittels elektromechanischer Aktuatorik". ZF Friedrichshafen AG, 2005

[120] Laube, F.: „Simulation Geschalteter Reluktanzmaschinen (SRM) mit SIMPLORER®". Aus dem Jahresbericht der Technischen Universität Braunschweig, 2001

[121] Lawrenson, P.J.: "Variable-speed Switched Reluctance Motors". IEE Proceedings, Vol. 127, Pt. B, No. 4, pp. 253-265, July 1980

[122] Le-Huy, H., Viarouge, P., Slimani, H.: "A Current Controlled Quasi-Resonant Converter for Switched Reluctance Motor". IEEE Transactions on Industrial Electronics, Vol. 38, No. 5, 1991

[123] Le-Huy, H., Viarouge, P., Francoeur, B.: "A novel unipolar converter for Switched Reluctance Motor". IEEE Transactions on Power Electronics, Vol. 5, No. 4, 1990

[124] Liuchen, Chang: "Design Procedures of a Switched Reluctance Motor for Automobile Applications". IEEE Canadian Conference on Electrical and Computer Engineering. Vol. 2, pp. 947-950, May 1996

[125] Löwenstein, L., Henneberger, G.: „Modellierung von Reluktanzmaschinen mit SIMPLORER". SIMPLORER Workshop 2001, Chemnitz 2001

[126] Lyons, J.P., MacMinn, S.R., Preston, M.A.: "Flux/Current Methods for SRM Rotor Position Estimation". IEEE IAS Annual Meeting, pp. 482-487, 1991.

[127] Materu, P., Krishnan, R., Farzenehfard, H.: "Steady-state analysis of the variable speed switched reluctance motor drive". IEEE Transactions on Industrial Electronics, Vol. 36, No. 4, November 1986

[128] Materu, P., Krishnan, R.: "Analytical prediction of SRM inductance profile and steady-state average torque". Conference Record of the 1990 IEEE Industry Applications Society Annual Meeting (Cat. No.90CH2935-5), p. 214-23 vol.1, Seattle, WA, USA; 7-12 Oct. 1990.

[129] Materu, P.N., Krishnan, R.: "Estimation of Switched Reluctance Motor Losses". IEEE Transactions on Industry Applications. Vol. 28, No. 3, May/June 1992

[130] Mese, E. Torrey, D.A.: "An approach for sensorless position estimation for switched reluctance motors using artificial neural networks". IEEE Transactions on Power Electronics, Vol. 17, No. 1, January 2002

[131] Michaelides, A.M., Pollock, C.: "Modelling and design of switched reluctance motors with two phases simultaneously excited". IEE Proceedings Electric Power Applications, Vol. 143, No. 5, 1996

[132] Miller, T.J.E.: "Converter Volt-Ampere Requirements of the Switched Reluctance Motor Drive". IEEE Transactions, Bd. IA-21, 1985

[133] Miller, T. J. E., McGilp, M.: "Nonlinear theory of the switched reluctance motor for rapid computer-aided design". Proc. Inst. Elect. Eng., pt. B, vol. 137, no. 6, pp. 337-347, Nov. 1990

[134] Miller, T.J.E., Glinka, M., McGilp, M., Cossar, C., Gallegos-Lopez, G., Ionel, D., Olaru, M.: "Ultra-fast model of the switched reluctance motor". Thirty-Third IAS Annual Meeting on Industry Applications Conference, pages 319-326, October 1998

[135] Moallem, M., Ong, C.-M.: "Predicting the steady-state performance of a switched reluctance machine". IEEE Transactions on Industry Applications, Vol. 27, No. 6, Nov./Dec. 1991

[136] Moallem, M., Chee-Mun Ong, Unnewehr, L.E.: "Effect of Rotor Profiles on the Torque of a Switched-Reluctance Motor". IEEE Transaction on Industry Applications, Vol. 28, No. 2, March/April 1992

[137] Moghbelli, H.H., Adams, G.E., Hoft, R.G.: "Prediction of instantaneous and steady-state torque of the switched reluctance motor using finite element method". IEEE Transactions on Industry Applications, Vol. 1, pp. 59-70, October 1988

[138] Moreira, J.C., Lipo, T.A.: "Simulation of a four phase switched reluctance motor including the effects of mutual coupling," Electric Machines Power Syst., vol. 16, pp. 281–299, 1989

[139] Neagoe, C., Foggia, A., Krishnan, R.: "Impact of pole tapering on the electromagnetic torque of the switched reluctance motor". IEEE International Electric Machines and Drives Conference Record, IEMDC 1997, pp. WA1 2.1-2.3

[140] Omekanda, A.M., Broche, C., Renglet, M.: "Calculation of the Electromagnetic Parameters of a Switched Reluctance Motor Using an Improved FEM–BIEM—Application to Different Models for the Torque Calculation". IEEE Transactions on Industry Applications, Vol. 33, No. 4, July/August 1997

[141] Ometto, A., Julian, A., Lipo, T.A.: "A novel low cost variable reluctance motor drive". Int. Conf. Electric Machines Rec., vol. 1, pp. 77–79, 1994

[142] Ong, C-M.: "Dynamic Simulation of Electric Machinery using Matlab/Simulink". Englewood Cliffs, NJ: Prentice-Hall, 1998

[143] Ozoglu, Y., Garip, M., Mese, E.: "New pole tip shapes mitigating torque ripple in short pitched and fully pitched switched reluctance motors". Industry Applications Conference, 2002. 37th IAS Annual Meeting. Conference Record of the Volume 1, 13-18 Oct. 2002, Page(s): 43 - 50

[144] Pekarek, S. D., Wasynczuk, O., and Hegner, H. J.: "An efficient and accurate model for the simulation and analysis of synchronous machine/converter systems". IEEE Trans. on Energy Conversion, 1998

[145] Pillay, P., Samuido, R., Ahmed, M., Patel, R.: "A chopper controlled SRM drive for reduced acoustic noise and improved ride through capability using super capacitors". IEEE Transactions on Industrial Applications, Vol. 31, No. 5, November 1986

[146] Pollack , C., Williams, B.W.: "Power converter circuits for switched reluctance motors with the minimum number of switches". Proc. Inst. Elect. Eng., vol. 137, pt. B, no. 6, pp. 373–384, 1990

[147] Preston M.A., Lyons, J.P.: "A switched reluctance motor model with mutual coupling and multi-phase excitation," IEEE Trans. Magn., vol. 27, pp. 5423–5425, Nov. 1991

[148] Radun, A.V.: "Generating with the switched reluctance motor". IEEE Transactions of Applied Power Electronics, pp. 41-46, 1994

[149] Radun, A.V..: "Switched reluctance starter/generator modelling results". Proceedings of SAE Aerospace Atlantic Conference, paper 951407, 1995

[150] Radun, A. V.: "Design Considerations for the Switched Reluctance Motor", IEEE Transaction on Industry Applications, Vol. 31, No. 5, September/October 1995

[151] Radun, A., "Analytical calculation of the switched reluctance motor's unaligned inductance", IEEE Transactions on Magnetics, Vol. MAG-35, No. 6, pp. 4473-4481, Nov. 1999

[152] Radun, A., "Analytically computing the flux linked by a switched reluctance motor phase when the stator and rotor poles overlap". IEEE Transactions on Magnetics, Vol. MAG-36, No. 4, pt. 2, July 2000.

[153] Ramshaw, R., Van Heeswijk, G.: "Energy Conversion: Electric Motors and Generators". Saunders College Publishing, 1990

[154] Rasmussen, P.O., Andersen, G.: "Fully automatic characterization system for Switched Reluctance Motors". International Conference on Electrical Machines (ICEM), Vol. 3, pp. 1692-1698, 1998, Istanbul, Turkey

[155] Raulin, V., Radun, A., Husain, L.: "Modelling of losses in switched reluctance machines". IEEE Transactions on Industry Application, Vol. 40, No. 6, Nov./Dec. 2004

[156] Reutling, K.M.: „Elektronische Einzelantriebssysteme für Textilmaschinen". ETZ Antriebstechnik, Heft 19, 1997

[157] Rim, G.-H., Kim, W.-H., Cho, J.-G.: "ZVT Single Pulse-Current Converter for Switched Reluctance Motor Drives". IEEE Applied Power Electronics Conference (APEC), Vol. 2, pp. 949-955, 1996

[158] Rizk, J., Nagrial, M.H., Hellani, A.: "Design and performance of switched reluctance motors". IEEE Transactions on electrical machines and systems, Vol. 1, pp. 211-216, November 2003

[159] Sahin, F., Ertan, H.B., Leblebicioglu, K.: "Optimum Geometry for Torque Ripple Minimization of Switched Reluctance Motors". IEEE Transaction on Energy Conversion, Vol. 15, No. 1, March 2000

[160] Sanada M., Morimoto S., Takeda Y.: "Novel Rotor Pole Design of Switched Reluctance Motors to Reduce the Acoustic Noise". Industry Applications Conference, 2000. Conference Record of the 2000 IEEE, Rome, Italy

[161] Sawata, T., Kjaer, P.C., Cossar, C., Miller, T.J.E.: "A control strategy for the switched reluctance generator". ICEM'98, Istanbul, Vol. 3, pp. pp. 2131-2136, September 1998

[162] Schülting, L., Brockmeyer, A.: "Modelling of dynamic losses in magnetic material". Proceedings of the EPE'93, vol. 3, Brighton, U.K., pp. 112–117, 1993

[163] Schulze, M.: Leistungselektronik: Moderne Bauelemente der Leistungselektronik. Technische Fachhochschule Berlin- Fernstudieninstitut, 1. Aufl. 1994

[164] Severns, R. "HF-core losses for nonsinusoidal waveforms". Proceedings of the HFPC, pp. 140–148, 1991

[165] Sharma, V.K., Murthy, S.S., Singh, B.: "An improved method for the determination of saturation characteristics of Switched Reluctance Machines". IEEE Transaction on Instrumentation and Measurement, Vol. 48, No. 5, October 1999

[166] Sitsha, L.M.M., Kamper, M.J.: "Some Design Aspects of Tapered and Straight Stator Pole 6/4 Switched Reluctance Machine". Proceedings of the 5th IEEE AFRICON Conference, Cape Town, South Africa, 1999; pp. 683 - 686.

[167] Skvarenina, Wasynczuk, Krause: "Simulation of a switched reluctance generator/more electric aircraft power system". Proceedings of ICEC, paper 96398, 1996

[168] Soares, F., Branco, C.: "Simulation of a 6/4 switched reluctance motor based on Matlab/Simulink environment". IEEE Transactions on Aerop. Electronic Systems, pp. 989-1009, 2000

[169] Sood, P.K.: "Power Converter for a Switched Reluctance Motor". U.S. Patent No. 5,115,181, May, 1992

[170] Stephenson, J.M., Khazendar, M.A.: "Saturation in doubly salient reluctance motors". IEEE Transactions on electric Power Applications, Vol. 136, No. 1, January 1989

[171] Srinivas, K.N., Arumugam, R.: "Dynamic characterization of switched reluctance motor by computer aided design and electromagnetic Transient simulation". IEEE Trans. on Magnetics, Vol. 39, No. 3, 2003

149

[172] Takayama, K., Takasaki, Y., Ueda, R., Sonoda, T., Iwakane, T.: "A new type switched reluctance motor". Conf. Record of the Industry Applications Society Annual Meeting, Vol. 1, pages 71-78, October 1988

[173] Tang, Y., "Characterization, Numerical Analysis, and Design of Switched Reluctance Motors". IEEE Transactions on Industry Applications, vol. 33, No. 6, pp. 1544-1552, Nov./Dec. 1997.

[174] Uematsu, T., Hoft, R.G.: "Resonant Power Electronic Control of Switched Reluctance Motor for Electric Vehicle Propulsion". IEEE Power Electronics Specialists Conference (PESC), Vol. 1, pp. 264-269, 1995

[175] Vijayraghavan, P., Krishnan, R.: "Noise in Electric Machines: A Review". IEEE Transactions on Industry Applications, Vol. 35, No. 5, September/October 1999

[176] Vukosavic, S., Stefanovic, V.R.: "SRM inverter topologies: a comparative evaluation". IEEE Transactions on Industry Applications, vol. 27, no. 6, Nov.-Dec. 1991

[177] Wei Wu, Dunlop, J.B., Collocott S.J., Kalan, B.A.: "Design Optimization of a Switched Reluctance Motor by Electromagnetic and Thermal Finite-Element Analysis". IEEE Transactions on Magnetics, Vol. 39, No. 5, September 2003

[178] Wichert, T.: "Influence of power electronics on design of Switched Reluctance Machines". Proceedings of the EPE 2005, Dresden, Germany 2005

[179] Williams, B.W., Pollock, C.: "A unipolar converter for a switched reluctance motor". IEEE Transactions on Industry Applications, Vol. 26, No. 2, 1990

[180] Wu, W., Kalan B.A., Lovatt, H.C.: "Time-stepping Analysis of a Switched Reluctance Motor by Coupling Electrical Circuit and Electromagnetic Finite Element Methods". Sixth International Conference on Electrical Machines and Systems, 2003. ICEMS 2003.

[181] Wu, C.Y., Pollack, C.: "Analysis and Reduction of Vibration and Acoustic Noise in the Switched Reluctance Drive". IEEE Transactions on Industry Applications, Vol. 31, No. 1, pp. 91-98, 1995

[182] Zhangjun Tang, Pillay, P., Yicheng Chen, Omekanda, A.M.: "Prediction of electromagnetic forces and vibrations in SRMs operating at steady state and Transient speeds". Industry Applications Conference, 2004. 39th IAS Annual Meeting. Conference Record of the 2004 IEEE, Volume 1, 3-7 Oct. 2004

Vita

Torsten Wichert was born on August 9, 1978 in Bad Frankenhausen, Germany. He received his 'Abitur' certificate in 1997 from the Kyffhäusergymnasium Bad Frankenhausen. After one year in community service he entered 1998 to the University of Applied Science Dresden (FH), studying towards a graduate engineer in Electrical Engineering in 2002. In October 2003 he received his Master's degree. Since 2004 he is working as scientific assistant at the Centre of applied Researches and Technology ZAFT Dresden e.V. His research interests include rotary Switched Reluctance Machines and their control and vector control of high speed induction machines. A further research project deals with the development of high resolution measurement electronics for nuclear γ-rays.

Życiorys

Torsten Wichert urodził się 9 sierpnia 1978 r. w Bad Frankenhausen – Niemcy. Zrobił maturę w 1997 r. w Kyffhäusergymnasium w Bad Frankenhausen. Po rocznej służbie społecznej w roku 1998 rozpoczął studia na Hochschule fuer Technik und Wirtschaft (FH) w Dreźnie. W roku 2002 otrzymal tytuł inżyniera a w grudniu 2003 roku tytuł magistra inżyniera. Od roku 2004 pracuje jako pracownik naukowy w Zentrum für Angewandte Forschung und Technologie (ZAFT) w Dreźnie. Do jego naukowych zainteresowań należą przełączane silniki reluktancyjne i ich sterowanie jak również sterowanie wektorowe wysoko-prędkościowych maszyn indukcyjnych. Obecnie zajmuje się projektem elektronicznego urządzenia o wysokiej rozdzielczości do pomiaru nuklearnych promieni γ.